Dynamic force measurement for milling using a constrained motion dynamometer and time domain signal analysis

A Dissertation Presented for the
Doctor of Philosophy
Degree
The University of Tennessee, Knoxville

Jose Alfonso Nazario Moreno
August 2025

ACKNOWLEDGEMENTS

I would like to begin thanking my amazing committee members, Dr. Chad Duty, Dr. Bradley Jared, Dr. Tony Shi, and Dr. Uday Vaidya, as well as my advisor Dr. Tony Schmitz. Dr. Schmitz, I appreciate all the opportunities you have provided me and the skills I have learned along the way. Additionally, I would like to thank Dr. Mark Rubeo, Dr. Mark Buckner, and Dr. Sean Nieme for their mentorship and keeping me sane with great conversations.

I would like to thank my family, my parents Jose and Cecilia, and my godparents, Pedro and Laura, for their years of countless support. As the first member of my family to graduate from college, I thank them for the strong work habits and undying sense of humor that has gotten me to this point in life.

A large thanks is necessary to my UTK friends, lab members, and peers who have been a part of this experience for me. I would like to give a very special dedication to my first intern Dylan Pollard, Dave Roberson, Dr. Aaron Cornelius, Dr. Tim No, Dr. Josh Penney, Dr. Dustin Gilmer, Dr. Ryan Garcia, Tyler Poon, Buddy Swan, and Zach Mason for making these past four years great. And my other interns, Mac P., Alex S., Imelia MB., Josh H., Tony S., Madison S., Andrew H., Joey L., and Nathan K. I thank you all for the work you assisted me in over the past four years and I hope I wasn't too hard on you.

Go vols!

ABSTRACT

The work in this dissertation describes a new milling force measurement method utilizing a constrained-motion dynamometer (CMD), an optical displacement transducer, and processing of a time-domain displacement signal. The research objective is to produce a testing system that accurately measures milling forces using (1) displacement, (2) derived velocity, (3) derived acceleration, and (4) the structural dynamics of the CMD, which is used to measure the displacement of a flexure supported platform due to milling forces. The new knowledge obtained is the ability to derive dynamic force from time-domain displacement and the mass, damping, and stiffness modal parameters for a constrained-motion dynamometer. The outcomes will be new milling force measurement capabilities that: 1) are relevant to industry; 2) provide the foundation for a low-cost, commercially viable dynamometer; and 3) supports Industry 4.0/5.0 efforts.

This approach expands prior low-cost methods based on frequency domain filtering analysis by using time domain displacement signals and modal parameters of the dynamic system [1]. In short, measured displacement and derived velocity and acceleration will be converted to individual force components using the modal mass, damping, and stiffness values and then these force components are summed to predict the milling force. The velocity and acceleration signals will be acquired by deriving the time-based displacement signal.

The new approach will be evaluated with multiple workpiece materials and cutting tools to validate its performance. Results will be compared to identical milling force tests conducted on a commercially available dynamometer system that cost two orders of magnitude more and requires detailed knowledge of digital filtering techniques to make the best use of the data. Additionally, comparison to the prior frequency domain inverse filtering approach will be compared to determine validity of both low-cost dynamometer approaches.
Keywords: Machining, milling, time-domain, force measurements, transducers, filtering

TABLE OF CONTENTS

LIST OF TABLES

LIST OF FIGURES

CHAPTER ONE

INTRODUCTION AND PROJECT DESCRIPTION

Introduction

As industrial machine tools have become an essential tool for the development of worldwide manufacturing practices, the need for intelligent, in-process data capabilities is becoming more apparent in modern times [2], [3] . With the rise of Industry 4.0, the fourth industrial revolution, the capability to create systems where all machine operations are not only monitored, but the data is used to assist in key production decisions, diagnostics, operational maintenance, and predictive digital models of key equipment is vital. This data can also be used to determine if any cyber security invasion could be occurring, causing the machine to operate in any way other than the operator's intentions.

Although some machine tools and other industrial equipment have built in transducers and data collection systems, many entry-level, affordable machines currently in industrial settings lack the ability to capture or store the valuable data during the machine's operation schedule. This creates a need for third party solutions that can be used within operations to better understand the machine's precision movements while collecting data to benchmarked to milling parameters set within the CNC machining code.

The purpose is to provide a low-cost, third-party solution to capture multiple levels of in process milling motions, characteristics, and forces on a designed single degree of freedom (SDOF) monolithic stage all from a single displacement signal measurement. The proposed method utilizes a Finite Impulse Response (FIR) derivation filtering method of time-based displacements by means of the Park McLellan approach to derive high fidelity velocity and acceleration signals. These motion signals are combined with the systems modal parameters to measure the time-based force produced on the workpiece material [4].

Additionally, the derived forces measured on the low-cost system will be used to obtain the specific cutting coefficient of various tool-workpiece combinations and compared to results produced by the same tool-workpiece on a commercial grade force dynamometer. The results in this paper are intended to propose a robust system validation over various tools and material workpieces and compared to costly, commercially available force measurement systems.

Originality

The usage of time-based multiple motion signals and modal parameters to construct milling forces and cutting force coefficients is a novel approach. The usage of time domain signals allows for an ease of understanding the physical phenomenon occurring in the system. Prior methods utilizing complex inverse force filtering methods have been used requiring various levels of frequency domain filtering to produce forces. As a result, the direct transformation from displacement to force is only in the frequency domain [1], [5], [6]. This method for combining time-based force elements in the time domain provides a larger amount of data can be collected from a single cut compared to the frequency domain approach or commercial grade systems that output force measurement.

With this method from one cut, a user can acquire displacement, velocity, acceleration, spring force, viscous damping force, inertial force, as well as the overall milling force. Additionally, these motion and force parameters can be compared to expensive industrial grade systems that currently serve as the standard in milling [7]. Capturing forces in both the *x* and *y* milling directions can also provide the user with additional cutting force coefficients that can be used to develop physics-based simulations for the process. Overall, this novel approach will reinforce the need for cost-effective milling measurement systems in the Industry 4.0 sector.

Broader impact

The broader impact is to provide a solution for data measurement collection that can universally be used on any CNC machine tool for a lost two orders of magnitude less cost than current industrial solutions. The intention is to provide an alternative for high-cost systems to both large and small manufacturing companies and encourage the need for in-process monitoring of data. The time-based solution also allows the system to be used by a wide array of machinists and operators of all experience levels.

CHAPTER TWO

BACKGROUND AND LITERATURE REVIEW

Introduction to machining

Introduction to milling parameters and process

Prior to the introduction of automated computer numerically controlled (CNC) machines, practical, manually driven machines were developed to remove material from geometrically defined pieces of stock material commonly referred to as workpieces. The operator manually moves the machine in a certain set of directions that the machine can travel in; commonly referred to axes as shown in **Figure 2.1**. Common practices of these manual machines were later translated into CNC machining operations with higher level of control and procession. These improvements came from introducing motor driven movements and embedded transducers to accurately control the machine simultaneously in multi-axis motions.

In either manual or CNC controlled, processes that physically remove material from the workpiece are known as subtractive manufacturing processes. Compared to other subtractive manufacturing processes, such as grinding or belt sanding, the milling process is defined as the shearing of material from a workpiece using rotating tool with defined cutting edge [8]. Common types of tooling used in milling processes with defined cutting edges are endmills, shell mills, drills, and taps as shown in Error! Reference source not found.**.** These cutting tools are used to remove material under certain machining conditions, resulting in a defined geometric feature on a stock workpiece. These tools are intended to be consumable items that eventually will wear out with use. The wearing of the tooling that then cause parts to fall out of the specified tolerances or potentially damage the workpiece is not monitored [9].

In cutting operations performed by a standard milling endmill, material removal is caused by a number defined cutting edges constantly entering and exiting the workpiece. These defined cutting edge of the tool known as flutes or teeth, N_t. As the tool revolves at a certain revolution per minute, Ω, the tool is moved at a prescribed linear feed rate, f, across the material workpiece. As the endmill runs across, each tooth of the cutting tool enters and exits the material resulting in the formation of volumetrically defined pieces of material known as chips. Prior to the removal process, the operator must have a set of defined geometrical parameters set to understand the specific chip volume that will be created every tooth pass. The three common parameters set for these milling operations on a three-axis machine are known as axial depth of cut ($b/ADOC$), radial depth of cut ($a/RDOC$), and chip thickness (h). ADOC refers to the amount axial contact that the endmill will have each pass on the workpiece material; commonly in the z-direction of the machine. The endmill will have a defined cutting length provided by the manufacturer that defined the largest ADOC that can be performed along the workpiece. The RDOC is the amount of material along the radial direction of the tool, based in the x and y directions of the machine. This is commonly referred to as the percentage of radial immersion (RI), which is the cutting depth, a , over the total diameter of the tool, d, engaged in the material per individual cutting pass. Visual representations for axial and radial depth of cut are shown in **Figure 2.3**.

As the RI changes, the degree at which is tooth enters, start angle, ϕ_S , and exits, exit angle, ϕ_E,does as well. These angles are also determined depending on the orientation of cut, determining if the largest magnitude of the tooth occurs as the start of tooth engagement, conventional milling or up milling, versus at the end of tooth engagement, climb mill or down milling. Equations 1-4 represent these angles for each case along with a graphical representation shown in **Figure 2.4**. **Figures 2.5** and **2.6** depict the time domain representation of both up milling and down milling cuts.

$$\phi_{S,up\ milling} = 0\ (\text{deg})\ (1)$$

$$\phi_{S,down\ \ milling} = 180 - \cos^{-1}\left(\frac{\frac{d}{2} - a}{\frac{d}{2}}\right)(\text{deg})\ (2)$$

$$\phi_{E,up\ milling} = \cos^{-1}\left(\frac{\frac{d}{2} - a}{\frac{d}{2}}\right)\ (deg)\ (2)$$

$$\phi_{E,up\ milling} = 180\ (\text{deg})\ (4)$$

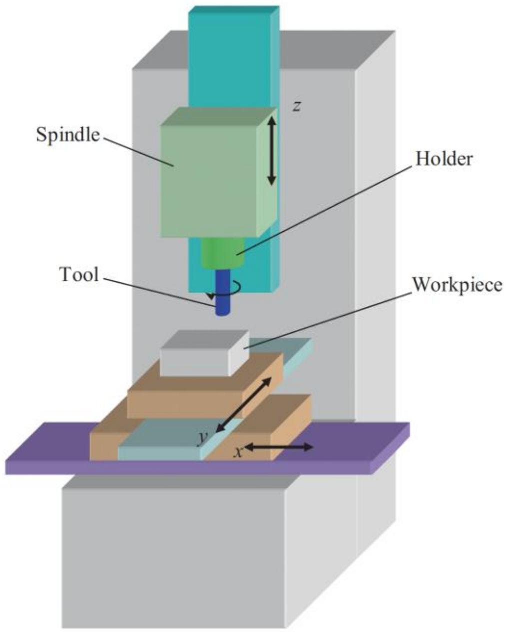

Figure 2.1 Visual representation of a vertical spindle machine tool design [1].

Figure 2.2 Visual representation of common milling tools.

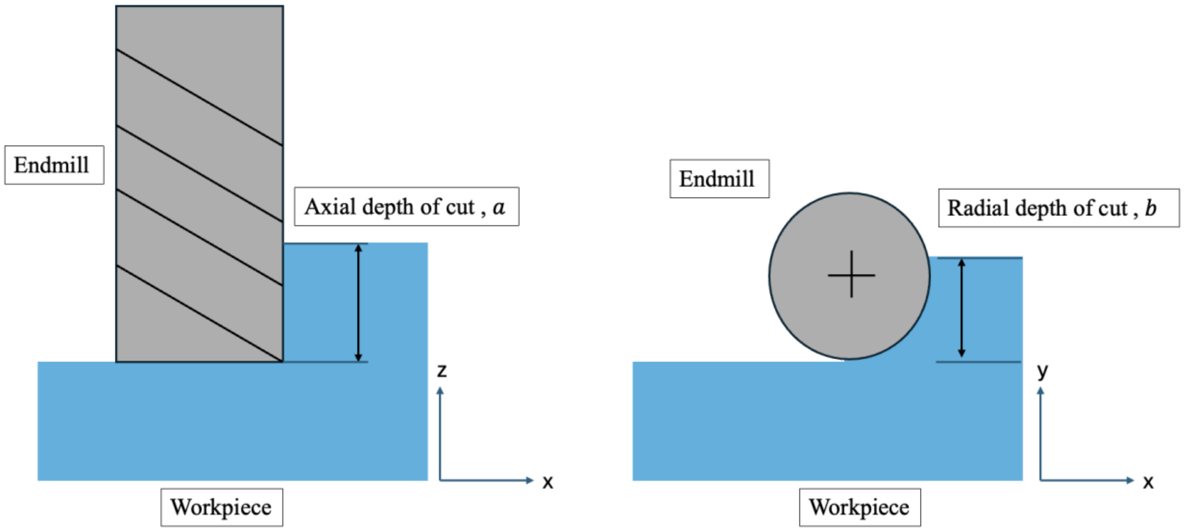

Figure 2.3 Visual representation of axial depth of cut, a, and radial depth of cut, b, on a 3-axis machine.

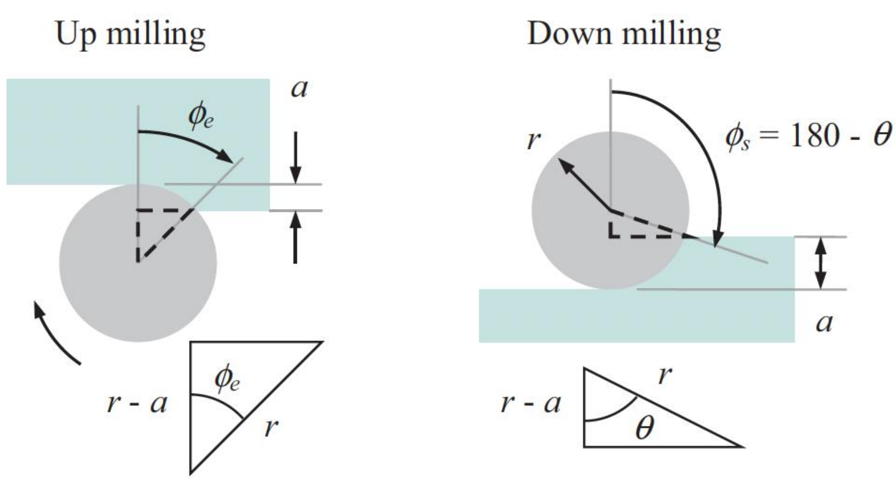

Figure 2.4 Visual representation of up milling and down milling [8].

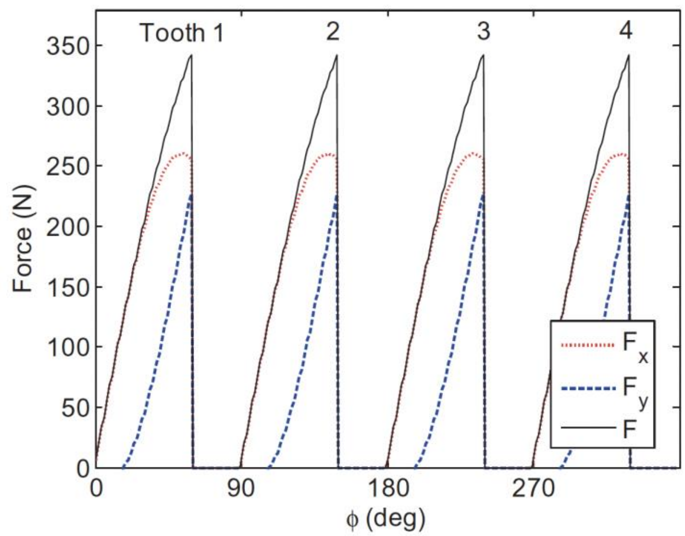

Figure 2.5 Time domain representation of up milling [8].

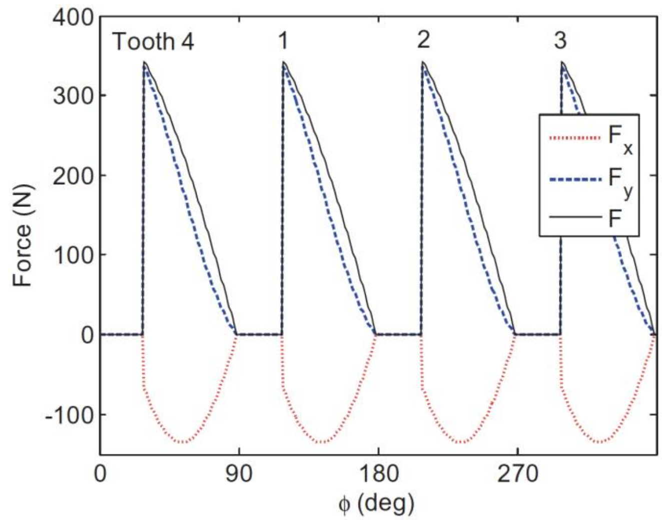

Figure 2.6 Time domain representation of down milling [8].

The third parameter, h, depends on the total degree engagement, Φ, along with the feed per tooth, f_t, which is the commanded amount of material that should be removed per tooth passing. Equations 5-6 show the mathematical formulas for calculation both h and f_t.

$$f_t = \frac{f}{\Omega\, N_t} \quad (5)$$

$$h = f_t \sin \phi \quad (6)$$

Once all milling parameters are defined, a milling operator has an understanding the rate at which material is being removed volumetrically from the workpiece. This rate is referred to as the material removal rate, MRR, and the calculation is represented in Equation 7. The intention of determining the MRR of a process is to optimize the CNC toolpath to remove the highest amount of material without unnecessary damage to the tool. As the result, decreasing the total time it takes to complete an operation is directly correlated to the size of the chip removed along with the spindle speed and linear feed rates. The major consideration is higher linear feed rates will cause the tool to wear faster.

$$MRR = abf = abf_t N_t \Omega \quad (7)$$

The usage of CNC machines allows for the movement of more controlled, simultaneous axes movements compared to that of manually operated milling equipment. This allows for a finer control of these milling parameters during cutting operations. Along with more robust control, the user can utilize the intended milling parameters to program movement codes by use of computer aided machining (CAM) programs, such as Mastercam and Autodesk Fusion, to create more complex movement paths that would not be possible for a human operator to perform with a high level of accuracy. The usage of CNC machines in milling operations has expanded the capability of the geometric features that can be completed along with increased machining throughput and quality [10]. An overall description of milling parameters in milling operations is shown below in **Table 2.1**.

Table 2.1 Milling parameters with description

Parameter	Description
Ω	Revolution per minute that the milling spindle is spinning during operation.
a	Radial depth of cut engagement during operation per pass
b	Axial depth of cut engagement during operation per pass
f_t	Commanded material removal per tooth pass
h	Material chip thickness removed per tooth pass

Introduction to milling forces

During milling operations, the tooth periodically entering and exiting the workpiece will result in a total amount of force produced during the shearing action. The force produced as each tooth passes along the feed direction depends on the tool and the workpiece material properties that dictate the total force necessary to remove an area of contact that is sheared away based on the axial depth of cut, b, and the chip thickness, h. This tool-workpiece combined force characterization referred to as the specific cutting force, K_s. A relationship of these parameters can be seen in Equation 8.

$$F = K_s bh \ (8)$$

While there are common material characteristics for alloys of the same material, or tool specifications, the K_s value is not a fixed value that can be predicted [11]. To determine the K_s, experimental cuts must be performed. These experimental cutting operation movements for milling are based along the *x* and *y* feed directions, while K_s is a result of the normal and tangential directions relative to the tool itself. **Figure 2.7** shows the relationship between the linear feed directions to the radial and tangential directions for a cutting operation.

This distinction represents that the cutting forces produced during the milling operation are not based initially based on the linear feed rate direction along the center of the tool, but into the normal, F_n, and tangential, F_t, directions based at the tip of the cutting edge of the tool. Additionally, the friction angle at the rake face of the tool, β, which is the angle difference between the resultant and normal forces plays a factor in calculation of the force. Equations 9-13 define the relationship between the resultant, tangential, and normal forces observed at the tool tip.

$$F_n = F\cos\beta = \cos\beta K_s bh = k_n bh \ (9)$$

$$F_t = F\sin\beta = \sin\beta\, K_s bh = k_t bh \ (10)$$

$$k_n = K_s\cos\beta \ (11)$$

$$k_t = K_s\sin\beta \ (12)$$

$$F = \sqrt{(F_n^2 + F_t^2)} \ (13)$$

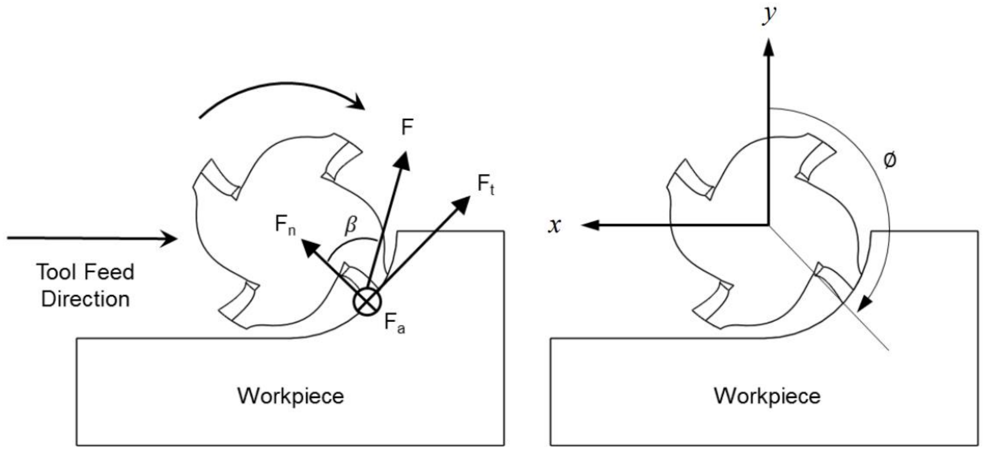

Figure 2.7 Feed-machine direction comparison to normal and tangential directions during milling operations [12].

For measurement purposes, the normal and tangential forms of the force model can then be oriented into the machine *x* and *y* feed rate directions using equations 14-17 by means of the shear angle Φ. For simplicity, h is replaced in Equations 9-10 to reflect Equation 6.

$$F_x = F_t \cos\phi + F_n \sin\phi \ (14)$$

$$F_y = F_t \sin\phi + F_n \cos\phi \ (15)$$

$$F_x = k_t b f_t \sin\phi \cos\phi + k_n b f_t \sin\beta \sin\beta \ \ (16)$$

$$F_y = k_t b f_t \cos\phi \cos\phi + k_n b f_t \cos\beta \sin\beta \ \ (17)$$

Experimental testing for cutting force coefficients

In mechanistic force models for milling processes, the milling parameters are referred to as the milling force coefficients $k_n, k_{ne}, k_t, k_{te}, k_a, k_{ae}$. These normal, tangential, and axial coefficients are modelled in terms of two phenomena, an edge force component due to rubbing or ploughing at the cutting edge disregarding the chip thickness, and a cutting component due to the shearing. For simplicity, the axial cutting and edge components can be neglected if the cutting teeth of the endmill are assumed to be straight. Equations 18-19 update Equations 9-10 to reflect the addition of the edge coefficients to the normal and tangential forces. Equations 20-21 update 16-17 to reflect the addition of the edge coefficients to the x and y feed directions.

$$F_n = k_n b h + k_{ne} b \ (18)$$

$$F_t = k_t b h + k_{te} b \ (19)$$

$$F_x = k_t b f_t \sin\phi \cos\phi + k_{te} \cos\beta + k_n b f_t \sin\beta \sin\beta + \ k_{ne} \sin\beta \ (20)$$

$$F_y = k_t b f_t \cos\phi \cos\phi + k_{te} \sin\beta + k_n b f_t \cos\beta \sin\beta + \ k_{ne} \cos\beta \ (21)$$

To determine the four cutting force coefficient values, a linear regression approach is used. The average mean force per tooth for five incremental f_t rates are measured by a milling force transducer referred to as a cutting dynamometer in the *x* and *y* feed directions. While the feed rate changes, all other milling parameters are kept constant between tests. Schmitz presents a method for determining the mean cutting force per revolution to account for multiple teeth of the cutter and interval regions where there are no teeth engaged with the tool [8]. Equations 22-23 show the bounded mean forces to account only for the regions between the start and exit angles of each tooth engagement.

$$\overline{F_x} = \left[\frac{N_t b f_t}{8\pi}\left(-k_t \cos(2\phi) + k_n(2\phi - \sin 2\phi)\right)\right) + \frac{N_t b}{2\pi}\left(k_{te} \sin\phi - k_{ne}\cos\phi\right)\Big]\begin{cases}\phi_e \\ \phi_s\end{cases} \quad (22)$$

$$\overline{F_y} = \left[\frac{N_t b f_t}{8\pi}\left(k_t\,(2\phi - \sin(2\phi)) + k_n \cos(2\phi)\right) - \frac{N_t b}{2\pi}\left(k_{te}\cos\phi + k_{ne}\sin\phi\right)\right]\begin{cases}\phi_e \\ \phi_s\end{cases} \quad (23)$$

Using Equations 22-23, the feed per tooth expressions can be used to approximate the linear regression between the incremental feed per tooth mean forces that are measured on the dynamometer as shown in **Figure 2.8**. The slope-intercept equations are showing in Equations 24-25 where j represent the linear feed rate axis, a_{1j} represents the slope, and a_{0j} represents the intercept.

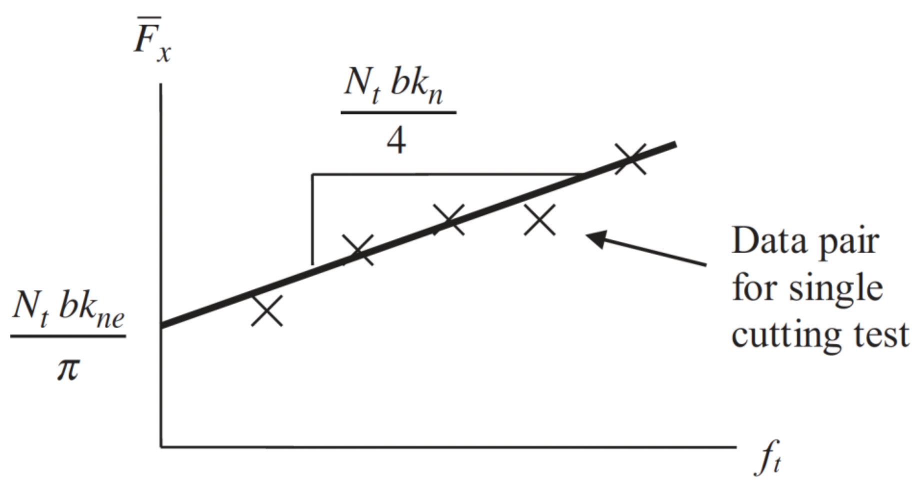

Figure 2.8 Slope representation of incremental feed rate cuts in the machine x-direction [8].

$$a_{1j} = \frac{n\sum_{i=1}^{n}\left(f_{t,i}\overline{F_{j,i}}\right) - \sum_{i=1}^{n} f_{t,i}\sum_{i=1}^{n}\overline{F_{j,i}}}{n\sum_{i=1}^{n} f_{t,i}^2 - \left(\sum_{i=1}^{n} f_{t,i}\right)^2} \quad (24)$$

$$a_{oj} = \frac{1}{n}\sum_{i=1}^{n}\overline{F_{j,i}} - \frac{1}{n}\sum_{i=1}^{n} f_{t,i} \quad (25)$$

Utilizing Equations 24-25, The 4 determined cutting force coefficients can be solved using Equations 26-29 and related to the specific cutting force K_s in Equation 30.

$$k_n = \frac{4a_{1x}}{N_t b} \quad (26)$$

$$k_{ne} = \frac{\pi a_{0x}}{N_t b} \quad (27)$$

$$k_t = \frac{4a_{1y}}{N_t b} \quad (28)$$

$$k_{te} = \frac{\pi a_{01}}{N_t b} \quad (29)$$

$$K_s = \sqrt{k_n^2 + k_t^2} \quad (30)$$

Through experimentation, the solution can find the specific cutting coefficient and its associated tangential and normal cutting force coefficients can be determined for each specific tool-workpiece combination. These values are then used in other predictive modeling techniques to account for the real-world system characteristics.

Introduction to vibration measurement

All structures of interest can be represented as combined bodies that possess both mass and elasticity or the ability to deform without permanently changing shape [13]. Due to no physical system being infinitely rigid, all systems can be described as a spring. As a spring, the level of compliance determines the amount a system can deflect when an external force is applied onto it. As the teeth of the endmill enters and exits the workpiece, both experience a level of vibration when a force is applied. This displacement varies for each depending on how compliant the tool and workpiece are relevant to one another.

For most systems that are struck by an external force, the vibration experienced by a body will be determined by certain modal characteristics of the system. These characteristics are the mass of the body, how stiff the body is, and the level of damping on the system. A common way of expressing this concept as a system that is composed of these three characteristics is referred to as a lumped spring-mass-damper. A representation of a mass being hung from both a spring and dashpot damped with an applied force acting on the mass is shown in **Figure 2.9**. For a simple milling case a harmonic external force, $fe^{i\omega t}$, is exerted on both the tool and workpiece body. This displacement due to this harmonic external force is referred to as forced vibration and shown in Equation 31. The lumped parameter model has a certain amount of mass, m, viscous damping, c, and stiffness, k. Once the force acts on the system, motion is created in the form of displacement, x, velocity, $\dot{x}$, and acceleration, $\ddot{x}$.

$$f = m\ddot{x} + c\dot{x} + kx \ (31)$$

Because the motion and forcing responses share the same frequency in this forced vibration state, the equation can convert the response into the frequency domain as shown in Equation 32-35.

$$x = Xe^{i\omega t} (32)$$

$$\dot{x} = i\omega Xe^{i\omega t} \ (33)$$

$$\ddot{x} = -\omega^2 Xe^{i\omega t} \ (34)$$

$$(-\omega^2 m + i\omega c + k)Xe^{i\omega t} = fe^{i\omega t} \ (35)$$

Rewriting Equation 35, the complex valued frequency response function (FRF) can be derived. An FRF is used in system dynamics to describe the changes in system due to different input frequencies. Equation 36 shows a receptance-based FRF, or compliance, which is the ratio of displacement to force within a system.

$$\frac{X}{F} = \frac{1}{-m\omega^2 + i\omega c + k} \ (36)$$

For milling processes the most common representation for the FRF is to use the real and imaginary approach as shown in Equations 37-38 where r is the frequency ratio of the selected frequency over the natural frequency of the system and ξ represents the damping ratio. **Figure 2.10** shows a SDOF representation of a complex receptance FRF separated into its real and imaginary components.

$$Re\left(\frac{X}{F}\right) = \frac{1}{k}\left(\frac{1 - r^2}{(1 - r^2)^2 + (2\xi r)^2}\right) \ (37)$$

$$Im\left(\frac{X}{F}\right) = \frac{1}{k}\left(\frac{-2\xi r}{(1 - r^2)^2 + (2\xi r)^2}\right) (38)$$

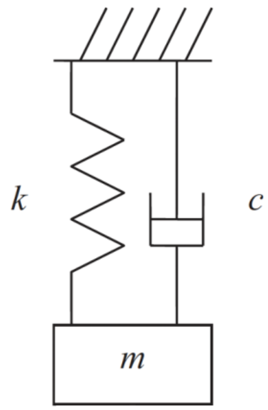

Figure 2.9 Single degree of freedom mass-spring-damped lumped model.

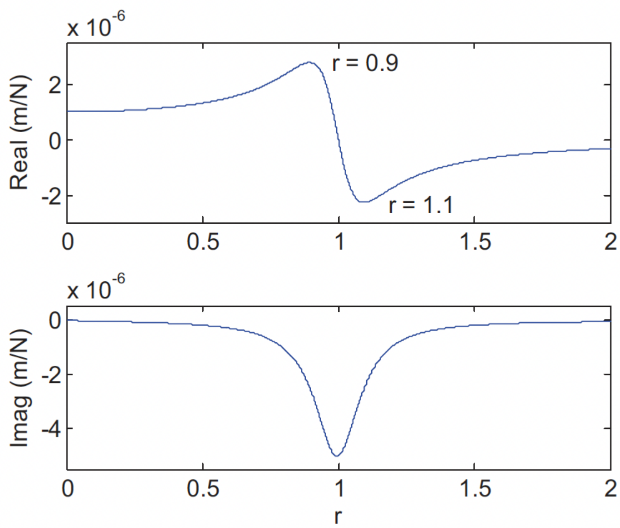

Figure 2.10 Real and imaginary FRF depiction.

Modal fitting and acquisition

For milling setups, it is common to experimentally measure the frequency response function of both the endmill and workpiece individually. This acquisition method will be described in chapter three of this work. When starting with a measured frequency response, a method must be implemented to derive the modal parameters for each mode within the FRF; $\xi, k, and\ \omega_n$. "Peak picking" is the modal fitting approach commonly used to derive the modal parameters utilizing both the real and imaginary components of the receptance FRF. This will be conducted for each direct FRF in both the x and y direction of the tool and workpiece components [8].

The natural frequency, f_n, can be determined by using only the imaginary component of the FRF, where is represented by the lowest point of each modal peak. An example for a SDOF FRF in shown in **Figure 2.11**. Equation 39 is used to convert natural frequency in hertz, f_n, to angular frequency, ω_n.

$$\omega_n = 2\pi f_n \text{ (39)}$$

The modal damping ratio, ξ, is a unitless parameter that is determined using both the real and imaginary component FRF. Equation 40 utilizes the frequencies highest peak on the real FRF, ω_1, the lowest peak of the real FRF, ω_2, and the natural frequency, ω_n. **Figure 2.12** depicts the three frequencies.

$$\xi_q = \frac{\omega_2 - \omega_1}{2\omega_n} = \frac{\pi f_2 - \pi f_1}{f_n} \text{ (40)}$$

The modal stiffness, k, can be determined using the amplitude of the peak of the imaginary component of FRF, A, along with the modal damping ratio, ξ, **Figure 2.13** and expressed in Equation 41.

$$k = \frac{-1}{2\xi A} \text{(41)}$$

To acquire the modal mass parameter, m, and modal damping parameter, c, additional calculations are necessary utilizing the prior acquired modal parameters. These calculations are expressed in Equations 42 and 43.

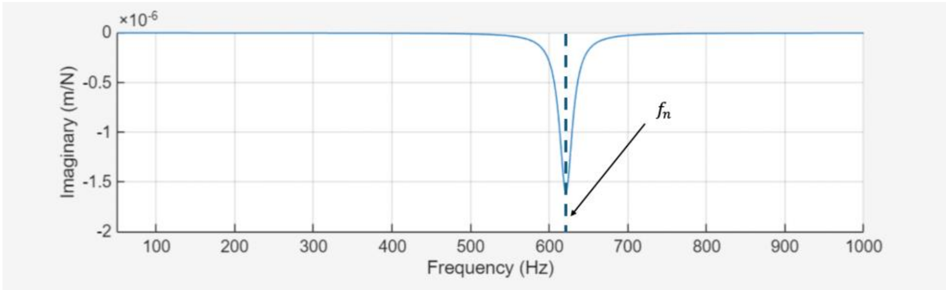

Figure 2.11 Graphical representation of determining natural frequency, f_n.

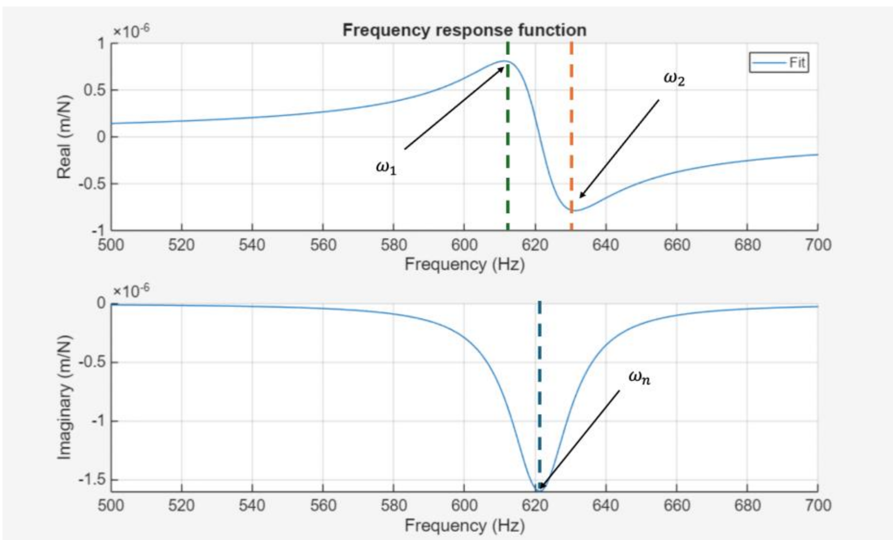

Figure 2.12 Peak picking method in real FRF plane

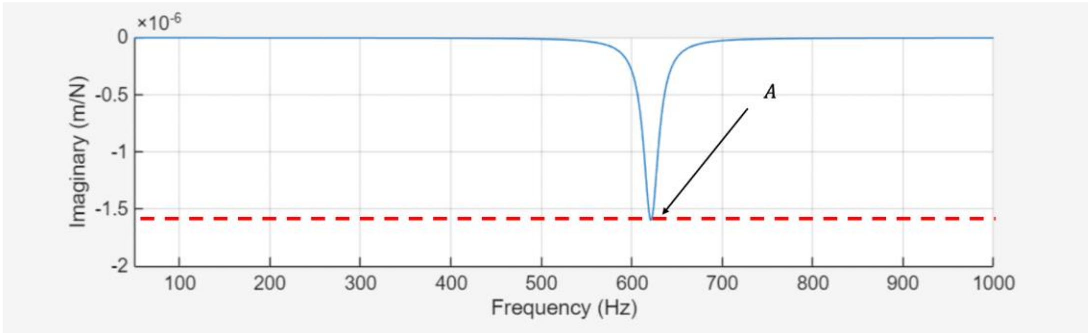

Figure 2.13 Compliance magnitude calculation

$$m = \frac{k}{\omega_n^2} \ (42)$$

$$c = 2\xi\sqrt{(km)} \ (43)$$

All modal parameters must be acquired for each mode within in the system and can be done by repeating this approach for each independently. **Table 2.2** below also shows each modal parameters designated units for reference. The results of this method will prove to vary depending on the tool geometry and specifications including the length and diameter. Due to the large variation in results in FRF modes and flexibility, Receptance Coupling where the tool, holder, and spindle-machine receptance are coupled analytically to pre-predict the response of similar sized tools [14].

Tooth passing frequency

In addition to the structural dynamic FRFs of both the tool and workpiece in a static state, the frequency at which the spindle is rotating the tool plays a large effect in the systems response during the cutting operation. In milling, the excitation force response occurs at the excitation frequency which is referred to as the tooth passing frequency. This frequency is defined by the product of the spindle speed and the number of flutes the tool has,N_t. Equation 44 describes the manner to convert the spindle-tooth rotation into a frequency in Hertz.

$$f_{tooth}(Hz) = \frac{\Omega N_t}{60} = \frac{revolutions}{1\ min} x \frac{1\ min}{60\ s} x \frac{N_t}{1\ revolution} \ (44)$$

As the spindle speed changes, the excitation frequency of the tool also changes. As the intention to avoid resonance is key, the tooth passing frequency must not fall close to the natural frequencies of the tool-workpiece system. More so, it must be considered that the tooth passing frequency has multiples that can be seen in the frequency bandwidth of interest that must also be avoided. Depending on the number of flutes on the tool, there will be individual frequency peaks and multiples related to those teeth as well that must be avoided to prevent resonance from occurring as well [15]. **Figure 2.14** depicts the primary tooth passing frequencies of a four fluted endmill spinning at 7,500 RPM [8].

Table 2.2 Modal parameters units

Modal Parameter	Units
f_n	Hz
ω_n	rad/s
k	N/m
ξ	$unitless$
m	kg
c	Ns/m

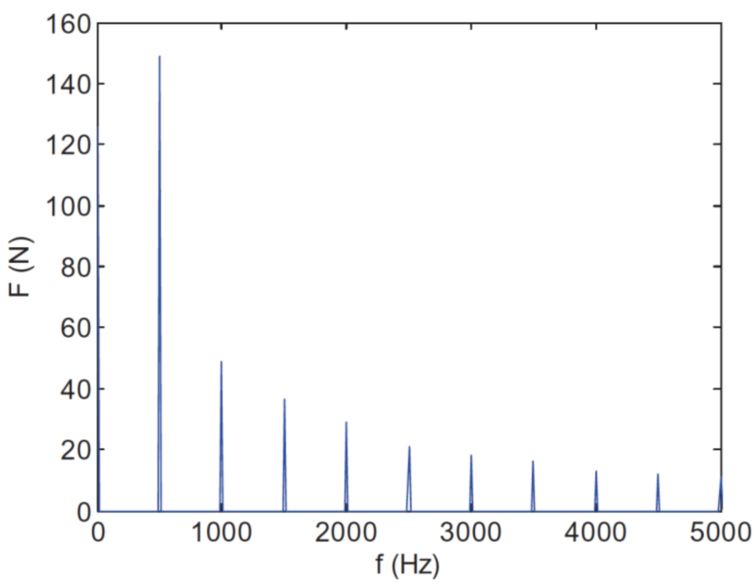

Figure 2.14 Frequency domain representation of tooth passing frequencies [8].

Self-excited vibration

During self-excited vibration, a constant harmonic force is applied at or near the system's natural frequencies. For milling tools, this is an undesirable condition during a cutting operation where the tool-workpiece combination enters a state of resonance. The level of vibration is much higher compared to a system that is maintained in forced vibration as shown in **Figure 2.15**. On the left, we can see the tooth enters and exits the workpiece in a constant, harmonic frequency, while on the right, the displacement grows uncontrollably due to resonance.

In manufacturing, this higher displacement is referred to as chatter [16]. Chatter is seen as imprinted marks on the surface of the workpiece and as audible noise during cutting. This chatter noise is distinguishable compared to normal forced vibrations operations due to the resonance amplifying the natural frequency of the system to a higher order, creating more of a tonal sound compared to the broadband 'white noise' of stable cutting. Due to this comparison, cutting conditions are commonly referred to as stable when undergoing forced vibration, and unstable when undergoing self-excited vibrations. **Figure 2.16** depicts a comparison between a surface machined in a stable versus unstable milling condition.

For many operators and machinists, experiencing chatter is a common occurrence in the occupation, and generally seen as a burden. Chatter marks can cause a part to fall out of both dimensioning and surface tolerances that can cause the part to be defective and scrapped due to not meeting industry requirements. Additionally, uncontrollable levels of resonant vibrations can cause damage to the endmill and even the spindle if increased to a high level of displacement. In some applications, the chatter can be characterized and measured using pre-predicting simulation models that account for the structural dynamics of the tool and workpiece. These simulations can consider the physical system and control cutting parameters to determine when chatter will occur [17].

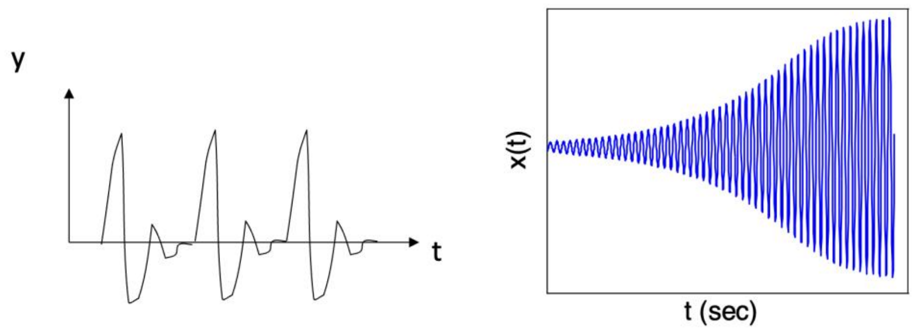

Figure 2.15 Visual comparison of forced vibration versus self-excited vibration

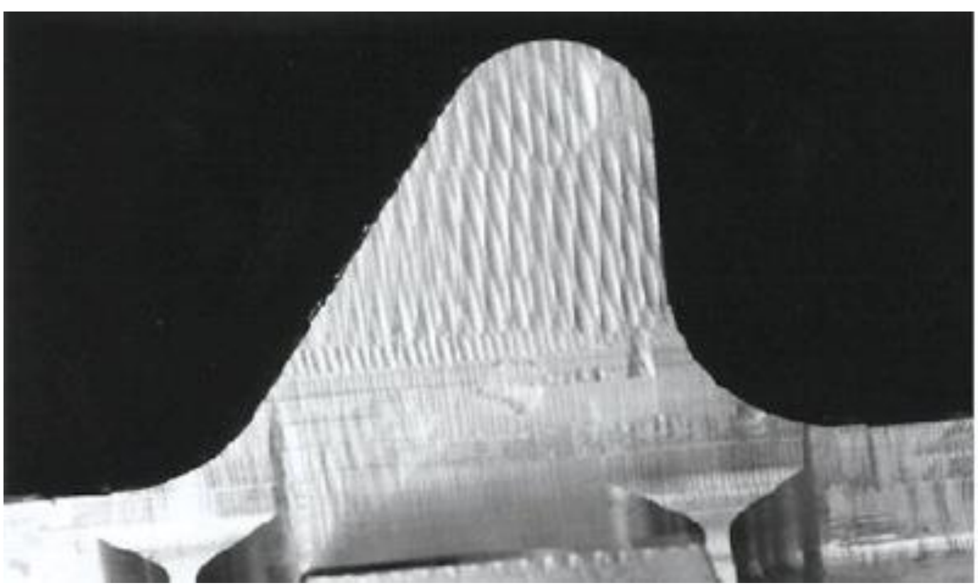

Figure 2.16 Visual representation of self-excited vibration, or chatter, on a workpiece

Milling stability

Many researchers have taken an interest in the effects of stability in machining, such as Merdol, Altintas, and Budak who have worked extensively to increase the MRR during cutting operations while determining milling parameters that are stable and optimized for manufacturing efficiency [16], [18], [19]. These researchers have focused on developing predictive models to reduce trial-and-error approaches. Tlusty proposed initial groundbreaking methods for mapping regions of stability and instability as a series of lobes over a certain range of spindle speeds that could be achieved by a machine tool compared to the maximum axial depth of cut that could be performed at a set radial depth of cut for a given material and tool combination [20]. This stability lobe diagram approach became the foundation for modern chatter prediction methods. Regions above the lobes would depict regions of instability where chatter is likely to occur, while those below show regions of stability where smooth cutting can be maintained. Altintas and Budak significantly expanded on this foundational approach with the introduction of both the zero-order solution that considers the average of the machining directional factors, and the more sophisticated multifrequency solution that considers the harmonics of the directional factors specifically designed for low radial immersion operations commonly found in finishing passes [19] [16]. The zero-order solution provides a simplified approach for initial parameter selection, while the multifrequency solution offers higher accuracy.

Both analytical methods provided by Tlusty and Altintas rely heavily on the FRFs of the tool-workpiece system and the mechanistic cutting force coefficients to accurately simulate the physical real-world system behavior under various cutting conditions. The frequency response functions are typically obtained through impact hammer testing to characterize the dynamic behavior. Having the frequency response of the system helps to account for the regions of resonant frequencies that would excite natural frequencies over a wide range of spindle speeds encountered in typical machining operations. These natural frequencies depend on tool geometry, tool holder configuration, and workpiece setup. Additionally, the specific cutting coefficient plays a critical role in determining the maximum axial depth of cut that can be taken per pass for the specific workpiece material without entering a region of instability that could compromise part quality or tool life [11], [21]. The cutting force coefficients are material-dependent parameters that must be determined experimentally. When placing both critical elements together, the stability map can be produced and is shown in **Figure 2.17**. The area in grey is the region of self-excited vibration representing unstable cutting conditions, while the region in white represents forced vibration indicating stable machining parameters. The line in black represents an additional important boundary known as the critical axial limit. This line refers to the maximum axial depth of cut that can be cut at all possible spindle speeds without risk of instability.

When recalling practical machinist's approaches to avoid chatter, most traditional methods can prove to be detrimental rather than beneficial as seen in **Figure 2.17**, the higher the spindle speed, the larger the regions of stable cutting parameters are available at a higher radial depth of cut become available for machining. This relationship challenges the traditional approach of reducing spindle speed when chatter occurs. Using Equation 7, increasing both the axial depth of cut and spindle speed vastly increases the material removal rate for the material being machined. This increase in material removal, while remaining in a stable region, vastly decreases operational machining time for each component and improves overall manufacturing efficiency. Reducing the spindle speed also causes a larger chance to enter a region of instability at a higher axial depth of cut, which could potentially cause the part to fall out of specifications and result in costly scrap. This is problematic in production environments where rework represents financial losses. Reducing the axial depth of cut below the critical limit is another common method in which machinists and operators approach reducing chatter effects in the system but prove to be ineffective in reducing machining operation time when there are significant regions of stability above the critical limit that could be effectively used to machine the component more efficiently. Modern CAM software packages are beginning to integrate stability prediction algorithms, though accuracy depends on quality input data including frequency response functions and cutting force coefficients.

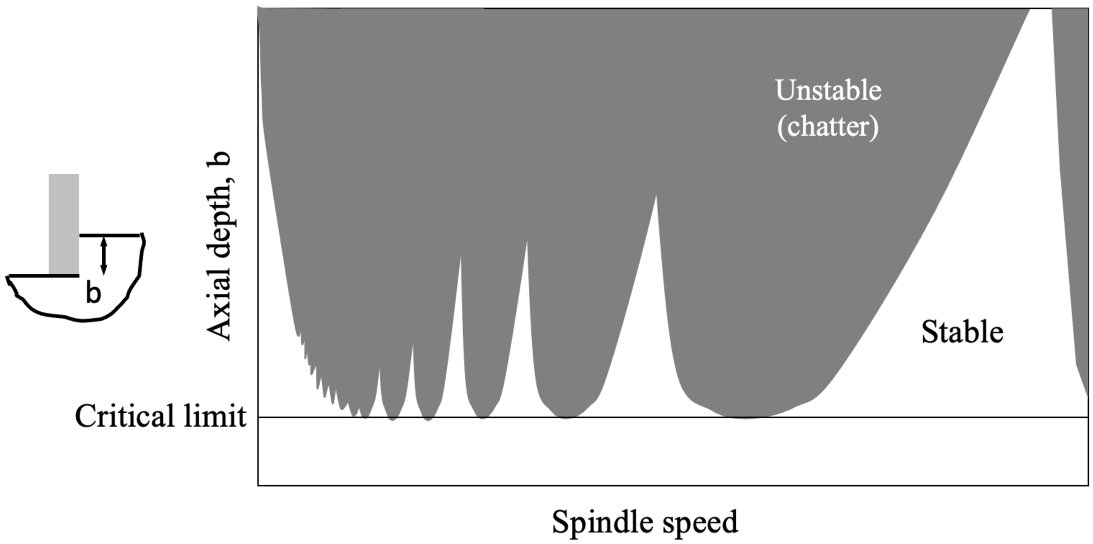

Figure 2.17 Milling stability map representation.

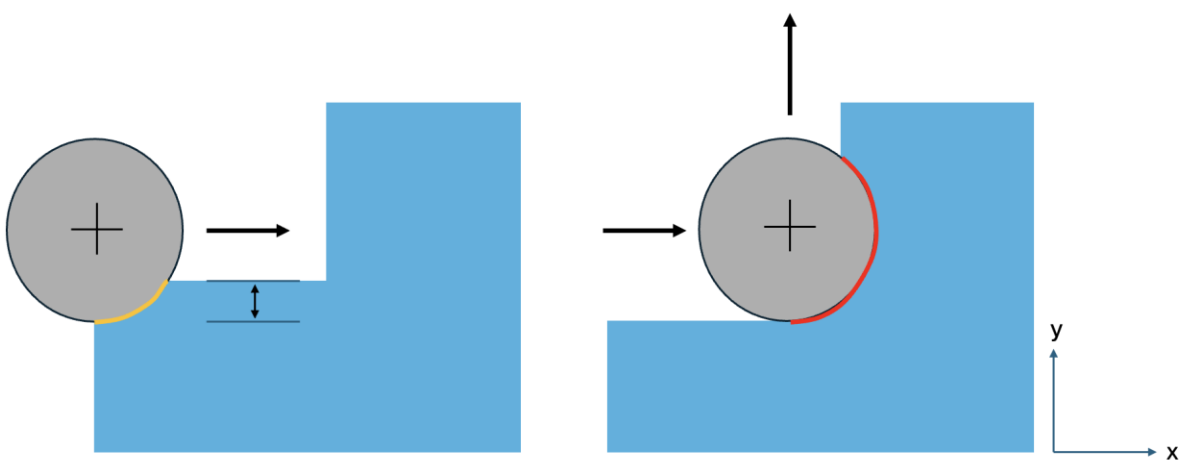

Figure 2.18 Comparison of radial immersion of an endmill within a pocketing operation

As a result, the usage of milling stability maps to determine optimal parameter for a specific tool-workpiece material is a highly efficient, preventative method for planning machining operations and will be used later. This approach is typically implemented prior to machining operations to avoid damaging any tooling or components; compared to traditional experimental guesses.

Introduction to time-based signal derivation

Digital signal processing challenges of numerical differentiation

Within the world of digital signal processing, the derivation of time-based signals proves to have certain challenges when attempting to get clean, usable data. Numerical differentiation is an inherently difficult problem since all real transducers are erroneous in precision and accuracy, which we collectively refer to high frequency interreference within the signal. Transducer noise is problematic due to the fat that the differentiation operator is unbounded and thus discontinuous on a dense subspace of a function space. The lack of continuity is manifested as amplification, and thus extremely sensitive to noise; this means that low amplitude, high frequency noise transducers can lead to large errors in the estimated derivative. In addition, these errors are exacerbated by estimates of higher order derivates [23], [24].

An example is the derivation of time-based motion signals. For this study, the use of a low-cost photo-interrupter transducer is used at a high sampling frequency to collect analog voltage and calibrated to relate the change in voltage to a change in displacement at the micron level. In industrial equipment cases, these types of low-cost transducers are susceptible to prior amounts of high frequency noise prior to differentiation. An example of this additional noise is high intensity electromagnetic fields from the milling spindle, axis motors, and power instrumentation that can affect these signals. Combined with these additional sources of noise, standard differentiation methods escalate noise to a higher order every time the signal is differentiated. This noise-to-signal ratio, the amplitude of the noise compared to that of the measured signal, can increase to the level where smaller voltage measurements are distinguishable to the noise that is present in the system. This challenge in digital signal processing is a reason why traditional methods of signal differentiation prove to be ineffective when dealing with time-based signals. For this study, the need for high fidelity displacement signals is critical to derive the system's velocity and acceleration measurements through the means of numerical differentiation.

Simplistic numerical differentiation approach

In digital signal processing, the traditional method of numerical differentiation acts as a filter applied to a time-based signal [25]. The time signal, measured using a transducer, is recorded using a data acquisition device at a certain sampling frequency over a certain period creating a data array. Using mathematical based software, such as MATLAB, functions can be called to determine the derivative of the signal. The common function used for performing a numerical differentiation is the diff function. The diff function is used to measure the difference between one point to the next in the time-based signal; with the output being the rate of change between one data point to another. The diff function calculates the difference between adjacent elements of the array [26]. This approach is logical with a baseline knowledge of the derivation of a motion-based signal; where velocity is the rate at which an object displaces, and acceleration being the rate at which velocity changes, such as a car driving. This method suffers greatly with transducers when the signal has a high rate of sampling and noise amplified along the signal. This noise can greatly influence the results of the subtractive operation based on noise-to-signal-ratio. Equations 45-47 represents the fundamental issues of the diff function when measuring the results of a first-order differentiation approach. As a result, the use of a simple subtractive method for differentiation proves to be a challenge in first order approximation and only worsen with higher-order approximations. Due to the unusable signals produced through the simplified method of differentiation, alternative methods must be implemented.

$$displacement_1 = true\ displacement\ value_1 + noise_1 \quad (45)$$

$$displacement_2 = true\ displacement\ value_2 + noise_2 \quad (46)$$

$$velocity_1 = (true\ displacement_2 + noise_2) - (true\ displacement_1 + noise_1)$$

$$velocity_1 = (true\ displacement_2 - true\ displacement_1) + (noise_2 - noise_1) \quad (47)$$

Finite Impulse Response (FIR) differentiator

A more complex numerical differentiation method must be used to acquire the derivatives of the time-based signals for this study that can correctly remove the unwanted noise from the system and consider a higher number of points to evaluate the rate of change [27]. A Finite Impulse Response (FIR) digital differentiator filter can be implemented to resolve these issues with a high level of robust control for noise attenuation[24] [23]. The elements of a FIR differentiator consider several key parameters that blend very well with the structural dynamic responses found in milling applications that make it a strong tool when analyzing time-based signals[28], [29], [30], [31]. Equation 48 defines the baseline structure of the FIR differentiator where $y(n)$ is the new derived signal, b_i represents the FIR filter coefficients, and $K+1$ denotes the FIR filter length. The FIR filter operations in this case involve only multiplying the filter inputs by their corresponding coefficient and accumulating them, making the implementation of this filter in real time straight forward (insert reference book).

$$y(n) = \sum_{i=o}^{K} b_i x(n-i)$$

$$y(n) = b_0 x(n) + b_1 x(n-1) + b_2 x(n-2) + \cdots + b_K x(n-K) \; (48)$$

As for the creation of the filter, various approaches of utilizing FIR differentiators have been made over the course of the last sixty years to attenuate and derive signals; with one being the developed by Tom Parks and James McClellan in 1971 [32]. The Parks-McClellan algorithm, also known as the Remez exchange algorithm with optimal Chebyshev approximation for FIR filters, is a specific filtering approach for time-based signals with known frequency content. For motion signals that need to be derived, the purpose of the filter is to ensure that all frequencies considered as noise to be attenuated[4]. For milling application this serves as a great tool due to the operator knowing both the structural dynamics of the tool-workpiece combination and the tooth passing frequency over a range of usable spindle speeds within the stability limits of the cut. This frequency must be conserved to ensure that no milling content is removed from the derived motion signals. The Parks-McClellan algorithm considers two filter values to control the region of content that needs to be kept and to be attenuated; the band pass and band stop frequencies for the system. The band pass frequency for a system determines the upper limit of frequency content that will be conserved during the differentiation processes and ensures that all relevant system-based frequencies are not removed from the operation. The band stop frequency then sets the region of attenuation for higher frequency signals outside of the region of interest. This band stop frequency is intended to set the lower limit of content that can be disregarded during the derivation process. The content above the limit can be high frequency noise that is present inside of the milling machine, as well as other sources of noise that can be present in the signal. Due to the nature of the band stop cutoff, this filter naturally behaves as a low-pass filter as well. For the structural dynamics of the CMD and resolution of the transducer for this testing, all frequency content that is relative to the system falls below 2,000 Hz can be assumed. This allows high level of confidence for determining the location of the band stop cutoff. As for the band pass, this will be relevant to the tooth passing frequency and natural frequency response to determine cutoff frequency and can change between different cutting operations. The significance of this approach is that it is adaptable to different cutting parameters and responses.

Additionally, the filter order, $K + 1$, determines the number of points that are being analyzed, with higher filter orders having higher number of points. With the current era of modern computing, processing, and memory, the usage of high order filters (ranging from 50 to 200) takes minimal computing time and cost when compared to the era when the algorithm was developed [4]. **Figure 2.19** depicts the usage of the Park-McClellan algorithm to apply the band pass and band stop filtering frequencies.
A case study was produced in MATLAB to show the difference comparing the first and second order differentiation of a time-based signal using the diff function compared to that of a 50-order Park-McClellan FIR differentiator shown in **Figure 2.20** [33].

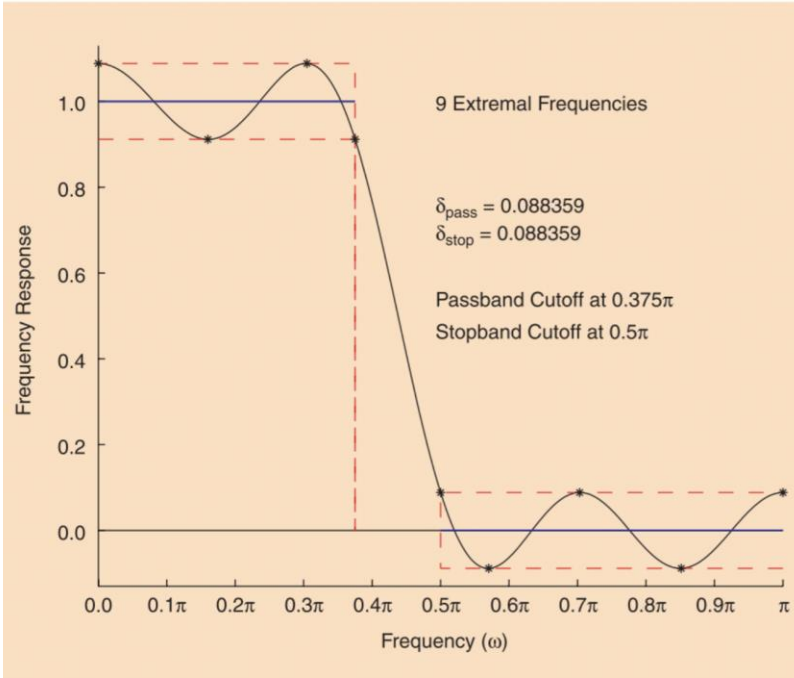

Figure 2.19 Optimal length 15-FIR linear phase filter designed using the Parks-McClellan algorithm [4].

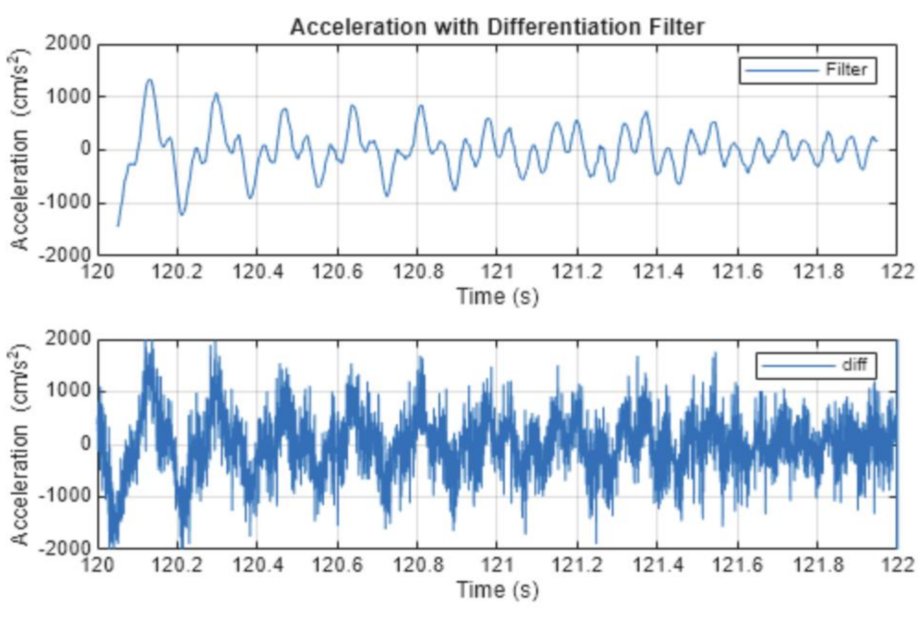

Figure 2.20 MATLAB simulated comparison of standard differentiator compared to 50th order FIR [33].

CHAPTER THREE

MATERIALS AND METHODS

Experimental dynamometer designs

Prior designs and iterations changes

In modern milling research and experimentation, tri-axial piezoelectric dynamometers, such as Kistler spindle and tabletop dynamometers, serve as the industry standard in measurement systems [34] [35]. These systems are helpful for the evaluation of more difficult to machine materials such as titanium and carbon fiber composites [9] [36]. Various milling dynamometer designs have been created to compare force results to that of commercial grade systems. Several researchers have taken influence from these commercial grade systems to provide lower cost transducers with similar characteristics and capabilities.

Rotational dynamometers that attach to the spindle housing of a CNC machine are used to capture milling forces being applied onto the tool. Totis et al. developed a tri-axial rotational dynamometer that served as a transducer with indexable teeth. The purpose of the system was to directly compare in process cutting forces to a commercial grade Kistler 9257B dynamometer [37]. Initial validation of machining was conducted on a workpiece attached to the tabletop dynamometer and simultaneously acquiring forces with both systems. Qin later expanded on rotational dynamometers by developing a piezoresistive micro-electromechanical systems (MEMS) dynamometer. This system was designed to measure the relationship of torque to strain produced by milling onto the MEMS strain gauges within the transducer [38].

Table mounted designs are also used in CNC milling operations to measure the forces applied onto the workpiece. Various designs have been manufactured to serve as replacements for commercial grade variations. Yaldiz created an initial calibrated strain gauge design capable of measuring in-process forces. The design was configured in a table-based orientation to measure static and dynamic cutting forces. The system was also capable of measuring torque within the milling process. Korkut developed a three-force component dynamometer design comprised of four octagonal rings placed between two plates and fixtured with screws [39].

Additional low-cost alternative flexures were also developed within the Machine Tool Research center to serve as variations of milling dynamometers [5], [40]. Rather than directly measuring the forces produced within milling operations, the intent was to capture motion measurements. Tyler and Schmitz developed an initial single degree of freedom, parallelogram leaf-type flexure. The flexure combined with an accelerometer was used to measure process damping effects within milling operations [41]. Honeycutt and Schmitz additionally created another single degree of freedom parallel leaf-type flexure paired with a laser Doppler vibrometer and capacitance transducer. The intent of the system was to use motion-based signals for stability identification in milling by means of once-per-tooth sampling [42]. Honeycutt also expanded on this work by creating a flexure-based platform with tunable dynamics with adjustable damping conditions for desired experimental conditions by means of a magnetic eddy current damper [43].

Constrained Motion Dynamometer

For this study, the chosen dynamometer selected for deriving force measurements is a monolithic, ideally single degree of freedom system designed by Gomez [5]. The low-cost, Constrained Motion Dynamometer (CMD), shown in **Figure 3.1** and **Figure 3.2**, is constructed from a solid wrought Aluminum 6061-T6 workpiece. The cost of the commercially available aluminum workpiece is $200.00. The design is comprised of the outer base that is mounted onto the CNC machine, the interior mounting platform that the workpiece is fastened onto, and the four bar leaf flexures. The basis for the design is a compliant platform connected to a base by four leaf-type flexure elements in a four-bar linkage arrangement. The motion is linear within the design-specific displacement range. The interior flexure cavities are removed by means of an Electrical Discharge Machining (EDM) process to ensure uniformity between the flexure elements. This will allow even movement as the stage displaces.

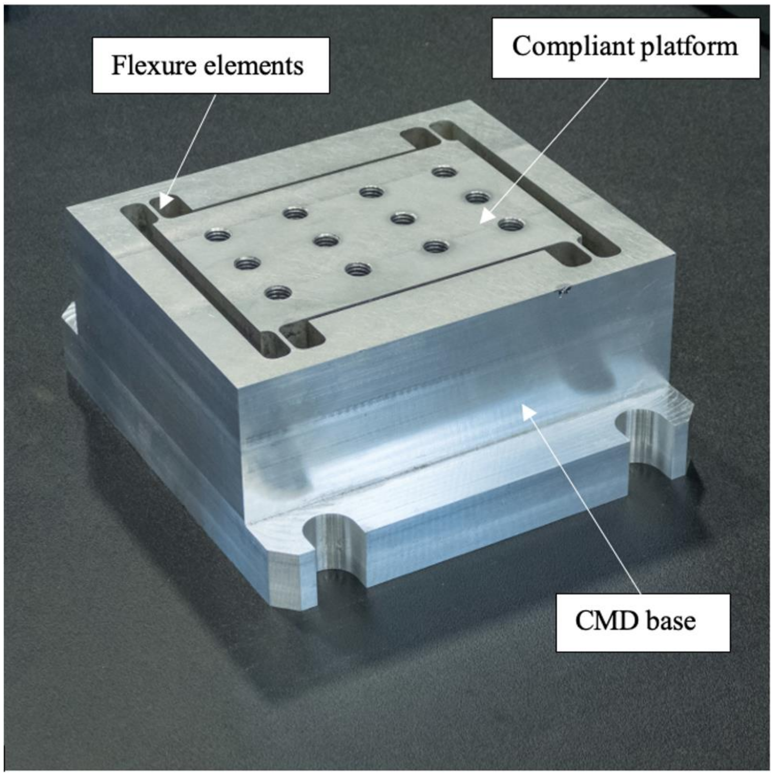

Figure 3.1 CMD layout.

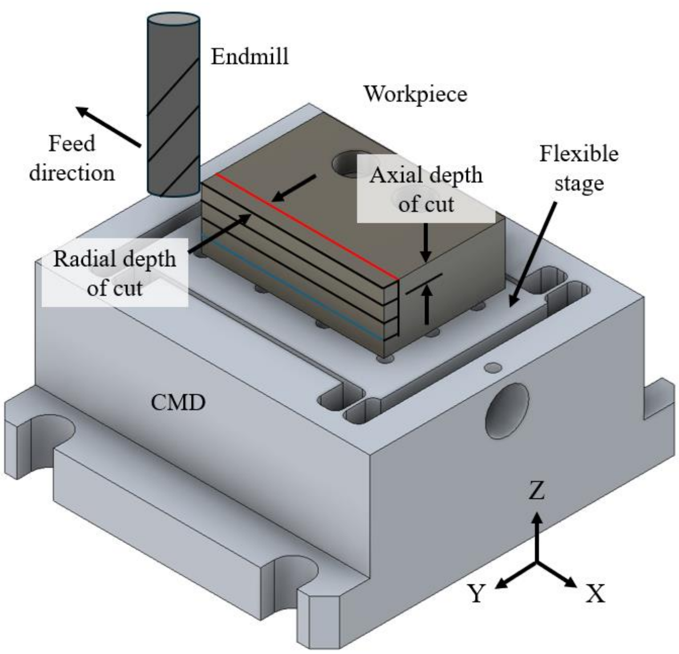

Figure 3.2 Visual representation of CMD-KES system design.

The design of the system must consider small milling parameter cuts to ensure the flexure elements do not fail during milling operations. The force ranges the CMD is capable of withstanding is found using Hooke's law due to the stage acting like a spring itself in the compliant direction. The spring constant of the structure is calculated using Equation 49, where n represents the number of flexure elements, E represents the modulus of elasticity, and σ_{yield} represents the yield strength for the aluminum alloy. E and σ_{yield} are 69 GPa and 276 MPa, respectively for Aluminum 6061-T6.

To allow the leaf deflection to move without deforming, the maximum allowable stress $\sigma_{allowable}$, is set to 60% of the yield strength (160 MPa). The maximum allowable deflection, $x_{allowable}$ is defined in Equation 50. The selected flexure element width, *b*, is 44.5 mm, the length, *L*, is 10 mm, and the thickness, *t*, is 1.27 mm and are shown on **Figure 3.3**. In **Figure 3.4** the radius of the flexure is shown from a top view.

$$K_{eq} = nK = \frac{n12EI}{L^3} = \frac{48EI}{L^3} \text{ (49)}$$

$$x_a = \frac{\sigma_{allowable}L^2}{3Et} \cong \pm 50\mu m \text{ (50)}$$

The second moment of area, I, is calculated using Equation 51. The expression is inserted into Equation 52 and expanded from Equation 49.

$$I = \frac{bt^3}{12} \text{ (51)}$$

$$K_{eq} = nK = \frac{n12EI}{L^3} = \frac{48EI}{L^3} = \frac{4Ebt^3}{L^3} \text{ (52)}$$

Using the dimensions of the flexure elements, the spring constant is $K_{eq} = 1.5x10^7$ N/m and the force range, *F*, is $\pm$1500 N as shown in Equation 53.

$$F = K_{eq} \cdot x_{allowable} = 1.5x10^7 \left(\frac{N}{m}\right) \cdot 5x10^{-5}m = 1500\ N \text{ (53)}$$

With an allowable range of motion of 100 μm and a total force of 1500 N, the standard cutting parameters for radial and axial depth of cut must be kept to 2 *mm* by 2 *mm* for all materials to evaluate each with identical cutting area.

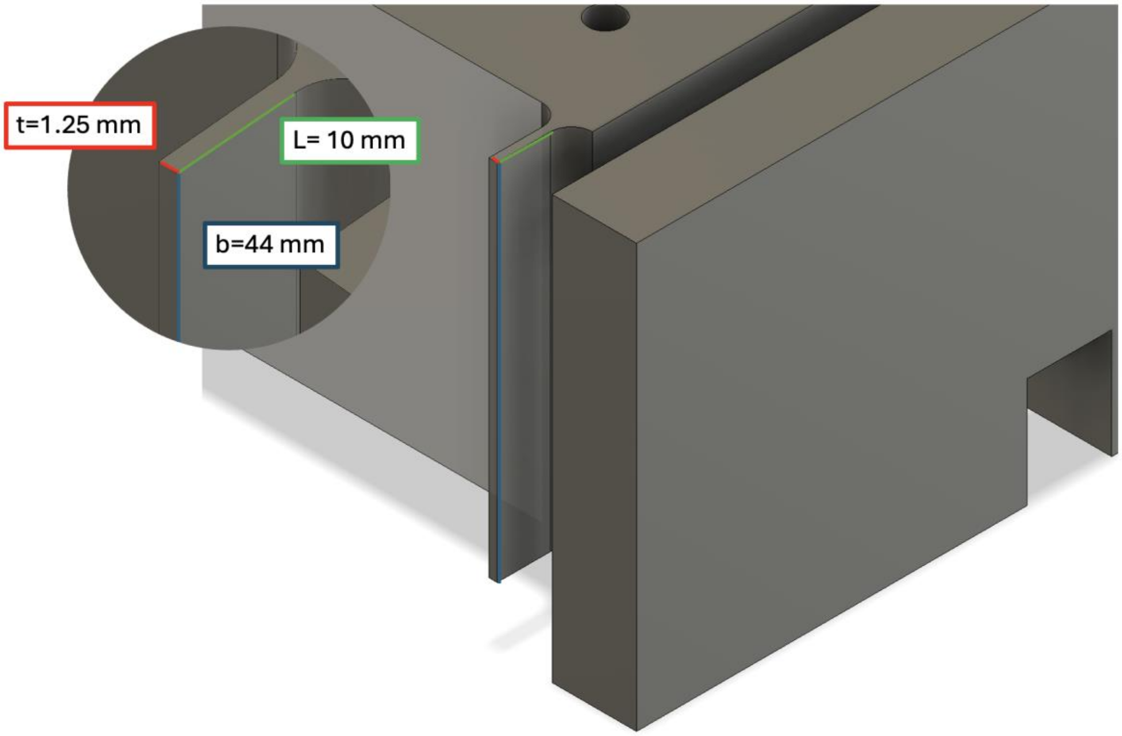

Figure 3.3 Model representation of flexure element.

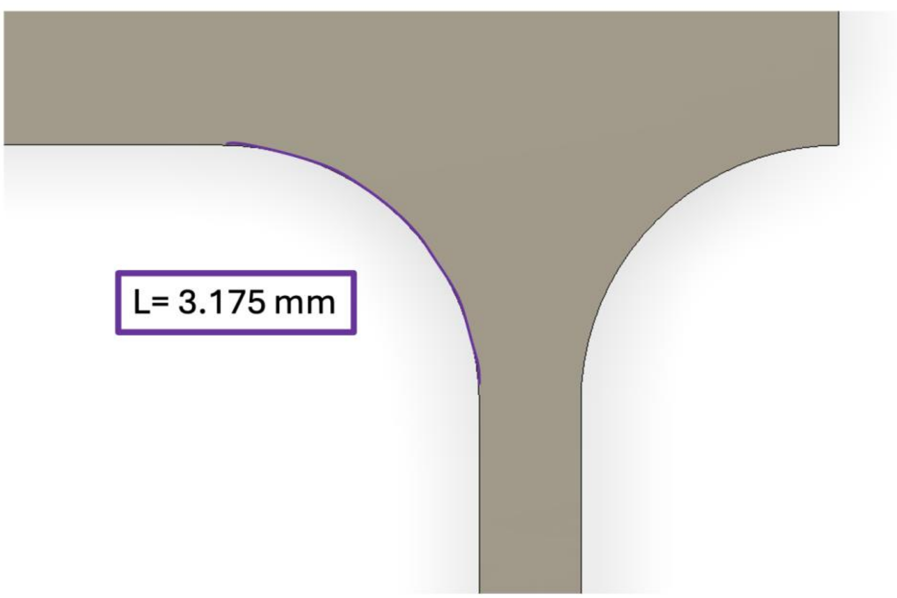

Figure 3.4 Model representation of flexure element.

Knife edge transducer

Design history and schematics

Prior work has been conducted to design and validate the usage of a low-cost photo-interrupter transducer paired with a standard, straight end cutting knife to relate the change in voltage due to a change in displacement. Gomez and Schmitz validated the initial usage of the pair and named the combined system a knife edge transducer (KES) transducer pairing. The KES is composed of a RHOM semiconductors RPI-0352E optical transducer and a commercially available trade No. 7 precision knife blade with the hollowing dimensions shown in **Figure 3.5**. The RHOM semiconductor optical transducer requires a PCB circuit board and circuit to be designed for operational usage as shown in **Figure 3.6**. The cost of this sensor commercially is $0.78 and will require a custom made circuit board to be ordered that cost $5.00 to produce in bulk.

The RPI-0352E is an eco-friendly, low-cost photo collector emitter pairing transducer, with one end being a light emitting diode (LED) and the other being the read transducer collector that detects the amount exposed LED light [44]. The overall dimensions of the transducer are show in **Figure 3.7**. The circuit design requires an input channel voltage of 5 volts to operate it. The output signal indicates the voltage between the collector and emitter and varies depending on the collector transducer’s output. The transducer has a range of visibility of 3.0 mm. The linear range of voltage is shown in **Figure 3.8**.

To power the transducer, a lab grade power supply with a dedicated 5-volt output source is used. Due to the knowledge of high electromagnetic fields derived from CNC servo and spindle motors, a braided, shielded cable is required to reduce effects of high frequency noise on the system. Additionally, a customed made aluminum box was designed to house the wiring and connected to a BNC type female connector for ease of connecting to the data acquisition device. The cost of this wiring harness setup is $35.00 for the cable and an additional $10.00 for the aluminum housing.

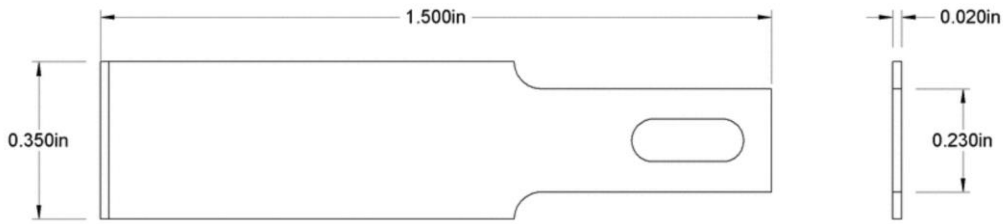

Figure 3.5 Number 17 blade dimensions

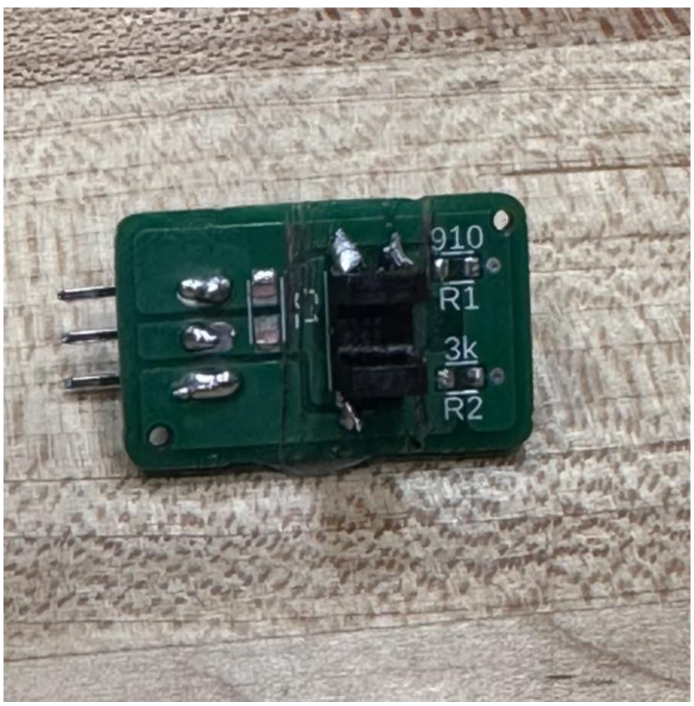

Figure 3.6 Circuit board layout for Rohm transducer

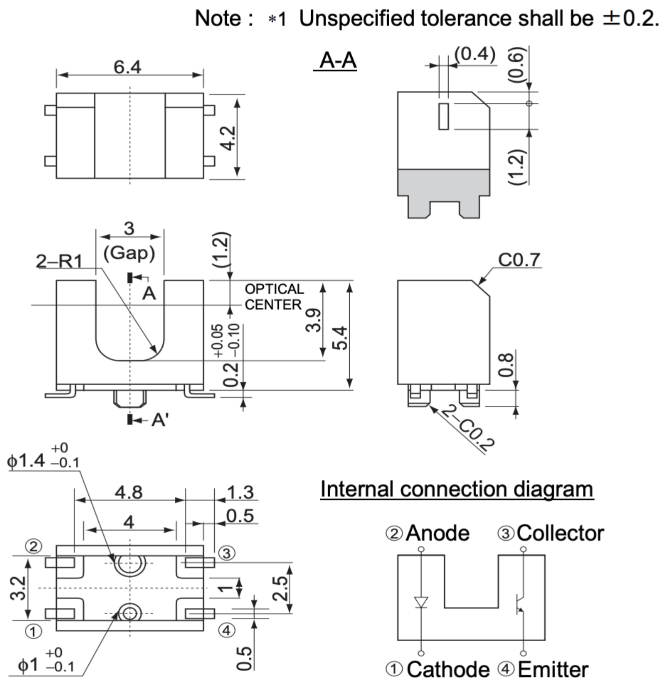

Figure 3.7 RPI-0352E dimensions [44].

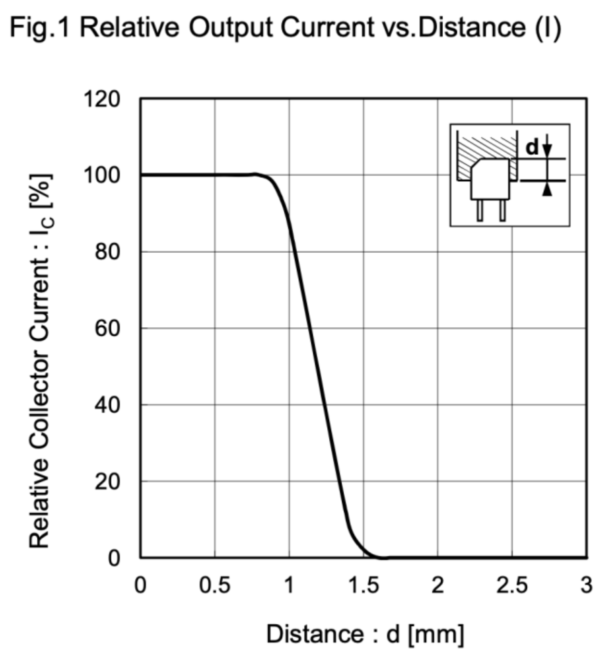

Figure 3.8 RPI-0352E current curve [44].

Coefficient Calibration

To utilize the KES as a displacement transducer, initial calibration is required. As the knife moves within the linear range the transducer, the change in voltage is correlated to the amount of displacement. Due to the transducer being an in-house displacement solution, there is no manufacturer calibration provided and must be experimentally measured. Prior development for a different photo-interrupter was conducted by Zameroski to produce a calibration procedure shown in **Figure 3.9** [45]. An Aerotech ABL 10100-LT Linear air bearing stage was used to measure the change in output voltage as the knife blade moves across the region of visibility. The knife edge is mounted on to the moving platform and the KES sensor on the stationary mount off the air bearing stage. The change in voltage over time is then converted to calibration coefficient of V/mm. The voltage is then measured with a multi-meter to set the knife edge directly at the center of the output voltage range.

Modification to this plan have been done to provide higher fidelity in measuring the calibration coefficient. For the ROHM RPI-0352E, the desired input voltage for the collector-emitter pairing is a 5 V input source. With this input voltage value, the output voltage transducer without any obstructions reads 1.35 V, and when completely blocked, the output voltage reads 0.0 V. The same linear air bearing stage is used for this testing. A small, continuous linear feed rate of 1 mm/min on the air bearing stage is used. The voltage for the KES is recorded using the same 16-bit ADC used for modal tap testing at a sampling frequency of 10 kHz. Like the current output shown in **Figure 3.8**, the change in the voltage shown in **Figure 3.10** follows a similar curve as shown in Zameroski's work in **Figure 3.11**.

Once measured, the data is then fit over the linear range of the transducer. Once the relationship for change in voltage versus time is set, the linear feed rate can be used to determine the change of voltage over the change of displacement. For this application, the transducer calibration is set to 0.814 mm/V with a mean voltage of 0.65 V. The transducer is then housed into its custom-made 3D printed hosing and then adhered to the frame of the CMD housing.

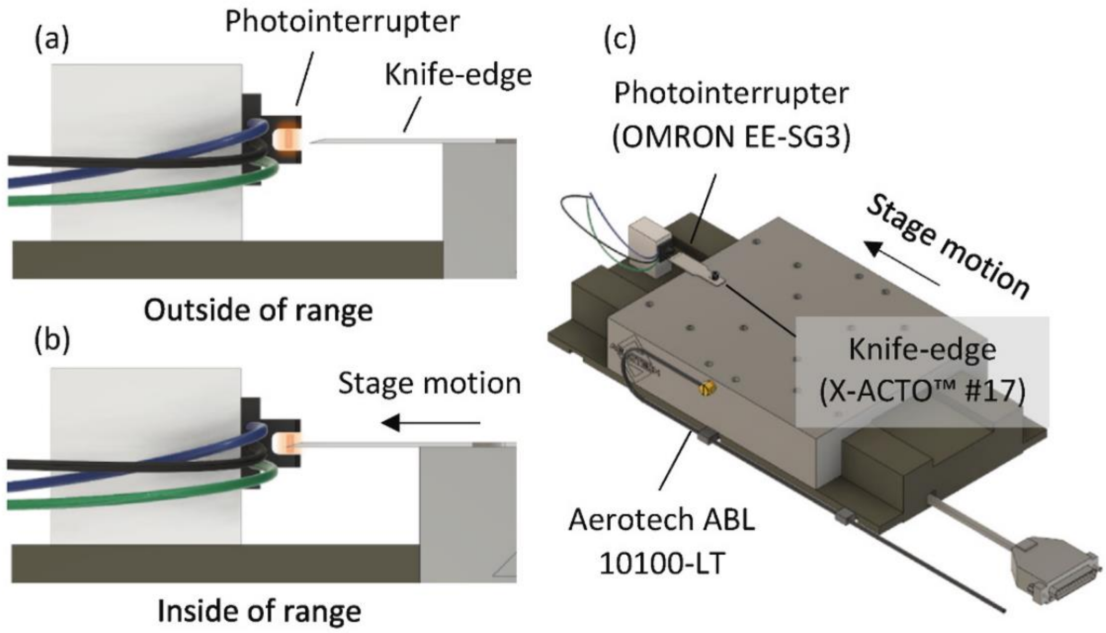

Figure 3.9 Modeled representation of air bearing stage testing performed by Zameroski [45].

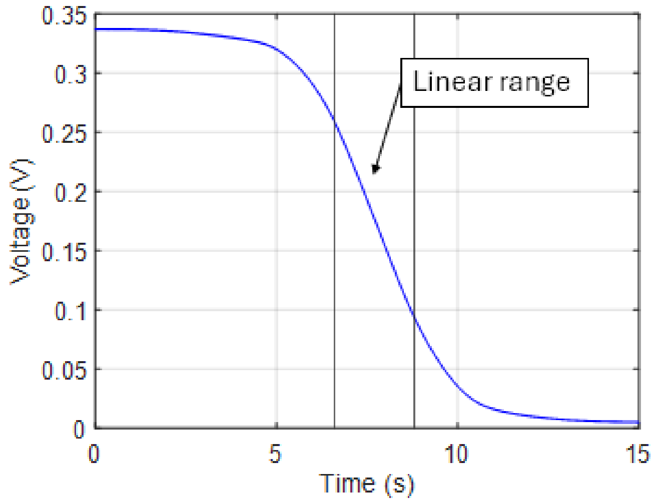

Figure 3.10 Calibration curve for the RHOM Photointerrupter

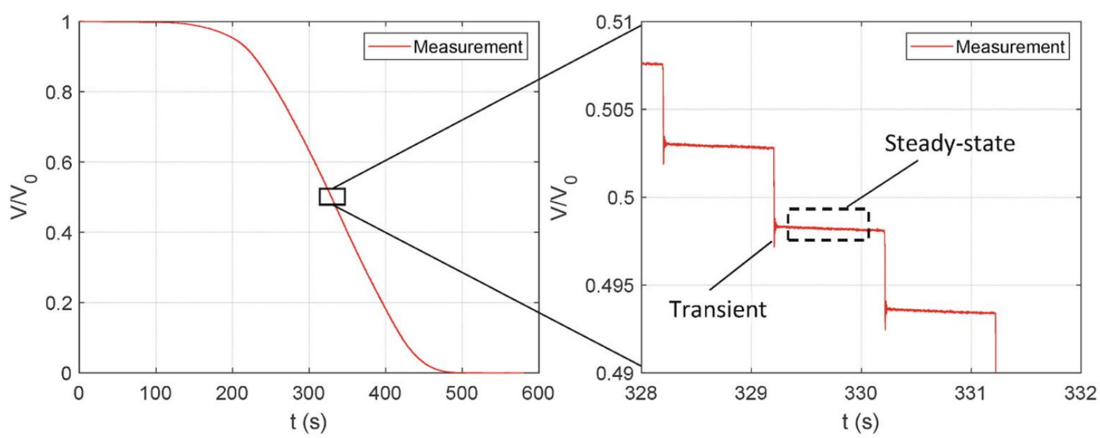

Figure 3.11 Zameroski Voltage to time calibration results [45].

Commercial grade measurement transducers

Kistler 9257b dynamometer

In modern research and industrial settings, the measurement of forces during operational cutting tests are conducted on a milling dynamometer. Most commercial grade dynamometers, such as those made by Kistler, are known to be piezoelectric transducers. This means that physical energy can be applied onto the system that will cause an electrical output reaction to be created because of deforming the piezoelectric material within the transducer housing. Quartz piezoelectric transducers consist essentially of thin piezoelectric slabs or plates cut in a precise orientation to the crystal axes depending on the application [34]. Most Kistler transducers incorporate a quartz element which is sensitive to either compressive or shear loads. The shear cut is used for patented multi-component force and acceleration measuring transducers. In the case of the Kistler 9257b force dynamometer shown in **Figure 3.12**, the stainless-steel enclosure utilizes four tri-axial quartz based piezoelectric crystals as shown in **Figure 3.13**. A sacrificial workpiece material is then mounted onto the workpiece utilizing the M8x1.25 mm hole pattern. Once the workpiece material is being cut by the tool, the overall workpiece-mounting structure experiences loads in the positive and negative x, y, and z milling directions. **Figure 3.14** depicts the overall orientation of the dynamometer's cutting directions and overall layout of the hole mounting positions. The orientation of the dynamometer is independent of the machining directions and must be considered when setting up the dynamometer within the CNC milling center.

The output of the system is an analog voltage that is sent into the dynamometer's charge amplifier with three appropriate voltages to force coefficients shown in **Figure 3.15**. The forces for x, y, and z milling directions are sent to the first three channels of the charge amplifier. The data signals are then sent from the charge amplifier to an analog to digital data acquisition device. The data will then be sampled at a 25,000 kHz frequency.

Figure 3.12 Kistler 9257 commercial grade force dynamometer.

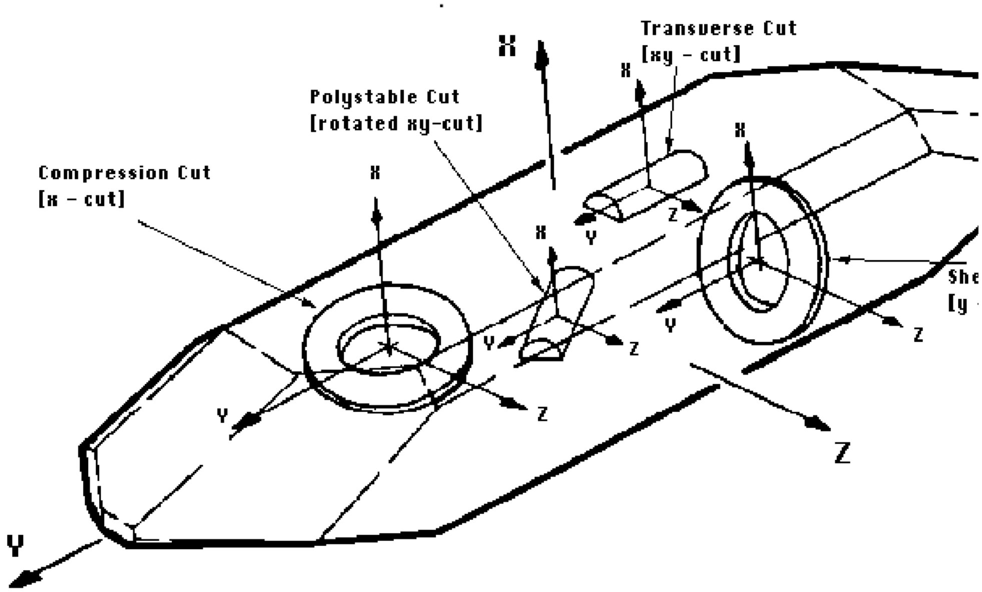

Figure 3.13 Piezoelectric system conceptual layout drawing [7].

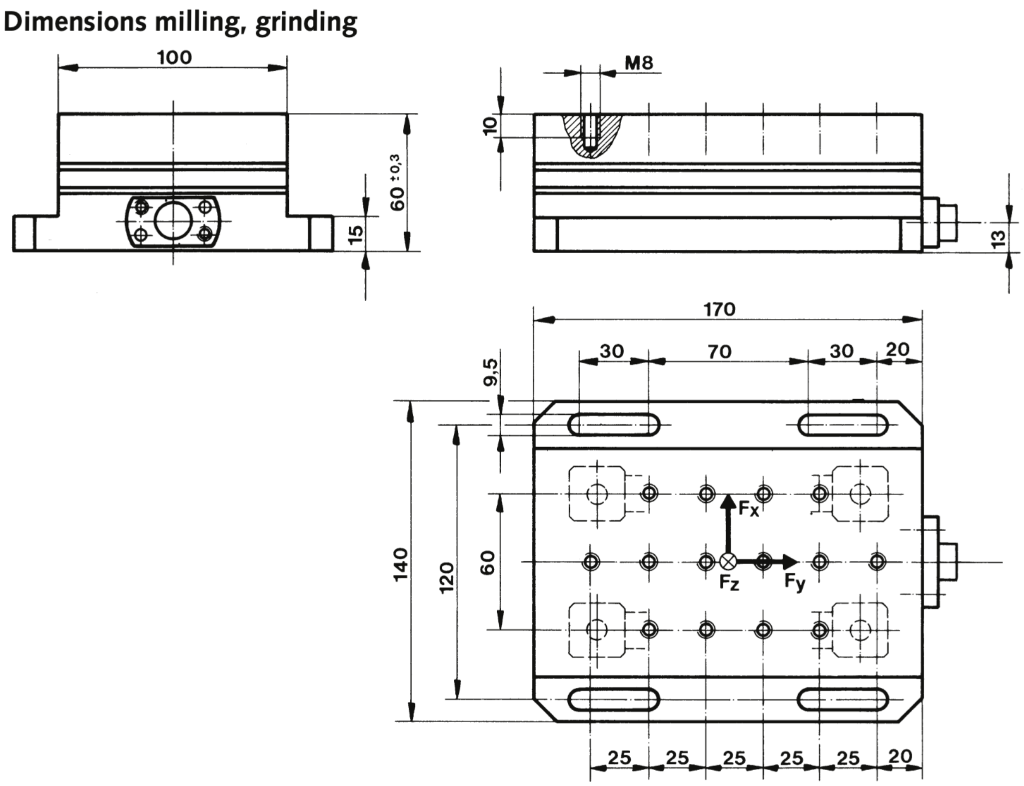

Figure 3.14 Kistler 9257 mounting diagram and dimensioning

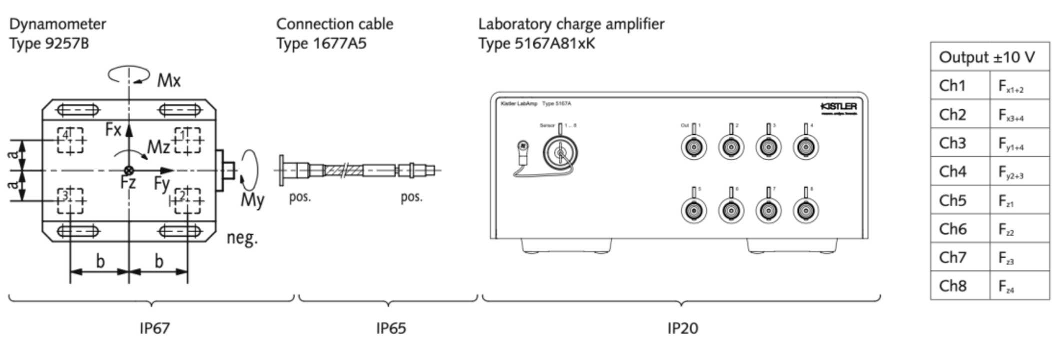

Figure 3.15 Kister 9257B charge amplifier layout

Force-to-force filtering of commercial dynamometer responses

Although the commercial grade system is known to be the industry standard for milling measurements, the signal produced by the transducer does not accurately represent the cutting forces occurring at the tool-workpiece interface. This is due to the structural dynamics of the dynamometer itself. As the sensor can pick up tri-axial forces, the structural dynamics of the semi-rigid casing appear in the signal. To remove these dynamics, a frequency-based filter must be created. Like the receptance-based FRFs of modal tap testing, a force-to-force (F2F) response is created by viewing the frequency response of the impulse hammer striking the workpiece along one of the Kistler 9257B channel directions. This directly compares the force input to the force output rather than force input to motion response. Once acquired, the unfiltered Kistler data is converted into the frequency domain and multiplied by the inverse F2F response to remove the structural dynamics within the frequency domain. The combined frequency content is then converted back into the time domain and compared to the unfiltered, initial measurement. This filtered data will then serve as the comparison to the other low-cost alternative methods presented in this dissertation.

Laser Doppler vibrometer

Due to the Kistler 9257B only producing force measurements, another commercial grade transducer is used to compare the motion measurements recorded on the CMD. For this testing, a Polytec Vibroflex Compact VFX-I-130 single-point laser Doppler vibrometer is selected. The laser vibrometer is a non-contact optical transducer that can measure the velocity of a vibrating surface The laser head of the system is calibrated a certain distance away from the target of interest and captures the motion by means of the Doppler effect and laser interferometry. The laser is pointed at a location on the target with the laser beam being split into two paths. One beam serves as the stationary reference while the other is used to detect the motion. The small displacement causes the frequency of the laser to shift slightly as the target workpiece moves. Both the reference and measurement beams are then recombined and used to determine the amount of motion based on the shift in frequency. An overall layout of the beam splitting is shown in **Figure 3.16**.

Piezoelectric accelerometer

Another common industrial grade transducer used to capture in process motion measurements is a piezoelectric accelerometer shown in **Figure 3.17**. Commonly used as a contact-based transducer, the accelerometer captures acceleration signals from the vibration of the workpiece when excited. Like the Kistler 9257B, as the quartz crystal begins to expand and contract, small voltage signals are produced by the crystal. By means of a charge amplifier, the signal is then amplified and sent to a data acquisition device. The accelerometer is calibrated by the manufacturer to relate the output voltage to a gravitational force, G. For milling experiments, the accelerometer is placed onto the sacrificial workpiece that is mounted onto the CMD to measure in-process acceleration measurements. An accelerometer is used to measure the FRF of both the tool and workpiece combinations by means of modal tap testing. For this situation, the acceleration signal is integrated twice to produce a displacement measurement to be paired with the force impulse produced by the modal hammer.

Modal tap testing acquisition, equipment, and testing

Modal tap testing hammer and accelerometer

To produce a frequency response function and modal parameters from a system, a force input transducer must be paired with a measurement transducer. A PCB modal impact hammer is used to excite the structure by means of an impulse. In the time domain, this is a short burst with a single force peak. Within the frequency domain, the impact from the hammer excites a region of frequencies to be evaluated. This method for exciting the system is preferred for milling operations compared to other frequency excitations that ramp up one frequency at a time. For milling application, a nylon hammer tip is used to avoid damaging the tool and preferred for the region of frequency excitations common to milling.

As mentioned above, the motion transducer is a PCB medium accelerometer whose signal is integrated twice to produce displacement. The measurement caused by

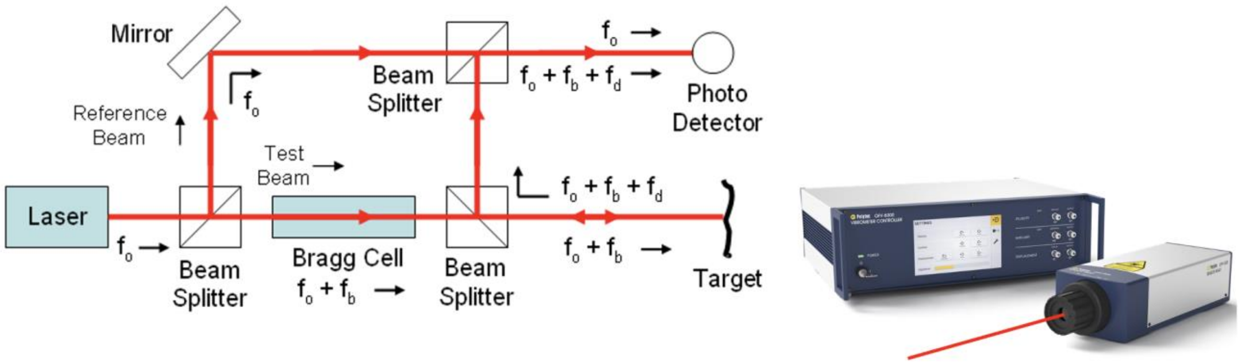

Figure 3.16 Laser Doppler vibrometer interferometry setup

Figure 3.17 Modal tap testing accelerometer usage

the modal hammer impulse will be captured as dissipating displacement and will be converted into the frequency domain. With both signals being converted into the frequency domain by means of a fast Fourier transform, the impulse hammer force measurement is divided over the accelerometer displacement measurement signal. This signal is the receptance of the system correlating the ratio of force over displacement produced by striking the workpiece.

When measuring the system's structural dynamics, there a few things that must be considered to ensure a high quality FRF is being produced. For all modal tap testing applications, the tools and workpiece materials are measured in both the x and y CNC milling directions; with both directions having asymmetric responses. For both directions, a minimum of five taps is standard to ensure repeatability and statistical confidence. When performing the impact testing by hand, all five measurements will result in a different amount of force and displacement measurements. This difference in forces is then averaged and used to find the overall FRF. For each of the strikes a level of coherence is validated along the frequency range. This is used to measure the percentage of the force being produced by the hammer that is measured by the accelerometer. For many accelerometers, a high level of coherence will be apparent for varying ranges of frequencies. This validates that the system is only reliable for frequency ranges that show a high level of coherence.

Once the FRF is produced, modal fitting can then be implemented to find all the modes over the measured frequency range for the system. For each mode, the associated modal parameters are then derived, recorded and used to create a normalized response fit to that of the original FRF. This fitted FRF will be fitted for both the tool and workpiece combination in both milling directions to produce the milling stability maps as explained in Chapter 2.

Analog to digital conversion hardware and software

For modal tap testing, additional hardware is required to convert the signals produced by both the modal impact hammer and accelerometer measurements. In the case of both transducers, the output signal is a small analog output voltage created by the piezoelectric material with the transducers. For those signals to be recognized by a standard personal computer, a Data Translation 16-bit analog to digital converter (ADC) is used to process the data. The ADC is a four-channel system that is capable of outputting 9 V DC to amplify the signals from the transducers connected by means of BNC connectors. Additionally, the Data Translation ADC is a multi-channel simultaneous system that is capable of recording multiple transducer signals at the same time. This is critical to the derivation of FRFs needed to record both force and motion signals rather than measuring each response sequentially. Additionally, the usage of a 16-bit ADC allows for high sampling frequencies to be recorded that is beneficial for the wide range of frequencies. **Figure 3.18** depicts the overall process of measuring the analog signals and producing a receptance-based FRF for tool a system. All equipment necessary for measuring the FRF is shown in **Figure 3.19**.

As for the software necessary to measure the FRF of both tool and workpiece combinations, a commercial grade licensed software for milling applications is used. TXF, created by MLI, is used to set up all necessary transducers and data acquisition systems. For both the impact hammer and accelerometer, the manufacturer’s calibration coefficients are inserted into the software. Additionally, internal preamps are activated to produce the voltage necessary to amplify each signal. The software is a guided platform to assist the user in performing tapping operations. Once all data is captured, TXF has the capability of fitting each mode within the system’s oriented FRF for both the tool and workpiece in each milling direction. Once all modal parameters are captured, the stability maps for the system can be produced. Additional inputs of milling parameters and specific cutting force values are applied to the software to model the true dynamics of the tool-workpiece system.

Frequency response function height compensation algorithm.

Once the KES-CMD workpiece configuration has been properly set up, an initial validation of the KES displacement calibration must be conducted. This is done to compare the calibration coefficient output for the in-house sensor to the measurements from the commercial grade systems described in the section above. For this purpose, the

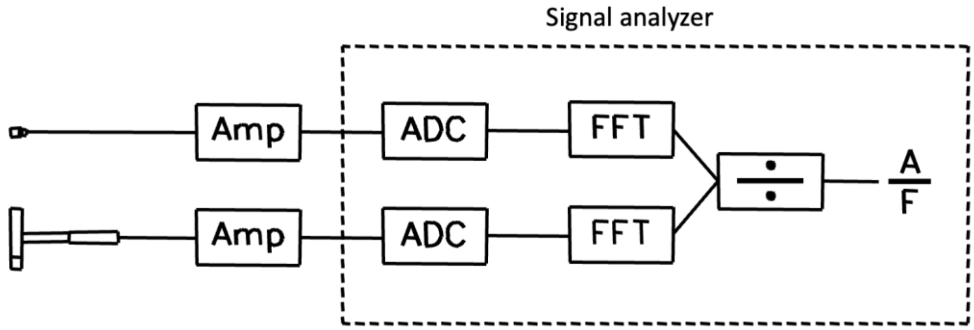

Figure 3.18 Schematic of signal analyzer paring with transducers for modal tap testing

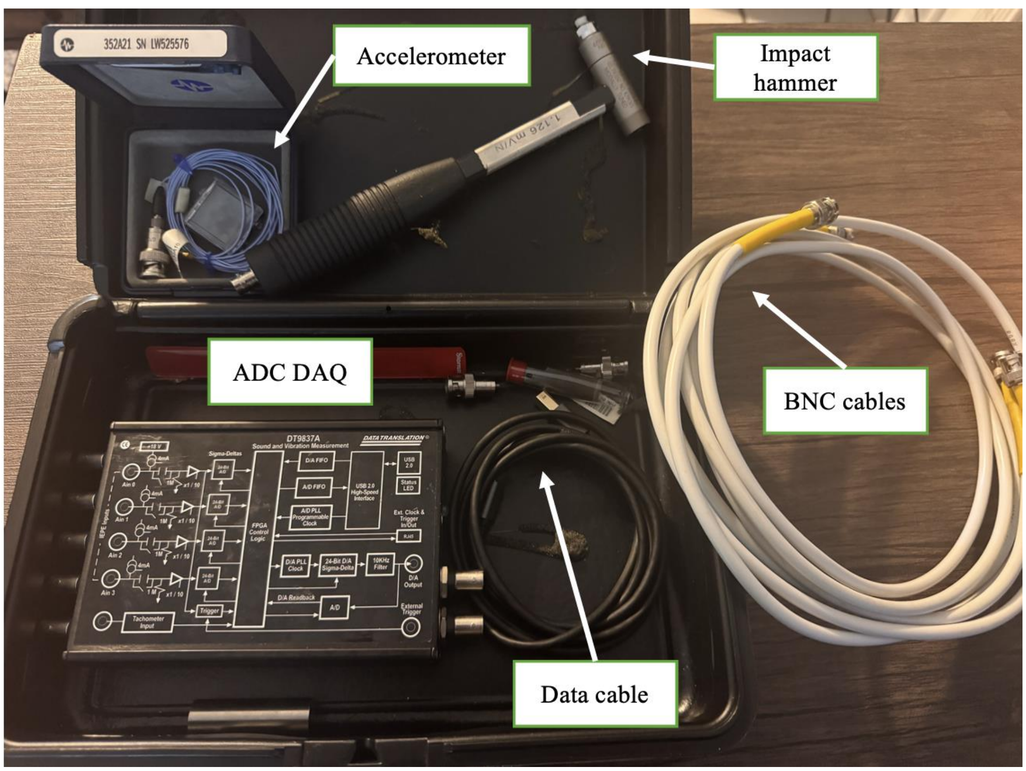

Figure 3.19 Modal tap testing instrumentation package

laser vibrometer was set to its displacement channel and compared to the measurements from the KES. The laser vibrometer was mounted onto the CNC machine worktable and directed at the workpiece material. The system was excited by striking the workpiece manually with the modal impact hammer. Both measurements for both transducers were simultaneously recorded over the course of one second to account for the impulse. Once recorded, the measurements are plotted using MATLAB. These plots show inconsistent results between both the transducer systems as shown in **Figure 3.20**.

This inconsistency was initially attributed to incorrect calibration coefficients derived from the linear air bearing stage. Due to the difference in how the motion occurs using the KES on the air bearing stage and then on the CMD, additional testing was conducted to find the root cause. Rather than comparing an experimentally derived transducer to a commercially available system, a benchmark test was conducted to directly compare to identical transducers from the same vendor. This second test was conducted using two medium sized PCB 352A21 accelerometers. One accelerometer was adhered to the lowest location of the CMD platform. The other accelerometer was placed as the highest location of the standard 25.4 mm tall workpiece. Additional sampling of the transducers was then taken by applying an impulse on the side of the workpiece with each accelerometer set with its own manufacturer calibration sensitivity. The measurements are then plotted using MATLAB shown in **Figure 3.21**. Comparing the results seen with the initial KES-vibrometer comparison, it is noted that a similar response is seen with the two accelerometers. This then dismisses the initial theory of an improper calibration of the KES and results in being a bias with the design of the CMD.

In both experiments, the difference shown between the transducer pairings show a higher amplitude of displacement and acceleration on the workpiece transducer. To determine the reasoning for these inconsistencies, a frequency response function grid testing was conducted on the CMD. This method was selected to analyze the modal parameters of the system at various locations on the stage and workpiece. The frequency response functions at different heights above the CMD surface shown in **Table 3.1**. Four additional lengths were selected away from the location of KES where the motion

Table 3.1 Height comparison distance from L5 KES location

Location	Distance (mm)
L4	51.55
L3	56.5
L2	66.75
L1	77.00

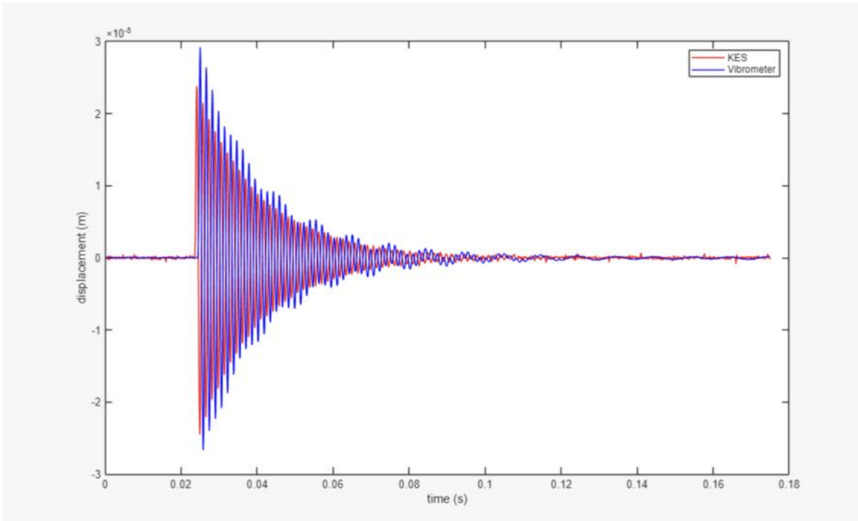

Figure 3.20 KES measurement compared to laser vibrometer displacement channel

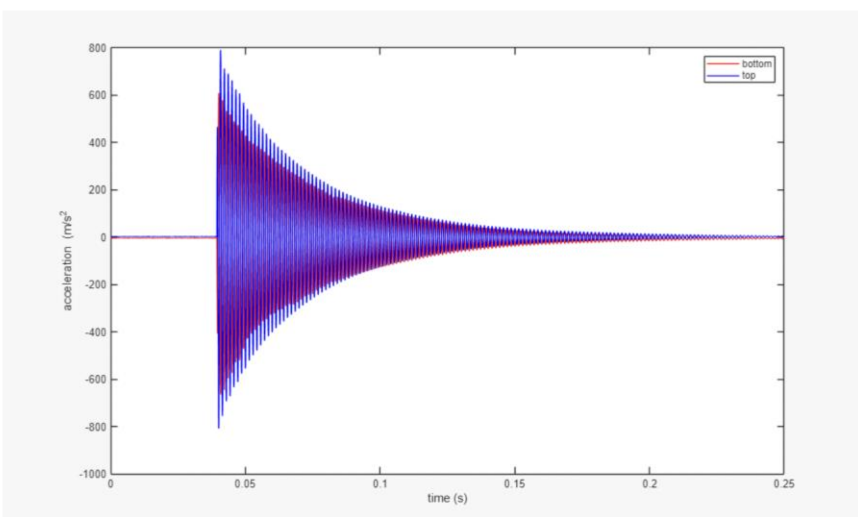

Figure 3.21 Two accelerometer comparison located at KES and workpiece.

measurement will be referenced. Three impact locations were selected to represent descending locations of cutting down the workpiece. A total of fifteen FRFs are then taken for each experiment shown in **Figure 3.22**. The impulse location was separated at 5 mm intervals from the top of the workpiece material, and the response locations were separated at five various lengths away from the top of the workpiece shown in **Table 3.1** Accelerometer measurements were double integrated to achieve a receptance-based FRF and for L5, the KES was used a standard displacement transducer. For each grid testing location, five impacts were performed.

Additional validation parameters were also selected to ensure the repeatability of these inconsistencies. Three initial materials were chosen for each grid test with a standard 12.7mm 4 fluted endmill. These common industrial-grade materials were selected to have a varying range of mass and damping properties compared to one another; aluminum 6061-T6, AISI 4140 steel, and titanium 6Al-4V. Additionally 15.875 mm length of cut endmill was selected. This selection is to ensure the compliance of the CMD is an order of magnitude more compliant than the tool to ensure a combined single degree of freedom system. For all testing cases, workpieces were machined to identical dimensions to ensure repeatability of the overall lengths of cut. These workpieces were also fixed on the CMD moving platform under a torque of 35 Nm. For each material, an initial FRF was measured along the center of the workpiece to capture the overall response of each tool-workpiece system. The varying FRF measurements were then plotted against one another to compare the system response under different mass and damping conditions. These results are shown in **Figure 3.23**. As a result, a large variation of the natural frequency for each system is heavily influenced by the change in mass of each block. AISI 4140 has the lowest natural frequency and the largest density, while 6061-T6 shows inverse results with the highest natural frequency and smallest density. The titanium 6Al-4V proves to be an intermediate response compared to the other two materials.

For each material, the FRF grid test was conducted for a total for 15 locations using both the accelerometer and KES. For each test, natural frequency, stiffness, and

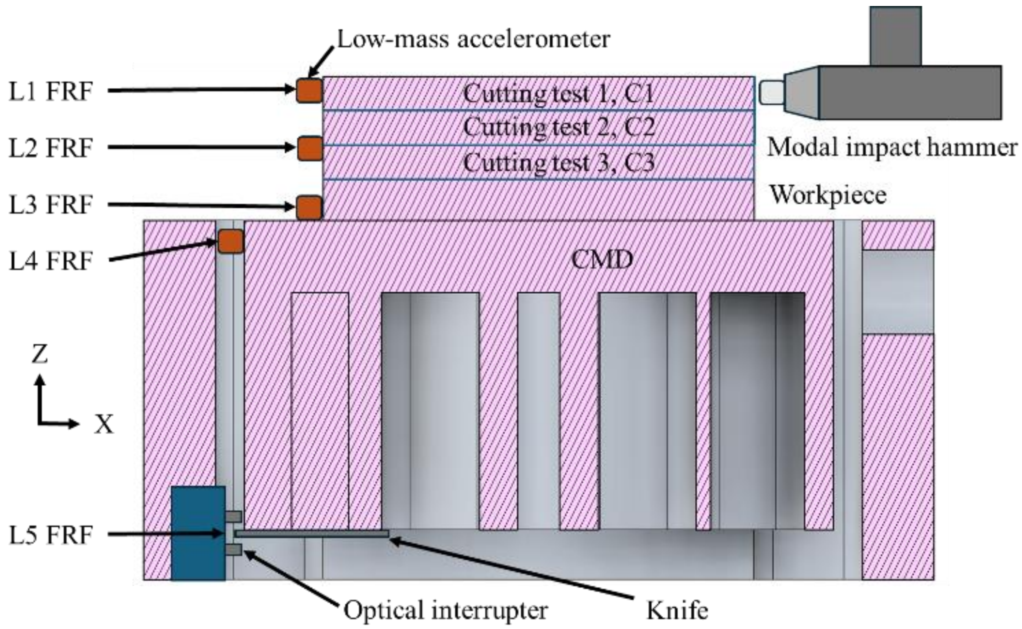

Figure 3.22 FRF grid testing layout.

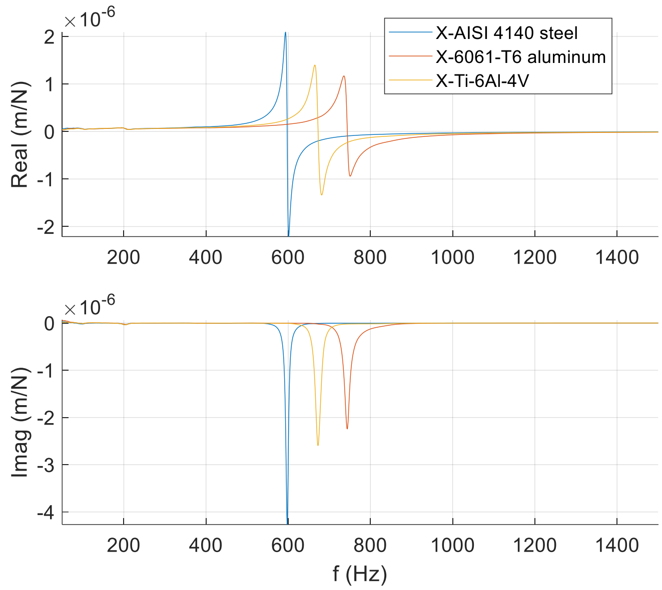

Figure 3.23 FRF comparison for three workpiece material

damping ratio were acquired using the modal peak picking technique. In each case the modal mass and damping parameters where calculated. The modal parameters for each height stage were measured for each cutting location on the workpiece. The data was then recorded on **Table 3.2-Table 3.10** and compared for each stage to determine the commonalities and differences between each FRF response. Small variation between testing on the same workpiece material could attribute to small inconsistencies in measurements due to manual tap testing not being completely repeatable.

Based on these results, there is a discrepancy in the structural dynamics of the system at various heights based on similar trends seen on all three samples. For each case, the natural frequency at each location various an insignificant amount. The variation for all testing cases is less than 5 Hz which can be attributed to slight inconsistencies in modal tap testing. For each of the fifteen tests performed on all three materials, a common trend is detected moving from L1 at the top of the workpiece to L5 at the KES. The mass and stiffness parameters both show incremental increases across all workpiece

Table 3.2 Grid testing Aluminum 6061-T6 Location C1

Location	f_n (Hz)	m (kg)	c (N-s/m)	k (N/m)
L1	743.1	0.852	44.77	$1.86\ x\ 10^7$
L2	743.7	0.866	48.54	$1.89\ x\ 10^7$
L3	743.6	0.884	50.81	$1.93\ x\ 10^7$
L4	743.4	0.898	54.55	$1.96\ x\ 10^7$
L5	744.0	0.915	51.34	$2.00\ x\ 10^7$

Table 3.3 Grid testing Aluminum 6061-T6 Location C2

Location	f_n (Hz)	m (kg)	c (N-s/m)	k (N/m)
L1	744.8	0.872	48.57	$1.91\ x\ 10^7$
L2	744.6	0.886	49.35	$1.94\ x\ 10^7$
L3	744.9	0.890	48.33	$1.95\ x\ 10^7$
L4	744.9	0.899	49.67	$1.97\ x\ 10^7$
L5	745.2	0.912	51.26	$2.00\ x\ 10^7$

Table 3.4 Grid testing Aluminum 6061-T6 Location C3

Location	f_n (Hz)	m (kg)	c (N-s/m)	k (N/m)
L1	745.8	0.874	46.30	$1.91\ x\ 10^7$
L2	745.5	0.893	49.75	$1.91\ x\ 10^7$
L3	745.9	0.897	48.76	$1.91\ x\ 10^7$
L4	745.8	0.902	48.17	$1.91\ x\ 10^7$
L5	746.0	0.910	50.35	$1.91\ x\ 10^7$

Table 3.5 Grid testing AISI 4140 steel location C1

Location	f_n (Hz)	m (kg)	c (N-s/m)	k (N/m)
L1	597.3	1.303	31.78	$1.84\ x\ 10^7$
L2	597.4	1.306	31.38	$1.84\ x\ 10^7$
L3	597.4	1.334	32.06	$1.88\ x\ 10^7$
L4	597.3	1.353	32.50	$1.91\ x\ 10^7$
L5	597.3	1.378	33.60	$1.94\ x\ 10^7$

Table 3.6 Grid testing AISI 4140 steel location C2

Location	f_n (Hz)	m (kg)	c (N-s/m)	k (N/m)
L1	598.9	1.311	31.58	$1.86\ x\ 10^7$
L2	599.0	1.311	31.58	$1.86\ x\ 10^7$
L3	599.0	1.341	32.31	$1.93\ x\ 10^7$
L4	599.0	1.363	33.33	$1.96\ x\ 10^7$
L5	598.9	1.384	33.33	$2.0\ \ x\ 10^7$

Table 3.7 Grid testing AISI 4140 steel location C3

Location	f_n (Hz)	m (kg)	c (N-s/m)	k (N/m)
L1	600.4	1.325	31.48	$1.89\ x\ 10^7$
L2	600.3	1.336	31.72	$1.90\ x\ 10^7$
L3	600.4	1.349	32.06	$1.92\ x\ 10^7$
L4	600.5	1.370	32.56	$1.95\ x\ 10^7$
L5	600.5	1.391	32.54	$1.98\ x\ 10^7$

Table 3.8 Grid testing titanium 6Al-4V steel location C1

Location	f_n (Hz)	m (kg)	c (N-s/m)	k (N/m)
L1	677.9	0.948	42.81	$1.72\ x\ 10^7$
L2	677.9	0.965	43.55	$1.75\ x\ 10^7$
L3	672.8	0.973	43.92	$1.76\ x\ 10^7$
L4	678.4	0.974	43.60	$1.77\ x\ 10^7$
L5	678.2	0.991	45.20	$1.80\ x\ 10^7$

Table 3.9 Grid testing titanium 6Al-4V steel location C2

Location	f_n (Hz)	m (kg)	c (N-s/m)	k (N/m)
L1	678.9	0.956	43.24	$1.74\ x\ 10^7$
L2	678.9	0.967	44.15	$1.76\ x\ 10^7$
L3	678.9	0.973	44.40	$1.77\ x\ 10^7$
L4	678.9	0.989	44.31	$1.80\ x\ 10^7$
L5	679.1	1.00	44.36	$1.82\ x\ 10^7$

Table 3.10 Grid testing titanium 6Al-4V steel location C3

Location	f_n (Hz)	m (kg)	c (N-s/m)	k (N/m)
L1	679.9	0.953	42.36	$1.74\ x\ 10^7$
L2	679.8	0.959	43.02	$1.75\ x\ 10^7$
L3	679.9	0.981	43.57	$1.79\ x\ 10^7$
L4	679.9	0.997	44.31	$1.82\ x\ 10^7$
L5	680.2	1.005	44.66	$1.84\ x\ 10^7$

materials. Due to no changes in mass occurs between taps at each location, the observed change in mass parameters should not be happening. Given the natural frequencies remain constant between each location and mass must stay constant, stiffness is the only parameter that should be changing between locations.

Due to this understanding of the CMD's structural dynamics, it can be assumed that inconsistencies between the measurement's location is based on a change in stiffness. The measurements for all the stiffness measurements are then plotted against one another for comparison as shown in **Figure 3.24**. Once plotted it is apparent that the system is piece-wise linear, and a linear function can define the change in stiffness ratio. The first linear region correlates to the height across the stage. This area is inaccessible for milling operations and can assume to be a fixed constant. The secondary linear fit is correlated to the change in height from the top of stage to the stop of the workpiece. As seen in **Figure 3.25**, a best fit line along with one standard deviation is applied to the second region to approximate the change of stiffness over the length of the workpiece. Equation 54 shows the expression for measuring the height compensation value, α.

$$\alpha = 0.987 - 0.0018(x - 52.5) \quad (54)$$

This coefficient is then applied to the measured displacement. **Figure 3.26** shows the same test on an aluminum applied at each cutting location before compensation and after compensation. **Figure 3.27** shows each location using the algorithm to compensate for the distance away from the KES L5 location. For all this case it can be seen that all cutting locations increase in level to agree with the measurements produced by the Kistler 9257B dynamometer.

CMD force measurement acquisition

Frequency domain structural deconvolution method

Prior methods of deriving force measurements from displacement using the CMD-KES transducer pairing have been conducted by Gomez and Schmitz [1], [5], [6], [46]. The initial method of deriving force from in-process displacements by means of frequency-based filtering was referred to as structural deconvolution. The process requires five critical steps to convert time-domain displacement into a time-domain force

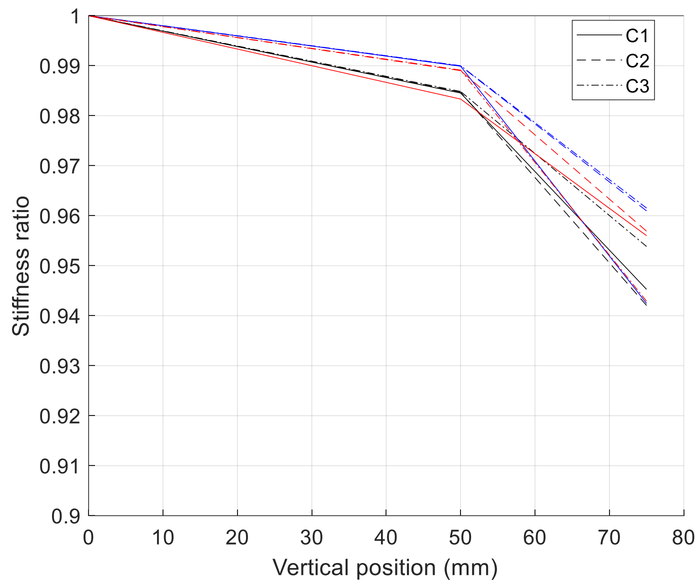

Figure 3.24 Stiffness ratio measurements for all cutting locations and materials.

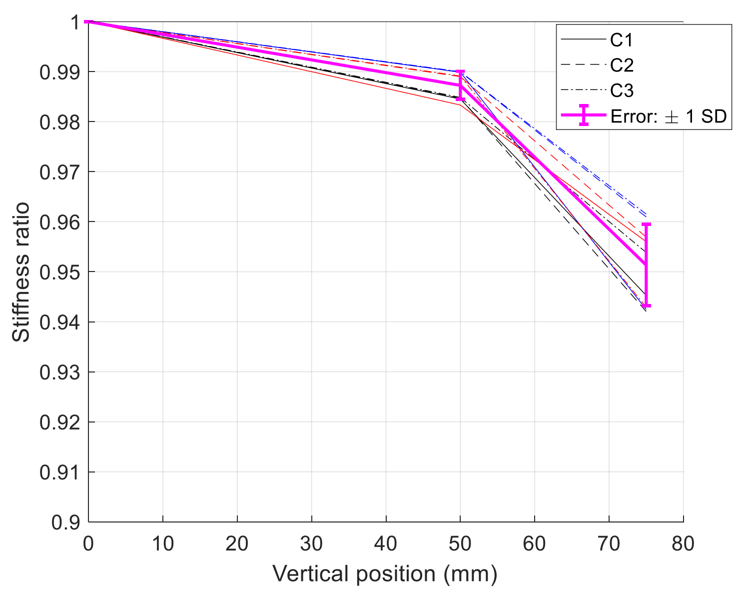

Figure 3.25 Piece-wise linear fit on stiffness ratio data.

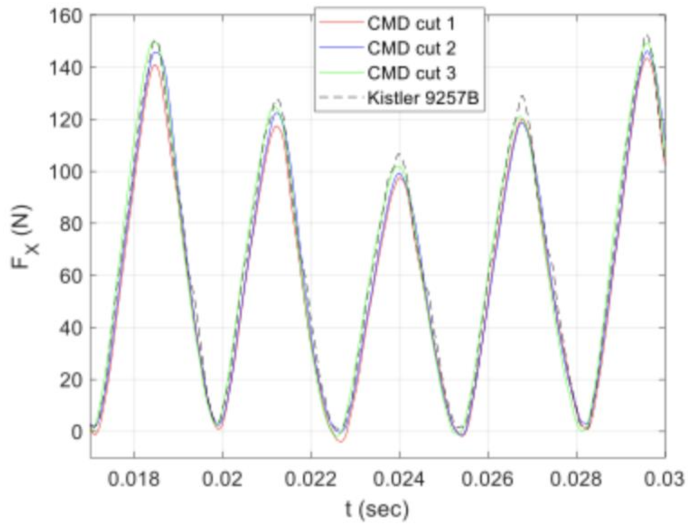

Figure 3.26 Aluminum 6061 T6 non-compensated measurement for C1, C2, and C3

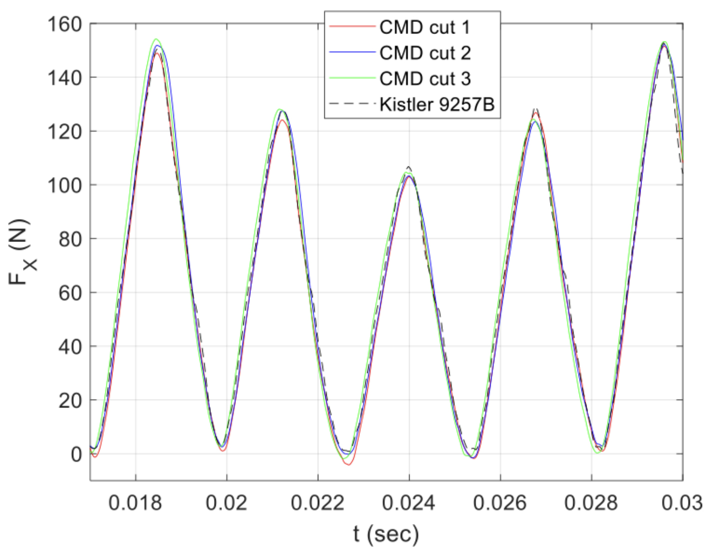

Figure 3.27 Aluminum 6061 T6 compensated measurement for C1, C2, and C3

measurement shown below.

1) Converting the time domain displacement to the frequency domain using the discrete Fourier transform method (DFT). Prior to converting to the frequency domain, the mean signal must be removed from the system. This mean is referred to as the DC offset of the measured displacement signal. Additionally, the transient portions of the cutting test at the entry and exit of the tool are removed to analyze the steady state cutting force. Once these conditions are met, the frequency content of the displacement signal will be used to obtain the force measurement using the next steps. The initial time-based displacement is shown in **Figure 3.28**.
2) The FRF for the CMD in the compliant direction must be measured using modal tap testing. Once the receptance FRF is obtained, the inverse of the response must be taken to apply it as a mechanical filter. Inverting the FRF is necessary because receptance is the displacement response over the input force This inversion will also attenuate the structural dynamics at the natural frequency of the system prior to cutting operations. This is shown in Equation 55.

$$F(\omega) = \left(\frac{X}{F}\right)^{-1} \cdot X(\omega) \quad (55)$$

   When inverting the response, the product of both the displacement and the filter will result in force. This filter will then remove the single degree of freedom structural dynamics from the system. When inverting the FRF, the values approaching zero will tend towards infinity. This issue must be addressed prior to converting the data back to the time domain. The inversion of the FRF is shown in **Figure 3.29**.
3) A low pass filtering method must be implemented to reduce the effects of the inverse FRF filter. This is corrected by means of a third order-Butterworth filter. This filter will attenuate all frequencies beyond the desired cutoff frequency. For these examples, an arbitrary cutoff frequency above the natural frequency of the system is utilized. A Butterworth filter is selected due to its flat frequency response and smooth roll-off characteristics, which minimizes distortion of the force signal below the cutoff frequency.

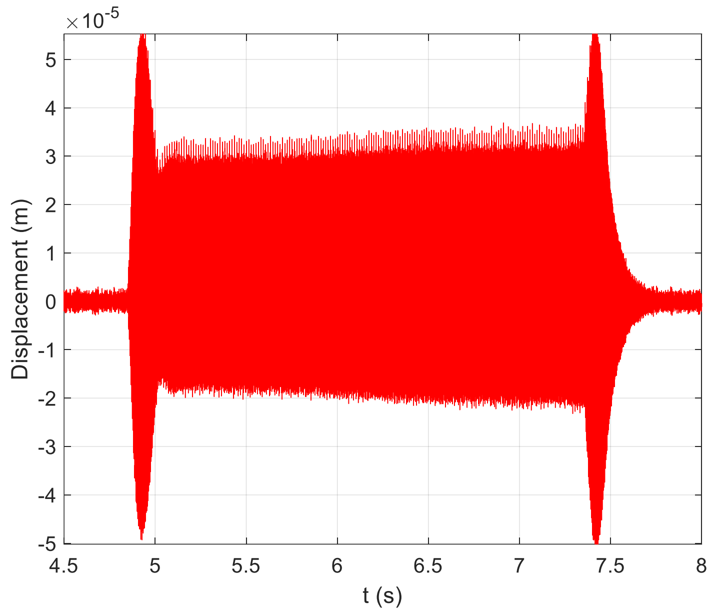

Figure 3.28 CMD 1018 steel workpiece displacement measurement example obtained with KES.

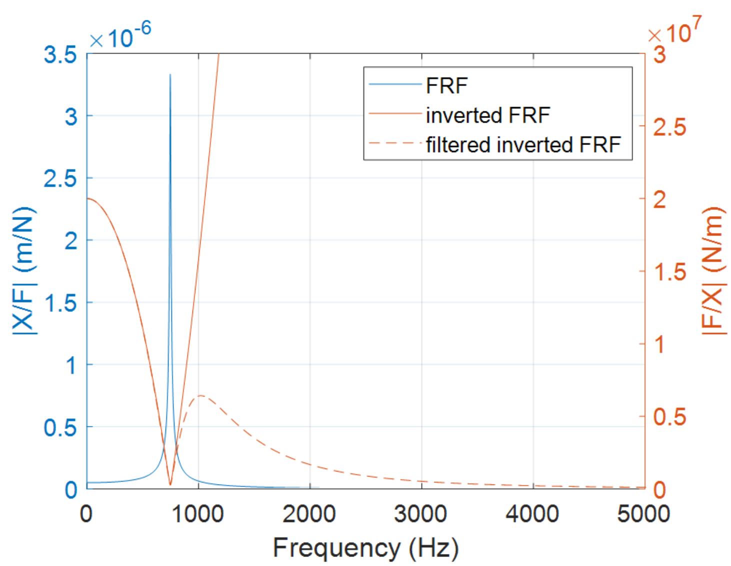

Figure 3.29 (Top) real and (bottom) imaginary components of CMD SDOF dynamics FRF compared with aluminum 6061-T6 workpiece FRF in the *x* and *y* directions.

4) The frequency content for both the displacement measurement and filters are then multiplied within the frequency domain as shown in Equation 56. The product will then be a filtered force measurement that removes the structural dynamics of the CMD from the response. **Figure 3.28** shows the frequency content before and after filtering.

$$F(\omega) = \left(\frac{X}{F}\right)^{-1} \cdot\ X(\omega) \cdot \text{butterworth}(\omega)\ (55)$$

5) The frequency domain content is then converted back into the time domain as shown in Figure 3.29. This process is done by the inverse discrete Fourier transform method (iDFT). During this process a small-time delay is caused due to the frequency conversion. The force measurement data is then compared to commercial grade dynamometer results as a benchmark.

Although an effective method of obtaining force measurements, this process is highly dependent on the conversion of the time-based displacement signal into the frequency domain. This approach requires signal processing expertise and computational resources that make real-time implementation challenging on a production level floor for operator usage. Additionally, this approach requires maintaining consistent system dynamics and accurate characterization of the CMD's frequency response. This is vital to removing the structural dynamics at the exact natural frequency of the system with the inverse FRF filtering. Cuts in both the *x* and *y* milling directions can be independently captured using this approach.

Time domain force summation method

The new method proposed in this dissertation takes a time-domain based approach to the obtain additional motion parameters and milling forces using the same CMD-KES system. The process will be broken into thirteen steps to convert the displacement into force but will also account for the additional motion and cutting parameters that will be conducted within the process.

1) A standard workpiece geometry will be used for all testing and mounted onto the CMD using a standard torque specification.

2) An initial receptance FRF is taken at the center of the workpiece my means of modal tap testing. Once obtained, modal tap testing will be implemented to obtain the single degree of freedom modal parameters. These parameters are the natural frequency of the structure, the stiffness at location L1, and the unitless damping ratio. The modal mass and damping parameters are then mathematically computed using the initial modal parameters.
3) A stability map will be produced using the Tlusty approach with the FRF from only the CMD and an experimental specific cutting force coefficient, K_s. The stability map will be used to determine a region where a standard 2 mm by 2 mm cut can be taken for each cutting test.
4) Once spindle speed is set for the cut, the tooth passing frequency will be calculated for the first five orders including any additional runoff frequencies. A bandwidth of 10% will be derived based on the natural frequency. The calculated tooth passing frequencies will be set to ensure it does not fall within the range of the natural frequency of the system to cause resonance to occur. If the initial spindle speed falls within the range, adjust using the tooth passing frequencies to obtain a new spindle speed.
5) Once cutting parameters are set, five continuous incremental feed per tooth cuts are performed on the workpiece in the *x* milling direction of the system. All these cuts will be in a down milling operation.
6) The displacement measurement will be passed through a low pass filter to remove any high content produced by the CNC milling center. The initial displacement measurement will be divided by the height compensation value α to compensate for the stiffness variation in the system
7) The filtered displacement is derived by means of a 150th-order FIR differentiator to obtain the velocity measurement of an in-process cutting operation. The measurements will be compared to the industrial-grade laser doppler vibrometer

8) The velocity will then be derived using the same 150th-order FIR differentiator to produce acceleration. The measurements will be compared to the industrial-grade accelerometer.
9) The time-based motion parameters will be defined as $(x, \dot{x}, \ddot{x})$. will be multiplied by the appropriate CMD workpiece modal parameter (k_{wx}, c_{wx}, m_{wx}) to represent the individual force components.
10) Spring force will be calculated using modal stiffness, k_{wx}, and displacement, x, signals using Equation 55.

$$F_s = k_{wx}x \quad (55)$$

11) Damping force will be calculated using the modal damping, c_{wx}, and velocity, $\dot{x}$, signals using Equation 56.

$$F_d = c_{wx}\dot{x} \quad (56)$$

12) Inertial force will be calculated using the modal mass, m_{wx}, and acceleration, $\ddot{x}$, signals using Equation 57.

$$F_i = m_{wx}\ddot{x} \quad (57)$$

13) The three forces will be summed as shown in Equation 58.

$$F_{sum} = F_s + F_d + F_i \quad (58)$$

Once the directional force measurement is obtained, the results will be compared to an identical cutting operation performed on the Kistler 9257B. Structural dynamics will be removed from the Kistler measurement to obtain the true, filtered cutting force. Additionally, the structural deconvolution method will be performed and set as the secondary comparison to determine the difference between both approaches. These steps will then be reproduced to perform five incremental cuts in the rigid *y* machine direction. The directional forces will then be compared to both the Kistler 9257B and structural deconvolution methods. Due to the manner that the KES collects data, the vibration of the cuts is still measured in the *x*-direction. Once all directional cuts are performed, the cutting force coefficient for each approach will be obtained by means of the linear regression approach. All normal, tangential, specific cutting, and beta angle coefficients will be measured and compared for each approach.

An initial repeatability test for aluminum 6061 with a 12.7 mm endmill was performed to verify the system. For these test, three identical cuts were taken to measure any changes between the recorded displacement with one standard deviation. Each signal is then derived into velocities and accelerations by means of the FIR differentiators and compared to the commercial grade transducers with one standard deviation. Force measurements are then derived and compared for each approach with one standard deviation. These experimental results are shown in **Figures 3.30- 3.34**.

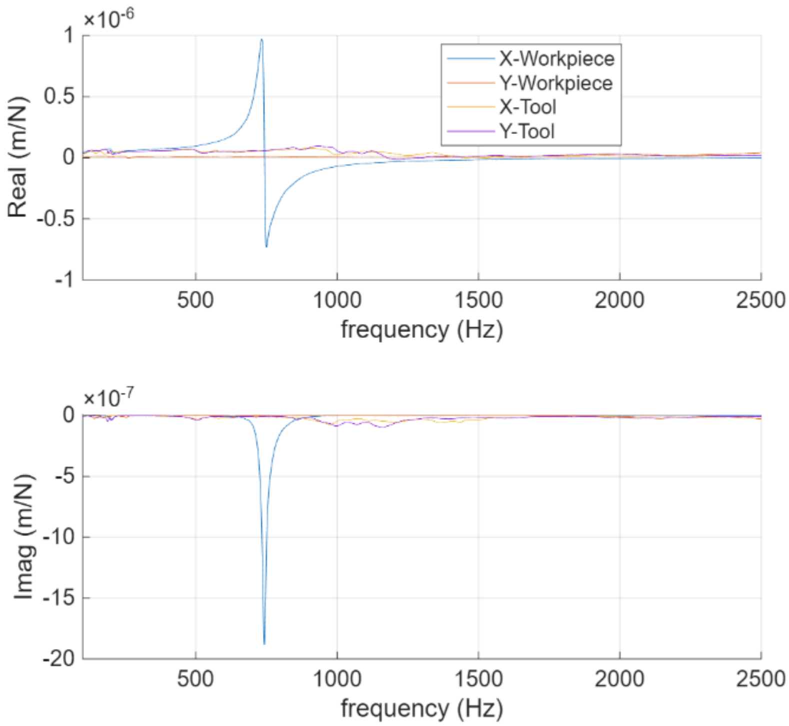

Figure 3.30 Aluminum 6061 – 12.7 mm tool combined FRF.

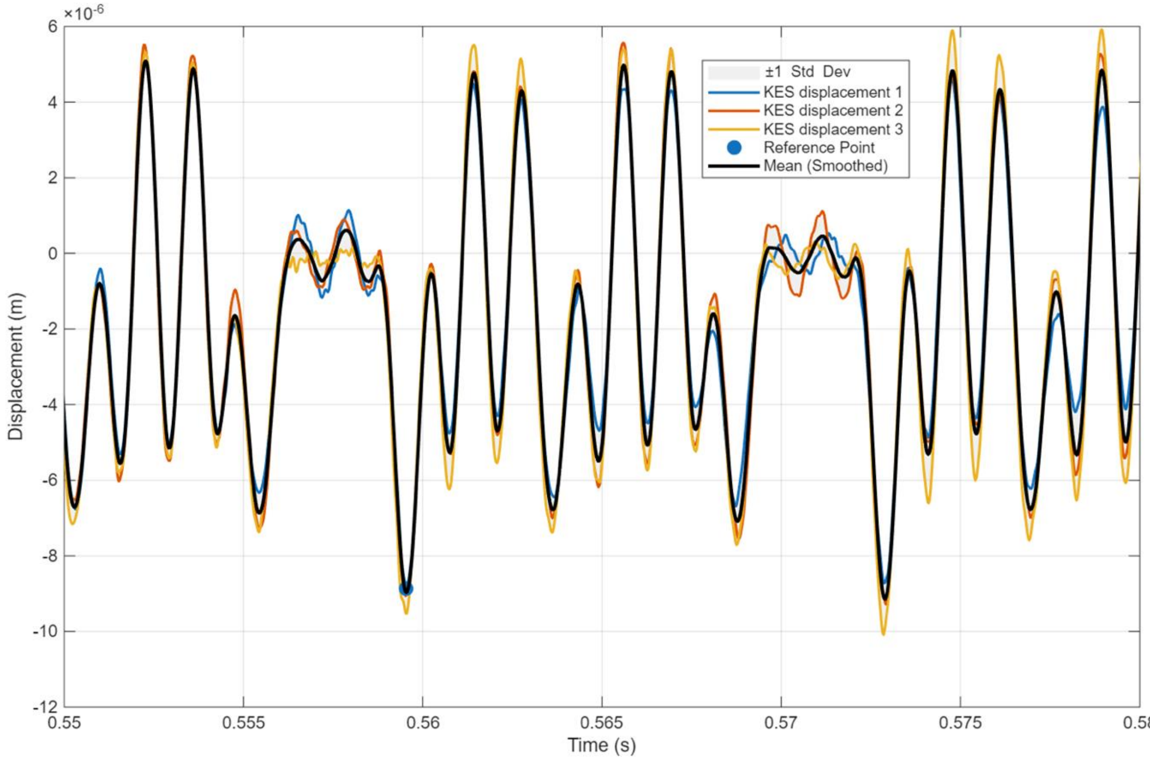

Figure 3.31 Repeatability displacement measurements for aluminum 6061 trial.

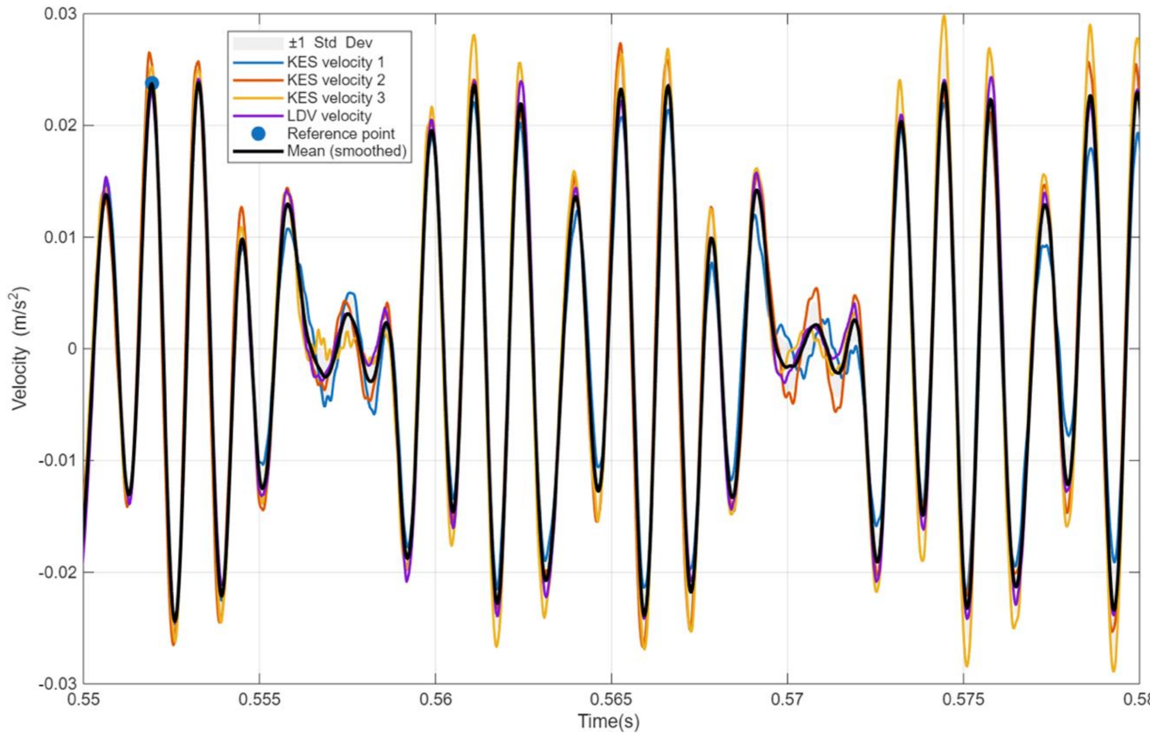

Figure 3.32 Repeatability derived velocity measurements compared to laser vibrometer for aluminum 6061 trial.

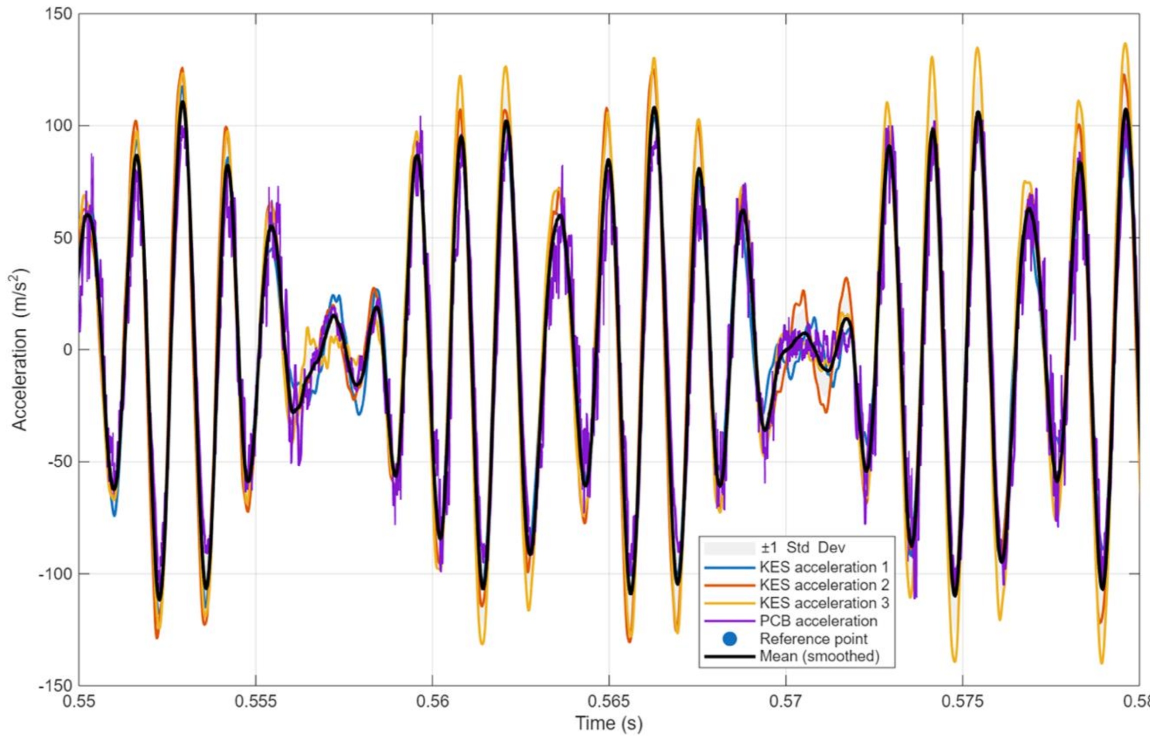

Figure 3.33 Repeatability acceleration measurements compared to accelerometer for aluminum 6061 trial.

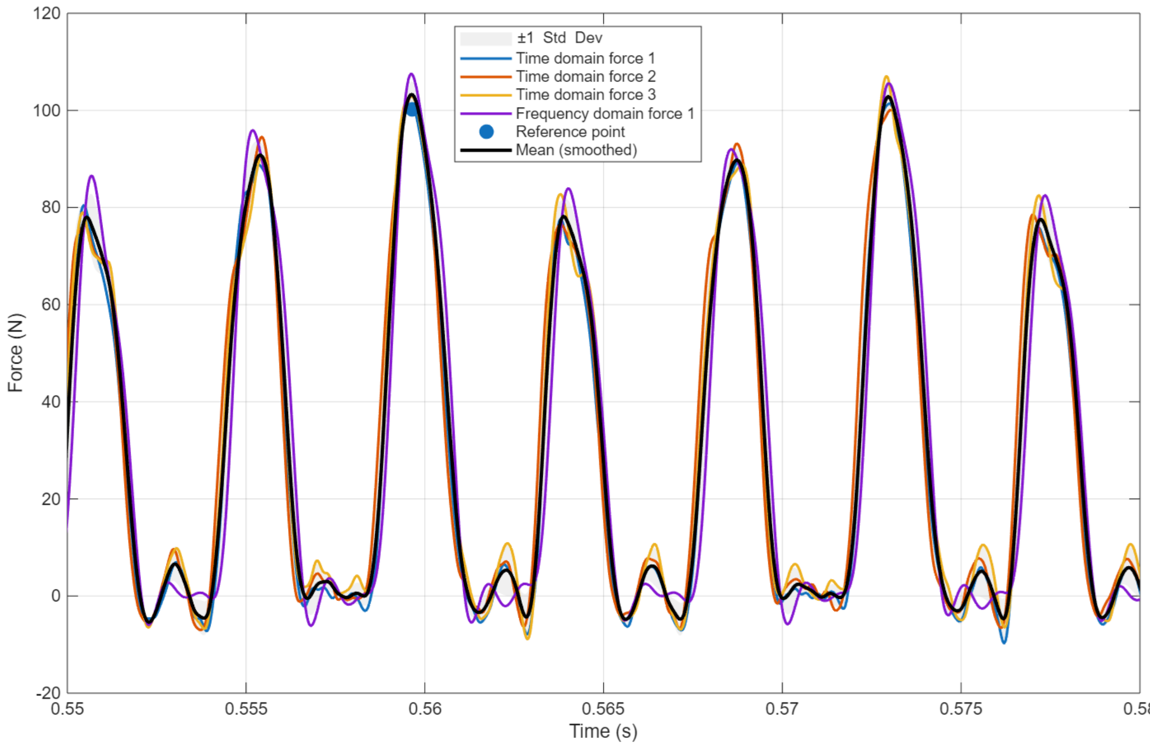

Figure 3.34 Repeatability force measurements compared to structural deconvolution approach for aluminum 6061 trial.

CHAPTER FOUR

EXPERIMENTAL METHOD

The purpose of this experiment is to be able to implement the novel time-based force summation method for various workpiece materials and milling tools. The forces measured with this approach will be compared to that of both the frequency structural deconvolution method as well as a commercial-grade dynamometer system for each tool-workpiece combination. For each method, five incremental cutting tests will be conducted to validate the system's response for varying cutting parameters. These five cuts will also be used to experimentally obtain each tool-workpiece cutting force coefficients and compare them to one another. The results will be used to determine if the time-based method is consistent with both the frequency-based method that requires higher expertise in frequency analysis and with commercial-grade system that costs orders of magnitude more.

Material and milling tool selection

For this testing a combination of seven metal workpiece materials has been selected. The range of these materials have been selected to allow for a wide range of specific cutting forces, densities and damping properties. For all materials, the workpiece has been machined to have identical dimensions shown in **Figure 4.1** Additionally, to the seven workpieces, three endmills have been selected as well for the cutting operations. All three endmills share the same 12.7 mm diameter but differ in the number of flutes and material coatings. These two distinctions allow for different milling parameters due to the varying tooth passing frequencies, capable feed per tooth values due to tooth spacing, and advantageous combination between the workpiece material and the tool. A new tool will be used for each iteration of the cut and will be used on both the CMD and commercial-grade dynamometer to ensure the tooth runout measurements remain identical between both systems. **Figure 4.2** depicts the tool-workpiece combinations creating a total of twelve combinations. **Table 4.1** depicts the specification of the workpiece materials used and Table 4.2 depicts the tool geometries used.

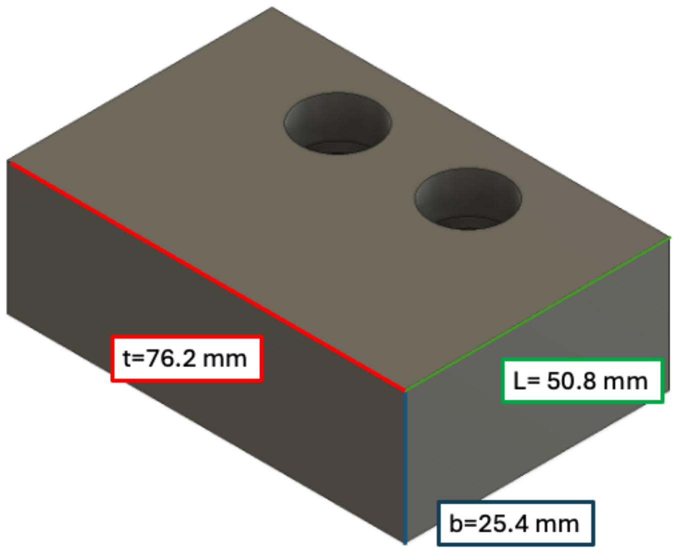

Figure 4.1 Standard geometry workpiece with reference dimensions.

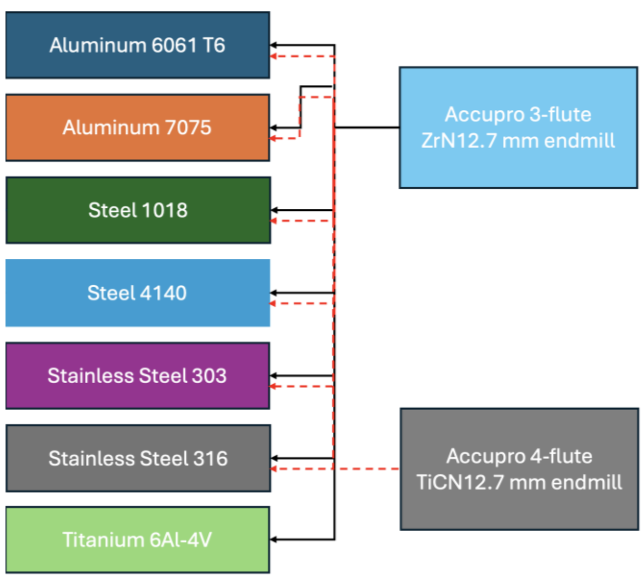

Figure 4.2 Twelve tool-workpiece combination chart.

Table 4.1 Material characterizations

Material	Density (kg/m^3)	Hardness
Aluminum 6061-T6	2,700	95 HB
Aluminum 7075	2,810	150 HB
Steel 1018	7,870	126 HB
Steel 4140	7,850	217 HB
Stainless Steel 303	8,030	201 HB
Stainless Steel 316	8,000	217 HB
Titanium 6Al-4V	4,430	334 HB

Table 4.2 12.7 mm endmill description

Tool	Number of teeth	Helix angle	Coating
Accupro 82976663	3	40 deg	Zirconium Nitride
Accupro 07771934	4	40 deg	Titanium Carbonitride

CNC machine setup

Figure 4.3 shows the experimental setup on a CNC milling center. For this testing a Haas VF4-SS vertical 3-axis milling center is used. The milling center operates within defined physical constraints set by the manufacturer, including spindle speed, axis travel, and feed rate ranges. The 20-horsepower spindle can spin up to 12,000 RPM to limit the range of the machine. All testing must consider these limitations when setting up stability map ranges for optimal cutting depths and speed.

The CMD will be oriented in the machine such that both the machine tool and stage x axes are aligned. For this study, an additional 304 stainless steel plate has been designed in order on ensure evenly distributed loads when mounting the CMD with a torque of $35\ Nm$. This is preferred to using toe clamps that can produce uneven forces on the system and potentially cause additional torsional modes to occur within the system. The selected workpiece for each test is fixtured to the CMD moving stage using two M8x1.5 bolts at $35\ Nm$ and aligned using a dial indicator as shown in **Figure 4.4**. Each workpiece will be removed once all five incremental feed rates are completed per tool and replaced with new stock. Displacement will then be recorded with KES at a sampling rate of 25,000 Hz to ensure that all FFT measurements reflect over 10,000 Hz due to the Nyquist criterion. The height compensation algorithm will be implemented for each KES measurement to compensation for the height discrepancy of the cut to the transducer. For all cuts experiments, the five incremental cuts will be done down the width of the block at the same height requiring no change in the α compensation coefficient.

The Kistler 9257B 3-axis dynamometer will be oriented to the machine x direction and clamped onto a stainless-steel plate with 8 M8x1.5 bolts at $35\ Nm$ as shown **in Figure 4.5**. For the commercial grade cuts, the same workpiece will be used for all tool-workpiece combinations. As a result, all cuts will be performed on one workpiece. All bolts are torqued with a calibrated torque wrench. These will be done in groups of five incremental cuts at the same height and then moved down axially for the other tooling.

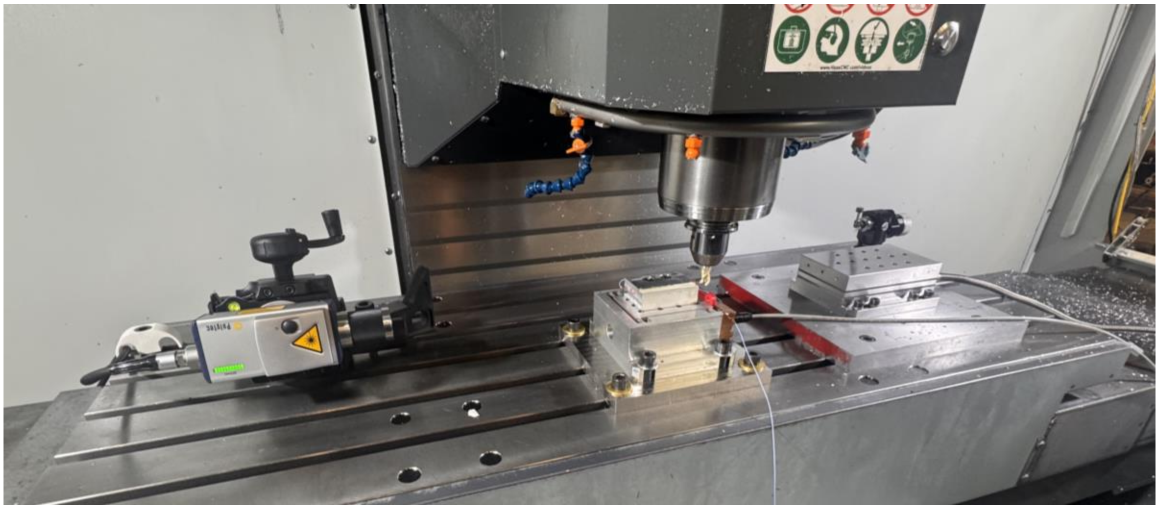

Figure 4.3 Experimental setup.

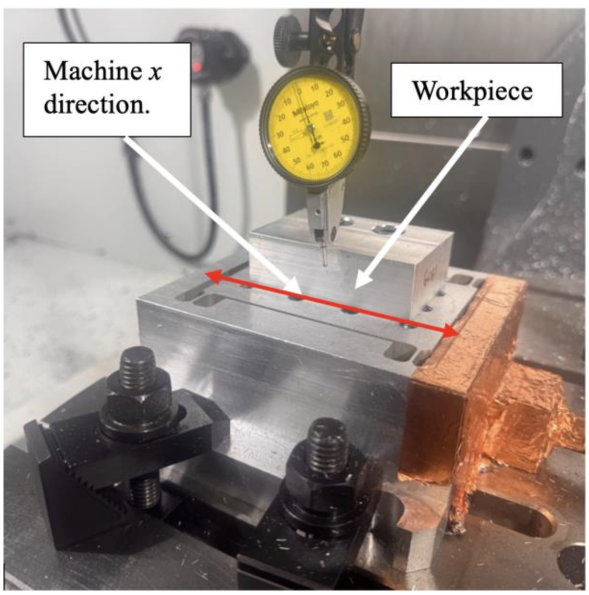

Figure 4.4 CMD workpiece alignment to the machine x axis with stainless steel plate.

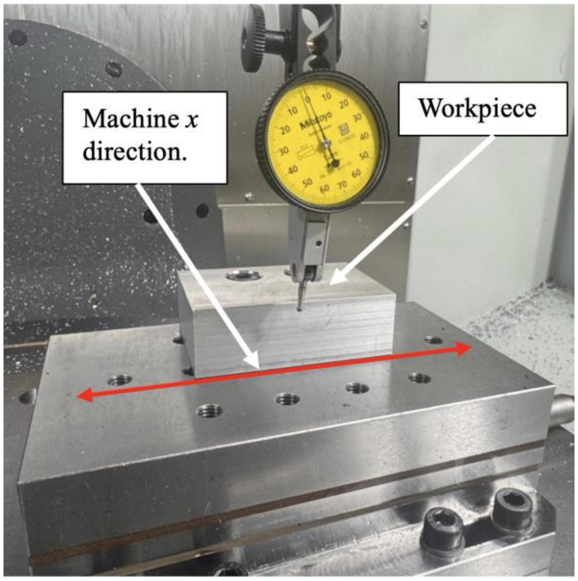

Figure 4.5 CMD workpiece alignment to the machine x axis with stainless steel plate.

The Polytech Vibroflex Compact VFX-I-130 laser Doppler vibrometer will be set up to compare the initial displacement measurements of the system. Additionally, the laser vibrometer is setup to measure the velocity to compare the first derivation of the KES signal to that of a commercial grade system. The laser vibrometer will be set up on a Manfrotto multi-axis rotary stage on the table of the machine and directed at the center of the workpiece. This orientation was selected over placing the laser vibrometer outside of the machine. The reasoning for this is to prevent the laser from moving out of focus as the worktables moves. Prior testing was conducted to ensure the movement of the table does not affect the overall signal of the laser vibrometer. Signal will be collected from the transducer at a sampling rate of 25,000 Hz through the third channel of the DAQ. The side window of the milling center is opened to allow the cable to be able travel as the worktable moves shown in **Figure 4.6**.

A piezoelectric PCB Piezoelectronics 352C23 ICP accelerometer is mounted using modal wax onto the workpiece as shown in **Figure 4.7**. The accelerometer will be used to compare the second order derivative of the KES displacement signal to that of the commercial grade transducer.

For tool fixturing, a CAT 40 Accupro hydraulic 12.7mm holder will be used to mount each tool and is pneumatically mounted into the Haas spindle. Compared to a traditional ER collect holder, the hydraulic holder will improve overall tool concentricity. Additionally, by removing the need additional components, the overall compliance of the tool mounting connection is reduced. For each tool, the gauge length for each tool is preset outside the machine on a tool setting machine. Although all the tools share the same length of cut and diameter, the helix region of the two fluted endmill is slightly longer than that of three and four fluted variants. Due to this all the gauge lengths are set to that of the two fluted endmill for tools shown in **Figure 4.8**. The tooling will be replaced for each tool-workpiece combination.

Figure 4.6 Laser vibrometer orientation mounted onto the worktable.

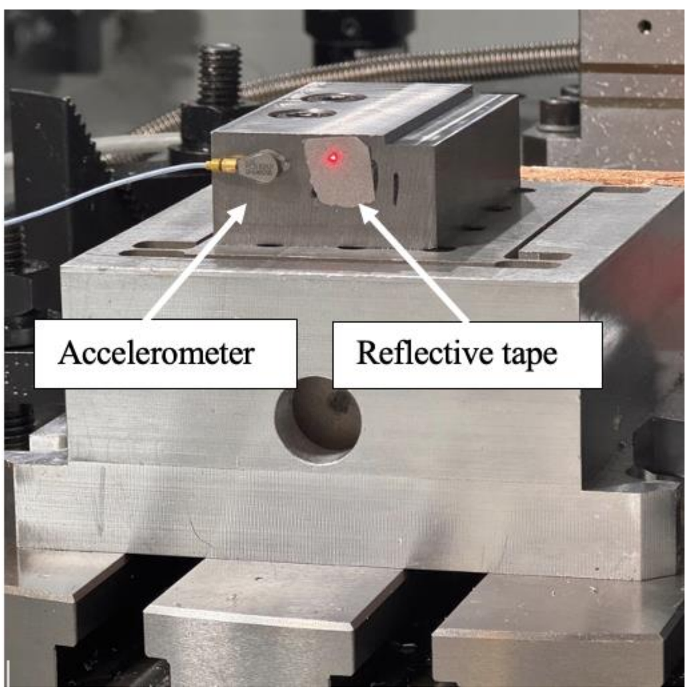

Figure 4.7 Accelerometer and laser vibrometer reflector tape mounted onto workpiece.

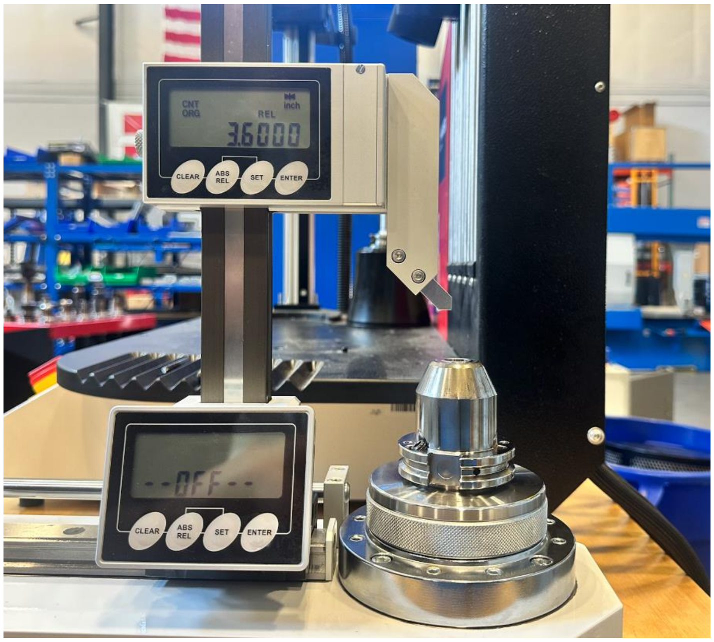

Figure 4.8 Accelerometer and laser vibrometer reflector tape mounted onto workpiece.

Tool-workpiece FRF and modal parameter acquisition for CMD testing

To obtain the true structural dynamics of each tool-workpiece combination, the FRFs of both the tool and workpiece are required. Modal tap testing will be conducted to measure (1) the FRFs of each tool, (2) each individual workpiece mounted on the CMD, and (3) the force-to-force structural dynamics of the Kistler dynamometer for each workpiece material.

For the CMD workpiece combinations, the SDOF FRF receptance measurements will be obtained by the Data Translational ADC DAQ with a truncated frequency bandwidth of 10,000 Hz. This process will be done in both the *x* and *y* machine directions due to asymmetric dynamics of the CMD. As for the tooling, the MDOF FRFs will be captured with the identical bandwidth. The FRFs are then fitted using modal fitting techniques to approximate the stiffness, k, natural frequency, w_n, and damping ratio, ζ, of each mode of interest. Additional calculations will be performed to determine the modal mass and viscous damping coefficient for each mode using Eqs. 42 and 43 in Chapter 2. Once measured both the tool and workpiece in both milling directions, both measurements are superimposed on one another to create a relative FRF for the *x* and *y* directions respectively.

Using the FRFs for the workpiece and tool combinations, general stability mappings are creating using the Tlusty method to determine boundary between stable combinations of axial depth of cut, *b*, and spindle speed and unstable (chatter) combinations [20]. In addition to the FRFs, an estimated specific cutting force coefficient will be used for each material. These estimated values were measured from previous cutting tests and used a baseline for developing the initial stability map. For all cuts, a 2 mm depth cut will be used initially for radial depth of cut, and axial depth cut, and spindle speed will be selected from the map.

For the Kistler, the workpiece dynamics are not necessary due to being a rigid MDOF system paired with a short gauge length tool. Identical cutting parameters will be replicated based on the cutting conditions for the CMD-tool pairings. The force-to-force output of the modal tap testing to the channel output for each direction is necessary to remove the structural dynamics of the dynamometer from the output force measurement to reflect the true cutting force occulting at the tool-workpiece interface. This measurement is also taken with a 10,000 Hz bandwidth for both the *x* and *y* milling directions. The *z* direction response is not necessary for this testing.

For the tooling, initial tap testing was done for a total of nine tools. Three of each two, three, and four flute endmills, were selected to determine the variance between the FRF responses. Although all the tools are the same diameter and gauge length, the amount of material carved out varies depending on the number of teeth on each tool. This will then cause a change the tool bending modes for each tool type. Compliance and damping of each tool will also vary due to the number of teeth based on mass removal from the helical flutes. Each tool FRF will be modally fitted and superimposed on a plot to show variation between each tool. These results are shown in **Figure 4.9**. A mean FRF will also be obtained to compare the system response of the workpiece materials FRF. In **Figure 4.10,** this mean tool FRF is compared to the initial Steel 4140 workpiece FRF utilizing the standard damping pad.

Figure 4.9 Tool setting for two-fluted endmill

Figure 4.10 Tool setting for three-fluted endmill

Initial experimental results for 1018 steel cutting tests.

An initial validation was conducted for one tool-workpiece combination and used as the standard for further cutting tests. 1018 steel was selected as the initial material using a Accupro 07765217 two-fluted endmill. Tap testing was conducted for the standard geometry 1018 steel workpiece material fixtured to the CMD to obtain the single degree of freedom FRF along the *x*-direction of the structure and is shown in **Figure 4.9**. The FRF for the *y*-direction is assumed to be infinitely more rigid than the compliant direction. The modal parameters for each direction are shown in **Table 4.2**. For the *y*-direction it is referenced as a single degree of freedom structure for simplicity. As for the specific cutting force coefficient, K_s, and beta angle, β,an initial estimate is used from prior experimental testing on the Kistler 9257B dynamometer. An initial estimate K_s value of $1{,}850\ N/mm^2$ and β of 70° are used. A stability map is obtained using the Tlusty method for the asymmetric system. A constant radial and axial depth of cut of $2\ mm$ is used for all cuts. A range of incrementing feed per tooth values of $0.150\ mm/tooth$ to $0.250\ mm/tooth$ is used for this testing and do not affect the stability map's results. **Figure 4.11** shows the stability map produced for the system.

Once the stability map is produced, a spindle speed must be selected in the region of stability that is $+/-\ 5\%$ outside of the range the first five tooth passing frequencies as well as the initial runout frequencies of the second tooth. This is an additional precaution to avoid resonance of the stage during cutting operations. For this testing a spindle speed, Ω, of 2,600 RPM is selected. Five incremental down milling cutting test are then taken along the compliant *x*-direction first and followed by incremental down milling cutting tests along the rigid *y*-direction.

For each CMD cutting test, the ADC DAQ is used to collect the data at a sampling rate of 25,000 Hz for a duration of fifteen seconds. Once measured, the data for all five tests are imported into MATLAB for the remaining procedures. To begin, the DC offset is removed from each set of data by taking the mean of the first two hundred data points of non-cutting data. A low-pass filter is then used to remove any data above 2,000 Hz that can be attributed to noise from the CNC milling center. 2,000 Hz is a valid cutoff

Figure 4.11 Tool setting for three-fluted endmill

frequency due to being over twice the natural frequency of the system at 621 Hz and well over the fifth tooth passing frequency of 433.33 Hz; so that no milling frequency content is removed. An example of this is shown for the first cutting test in **Figure 4.12**. These measurements are shown in **Figures 4.13-4.14** as a cluster. As noted, as the incrementing feed per tooth value increases, the amplitude of displacement increases while the overall time for each cut decreases. Additionally, the height compensation coefficient, α, of 0.92 is applied to all CMD measurements in both directions.

Once all cutting tests have been performed on the CMD, five identical cuts will be taken on the Kistler 9257B commercial grade dynamometer along the machine *x*-axis. Each cut will capture both *x* and *y* milling cuts simultaneously. Prior to the cuts, F2F frequency is captured for the workpiece to create the inverse filter for each direction. All cutting tests will be measured for fifteen seconds at a sampling rate of 25,000 Hz. Once performed on all cuts, all data will be exported to MATLAB. The initial recorded measurements for both directions are shown in **Figures 4.15-4.16** as a cluster. F**igure 4.17** shows an example of the structural dynamics being removed from the signal from all the cutting tests.

All CMD displacement data is used to construct for using both the structural deconvolution and time summation approach. For the time summation approach, each set of data will be run through the 150th-order FIR differentiation filter twice to produce derived velocity and acceleration measurements. For this FIR filter, the bandpass frequency is set to 130% of the value of the natural frequency of the CMD. The band stop frequency set to properly attenuate the noise caused by differentiation is set to 200% of the CMD natural frequency. Once all three motion parameters are acquired, they are scaled by their respective modal parameters to produce spring, damping, and inertial forces for the system. These forces are then summed to produce the overall cutting force for each direction. **Figures 4.18-4.22** show the derived velocity measurements for each cut in the x-direction. **Figures 4.23-4.27** show the derived acceleration measurements for each cut in the x-direction. **Figures 4.28-4.33** show the derived acceleration measurements for each cut in the x-direction. **Figures 4.34-4.38** show the derived

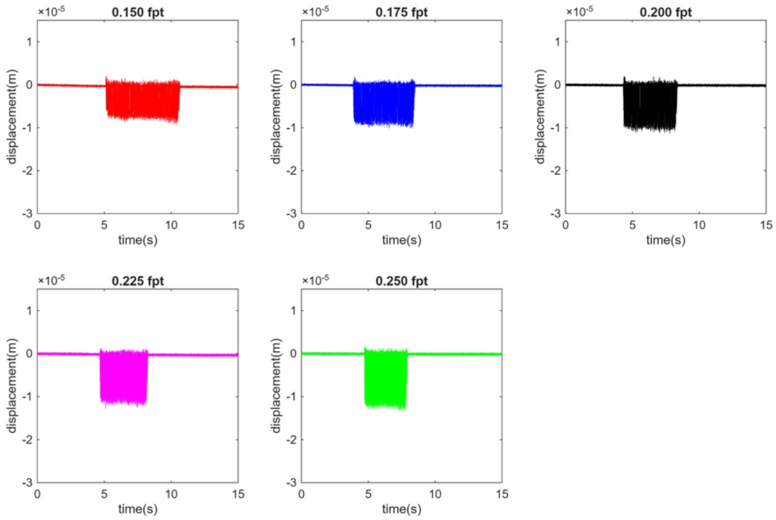

Figure 4.12 Ti 6Al-4V x-direction displacement measurements.

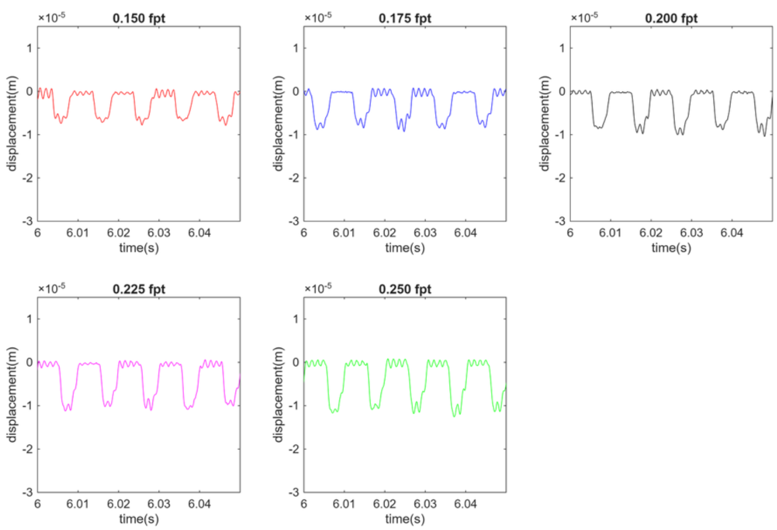

Figure 4.13 Zoomed Ti 6Al-4V x-direction displacement measurements.

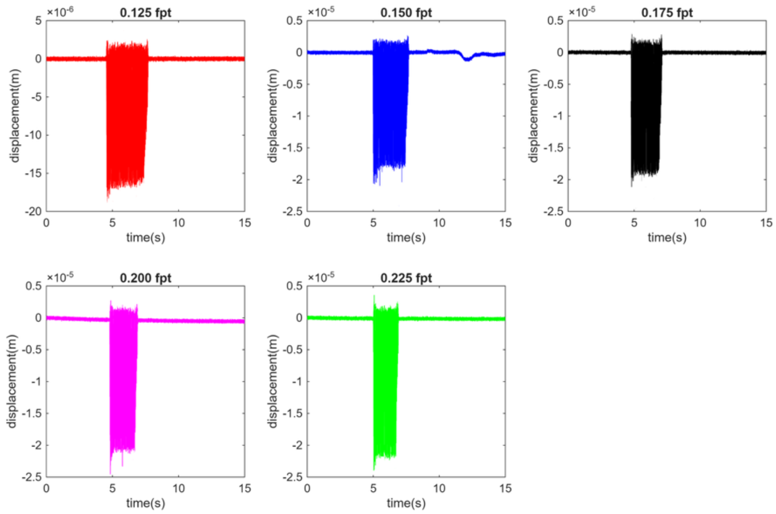

Figure 4.14 Ti 6Al-4V y-direction displacement measurements.

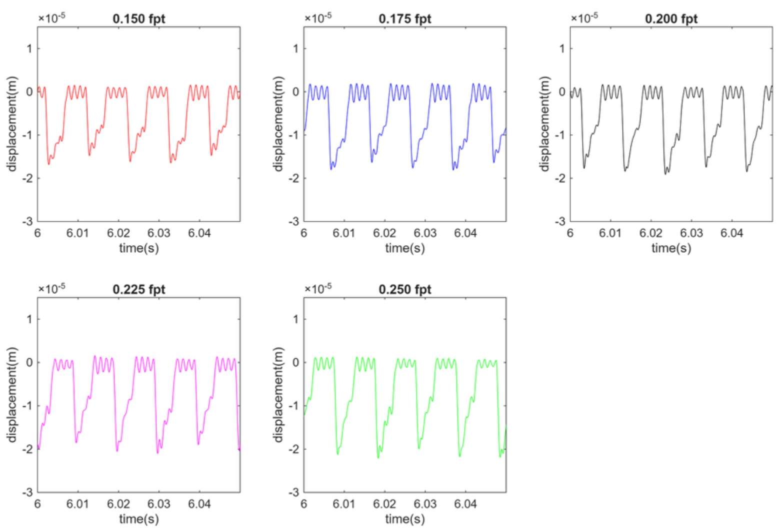

Figure 4.15 Zoomed Ti 6Al-4V y-direction displacement measurements.

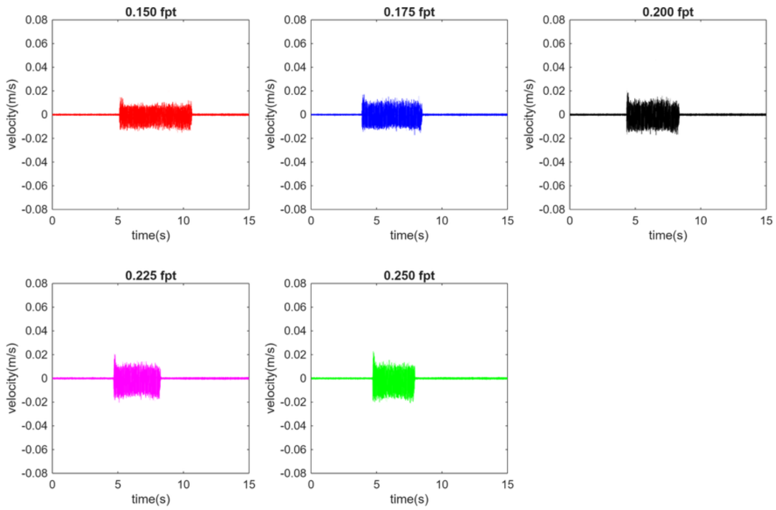

Figure 4.16 Ti 6Al-4V x-direction velocity measurements.

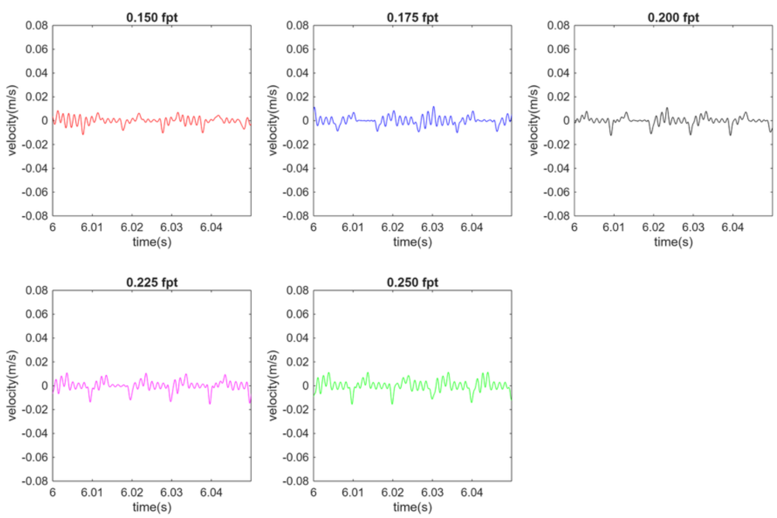

Figure 4.17 Zoomed Ti 6Al-4V x-direction velocity measurements.

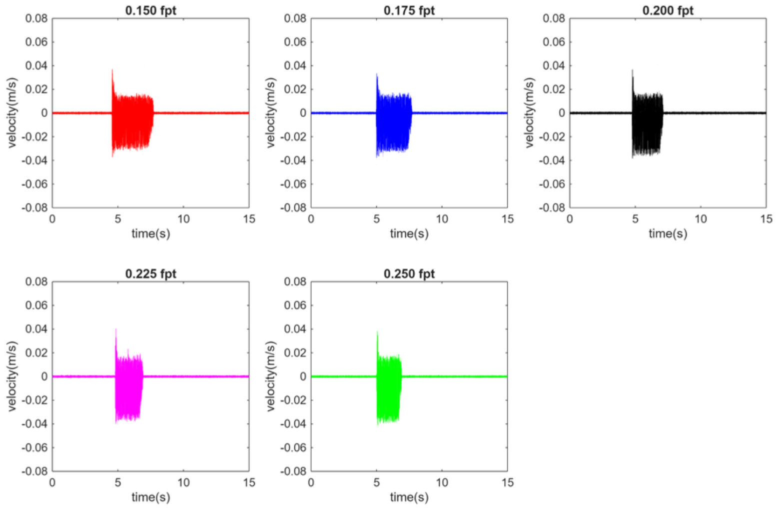

Figure 4.18 Ti 6Al-4V y-direction velocity measurements.

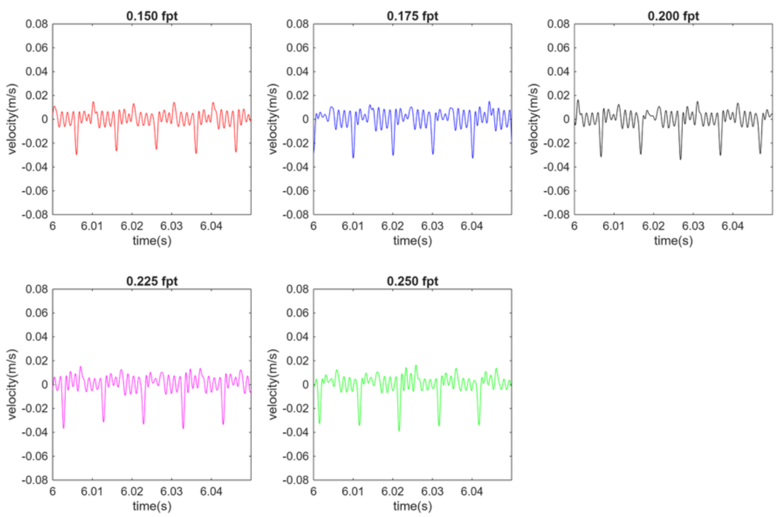

Figure 4.19 Zoomed Ti 6Al-4V y-direction velocity measurements.

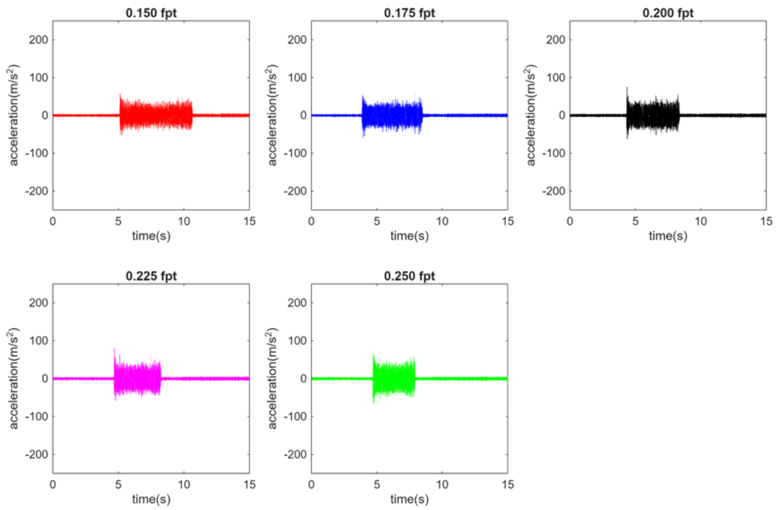

Figure 4.20 Ti 6Al-4V x-direction acceleration measurements.

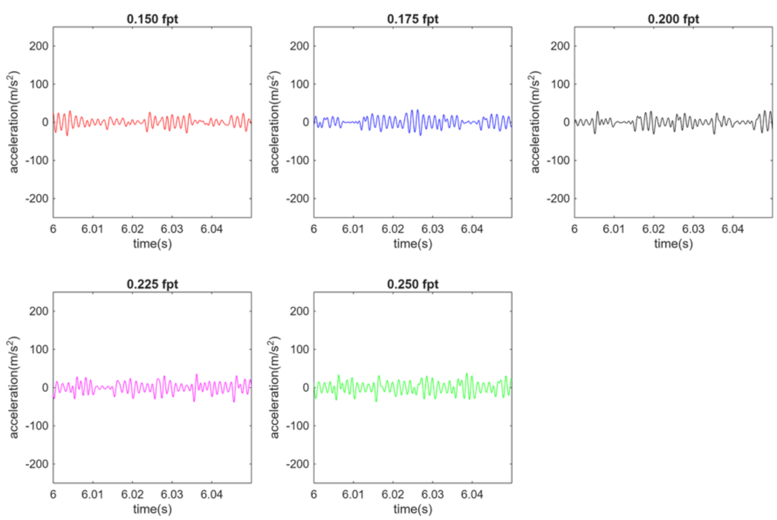

Figure 4.21 Zoomed Ti 6Al-4V x-direction acceleration measurements.

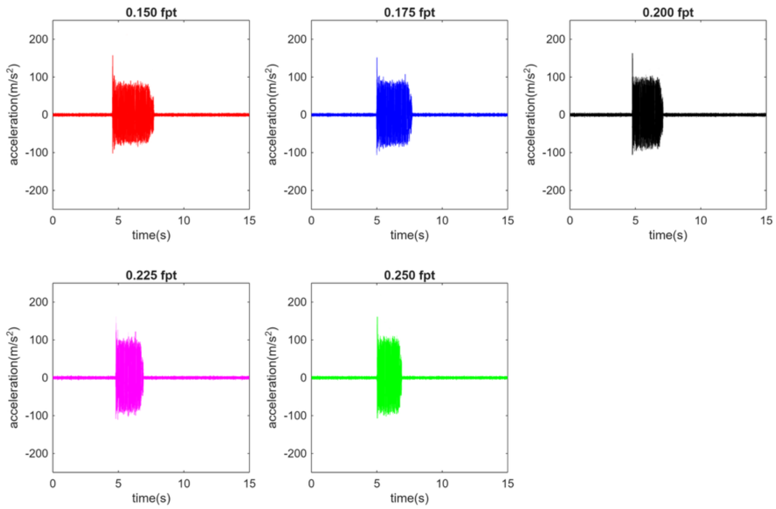

Figure 4.22 Ti 6Al-4V y-direction acceleration measurements.

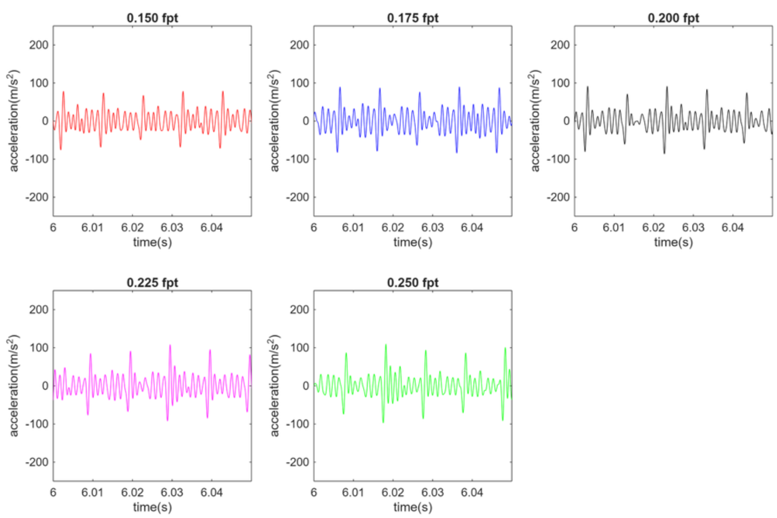

Figure 4.23 Zoomed Ti 6Al-4V y-direction acceleration measurements.

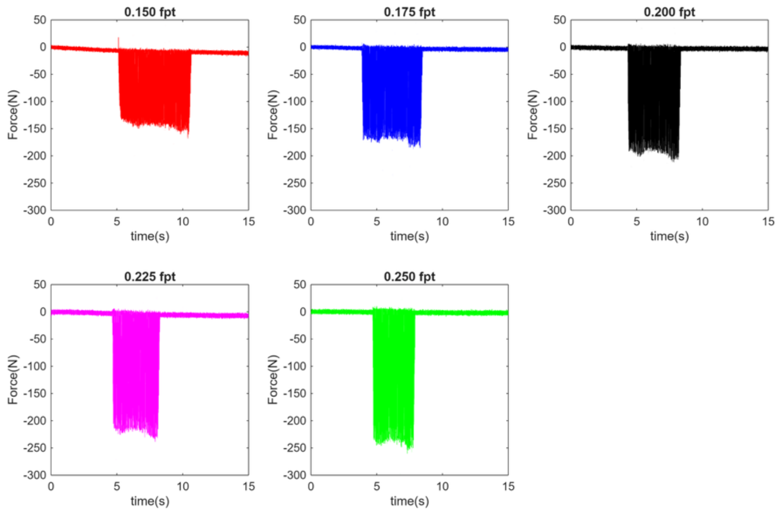

Figure 4.24 Ti 6Al-4V x-direction force measurements - time summed approach.

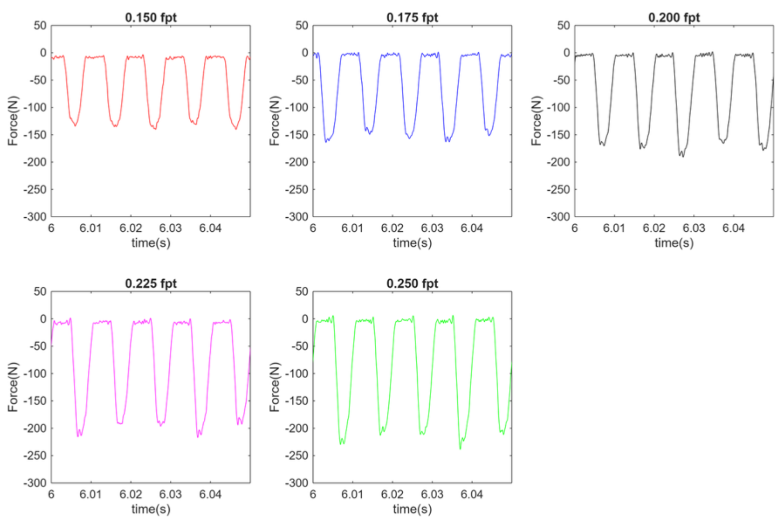

Figure 4.25 Zoomed Ti 6Al-4V x-direction force measurements - time summed approach.

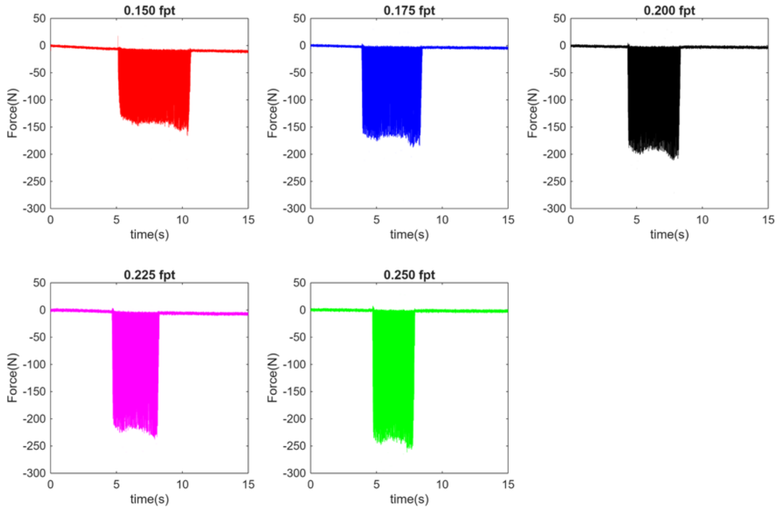

Figure 4.26 Ti 6Al-4V x-direction force measurements - structural deconvolution.

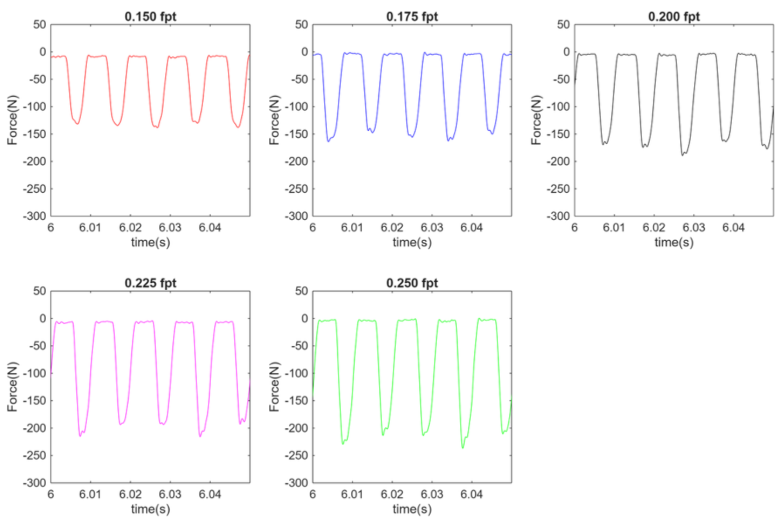

Figure 4.27 Zoomed Ti 6Al-4V x-direction force measurements - structural deconvolution.

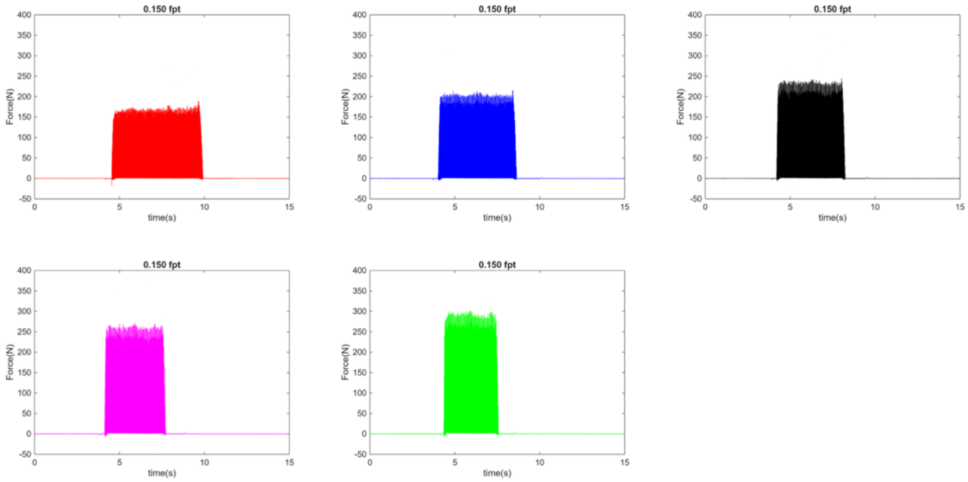

Figure 4.28 Ti 6Al-4V x-direction force measurements - Kistler 9257B.

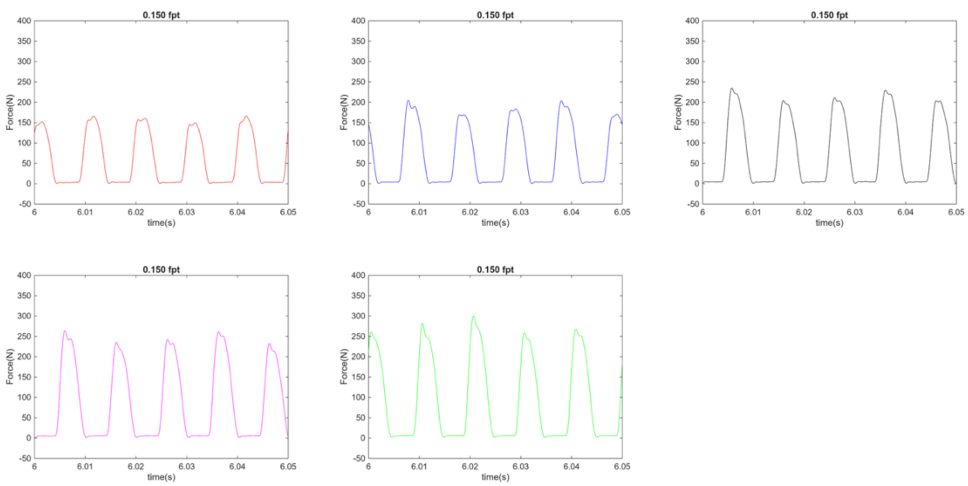

Figure 4.29 Zoomed Ti 6Al-4V x-direction force measurements – Kistler 9257B.

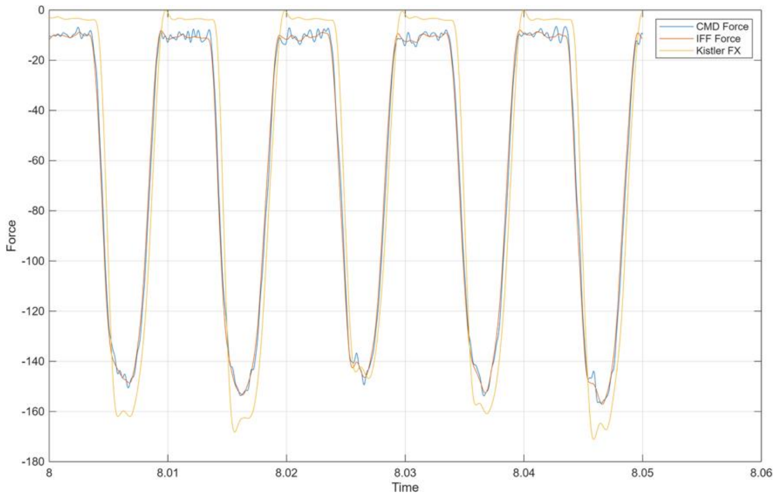

Figure 4.30 Ti 6Al-4V x-direction force measurements comparison 0.150 mm/tooth.

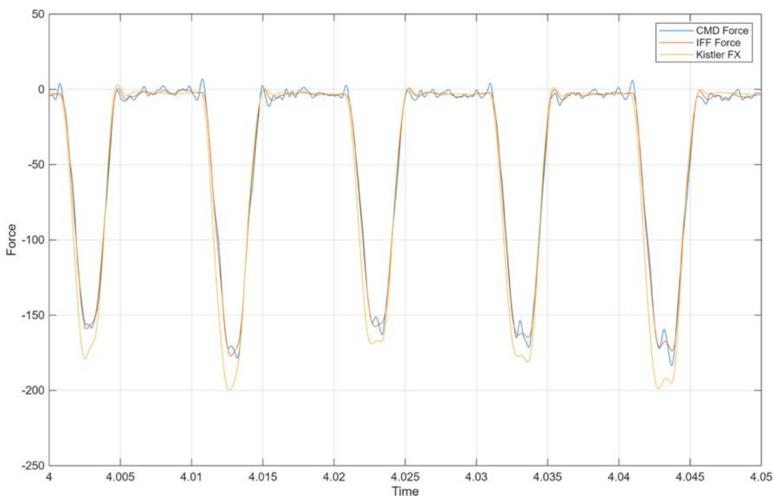

Figure 4.31 Ti 6Al-4V x-direction force measurements comparison 0.175 mm/tooth.

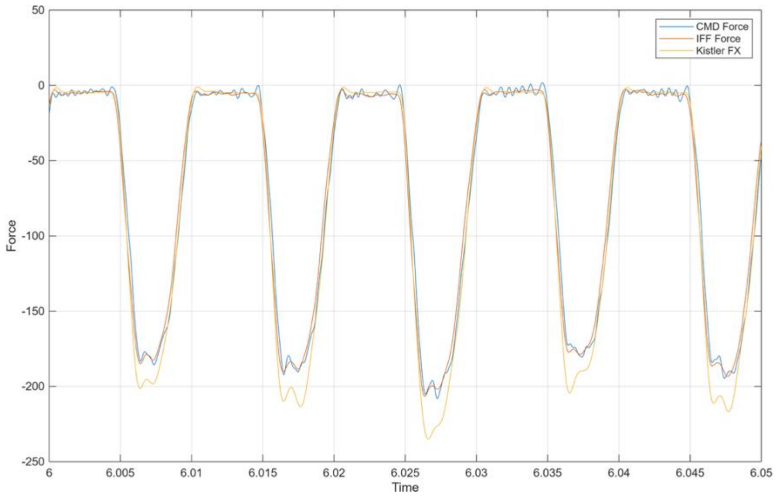

Figure 4.32 Ti 6Al-4V x-direction force measurements comparison 0.200 mm/tooth.

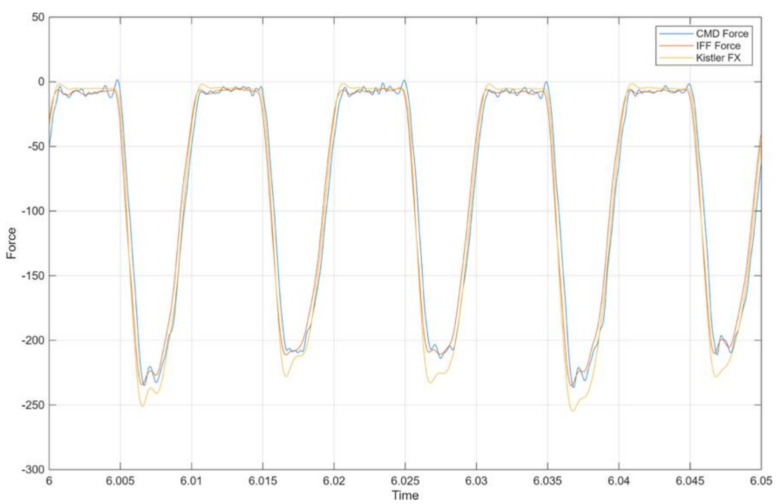

Figure 4.33 Ti 6Al-4V x-direction force measurements comparison 0.225 mm/tooth.

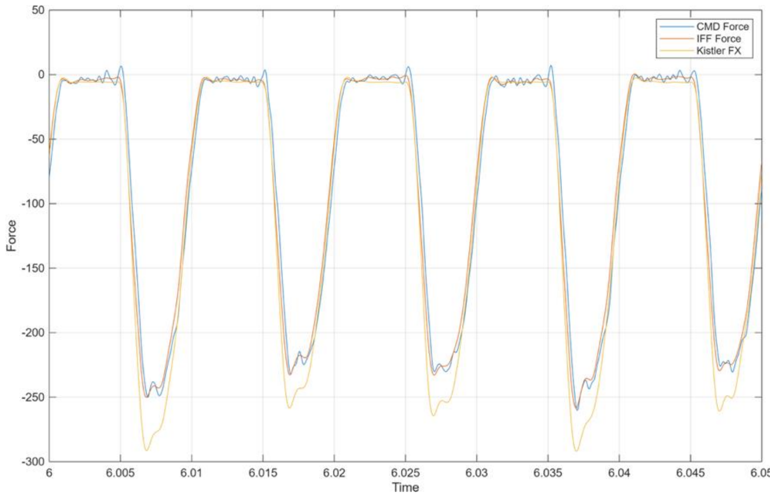

Figure 4.34 Ti 6Al-4V x-direction force measurements comparison 0.250 mm/tooth.

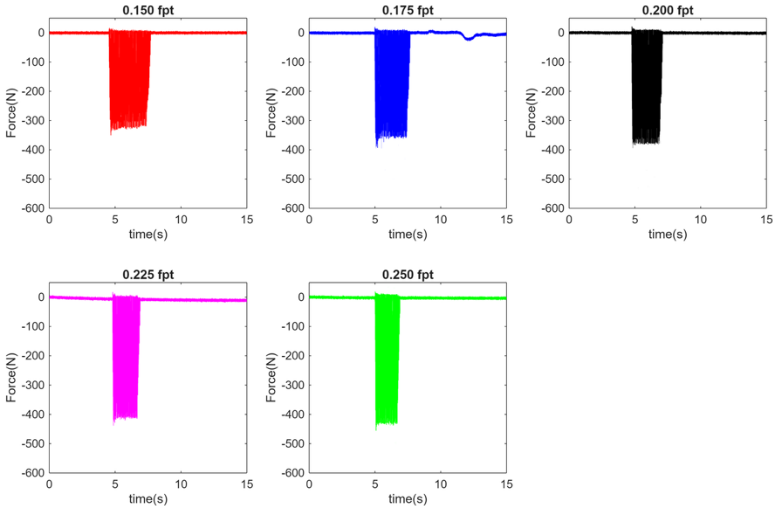

Figure 4.35 Ti 6Al-4V y-direction force measurements - time summed approach.

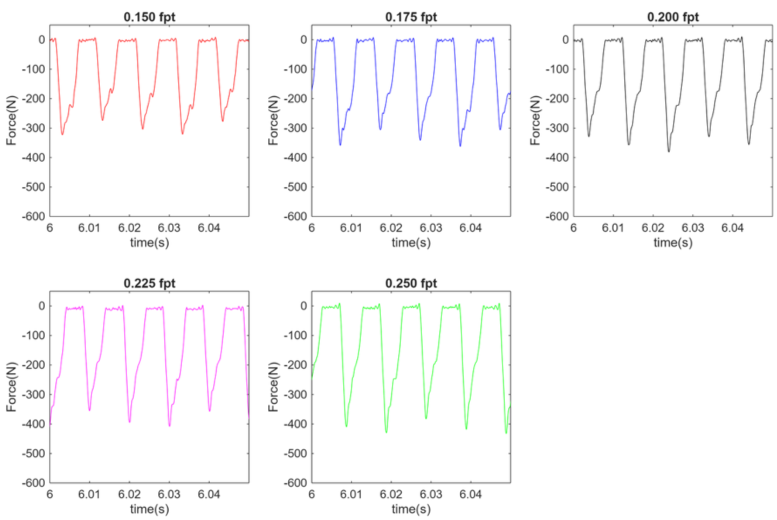

Figure 4.36 Zoomed Ti 6Al-4V y-direction force measurements - time summed approach.

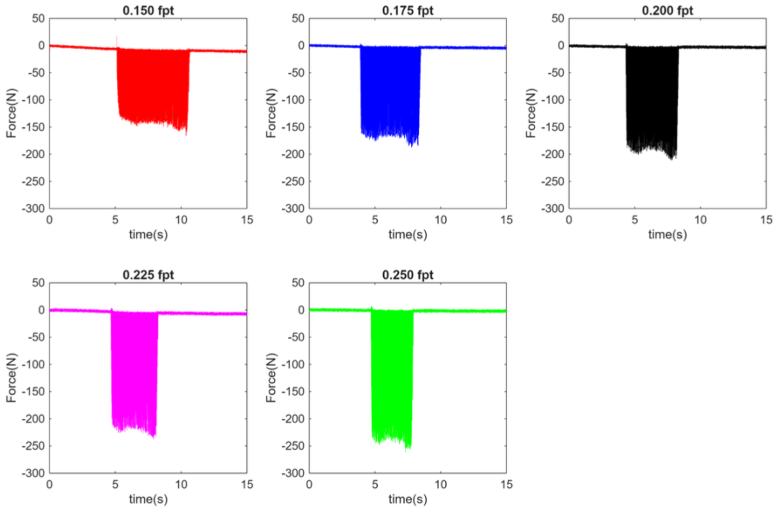

Figure 4.37 Ti 6Al-4V y-direction force measurements - structural deconvolution.

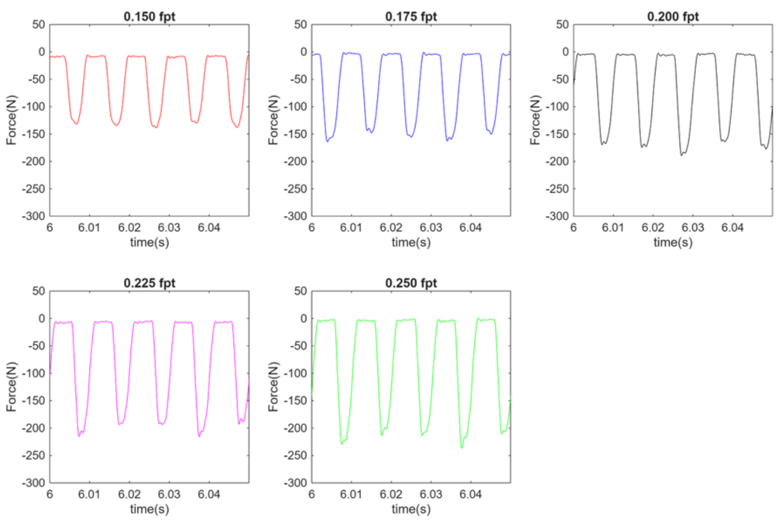

Figure 4.38 Zoomed Ti 6Al-4V y-direction force measurements - structural deconvolution.

velocity measurements for each cut in the x-direction. **Figures 4.39-4.44** show the derived acceleration measurements for each cut in the x-direction. **Figures 4.45-4.49** show the derived acceleration measurements for each cut in the x-direction.

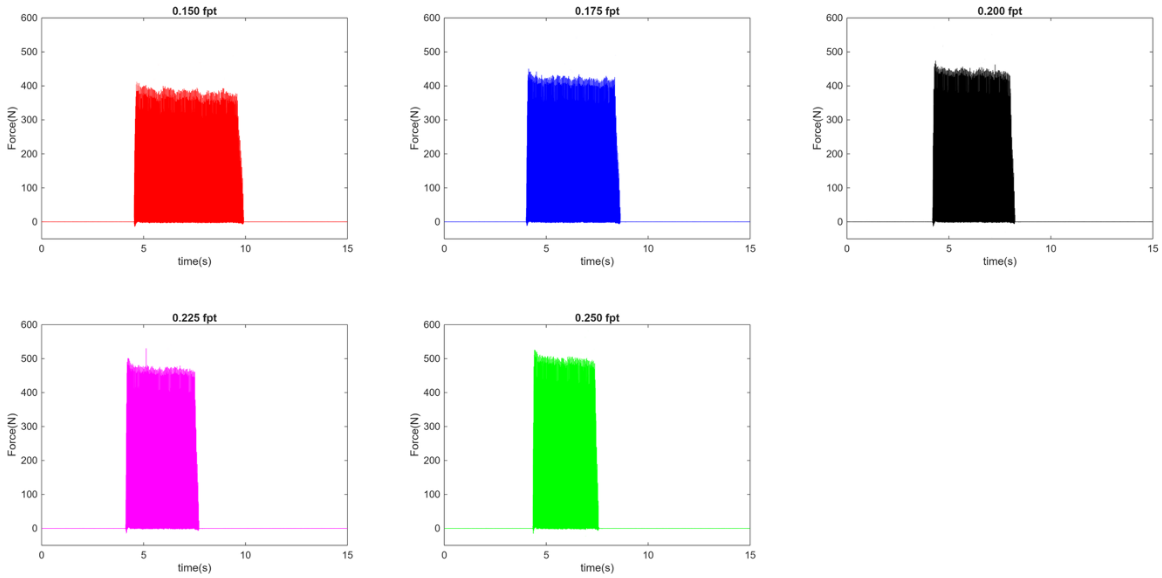

Figure 4.39 Ti 6Al-4V y-direction force measurements – Kistler 9257B.

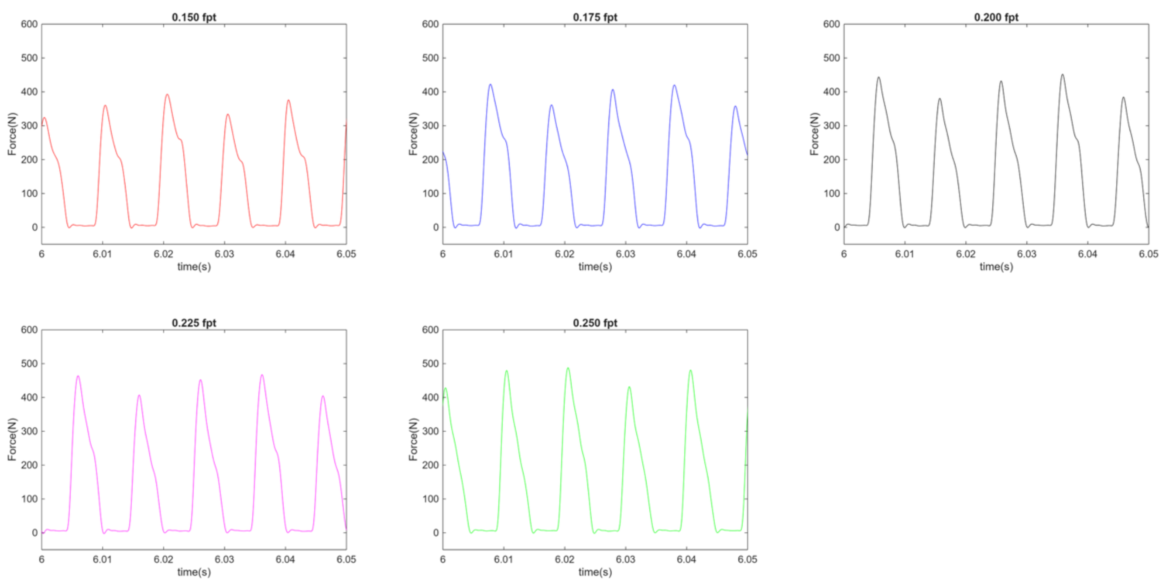

Figure 4.40 Zoomed Ti 6Al-4V y-direction force measurements – Kistler 9257B.

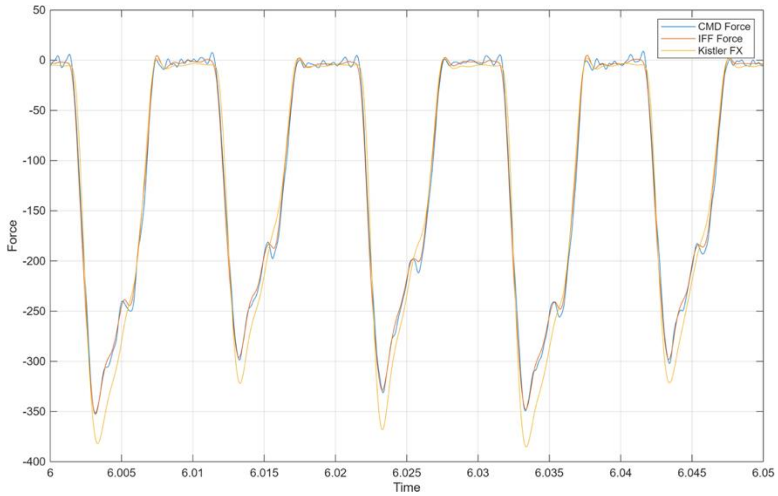

Figure 4.41 Ti 6Al-4V y-direction force measurements comparison 0.150 mm/tooth.

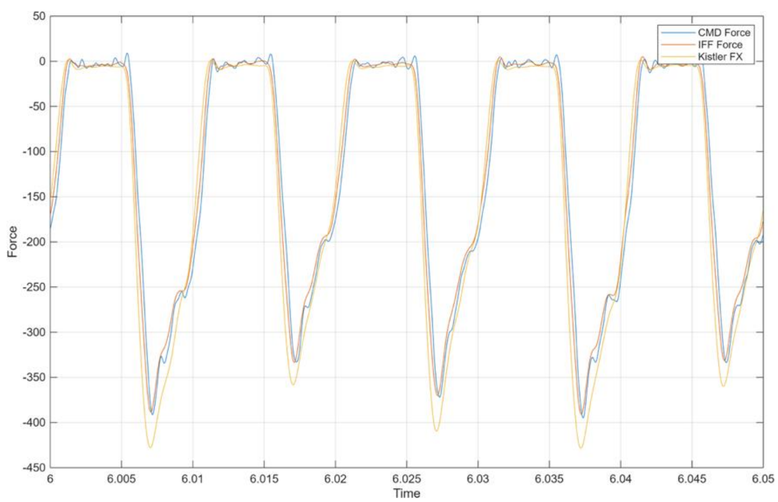

Figure 4.42 Ti 6Al-4V y-direction force measurements comparison 0.175 mm/tooth.

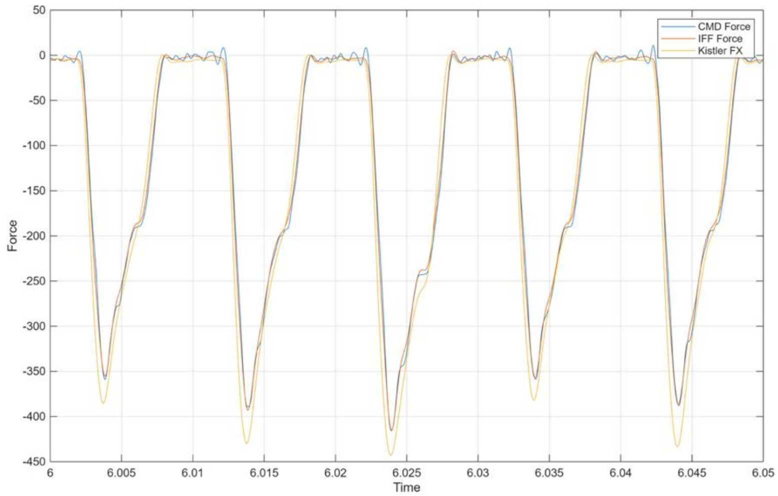

Figure 4.43 Ti 6Al-4V y-direction force measurements comparison 0.200 mm/tooth.

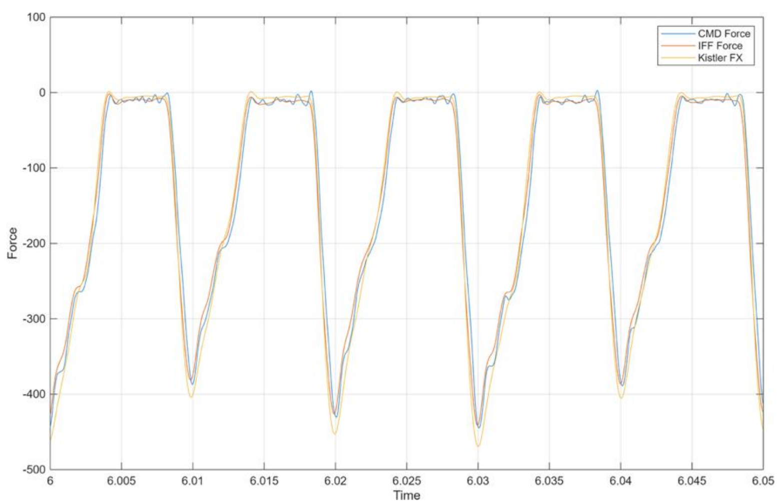

Figure 4.44 Ti 6Al-4V y-direction force measurements comparison 0.225 mm/tooth.

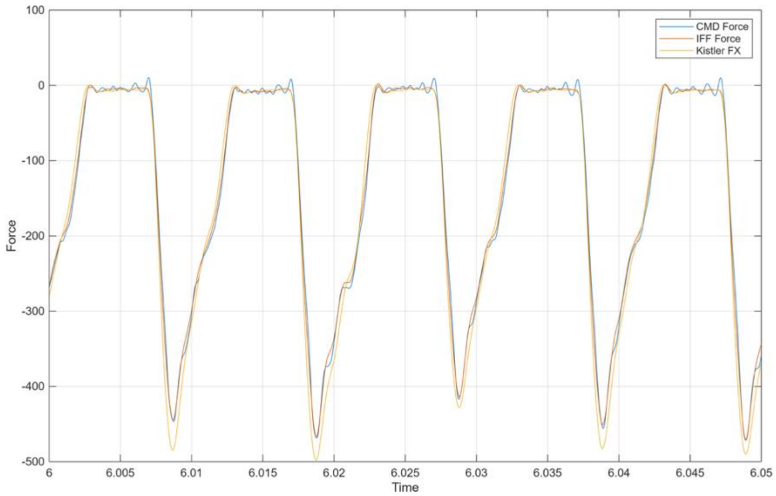

Figure 4.45 Ti 6Al-4V y-direction force measurements comparison 0.250 mm/tooth.

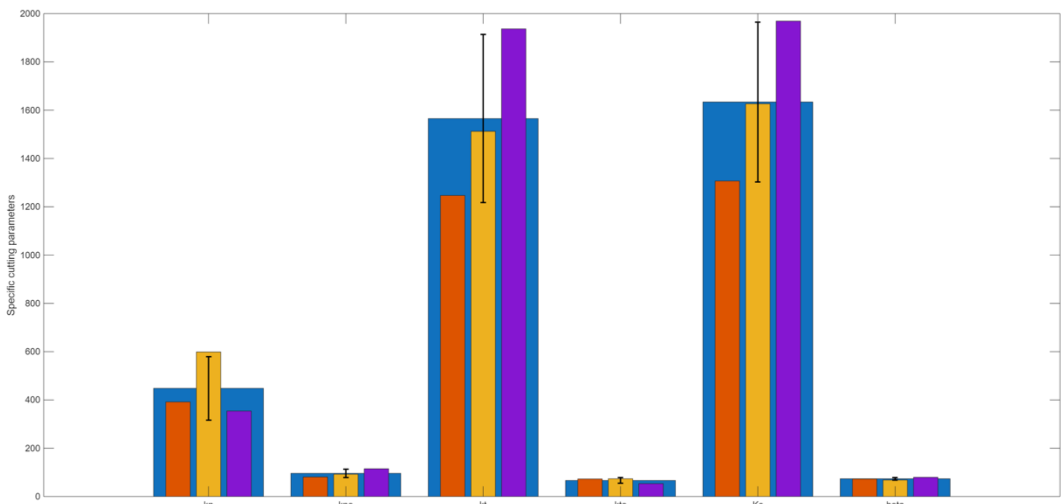

Figure 4.46 Ti 6Al-4V cutting force coefficient measurements

Table 4.3 Ti 6Al-4V cutting parameters

RPM	2600	Tooth passing frequency (Hz)	Runout frequency (Hz)
		86.67	43.33
+5% region (Hz)	589.95	173.33	130.00
Natural frequency (Hz)	621	260.00	216.67
-5% region (Hz)	652.05	346.67	303.33
		433.33	390.00

CHAPTER FIVE

RESULTS AND CONCLUSIONS

This section will review the force measurements collected from all Twelve tool workpiece cutting tests recorded using the CMD-KES system and Kistler 9257B dynamometer systems. For all tests, the *x*-direction forces are recorded for each process. The time summation approach is then compared to the structural deconvolution method based on minimum force peak measurements. Both methods are compared to determine the viability of the novel approach compared to the work done by Gomez. Both methods are then benchmarked to the Kistler 9257B results using a standard 0.92 α height compensation coefficient. Each test will be parsed to a 0.05 second sample to view the entry and exit of every tooth for each tool. **Table 5.1** and **Table 5.2** are the minimum peak values for each parsed data set and compared against the commercial grade system.

Additionally, two materials were selected to complete a complete analysis of the cutting force coefficients for the tool-workpiece combination. For these tests aluminum 6061-T6 and 303 stainless steels are selected and combined with a three-fluted zirconium nitride tool. The results from the time summation approach will be compared to the commercial dynamometer system.

The recorded cutting force coefficients will be shown in Table 5.3. For each system, all collected measurements will be shown for displacement, velocity, acceleration, spring force, damping force, inertial force, and cutting force will be depicted for all five incremental feed rate cuts. **Figures 5.1-5.23** show the results for the aluminum 6061-T6 cutting tests. **Figures 5.24-5.46** show the results for the stainless steel 303 cutting tests.

For validation of the overall approach, measurements for the *x*-direction forces for all three approaches are shown within the appendix using **Figures A.1 to A.49** for all six materials machined with both the three fluted and four fluted Accupro endmills. **Tables A.3 to A.14** show the maximum peak of each measurement for all tests and compared to the values measured by the filtered Kistler 9257B measurements.

CFC validation for aluminum 6061-T6

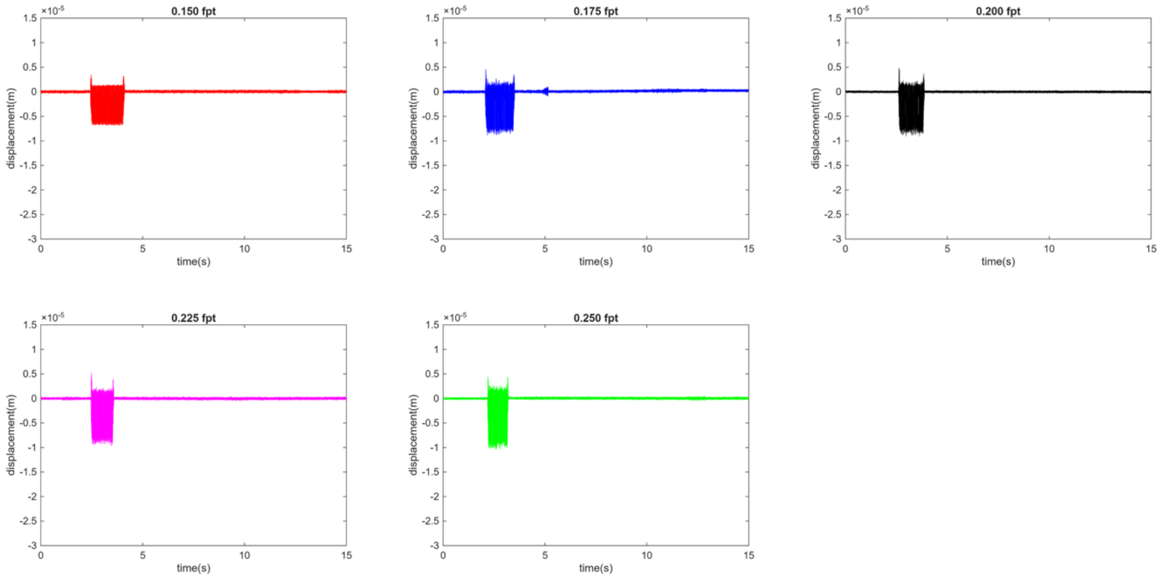

Figure 5.1 6061 *x*-direction displacement measurements.

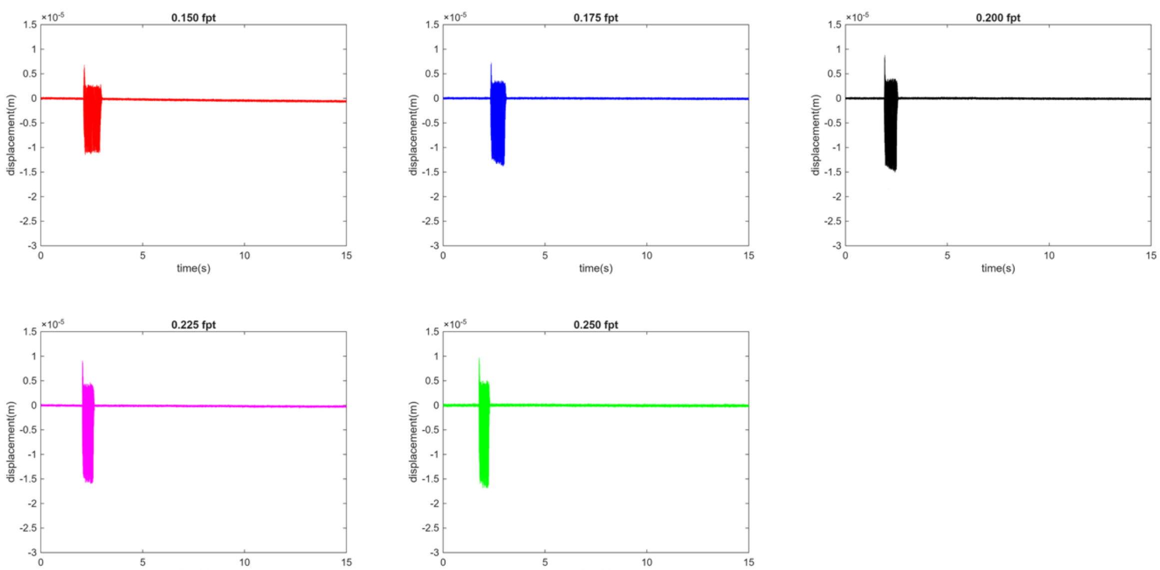

Figure 5.2 6061 *y*-direction displacement measurements.

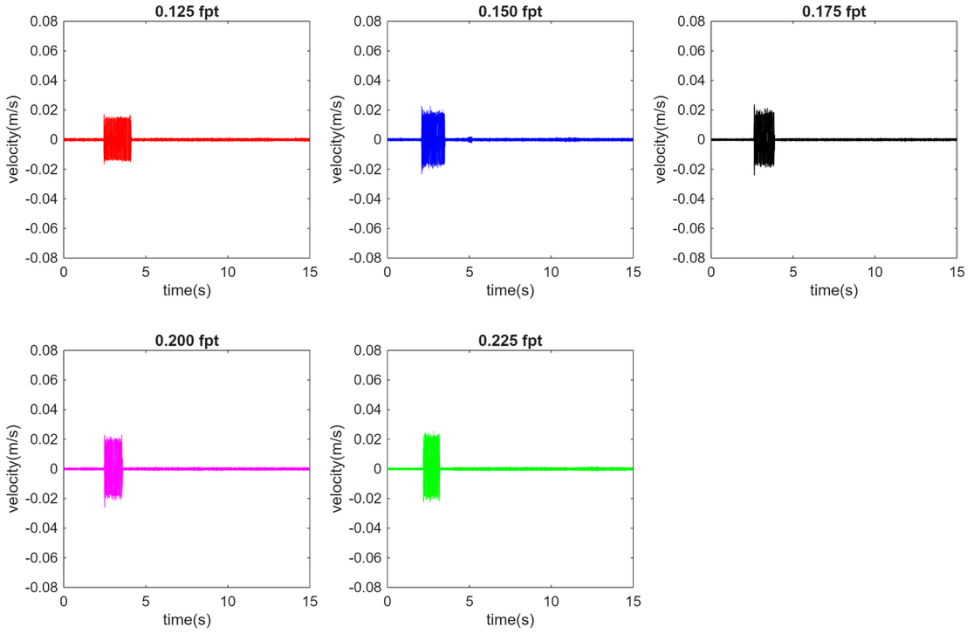

Figure 5.3 6061 x-direction velocity measurements.

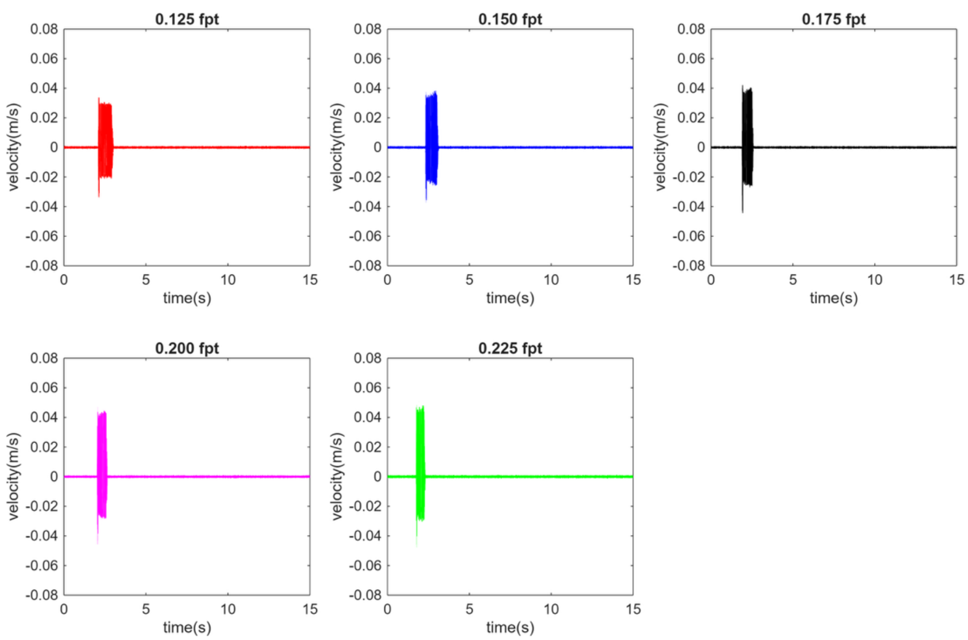

Figure 5.4 6061 y-direction velocity measurements.

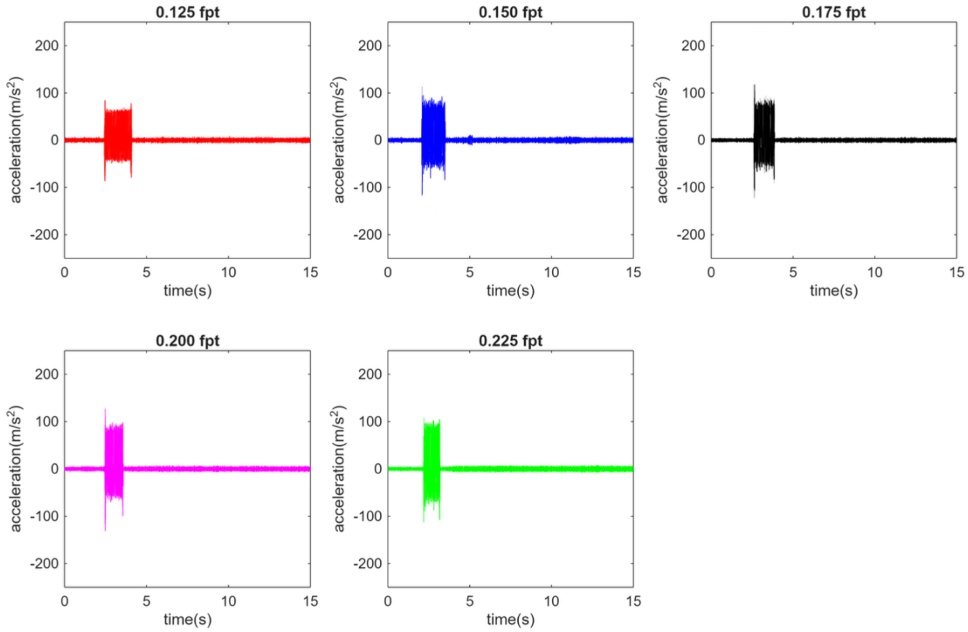

Figure 5.5 x-direction acceleration measurements.

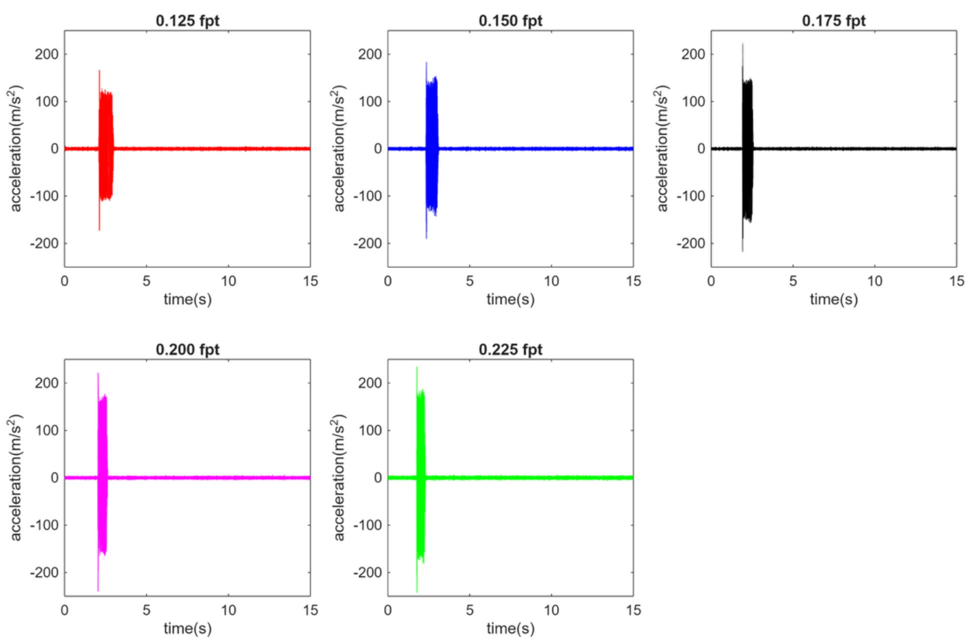

Figure 5.6 6061 y-direction acceleration measurements.

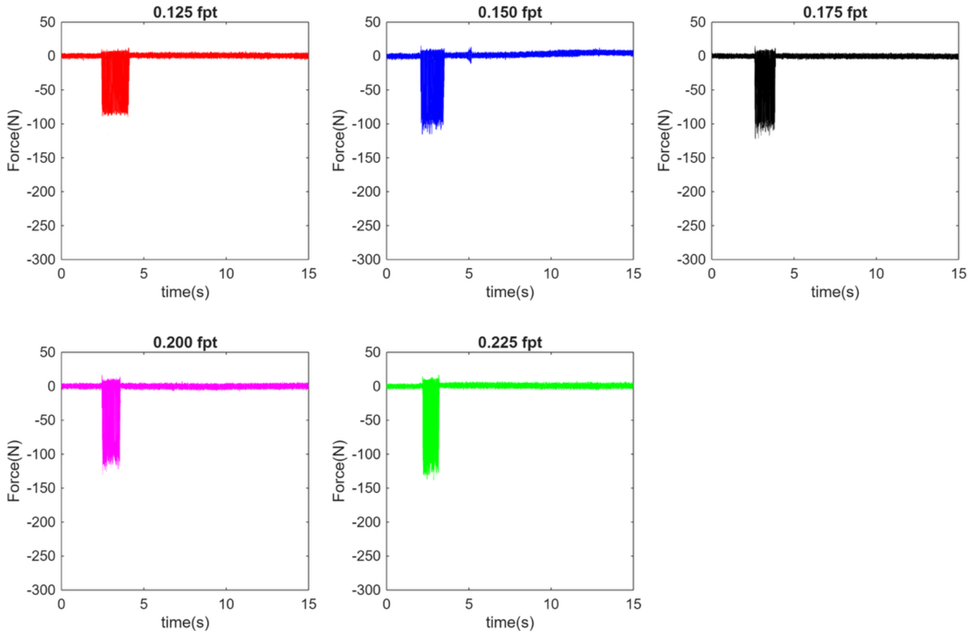

Figure 5.7 6061 x-direction milling force measurements using time summation approach.

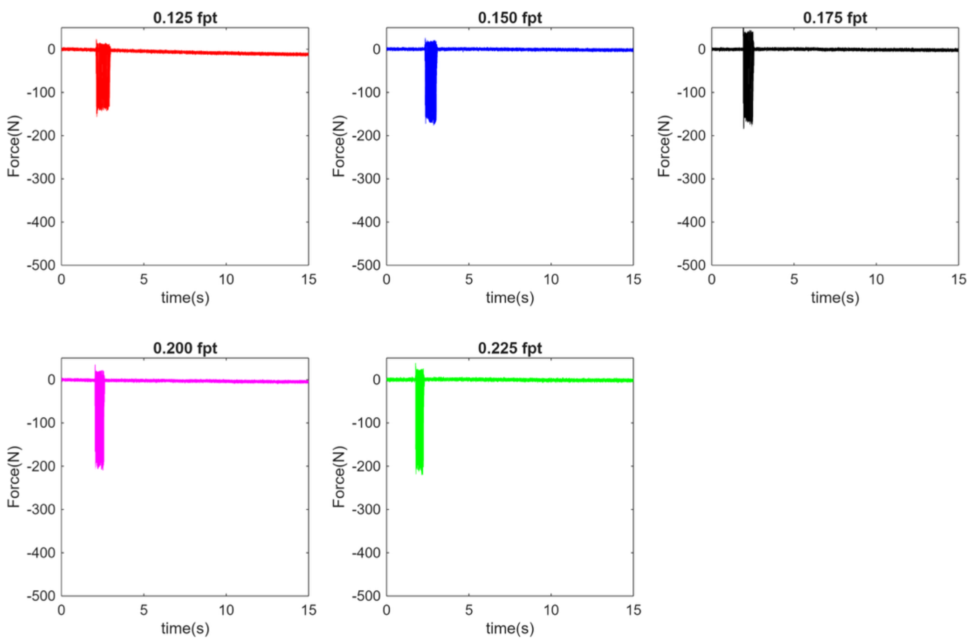

Figure 5.8 6061 y-direction milling force measurements using time summation approach.

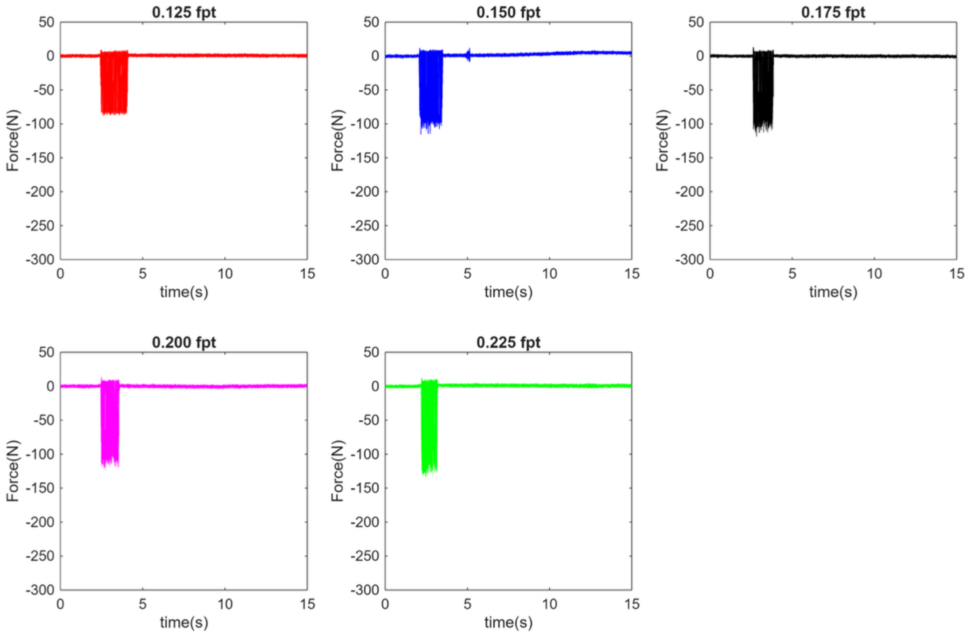

Figure 5.9 6061 x-direction milling force measurements using structural deconvolution.

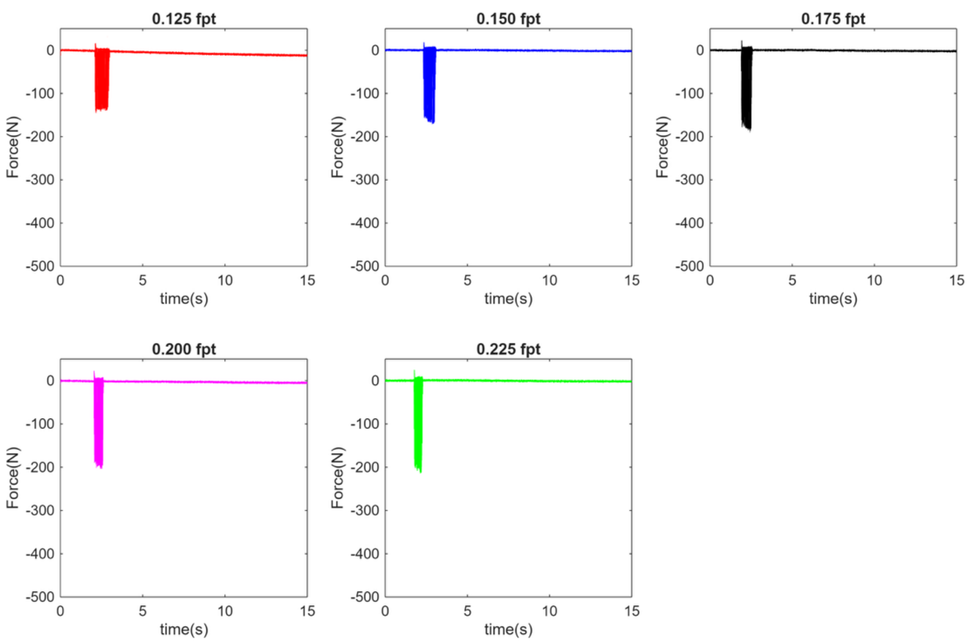

Figure 5.10 6061 y-direction milling force measurements using structural deconvolution.

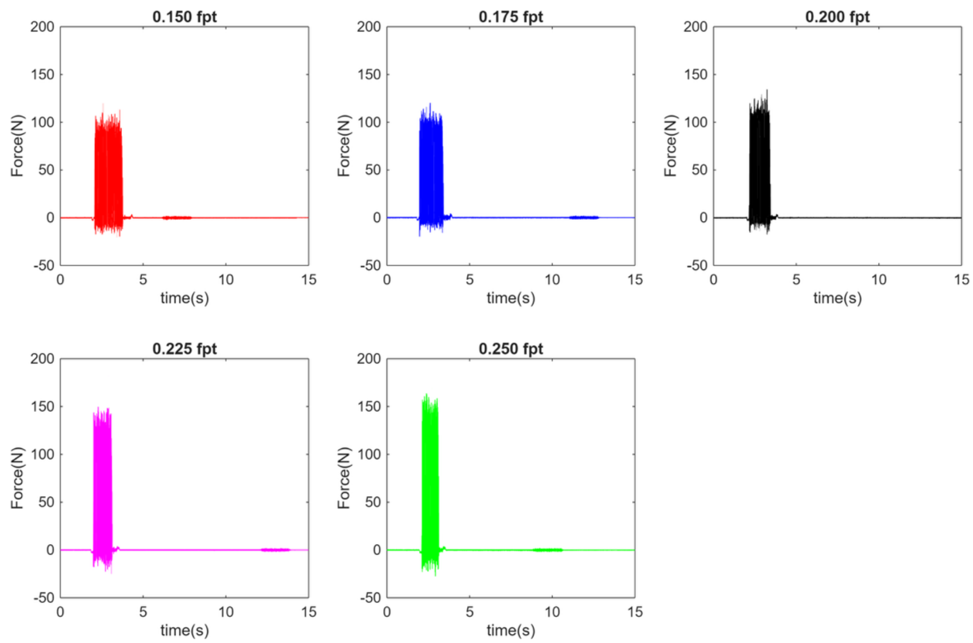

Figure 5.11 6061 x-direction filtered milling force measurements using Kistler 9257B.

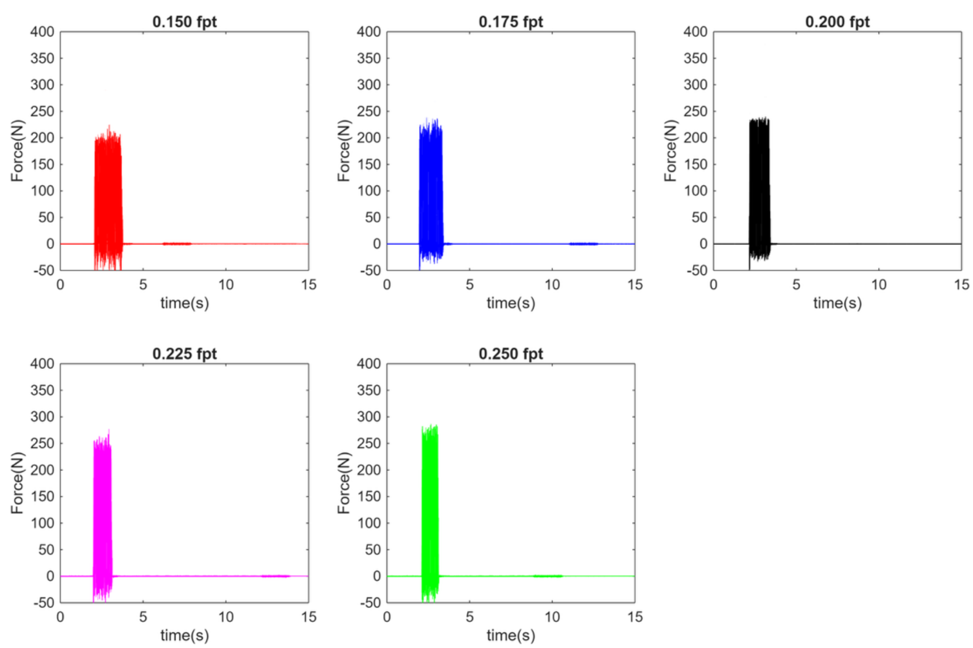

Figure 5.12 6061 y-direction filtered milling force measurements using Kistler 9257B.

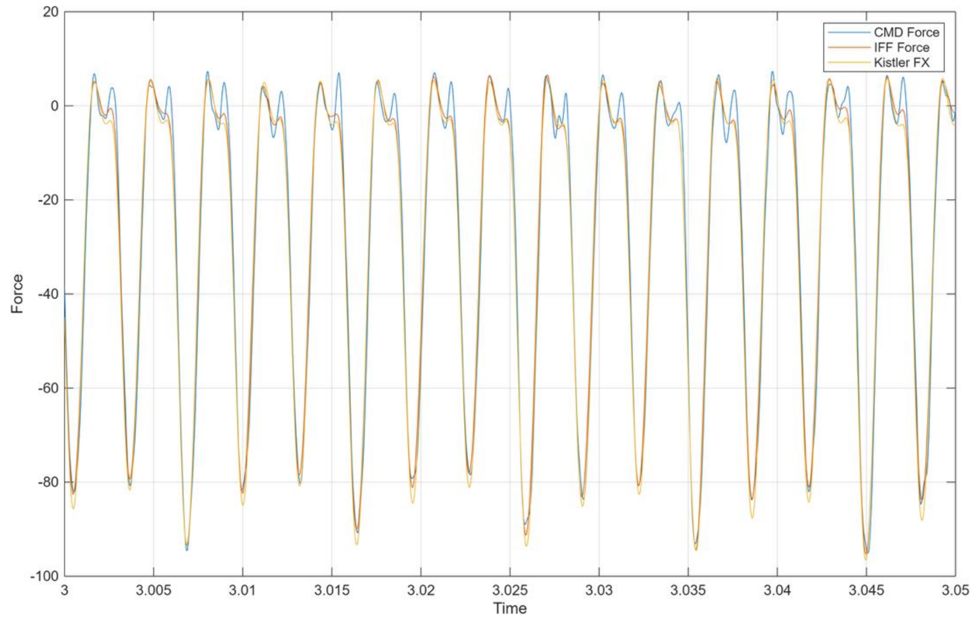

Figure 5.13 6061 x-direction milling force comparison 0.150 mm/tooth

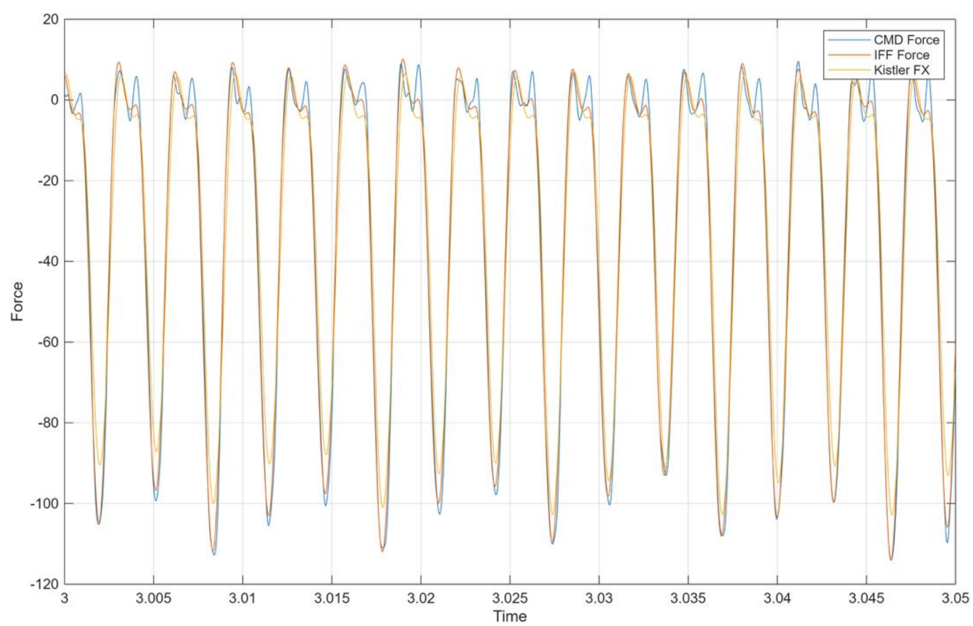

Figure 5.14 6061 x-direction milling force comparison 0.175 mm/tooth

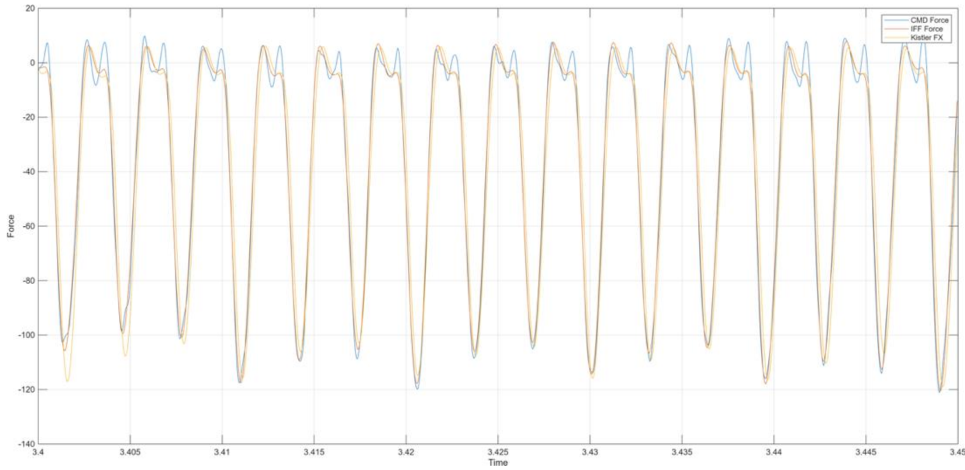

Figure 5.15 6061 x-direction milling force comparison 0.200 mm/tooth

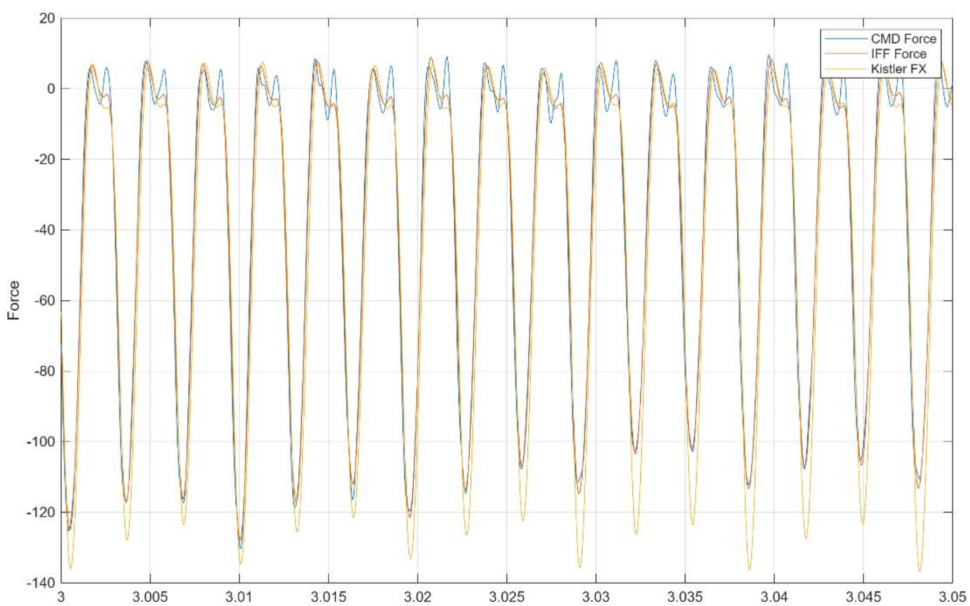

Figure 5.16 6061 x-direction milling force comparison 0.225 mm/tooth

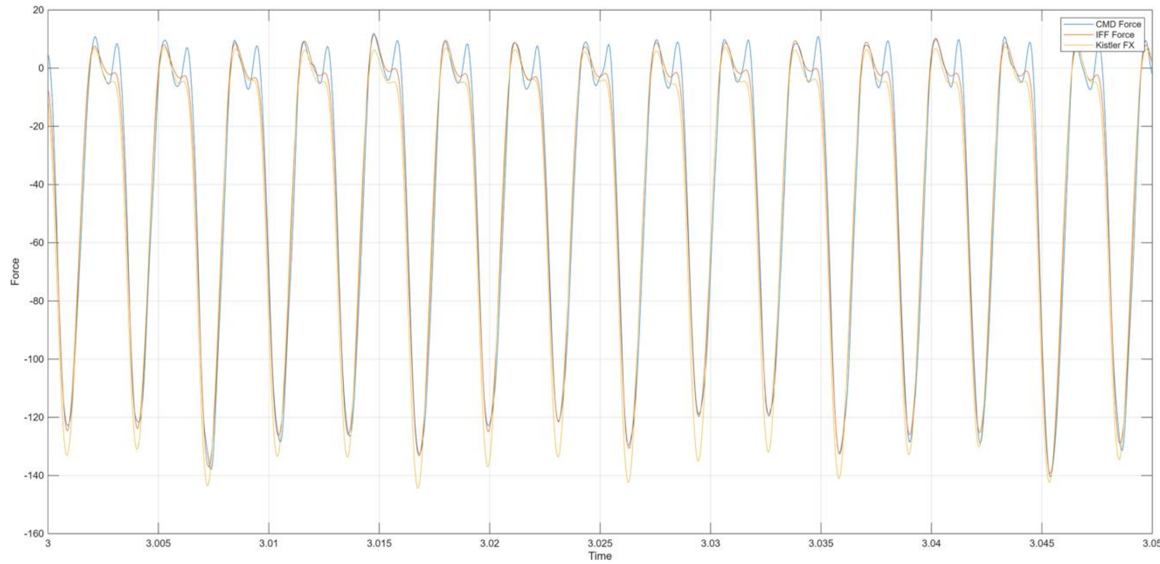

Figure 5.17 6061 x-direction milling force comparison 0.250 mm/tooth

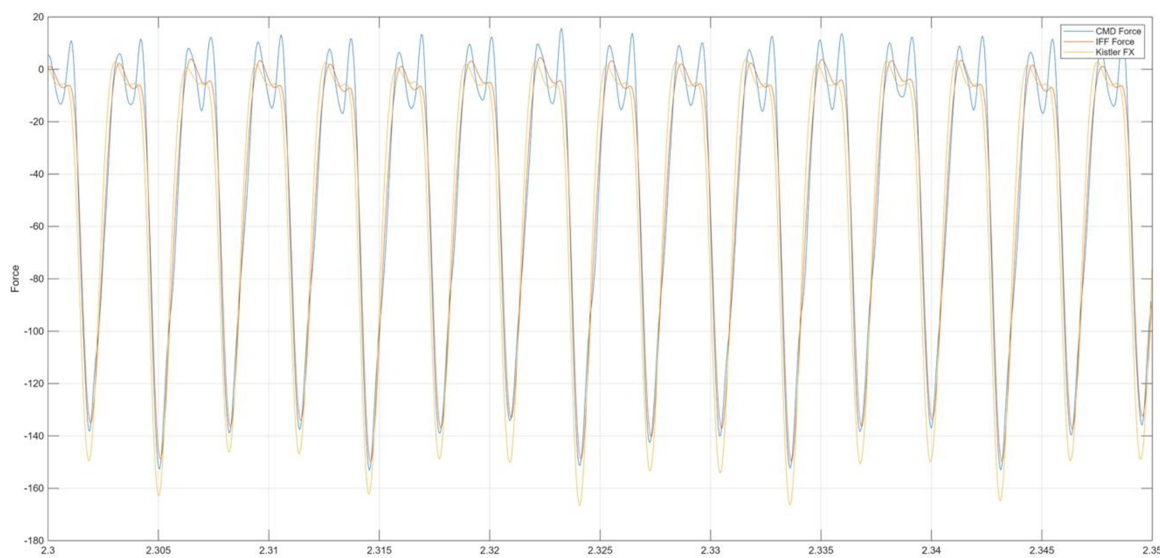

Figure 5.18 6061 y-direction milling force comparison 0.150 mm/tooth

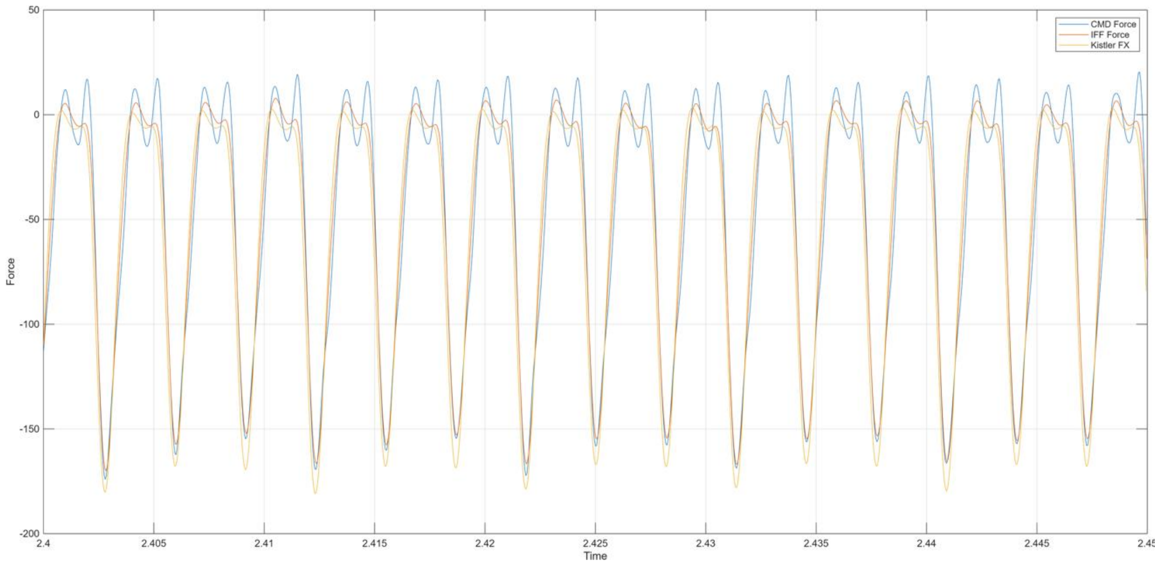

Figure 5.19 6061 y-direction milling force comparison 0.175 mm/tooth

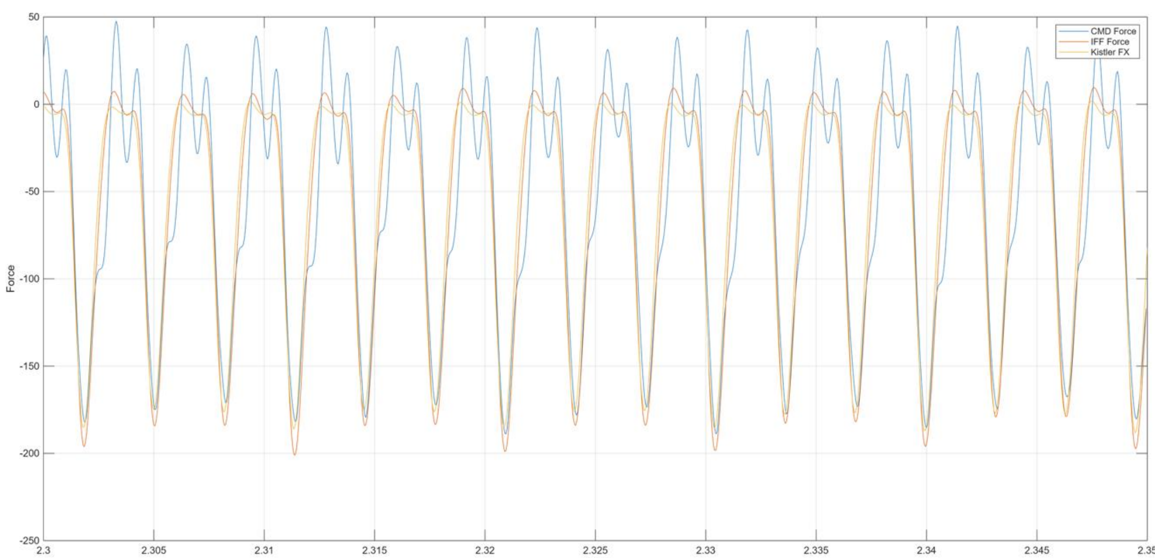

Figure 5.20 6061 y-direction milling force comparison 0.200 mm/tooth

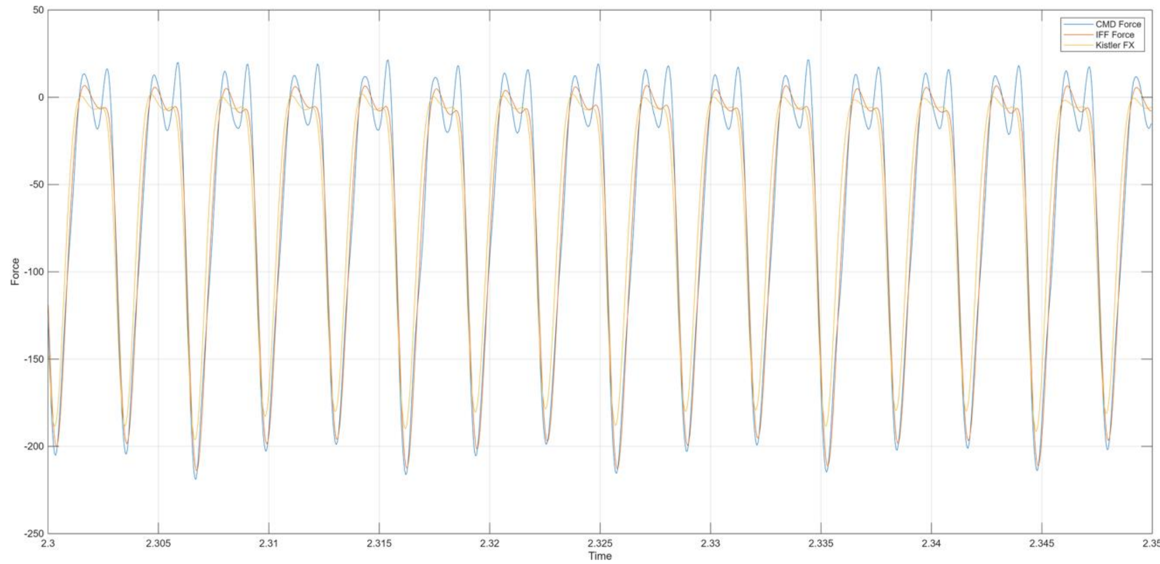

Figure 5.21 6061 y-direction milling force comparison 0.225 mm/tooth

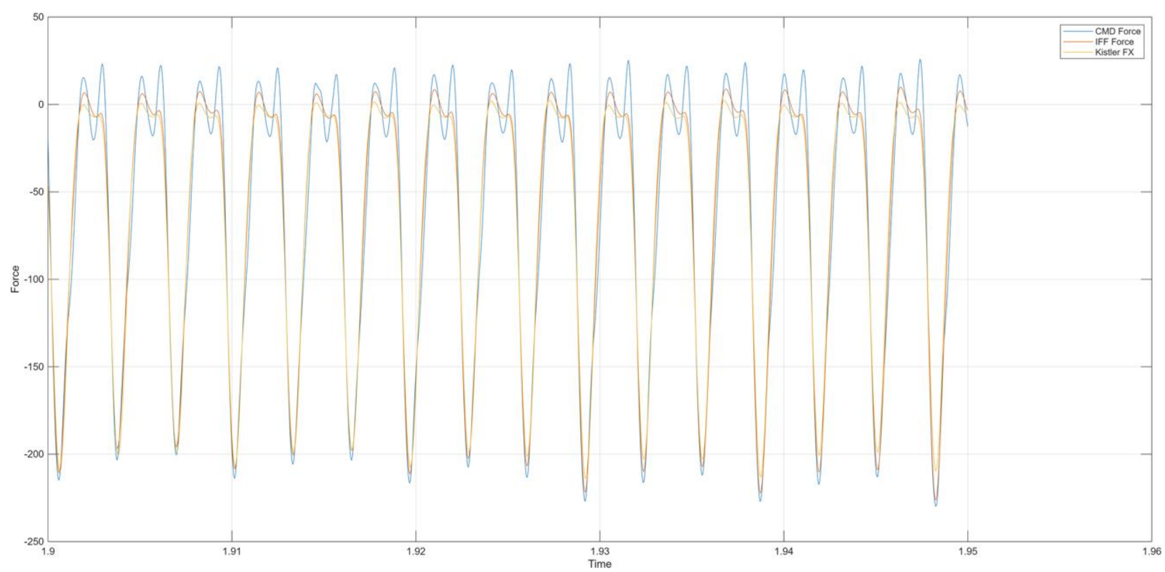

Figure 5.22 6061 y-direction milling force comparison 0.250 mm/tooth.

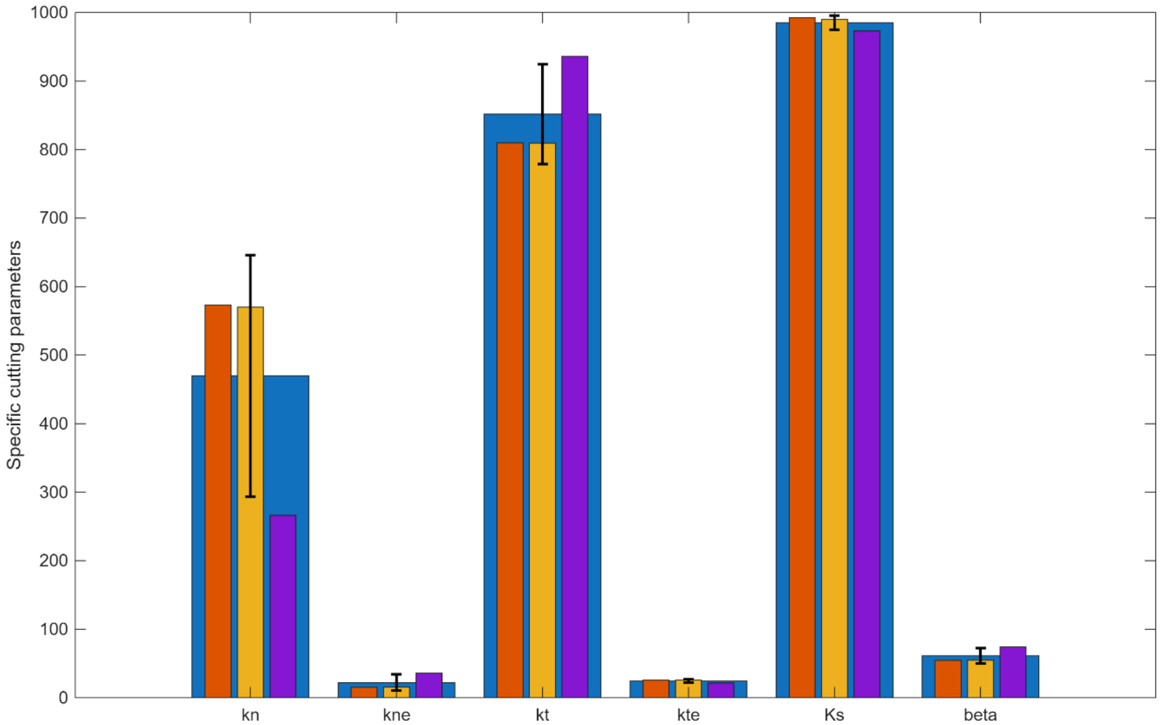

Figure 5.23 6061 cutting force coefficient results.

CFC validation for 303 stainless steel

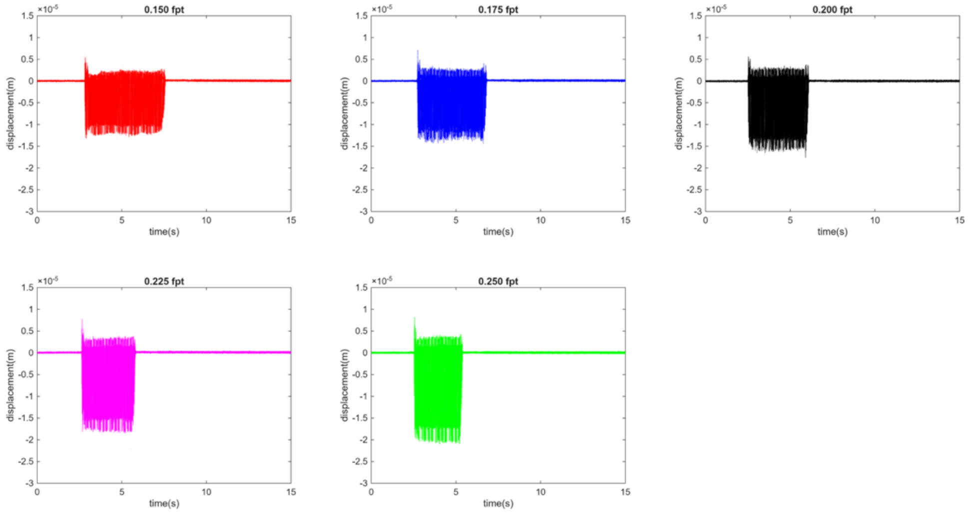

Figure 5.24 303 x-direction displacement measurements.

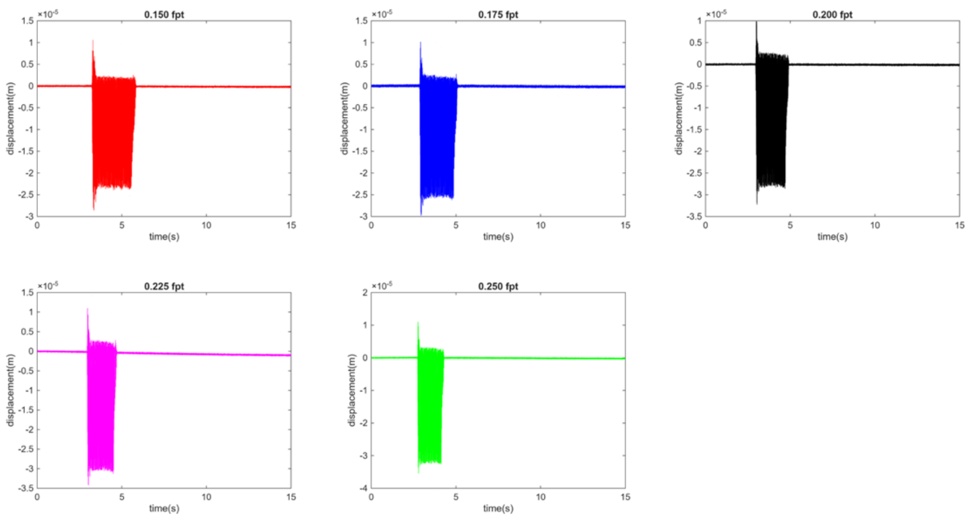

Figure 5.25 303 y-direction displacement measurements

.

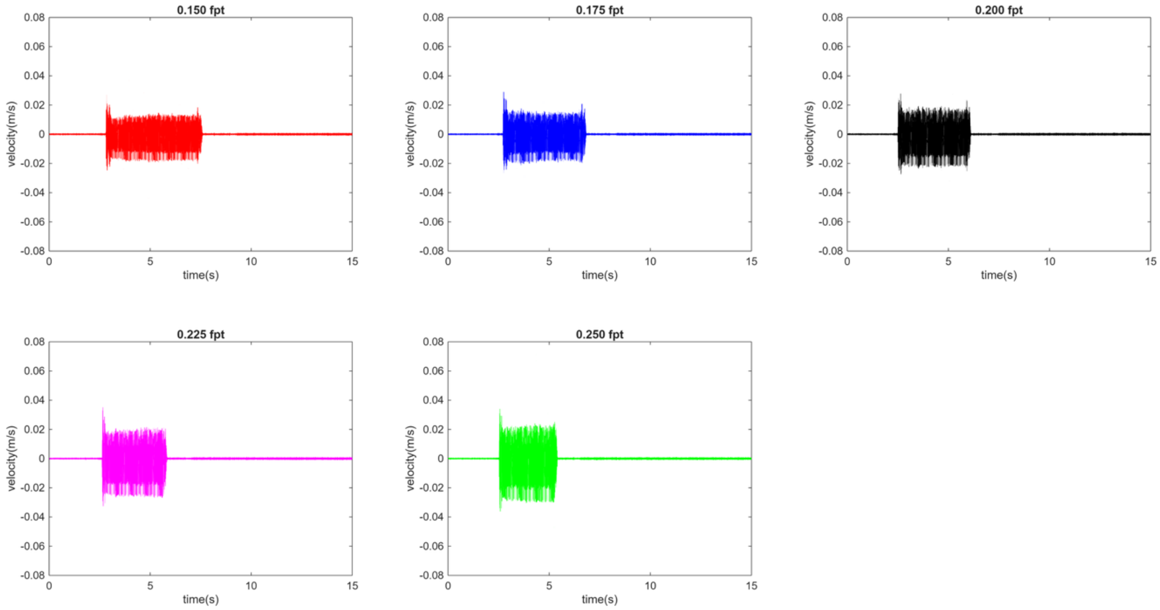

Figure 5.26 303 x-direction velocity measurements.

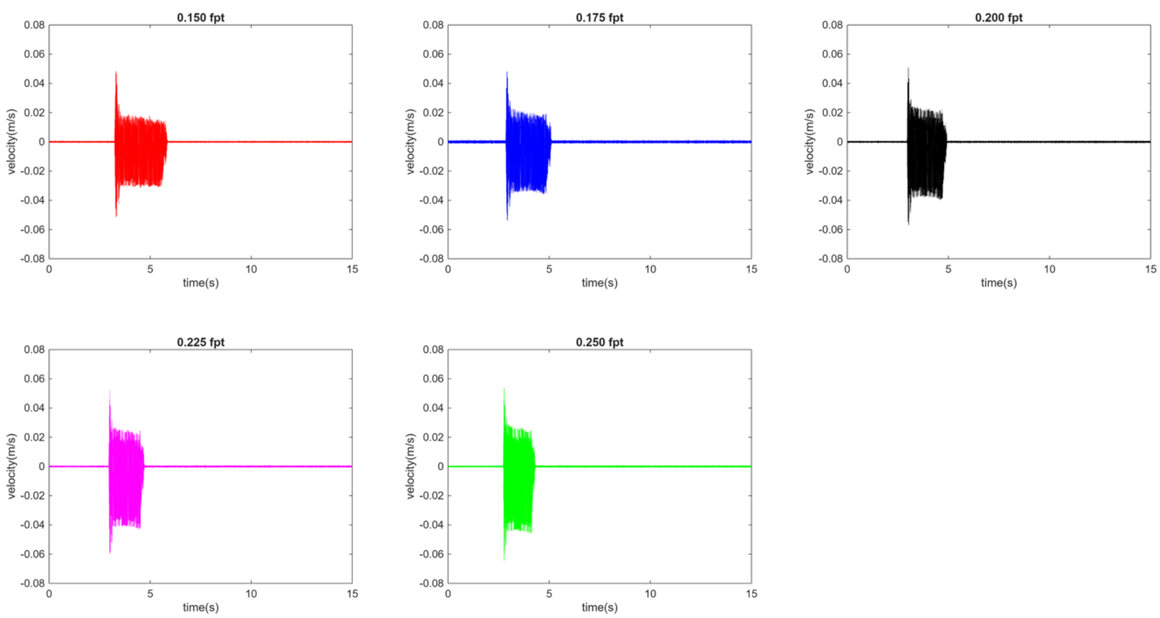

Figure 5.27 303 y-direction velocity measurements.

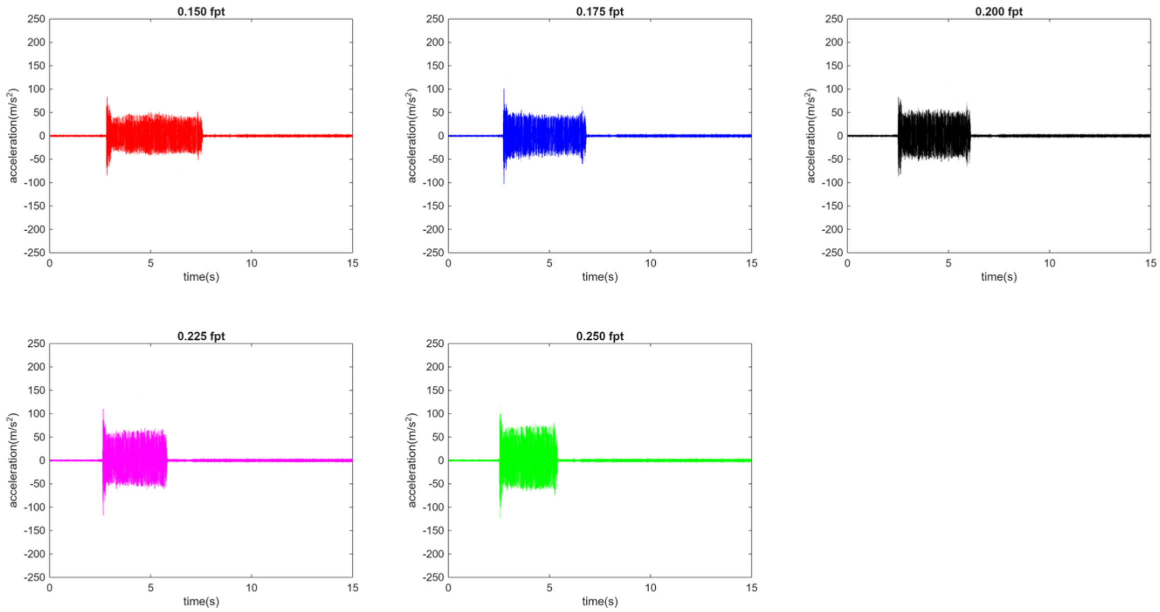

Figure 5.28 303 x-direction acceleration measurements.

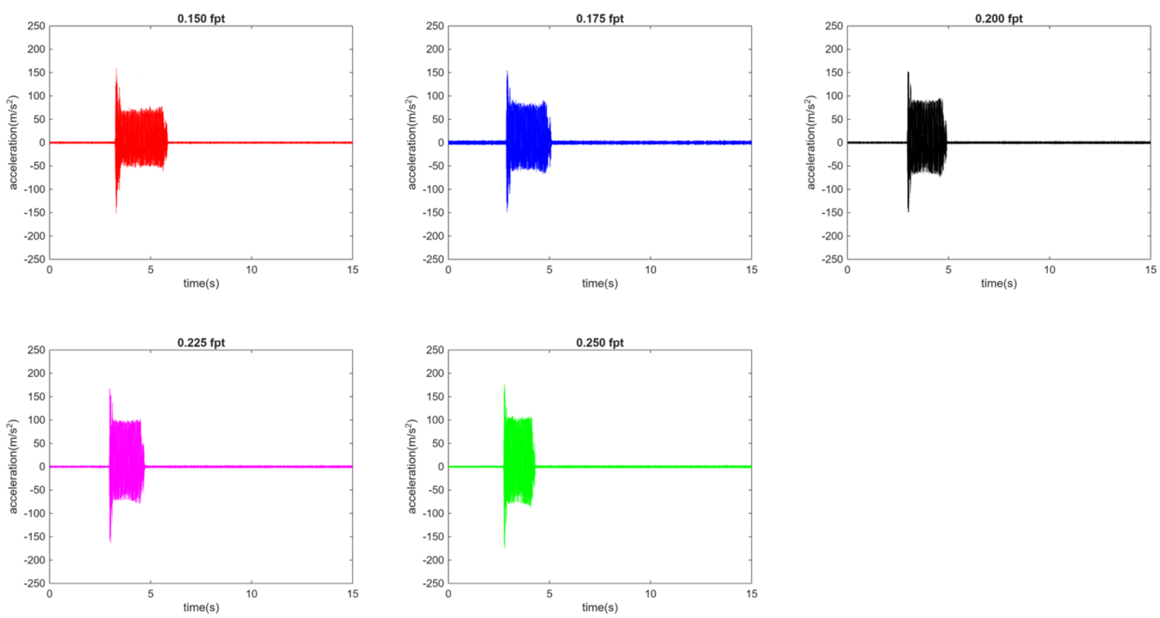

Figure 5.29 303 y-direction acceleration measurements.

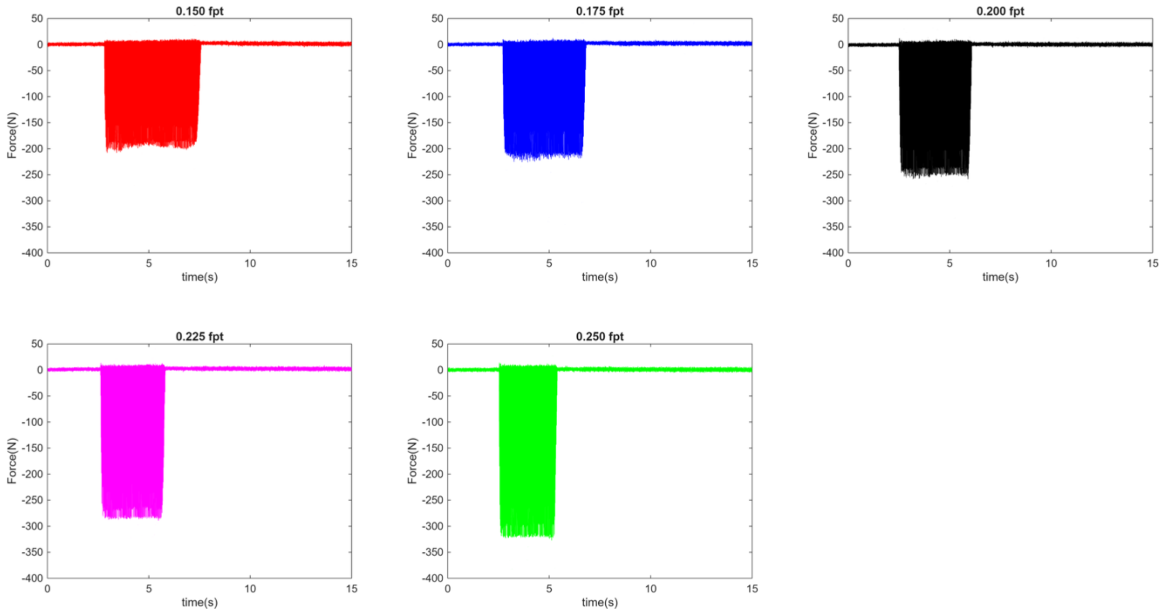

Figure 5.30 303 x-direction milling force measurements using time summation approach.

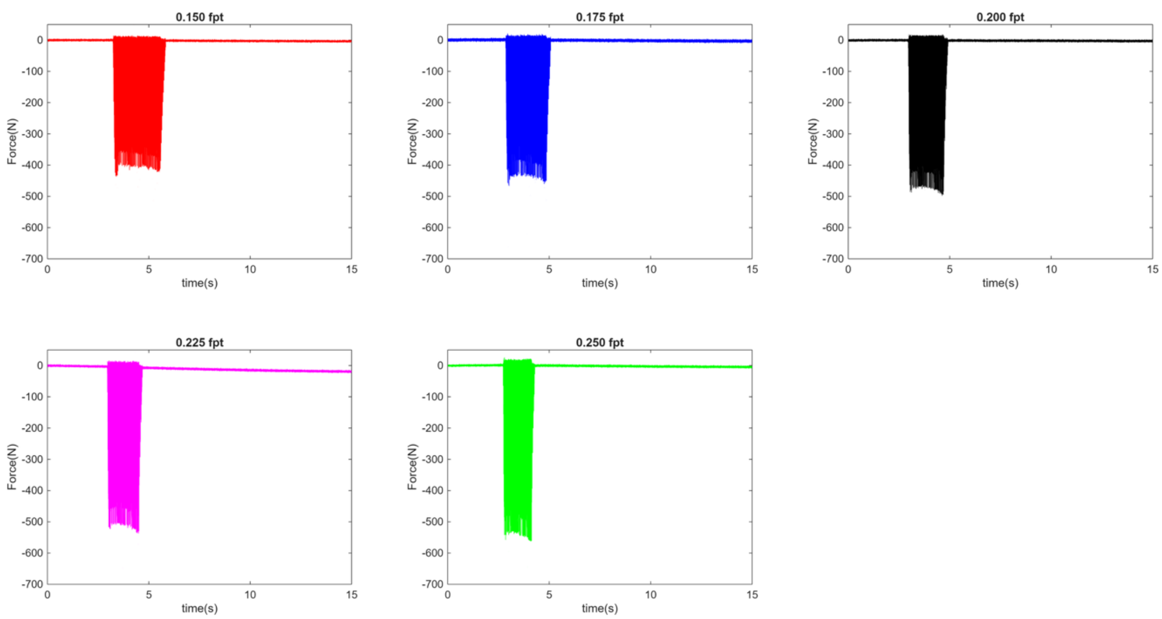

Figure 5.31 303 y-direction milling force measurements using time summation approach.

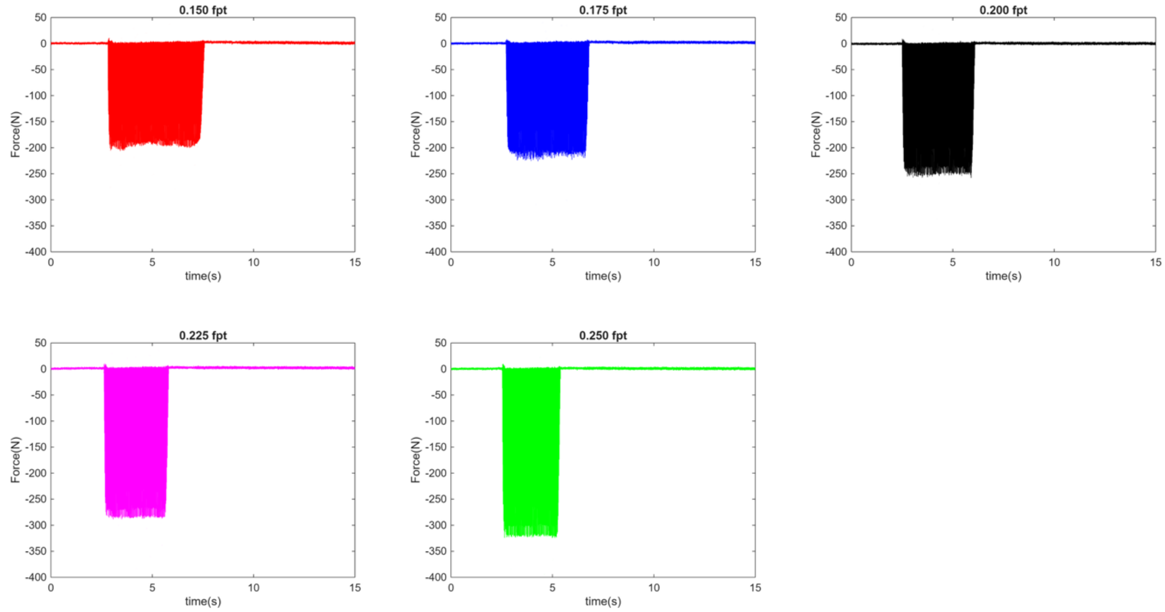

Figure 5.32 303 x-direction milling force measurements using structural deconvolution.

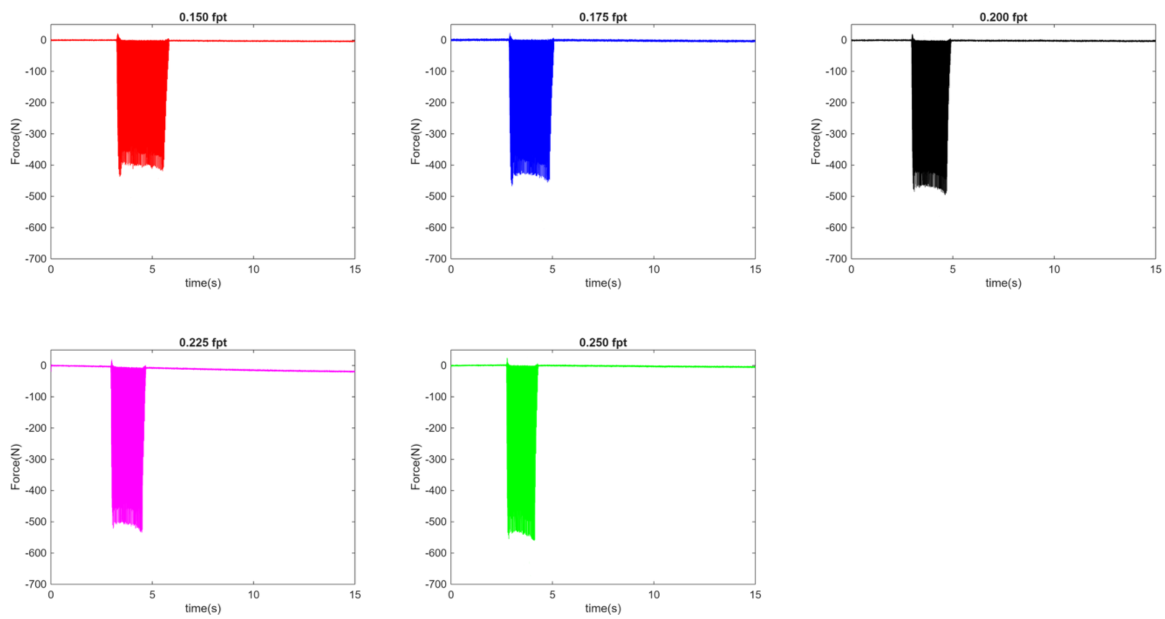

Figure 5.33 303 y-direction milling force measurements using structural deconvolution.

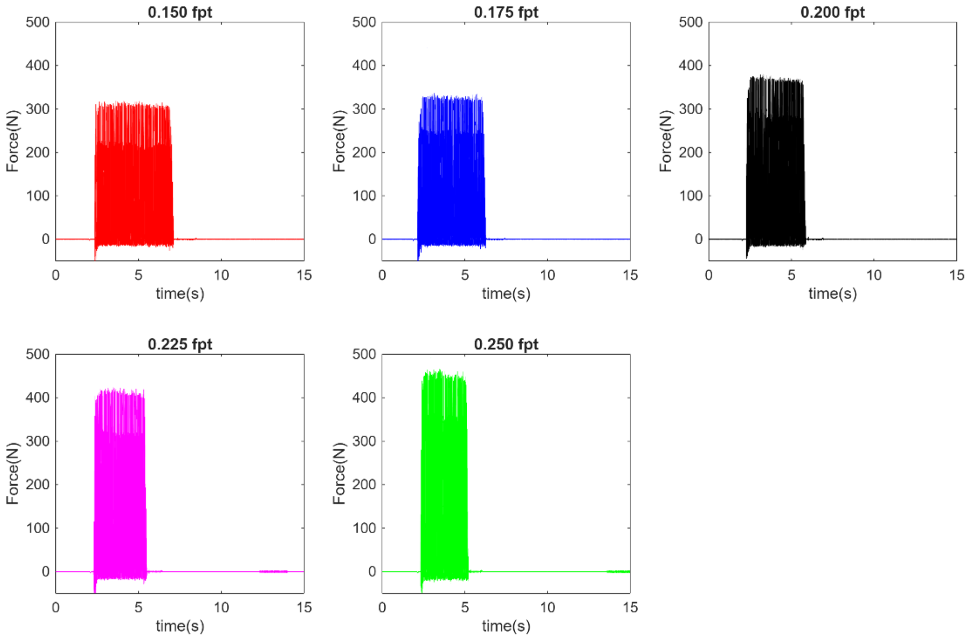

Figure 5.34 303 x-direction filtered milling force measurements using Kistler 9257B.

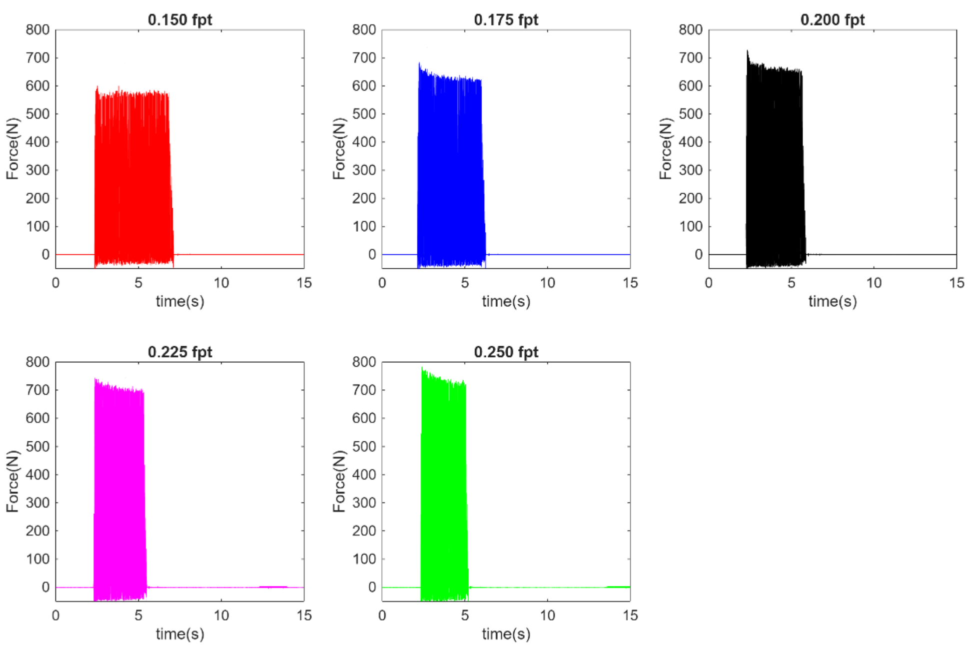

Figure 5.35 303 y-direction filtered milling force measurements using Kistler 9257B.

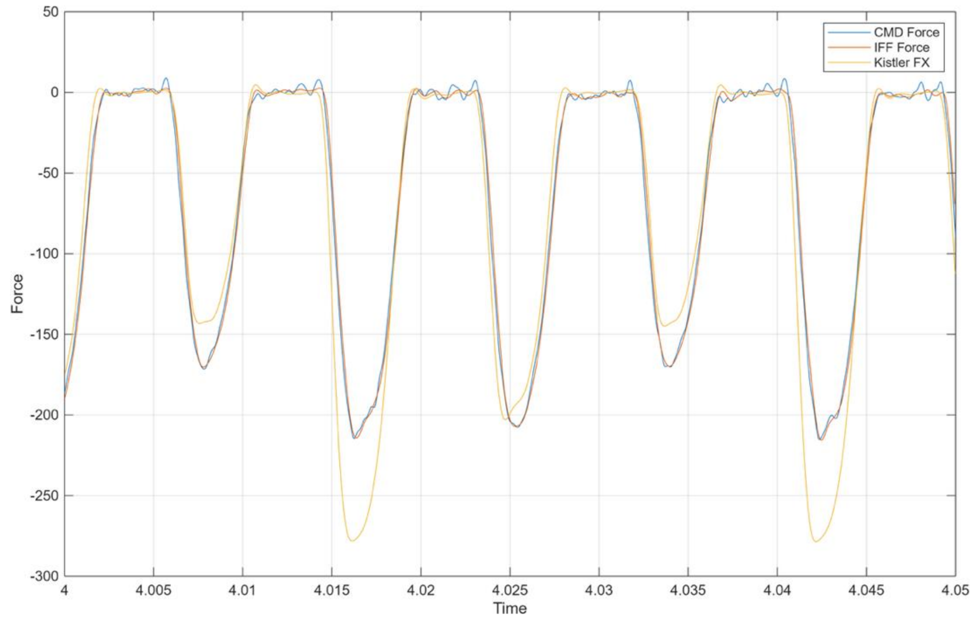

Figure 5.36 303 x-direction milling force comparison 0.150 mm/tooth

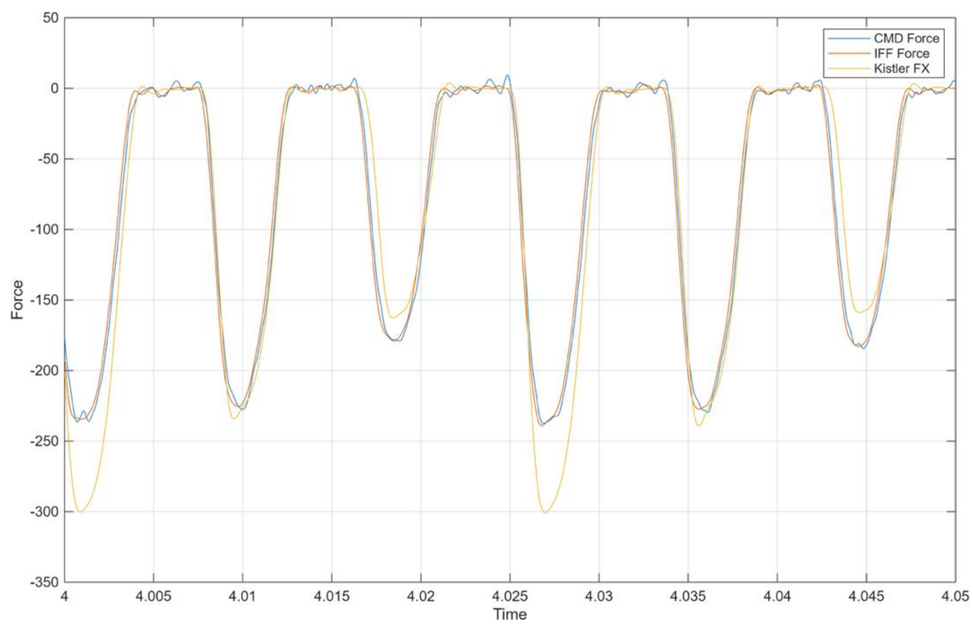

Figure 5.37 303 x-direction milling force comparison 0.175 mm/tooth

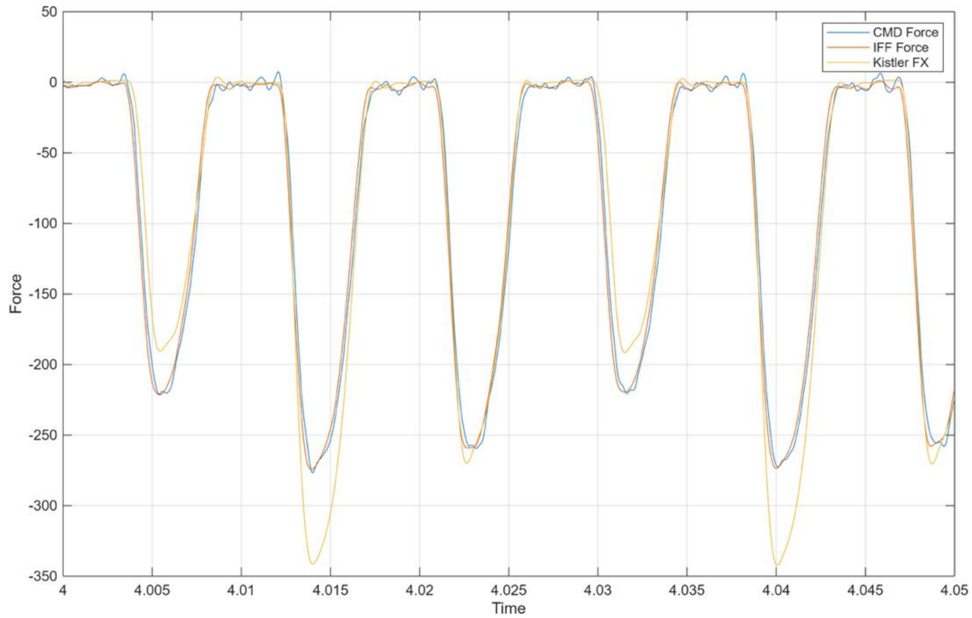

Figure 5.38 303 x-direction milling force comparison 0.200 mm/tooth

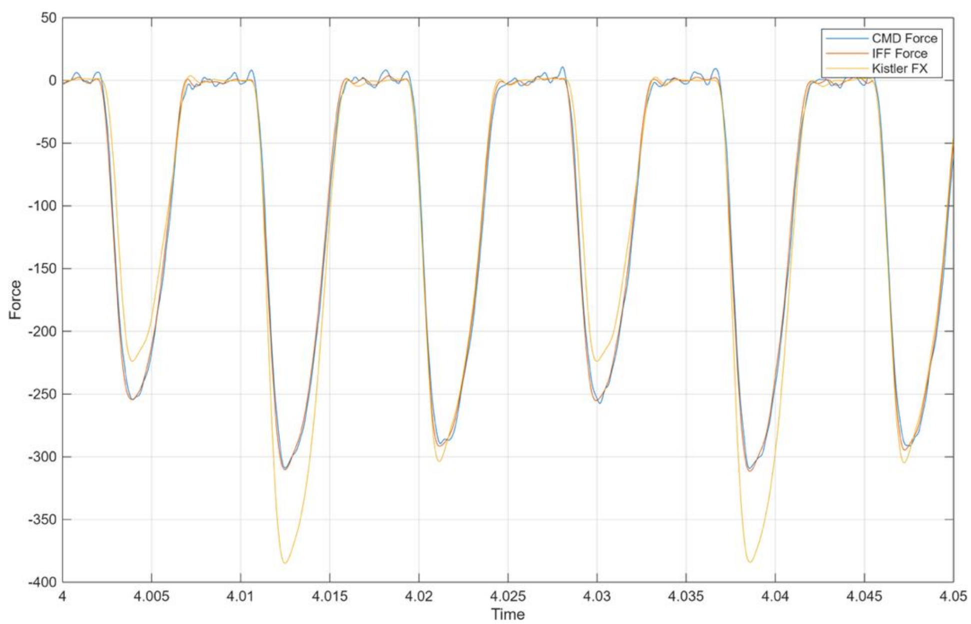

Figure 5.39 303 x-direction milling force comparison 0.225 mm/tooth

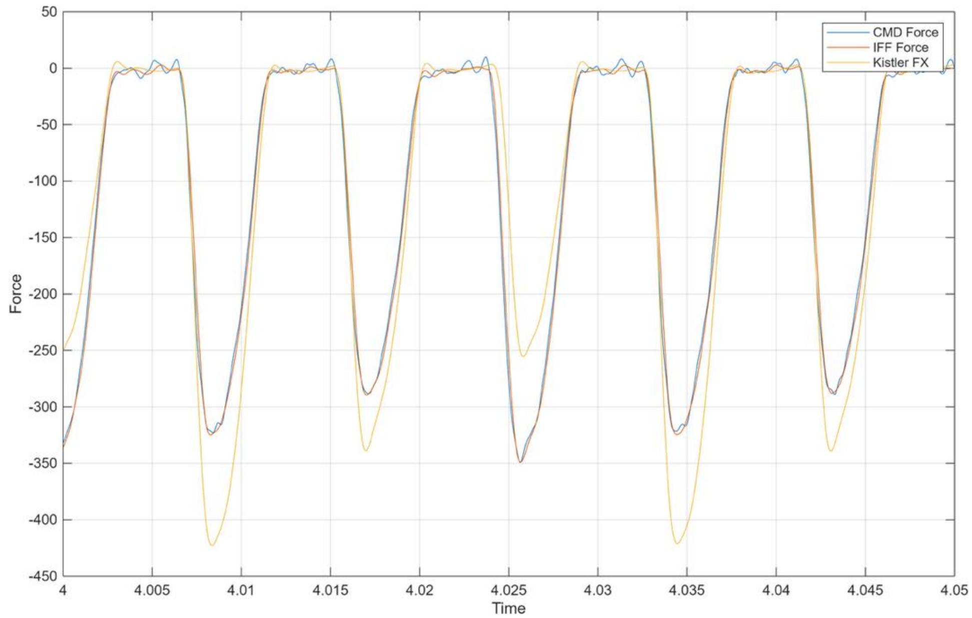

Figure 5.40 303 x-direction milling force comparison 0.250 mm/tooth

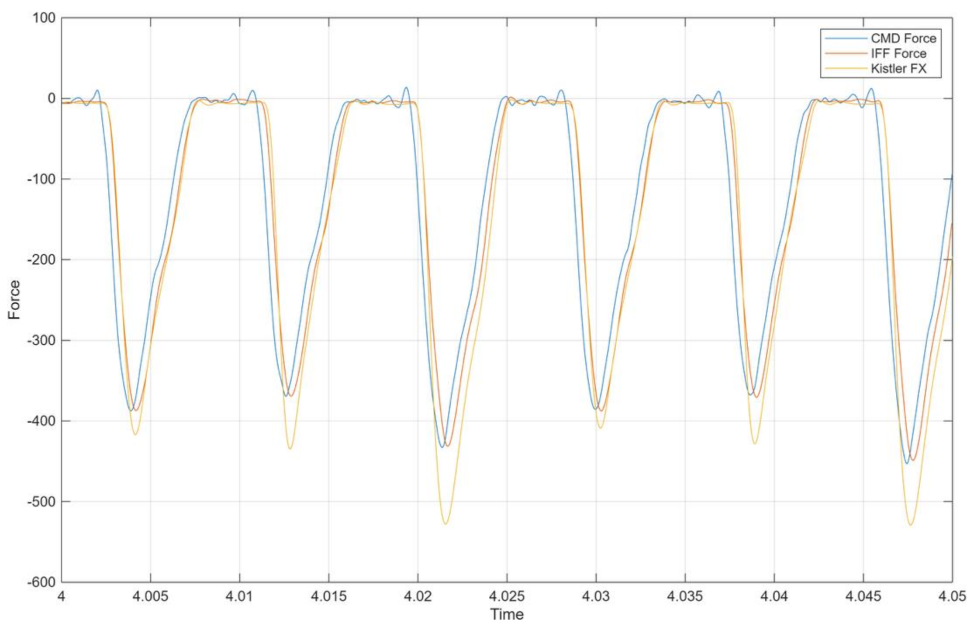

Figure 5.41 303 y-direction milling force comparison 0.150 mm/tooth

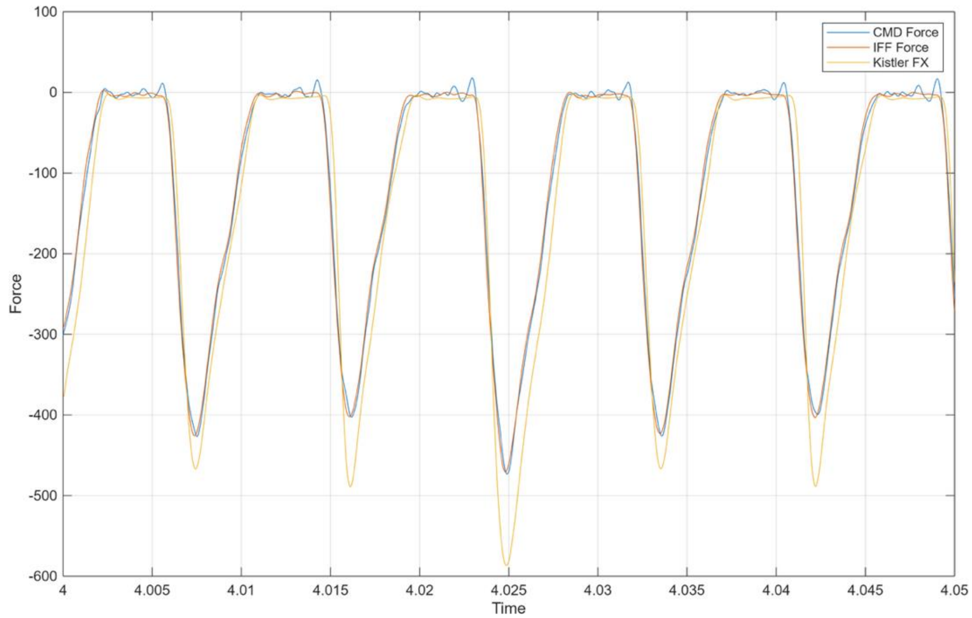

Figure 5.42 303 y-direction milling force comparison 0.175 mm/tooth

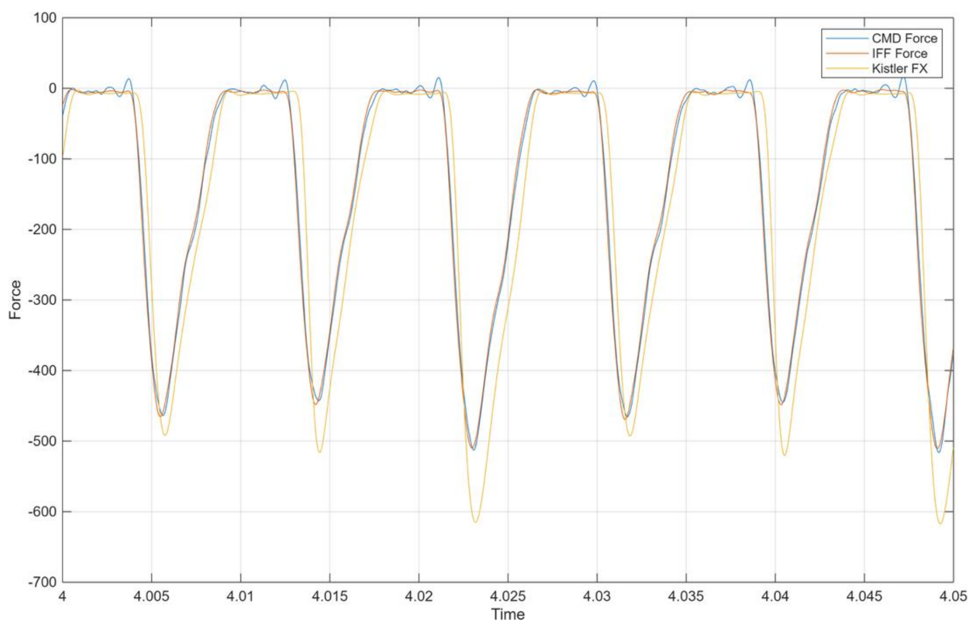

Figure 5.43 303 y-direction milling force comparison 0.200 mm/tooth

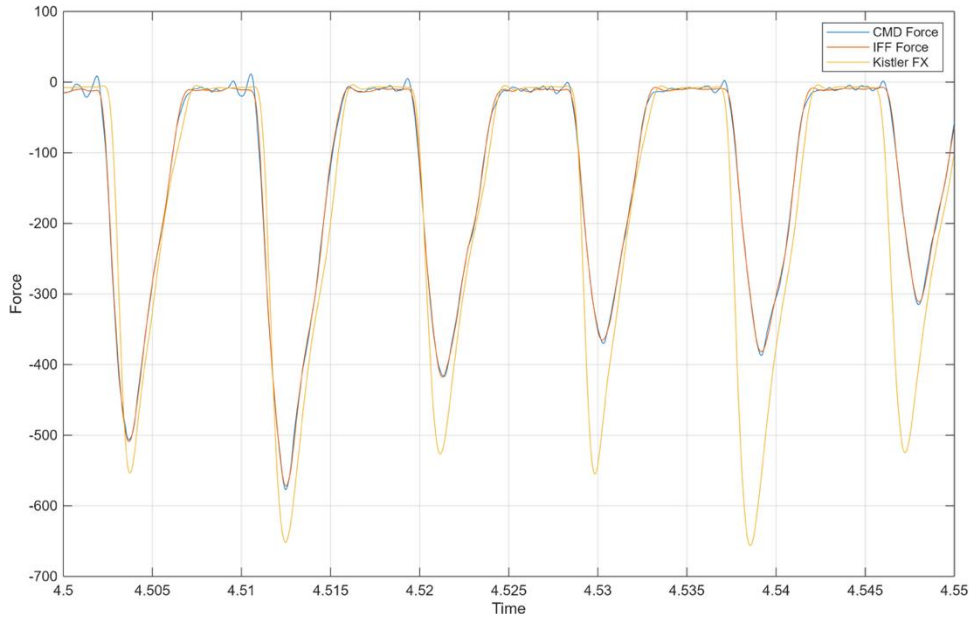

Figure 5.44 303 y-direction milling force comparison 0.225 mm/tooth

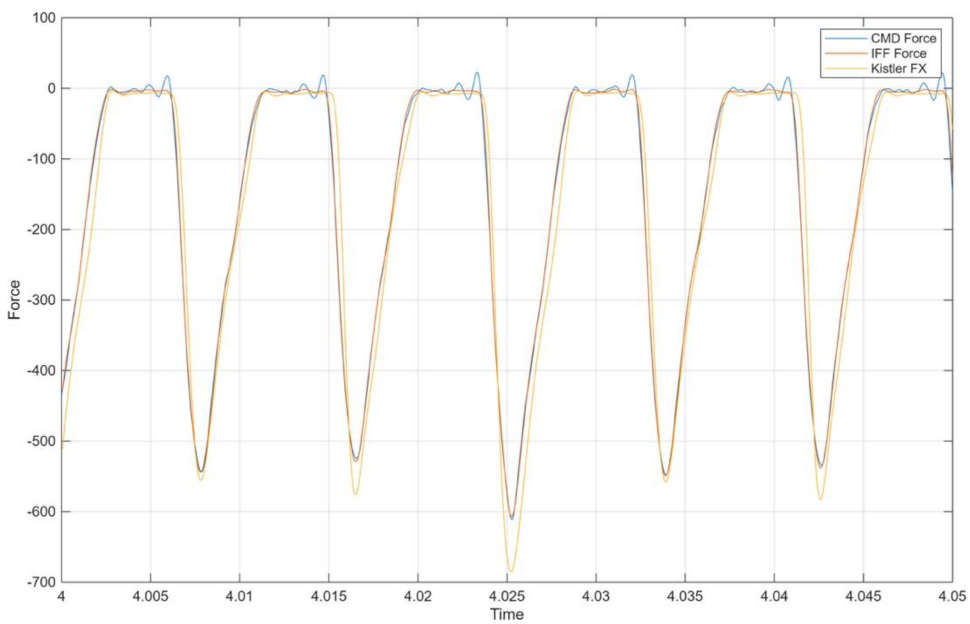

Figure 5.45 303 y-direction milling force comparison 0.225 mm/tooth

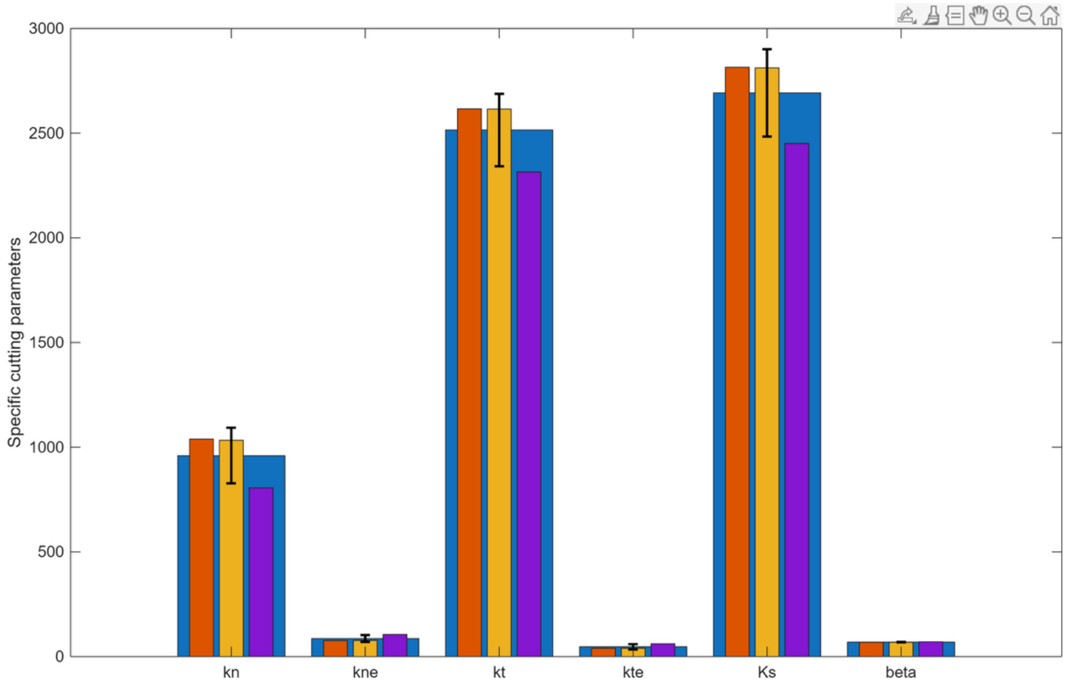

Figure 5.46 303 cutting force coefficient results.

Conclusion

This research demonstrates that high-precision milling force measurements can be achieved at 1.25% the cost of commercial systems with a low cost photo interrupter without need for complex frequency based filtering – a breakthrough that makes advanced process monitoring accessible to any manufacturer. The work in this dissertation validates a new milling force measurement method utilizing a single degree of freedom constrained motion dynamometer, an optical displacement transducer, and processing of a time-domain displacement signal. The research objective was to produce an instrument that accurately measures milling forces using (1) displacement, (2) derived velocity, (3) derived acceleration, and (4) the structural dynamics of the CMD.

For testing and validation purposes, it was necessary to expand on prior research to account for inconsistent results between motion measurements taken at the tool-workpiece interface and those taken at the knife edge sensor location. An algorithm was derived to compensate for these inconsistencies due to the rotational bending mode generated when milling on the CMD-workpiece combination at different heights away from the knife edge sensor location. The compensation was then applied to all cutting experiments conducted on six materials to capture the displacement measurements for the system.

Once acquired, velocity and acceleration were successfully derived from the displacement data. By means of a 150th order finite impulse response differentiator, velocity and accelerations motion measurements were able to be derived with successful high frequency attenuation when compared to traditional numerical differentiation techniques. These derived motion measurement results were compared to industrial grade transducers (laser Doppler vibrometer and piezoelectric accelerometer). Measurements for the derived acceleration successfully showed high fidelity with noise attenuation and measurements when compared to the accelerometer. Agreement with the derived velocity measurement compared to the laser Doppler vibrometer showed similar agreement.

Additionally, the structural dynamics of the CMD-workpiece combination for all six workpieces were acquired. The system response was captured with high confidence utilizing peak picking with a single degree of freedom frequency response function for all cases. A thermoplastic pad proved to be a reliable and repeatable source of additional damping for all testing cuts and was used for all six materials.

For all tests, displacement, velocity, and acceleration motion signals were scaled by their respective modal parameter: stiffness with displacement, damping with velocity, and mass with parameters of each CMD-workpiece result. This approach successfully captured the spring, damping, and inertial force measurements during in-processing cutting operations. These scaled signals were then summed to produce the total cutting force in the compliant direction of the CMD. The phase relationship between displacement, velocity, and acceleration- where displacement lags velocity by 90° and acceleration by 180° - results in force cancelation effects that influence the total force summation.

The same displacement data and frequency response functions used for the time summation approach were used to construct force measurements in the compliant CMD direction by means of structural deconvolution. These methods were compared to the time-based force summation for five incremental cuts for all six test materials. The results proved to be consistent between both measurements for all cuts using both three and four fluted carbides endmills: nearing a 98% similarity in measurement. This similarity validates the novel method of capturing milling forces along with various in-process motion measurements that were not previously acquired in past iterations and experiments. Additionally, by utilizing an FIR differentiator, the need for additional frequency domain filters has been reduced substantially.

For both approaches used on the CMD, all cuts were compared to identical operations performed on the commercial grade Kistler 9257B dynamometer. The data was then filtered by means of a force-to-force frequency filter to remove the structural dynamics of the dynamometer from the force measurement. This post processing of data represents a critical flaw for a high cost commercial grade system. As a result, the compensated measurements from the Kistler compared to the CMD results varied between both tool-workpiece materials: with an agreement between both CMD approaches and the Kistler to an average of 93%.

For three material cases, the cutting force coefficients utilizing a linear regression approach for the five incremental cuts were also determined. For these three cases, the *y*-direction forces were captured for the CMD along with the Kistler 9257B for these tests. A comparison of the cuts captured in this direction proved to have similar results to the *x*-direction cuts. This then proves an additional capability of the CMD force acquisition utilizing the stage displacement in the non-compliant direction to capture both milling force directions. The results in measuring the radial and tangential cutting force coefficients for both rubbing and shearing effects, as well as the beta angle calculation and the overall specific cutting force coefficient, varied between materials.

These results establish this novel time-based summation method as an effective tool for milling force measurement, achieving a 98% agreement with the structural deconvolution method and 93% accuracy compared to the commercial grade milling dynamometer at unprecedented cost savings. This approach surpasses prior methods by providing not only force measurements from the displacement, but also velocity, acceleration, spring force, damping force, and inertial force.

Future work and discussion

Having derived force measurements for the Twelve tool-workpiece combinations utilizing the CMD and KES, additional data and processes were found that can be used to expand further into this work and field of research. These elements provided a more robust method of utilizing this system.

The first critical point is that the addition of multiple fluted endmills proved to be a challenge when determining regions of stability due to runout. In past experiments, the utilization of single fluted endmills only considered the tooth passing frequency without additional runout values being considered within the frequency domain analysis. Due to the system being approximately ten times more compliant when compared to the tooling selection, an additional requirement is needed that no tooth passing frequency be more than 5% of the natural frequency proved to be a challenge with a higher number of teeth.

In most cases, this avoidance of resonance was nearly impossible to reach depending on the natural and tooth passing frequencies for higher spindle speed applications, such as aluminum cutting. The tooth passing frequency mapping in this work proves to be effective in reducing the runout frequency effects in the system that is not considered for high rigidity workpieces on which most fundamentals of machining dynamics are based.

Additionally, the mapping of the structural dynamic modal parameters when compared for all six workpiece materials allows the user to characterize the changes within the system based on what group of materials is used. In all cases, the stiffness of the system remains relatively unchanged due to changes in the mass of each workpiece material. As for the natural frequency, the change in density for the standard dimension blocks proves to be very important for the system. Due to the lack of change in stiffness, the larger changes in mass between steels and aluminum materials proves a large shift in natural frequency. This understanding allows for the determination of the potential bandwidth that can be expected for the CMD natural frequency response and can be calculated based on the weight of the workpiece itself. As for damping of the system, it is evident that this depends on the material properties of the workpiece. Steels proved to have a higher percentage of damping when compared to both titanium and aluminum workpieces, and for all materials the damping can be characterized to have a good estimate in all cases. As a result, these measurements have the potential to get an algorithmic approach to determine modal parameters for the system without the need for performing peak picking from an experimentally derived frequency response function. This method would then greatly reduce the need expensive data acquisition methods when using the CMD.

The time summation approach removes some issues seen with the structural deconvolution method that must be addressed as well. Due to mass being removed from the system each time a cut is performed on the CMD, the natural frequency will be increasing and moving further away from the initial measurement. In all cases when material is removed, the mass parameter will lower in value, and the natural frequency will increase in value. Due to the inverse FRF filter being measured prior to cutting, the fidelity to the sensor decreases as mass is taken out and natural frequency changes.

As for the CMD itself, the need for the height compensation due to the presence of the rotational moment when milling requires an evaluation of the design. The intention of the design is to displace purely in linear motion due to the forces applied on the CMD but is not currently the case. To mitigate the rotational moment effects, a simple change in the location of the KES to be at the location of the tool-workpiece interaction would immediately remove the need height compensation. The design of stowing the KES away from debris, chips, and coolant that are present in an industrial manufacturing setting reduces the feasibility for the sensor to be exposed above the stage. Further research into a more robust sensor, such as an eddy current sensor, would also reduce the amount of noise embedded into the signal and concerns with environmental factors.

Additional finite element modeling (FEM) can be conducted on the CMD design to remove the torsional effects when applying load on the system at the tool-workpiece interaction. This also proves to be a challenge due to the asymmetric stiffness design and must be further inspected. This could result in adjusting the thickness of the spring leaves for the complaint direction or the overall design of the four-bar stage. The changes must result in the remove of this torsional effect and prove a method for capturing pure linear motion of the system without changes in stiffness over any condition.

Additional work in developing a muti-degree of freedom system to capture *x* and *y* direction forces would prove to be effective when directly comparing the results to a commercial grade dynamometer. Although capable in measuring both force directions with this system, the need for two cuts continues to leave this work desiring more and having a true comparison to all in one commercial grade system. Designs have been proven by others to have various degrees of freedom but prove to be more challenging when deriving the force measurements.

The time summation approach utilizing a SDOF CMD in its current stage demonstrates exemptional value a simple, yet highly effective tool for measuring in-processes cutting operations at under $1,000. When compared to the $80,000 commercial system, the novel approach achieves results within 10% difference at a fraction of the cost. Compared to a traditional milling dynamometer also provides more data into a digital thread, such as velocity and acceleration signals. These signals can be used within a Industry 4.0 setting to develop more complex algorithms to simulation machine motions and processes.

LIST OF REFERENCES

[1] M. F. Gomez, “Displacement-based dynamometer for milling force measurement Displacement-based dynamometer for milling force measurement Recommended Citation Recommended Citation "Displacement-based dynamometer for milling force measurement,” 2021. [Online]. Available: https://trace.tennessee.edu/utk_graddiss/6654

[2] A. Shokrani *et al.*, “Sensors for in-process and on-machine monitoring of machining operations,” *CIRP J Manuf Sci Technol*, vol. 51, pp. 263–292, Jul. 2024, doi: 10.1016/j.cirpj.2024.05.001.

[3] S. Smith, T. Schmitz, T. Feldhausen, and M. Sealy, “Hybrid metal additive/subtractive machine tools and applications,” *CIRP Annals*, vol. 73, no. 2, pp. 615–638, Jan. 2024, doi: 10.1016/j.cirp.2024.05.002.

[4] J. H. Mcclellan and T. W. Parks, “A Personal History of the Parks-McClellan Algorithm,” Mar. 2005.

[5] M. Gomez and T. Schmitz, “Low-cost, constrained-motion dynamometer for milling force measurement,” *Manuf Lett*, vol. 25, pp. 34–39, Aug. 2020, doi: 10.1016/j.mfglet.2020.07.001.

[6] M. F. Gomez and T. L. Schmitz, “Displacement-based dynamometer for milling force measurement,” Elsevier B.V., 2019, pp. 867–875. doi: 10.1016/j.promfg.2019.06.161.

[7] “The Piezoelectric Effect, Theory, Design and Usage.” [Online]. Available: http://www.designinfo.com/kistler/ref/tech_theory_text.htm

[8] T. L. Schmitz and K. S. Smith, *Machining Dynamics*. Springer International Publishing, 2019. doi: 10.1007/978-3-319-93707-6.

[9] A. R. Zareena and S. C. Veldhuis, “Tool wear mechanisms and tool life enhancement in ultra-precision machining of titanium,” *J Mater Process Technol*, vol. 212, no. 3, pp. 560–570, Mar. 2012, doi: 10.1016/j.jmatprotec.2011.10.014.

[10] Mastercam, “What is dynamic motion and should I be using it?” Mastercam Blog. [Online]. Available: https://www.mastercam.com/news/blog/what-is-dynamic-motion-and -should-i-be-using-it/.

[11] M. A. Rubeo and T. L. Schmitz, “Mechanistic force model coefficients: A comparison of linear regression and nonlinear optimization,” *Precis Eng*, vol. 45, pp. 311–321, Jul. 2016, doi: 10.1016/j.precisioneng.2016.03.008.

[12] M. A. Rubeo and T. L. Schmitz, “Milling Force Modeling: A Comparison of Two Approaches,” *Procedia Manuf*, vol. 5, no. 44th Proceedings of the North American Manufacturing Research Institution of SME, pp. 90–105, 2016, doi: 10.1016/j.promfg.2016.08.010.

[13] S. Ratchev, E. Govender, S. Nikov, K. Phuah, and G. Tsiklos, “Force and deflection modelling in milling of low-rigidity complex parts,” in *Journal of Materials Processing Technology*, Dec. 2003, pp. 796–801. doi: 10.1016/S0924-0136(03)00382-0.

[14] T. Schmitz, E. Betters, E. Budak, E. Yüksel, S. Park, and Y. Altintas, “Review and status of tool tip frequency response function prediction using receptance coupling,” Jan. 01, 2023, *Elsevier Inc.* doi: 10.1016/j.precisioneng.2022.09.008.

[15] W. A. Kline and R. E. Devor~, “THE EFFECT OF RUNOUT ON CUTTING GEOMETRY AND FORCES IN END MILLING,” 1983.

[16] Y. Altintas, G. Stepan, E. Budak, T. Schmitz, and Z. M. Kilic, “Chatter Stability of Machining Operations,” *Journal of Manufacturing Science and Engineering, Transactions of the ASME*, vol. 142, no. 11, Nov. 2020, doi: 10.1115/1.4047391.

[17] S. Smith and J. Tlusty, “Efficient Simulation Programs for Chatter in Milling,” CIRP Annals – Manufacutring Technology, vol. 42, no. 1, pp. 463-466. 1993.

[18] Y. Altintas, G. Stepan, E. Budak, T. Schmitz, and Z. M. Kilic, “Chatter Stability of Machining Operations,” *Journal of Manufacturing Science and Engineering, Transactions of the ASME*, vol. 142, no. 11, Nov. 2020, doi: 10.1115/1.4047391.

[19] S. D. Merdol and Y. Altintas, “Multi frequency solution of chatter stability for low immersion milling,” *J Manuf Sci Eng*, vol. 126, no. 3, pp. 459–466, 2004, doi: 10.1115/1.1765139.

[20] J. Tlusty, W. Zaton, and F. Ismail, “Stability Lobes in Milling.”

[21] E. Budak, Y. Altintaş, and E. J. A. Armarego, “Prediction of milling force coefficients from orthogonal cutting data,” *Journal of Manufacturing Science and Engineering, Transactions of the ASME*, vol. 118, no. 2, pp. 216–224, 1996, doi: 10.1115/1.2831014.

[22] J. Nazario, T. No, M. Gomez, G. Corson, and T. Schmitz, “Manufacturing Letters Dynamic force and stability prediction for milling using feed rate scheduling software and time-domain simulation,” 2022, [Online]. Available: www.sciencedirect.com

[23] J. Kruttiventi, J. Wu, and J. I. Frankel, “Obtaining time derivative of low-frequency signals with improved signal-to-noise ratio,” *IEEE Trans Instrum Meas*, vol. 59, no. 3, pp. 596–603, Mar. 2010, doi: 10.1109/TIM.2009.2025069.

[24] M. L. Simpson, C. D. Cox, and G. S. Sayler, “Frequency domain analysis of noise in autoregulated gene circuits,” Knoxville, TN, Feb. 2003. [Online]. Available: www.pnas.orgcgidoi10.1073pnas.0736140100

[25] Saeid. Sanei, *2013 IEEE International Workshop on Machine Learning for Signal Processing : September 22-25, Southampton, United Kingdom : proceedings of MLSP2013*. IEEE, 2013.

[26] MathWorks, “diff.” MathWorks Documentation. [Online]. Available: https://www.mathworks .com/help/matlab/ref/double.diff.html.

[27] F. van Breugel, J. N. Kutz, and B. W. Brunton, “Numerical differentiation of noisy data: A unifying multi-objective optimization framework,” *IEEE Access*, vol. 8, pp. 196865–196877, 2020, doi: 10.1109/ACCESS.2020.3034077.

[28] L. Tan and J. Jiang, “Finite Impulse Response Filter Design,” in *Digital Signal Processing*, Elsevier, 2013, pp. 217–299. doi: 10.1016/b978-0-12-415893-1.00007-x.

[29] L. D. Milić, M. D. Lutovac, and J. D. Ćertić, “Design of first-order differentiator utilising FIR and IIR sub-filters,” in *International Journal of Reasoning-based Intelligent Systems*, Inderscience Publishers, Jan. 2013, pp. 3–11. doi: 10.1504/IJRIS.2013.055122.

[30] R. C. Kavanagh, "FIR differentiators for quantized signals," in IEEE Transactions on Signal Processing, vol. 49, no. 11, pp. 2713-2720, Nov. 2001, doi: 10.1109/78.960418.

[31] C. C. Tseng and S. L. Lee, “Linear phase FIR differentiator design based on maximum signal-to-noise ratio criterion,” *Signal Processing*, vol. 86, no. 2, pp. 388–398, Feb. 2006, doi: 10.1016/j.sigpro.2005.06.004.

[32] T. W. Parks and J. McClellan, “Chebyshev Approximation for Nonrecursive Digital Filters with Linear Phase,” 1972.

[33] Mathworks, “Take Derivatives of a Signal.” Mathworks Documentation. [Online]. Available: https://www.mathworks.com/help/signal/ug/take-derivatives-of-a-signal.html.

[34] Kistler, “Stationary dynamometer for measuring cutting forces.” [Online]. Available: https://www.kistler.com/US/en/stationary-dynamometer-for-measuring-cutting-forces/C00000545.

[35] E. Kuljanic, M. Sortino, and F. Miani, “Application of a Rotating Dynamometer for Cutting Force Measurement in Milling,” in *AMST’02 Advanced Manufacturing Systems and Technology*, Springer Vienna, 2002, pp. 159–166. doi: 10.1007/978-3-7091-2555-7_15.

[36] C. Wang, G. Liu, Q. An, and M. Chen, “Occurrence and formation mechanism of surface cavity defects during orthogonal milling of CFRP laminates,” *Compos B Eng*, vol. 109, pp. 10–22, Jan. 2017, doi: 10.1016/j.compositesb.2016.10.015.

[37] G. Totis, G. Wirtz, M. Sortino, D. Veselovac, E. Kuljanic, and F. Klocke, “Development of a dynamometer for measuring individual cutting edge forces in face milling,” *Mech Syst Signal Process*, vol. 24, no. 6, pp. 1844–1857, 2010, doi: 10.1016/j.ymssp.2010.02.010.

[38] Y. Qin, Y. Zhao, Y. Li, Y. Zhao, and P. Wang, “A high performance torque sensor for milling based on a piezoresistive MEMS strain gauge,” *Sensors (Switzerland)*, vol. 16, no. 4, Apr. 2016, doi: 10.3390/s16040513.

[39] I. Korkut, “A dynamometer design and its construction for milling operation”, doi: 10.1016/S0261-3069Ž03.00122-5.

[40] R. Zameroski, C. Ramsauer, C. Habersohn, F. Bleicher, and T. Schmitz, “Flexure-based torque and thrust force drilling dynamometer with Hall effect sensor displacement measurement,” *CIRP Annals*, vol. 73, no. 1, pp. 281–284, Jan. 2024, doi: 10.1016/j.cirp.2024.04.086.

[41] C. T. Tyler and T. L. Schmitz, “Analytical process damping stability prediction,” *J Manuf Process*, vol. 15, no. 1, pp. 69–76, 2013, doi: 10.1016/j.jmapro.2012.11.006.

[42] A. Honeycutt and T. L. Schmitz, “A Study of Milling Surface Quality during Period-2 Bifurcations,” in *Procedia Manufacturing*, Elsevier B.V., 2017, pp. 183–193. doi: 10.1016/j.promfg.2017.07.046.

[43] T. Ransom, A. Honeycutt, and T. Schmitz, “A new tunable dynamics platform for milling experiments,” *Precis Eng*, vol. 44, pp. 252–256, Apr. 2016, doi: 10.1016/j.precisioneng.2016.01.005.

[44] “Datasheet,” 2015. [Online]. Available: www.rohm.com

[45] R. Zameroski, M. Gomez, and T. Schmitz, “Geometry-based, Gaussian profile model for optical knife-edge displacement sensor,” *Precis Eng*, vol. 73, pp. 470–476, Jan. 2022, doi: 10.1016/j.precisioneng.2021.10.011.

[46] M. Gomez and T. Schmitz, “Stability Evaluation for a Damped, Constrained-Motion Cutting Force Dynamometer,” *Journal of Manufacturing and Materials Processing*, vol. 6, no. 1, Feb. 2022, doi: 10.3390/jmmp6010023.

APPENDIX

Three flute x-direction endmill force comparison

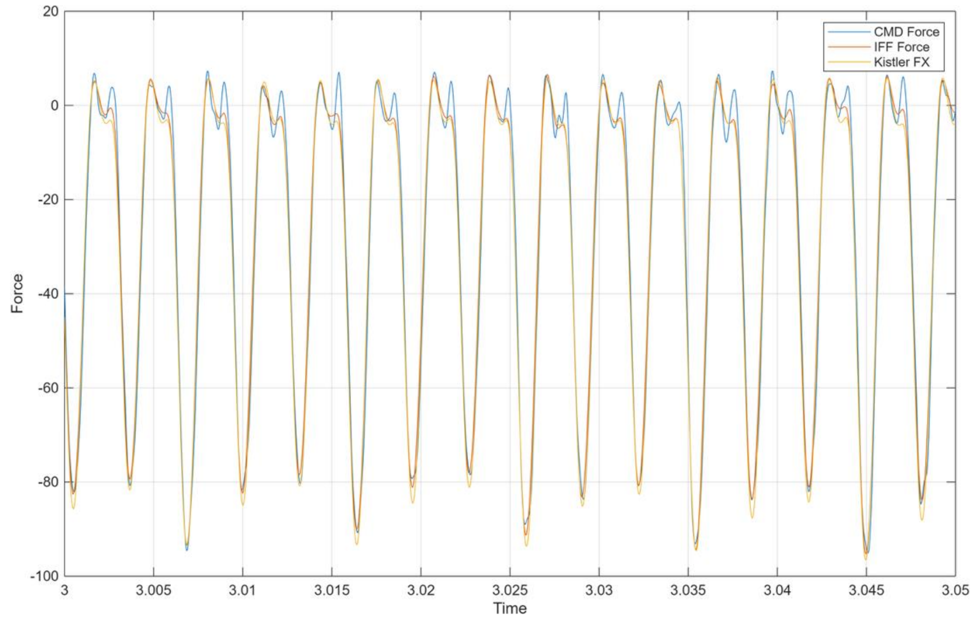

Figure A.1 6061 x-direction milling force comparison 0.150 mm/tooth

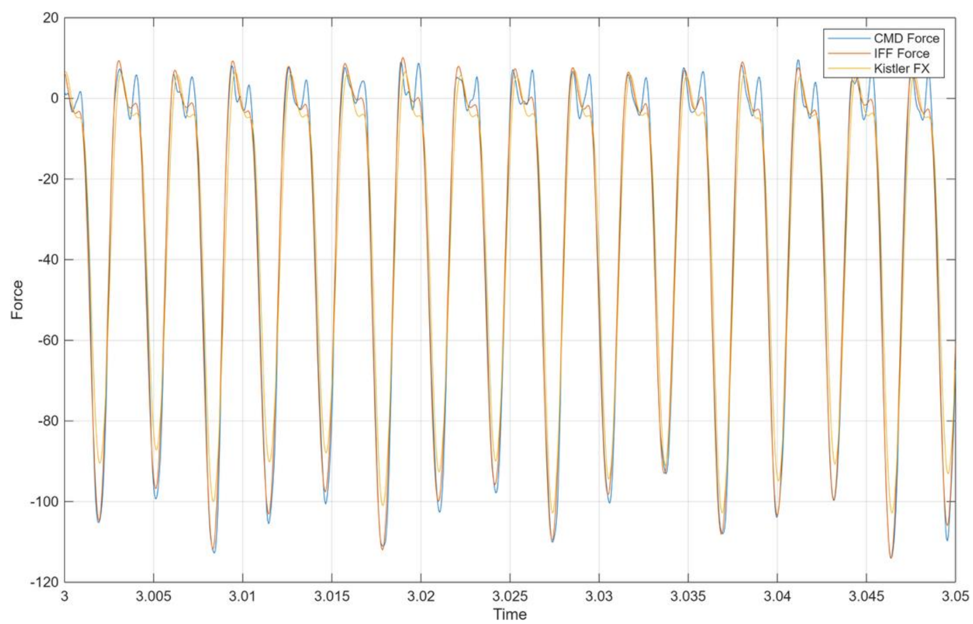

Figure A.2 6061 x-direction milling force comparison 0.175 mm/tooth (3-flute endmill)

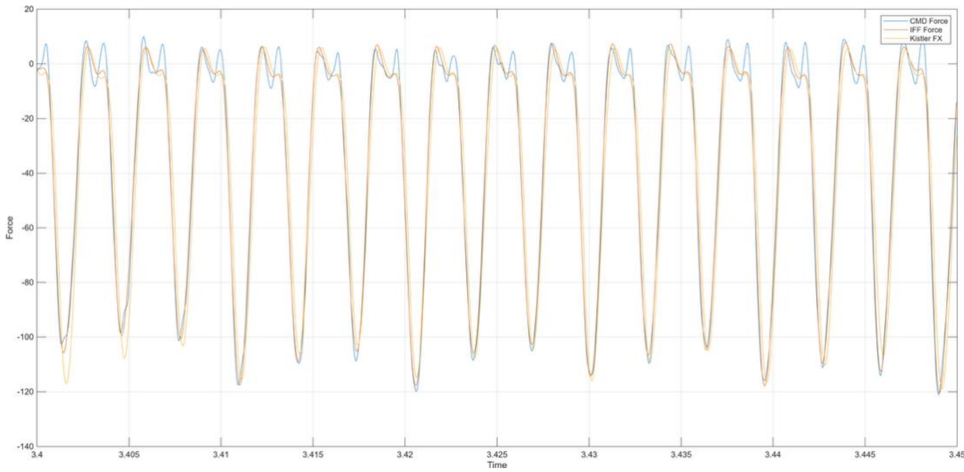

Figure A.3 6061 x-direction milling force comparison 0.200 mm/tooth (3-flute endmill)

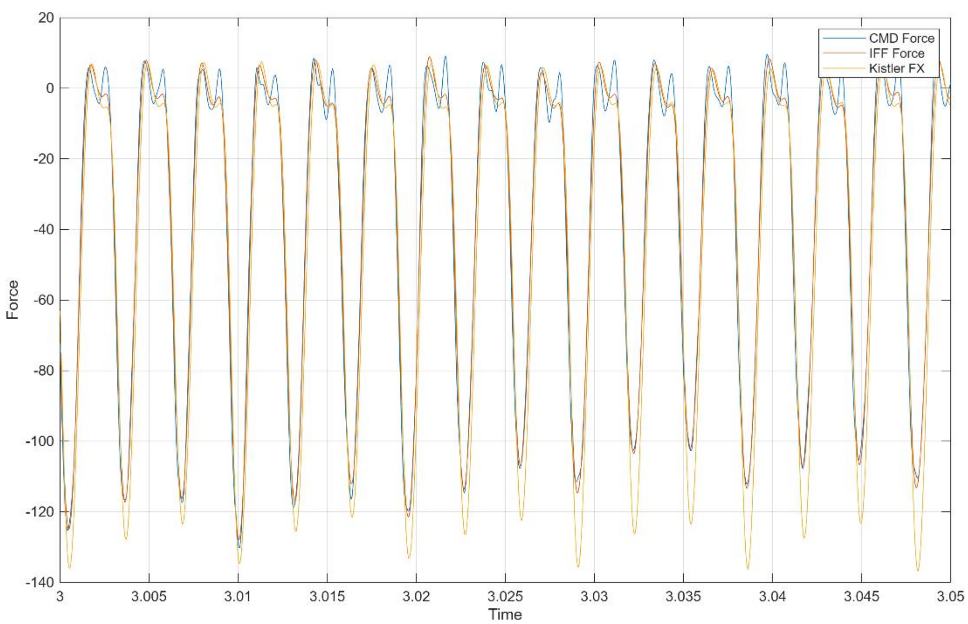

Figure A.4 6061 x-direction milling force comparison 0.225 mm/tooth (3-flute endmill)

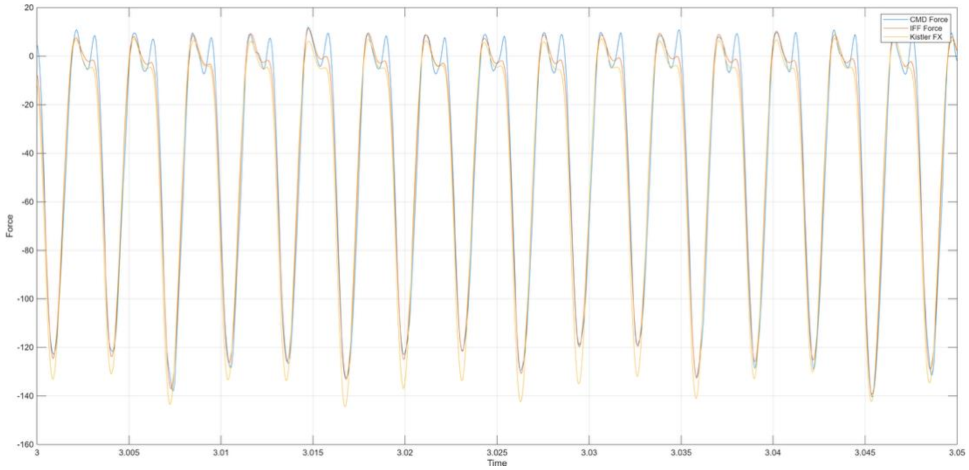

Figure A.5 6061 x-direction milling force comparison 0.250 mm/tooth (3-flute endmill)

Table A.1 6061-T6 measurement comparison for three fluted endmill

	FPT	TSA	SD	Kistler	TSA/Kister	TSA/SD
	0.150	95.260	95.070	96.110	99%	100%
	0.175	114.086	114.050	102.840	111%	100%
	0.200	120.480	121.080	118.960	101%	100%
	0.225	127.970	130.210	136.710	94%	98%
6061-T6 3 Flute	0.250	139.470	140.440	144.420	97%	99%

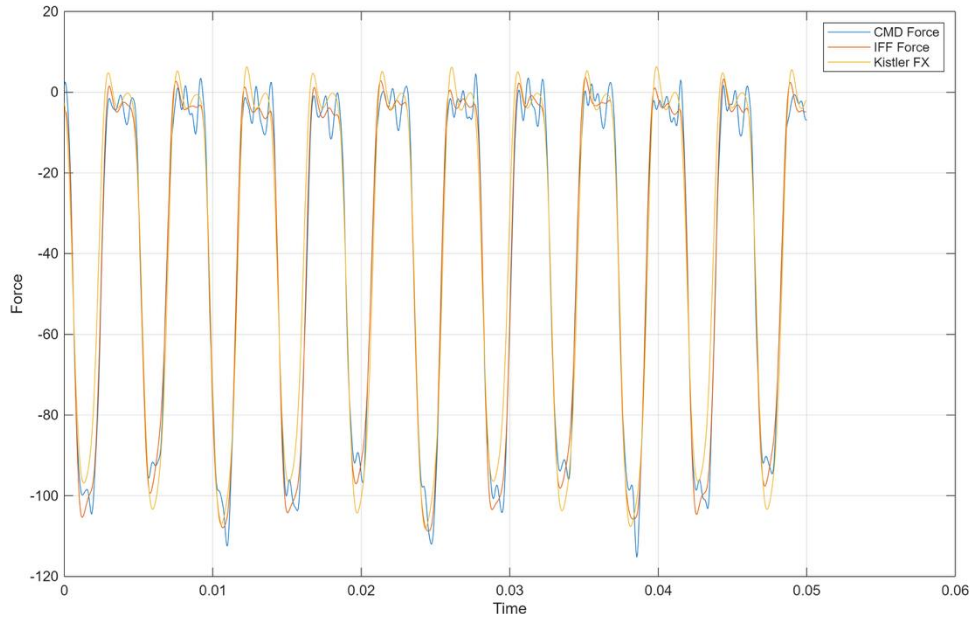

Figure A.6 7075 x-direction milling force comparison 0.150 mm/tooth (3-flute endmill)

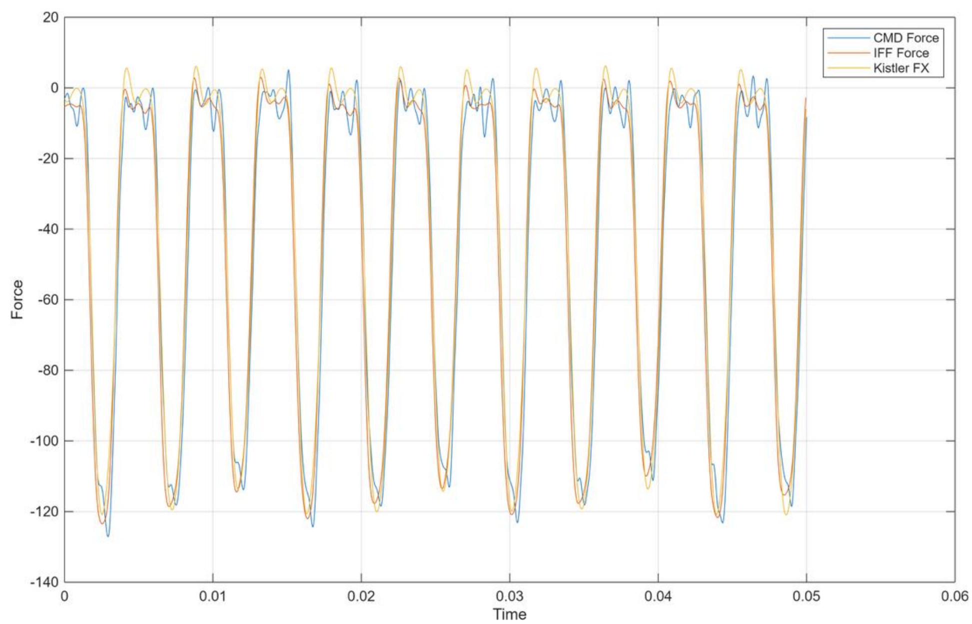

Figure A.7 7075 x-direction milling force comparison 0.175 mm/tooth (3-flute endmill)

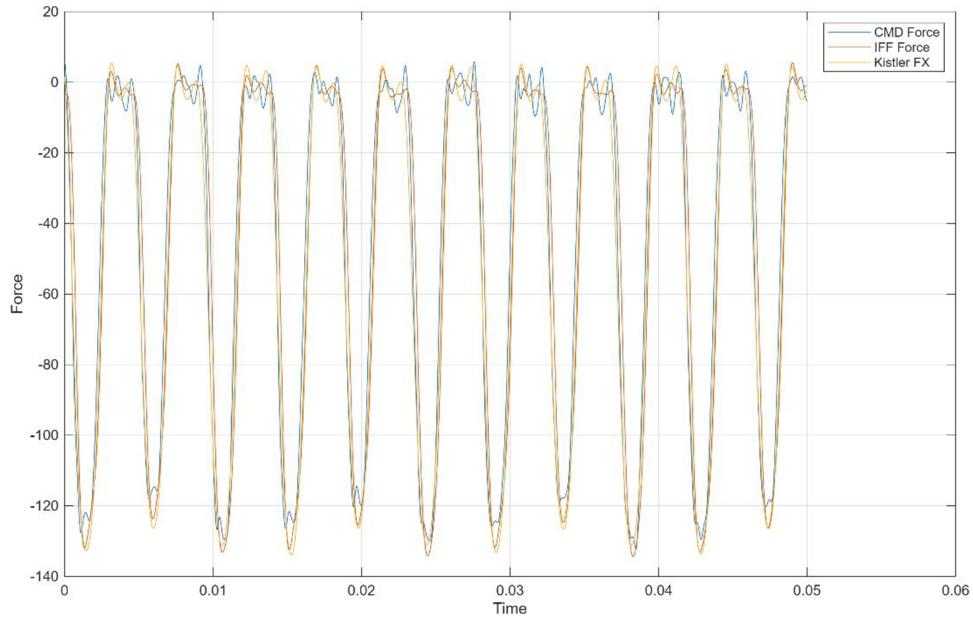

Figure A.8 7075 x-direction milling force comparison 0.200 mm/tooth (3-flute endmill)

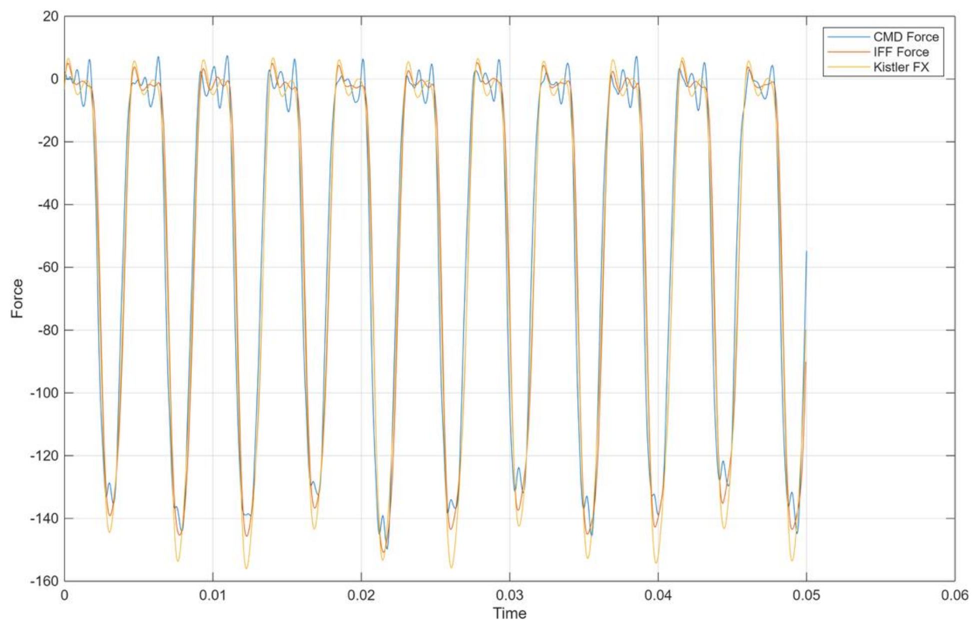

Figure A.9 7075 x-direction milling force comparison 0.225 mm/tooth (3-flute endmill)

Table A.2 1018 measurement comparison for three fluted endmill

	FPT	TSA	SD	Kistler	TSA/Kister	TSA/SD
	0.150	108.790	115.220	108.120	101%	94%
	0.175	123.460	127.110	120.970	102%	97%
	0.200	134.390	132.270	133.900	100%	102%
	0.225	150.780	149.770	156.060	97%	101%
7075 3 Flute	0.250	XXX	XXX	XXX	#VALUE!	#VALUE!

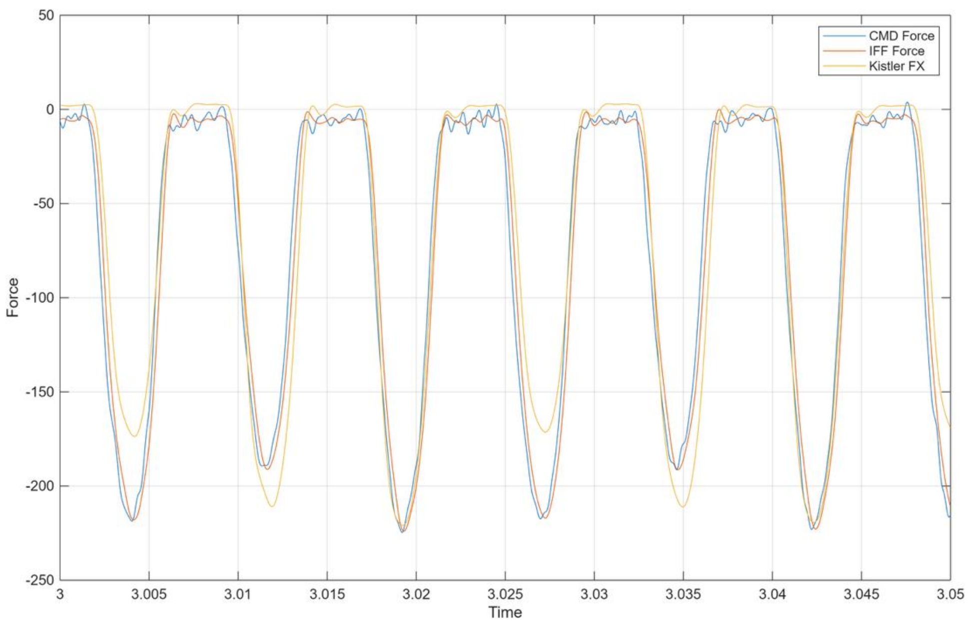

Figure A.10 1018 x-direction milling force comparison 0.150 mm/tooth (3-flute endmill)

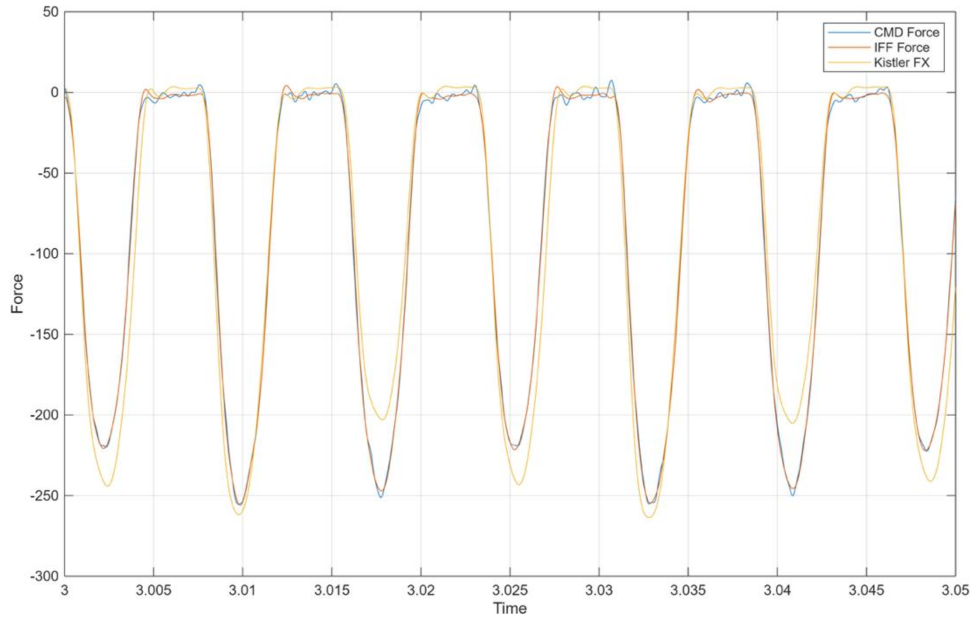

Figure A.11 1018 x-direction milling force comparison 0.175 mm/tooth (3-flute endmill)

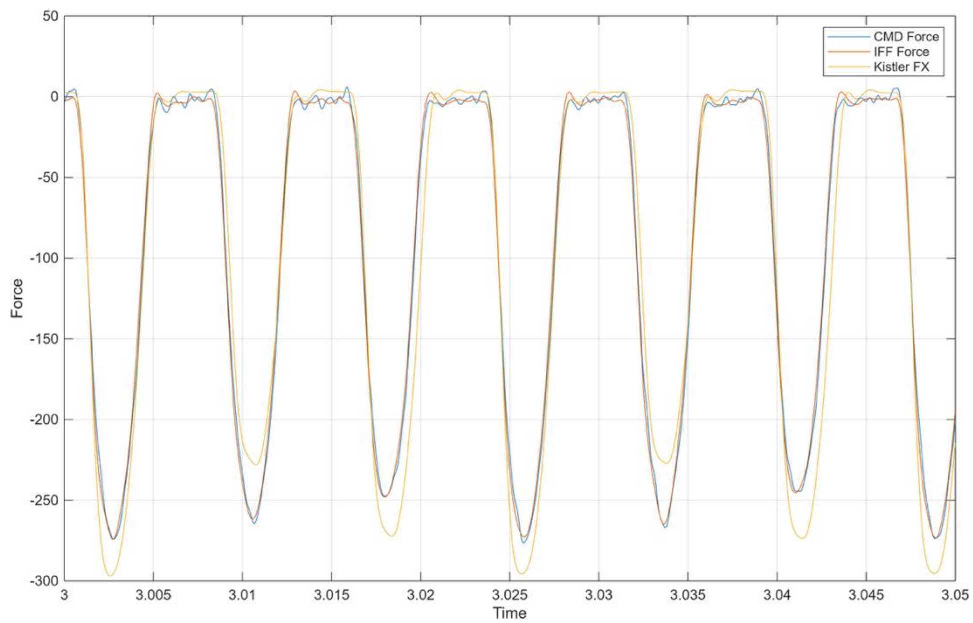

Figure A.12 1018 x-direction milling force comparison 0.200 mm/tooth (3-flute endmill)

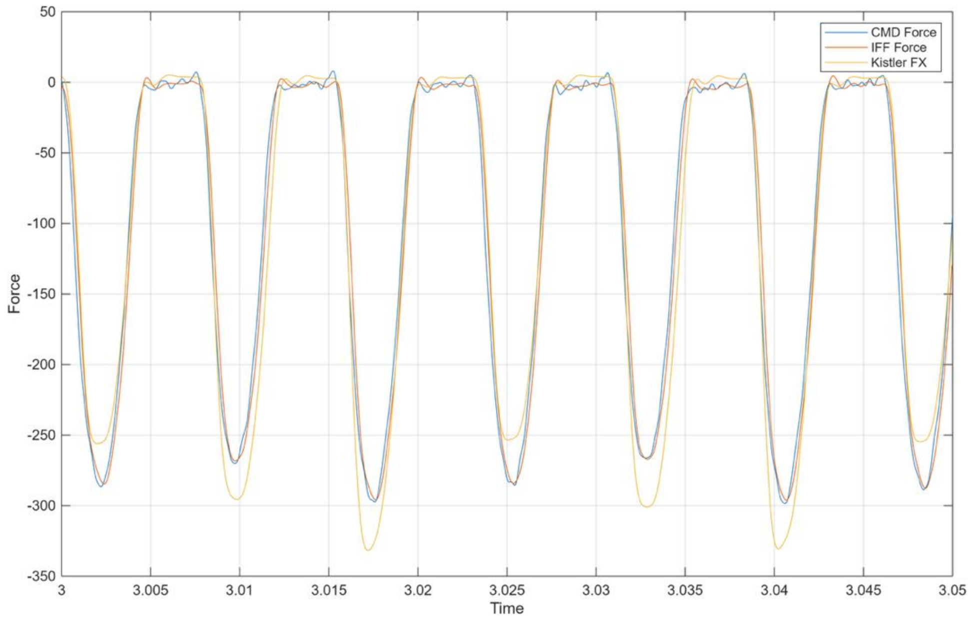

Figure A.13 1018 x-direction milling force comparison 0.225 mm/tooth (3-flute endmill)

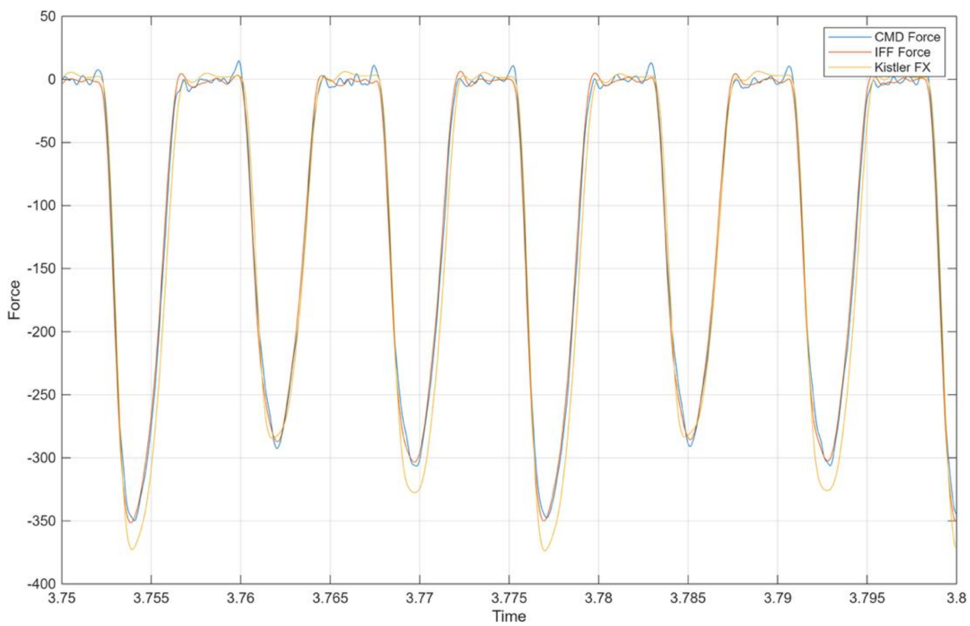

Figure A.14 1018 x-direction milling force comparison 0.250 mm/tooth (3-flute endmill)

Table A.3 1018 measurement comparison for three fluted endmill

	FPT	TSA	SD	Kistler	TSA/Kister	TSA/SD
	0.150	224.660	223.990	220.870	102%	100%
	0.175	255.280	256.070	263.700	97%	100%
	0.200	276.340	274.300	296.870	93%	101%
	0.225	298.417	296.050	331.800	90%	101%
1018 3 Flute	0.250	349.900	351.440	373.580	94%	100%

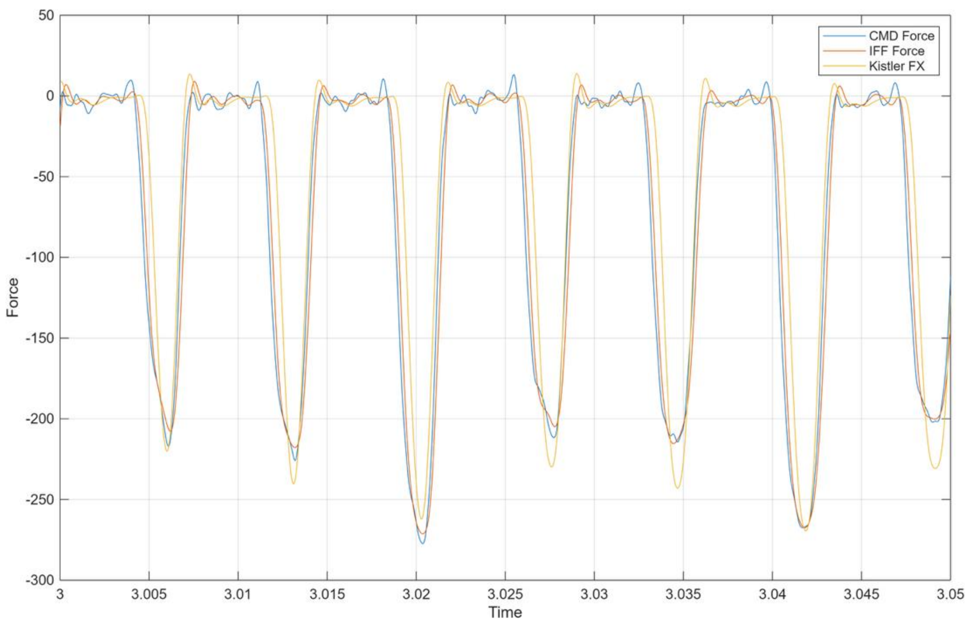

Figure A.15 4140 x-direction milling force comparison 0.150 mm/tooth (3-flute endmill)

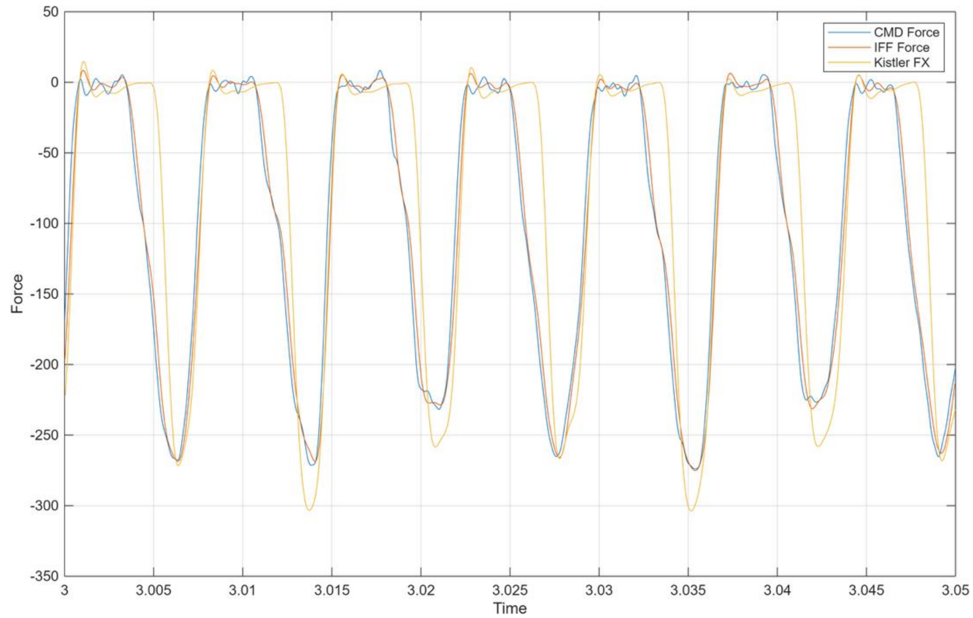

Figure A.16 4140 x-direction milling force comparison 0.175 mm/tooth (3-flute endmill)

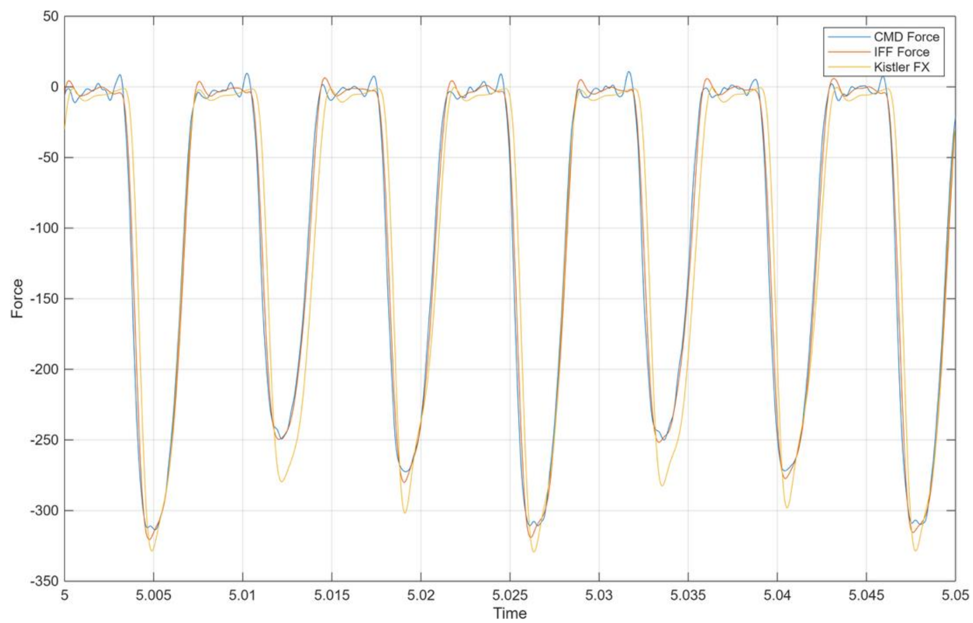

Figure A.17 4140 x-direction milling force comparison 0.200 mm/tooth (3-flute endmill)

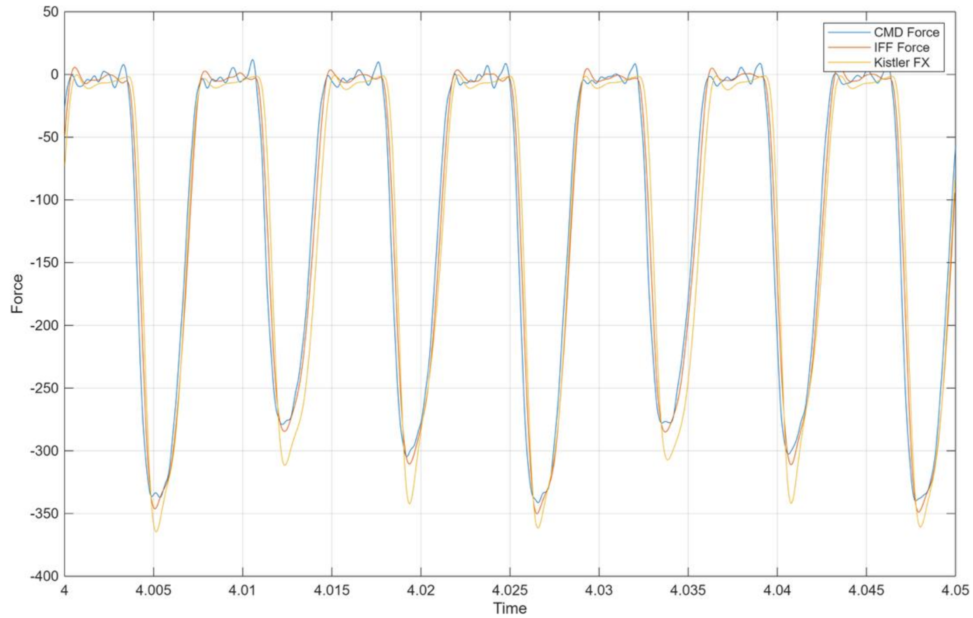

Figure A.18 4140 x-direction milling force comparison 0.225 mm/tooth (3-flute endmill)

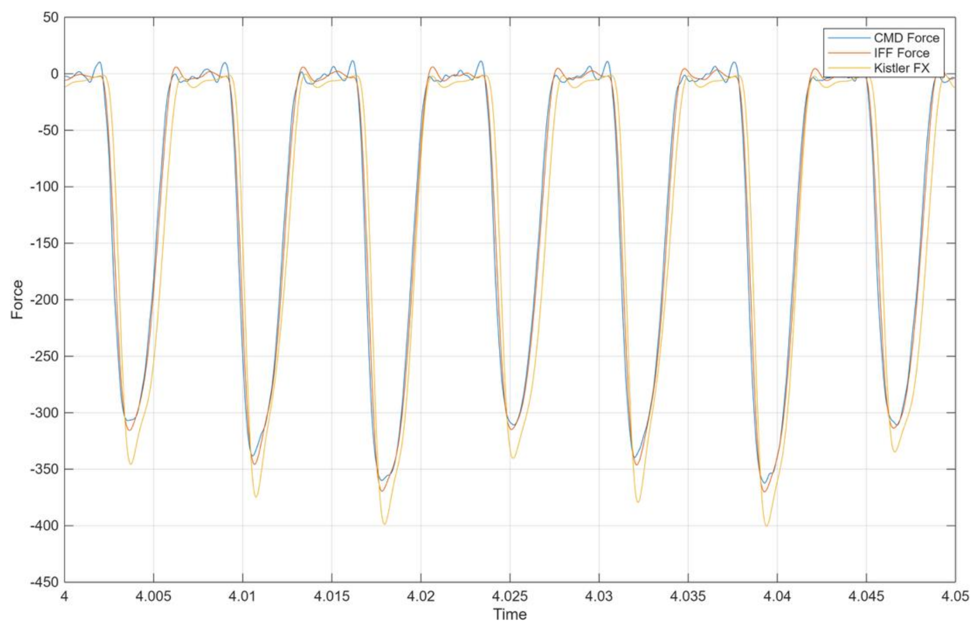

Figure A.19 4140 x-direction milling force comparison 0.250 mm/tooth (3-flute endmill)

Table A.4 4140 measurement comparison for three fluted endmill

	FPT	TSA	SD	Kistler	TSA/Kister	TSA/SD
	0.150	271.270	277.350	269.390	101%	98%
	0.175	275.090	273.980	303.680	91%	100%
	0.200	320.550	313.640	329.360	97%	102%
	0.225	350.260	341.330	364.530	96%	103%
4140 3 Flute	0.250	369.990	362.240	400.470	92%	102%

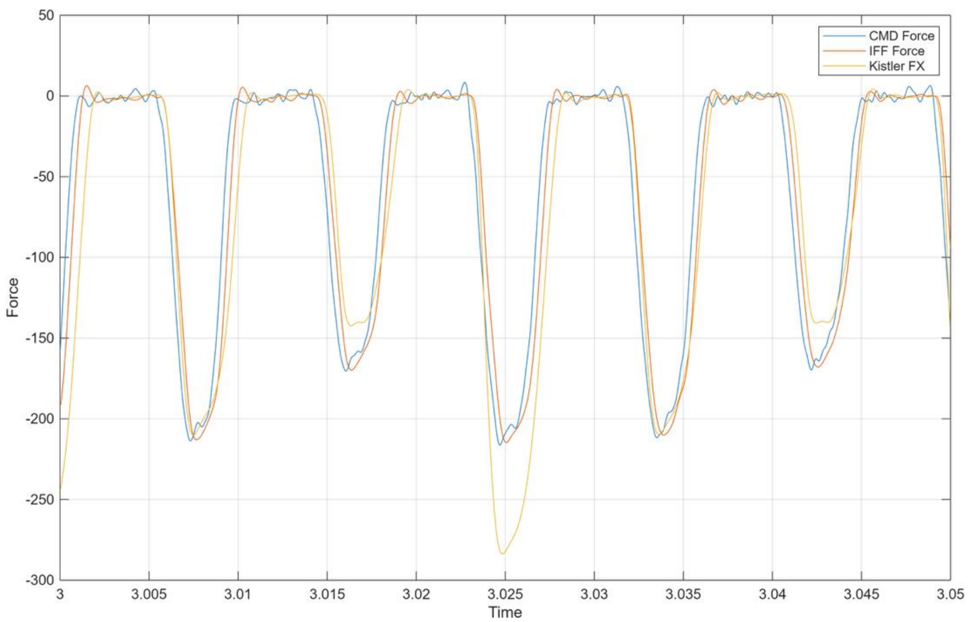

Figure A.20 303 x-direction milling force comparison 0.150 mm/tooth (3-flute endmill)

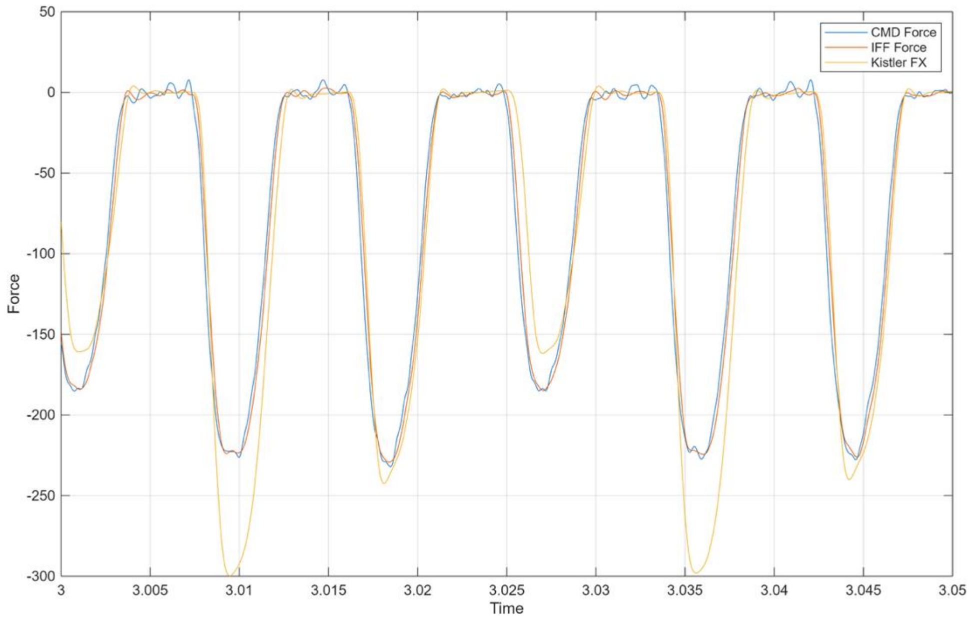

Figure A.21 303 x-direction milling force comparison 0.175 mm/tooth (3-flute endmill)

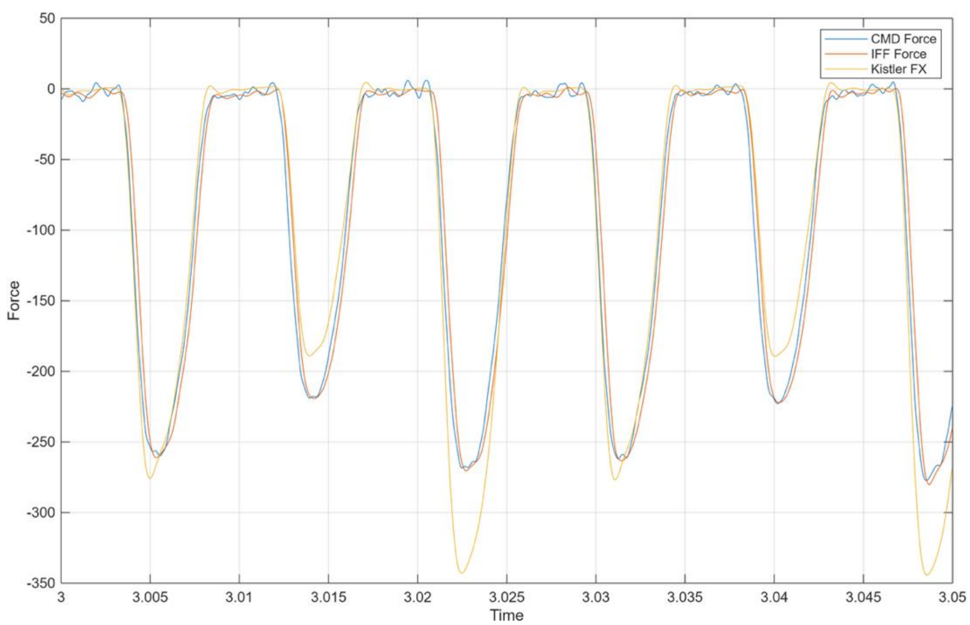

Figure A.22 303 x-direction milling force comparison 0.200 mm/tooth (3-flute endmill)

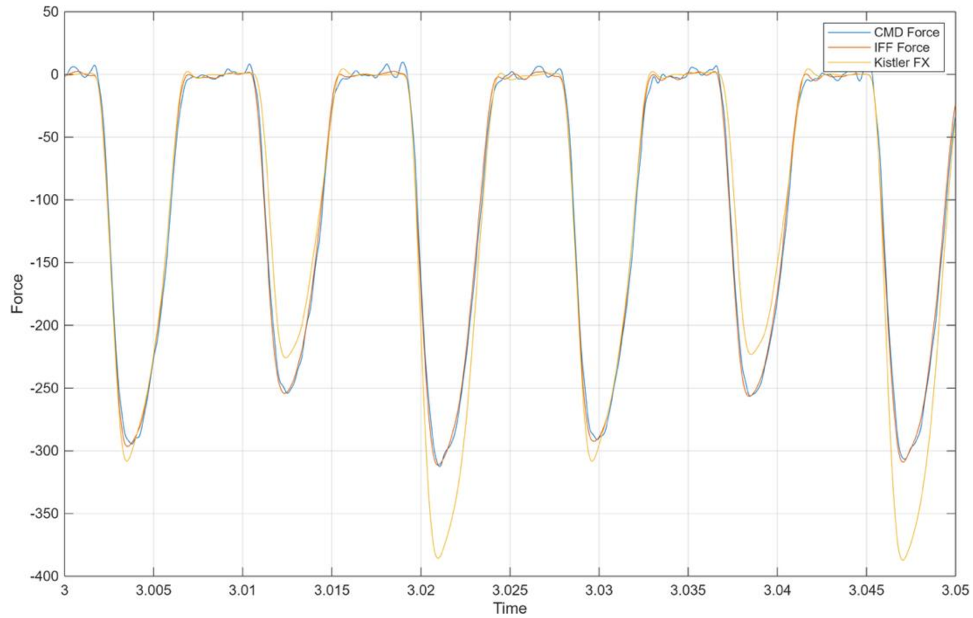

Figure A.23 303 x-direction milling force comparison 0.225 mm/tooth (3-flute endmill)

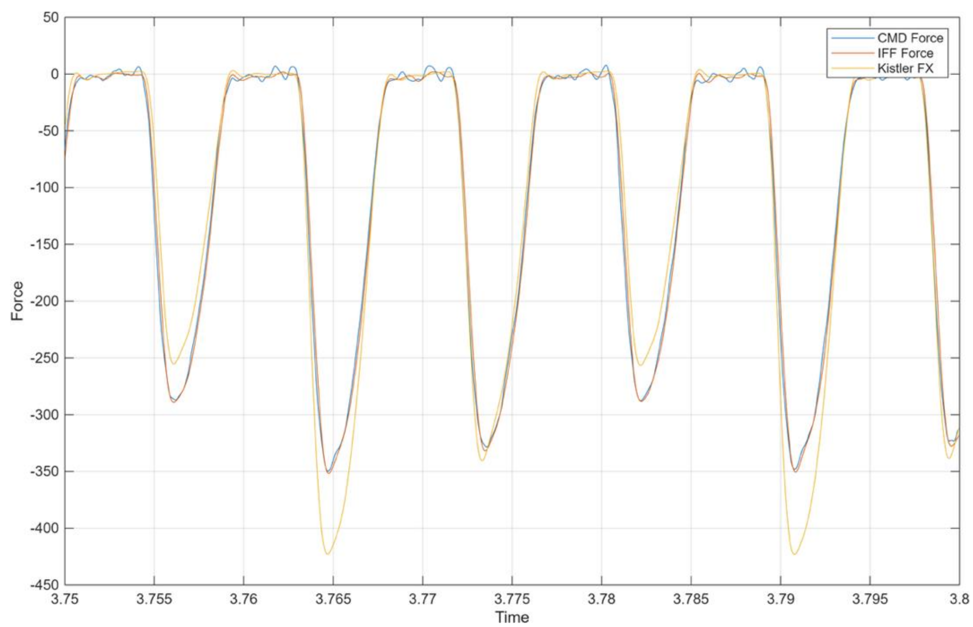

Figure A.24 303 x-direction milling force comparison 0.250 mm/tooth (3-flute endmill)

Table A.5 303 measurement comparison for three fluted endmill

	FPT	TSA	SD	Kistler	TSA/Kister	TSA/SD
	0.150	216.360	214.820	283.770	76%	101%
	0.175	232.060	229.300	299.800	77%	101%
	0.200	277.260	280.200	344.340	81%	99%
	0.225	312.540	311.340	387.220	81%	100%
303 3 Flute	0.250	349.860	351.800	423.070	83%	99%

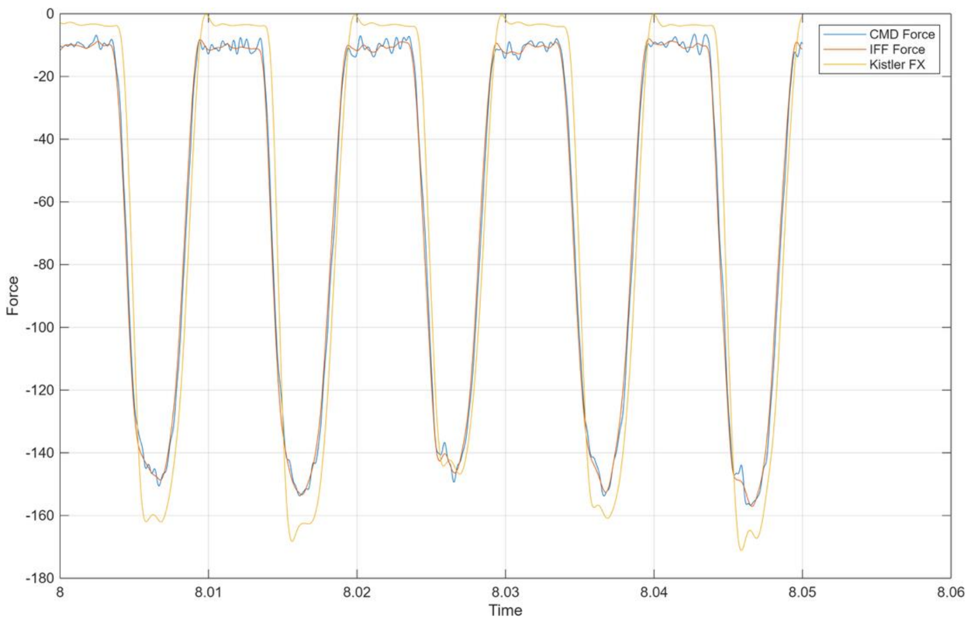

Figure A.25 Ti 6Al-4V x-direction milling force comparison 0.150 mm/tooth (3-flute endmill)

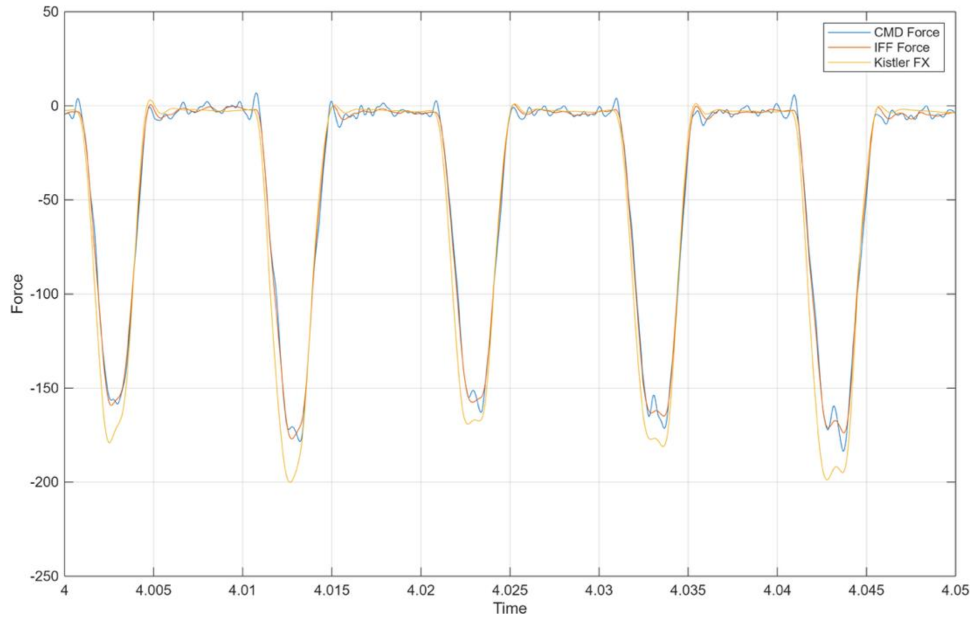

Figure A.26 Ti 6Al-4V x-direction milling force comparison 0.175 mm/tooth (3-flute endmill)

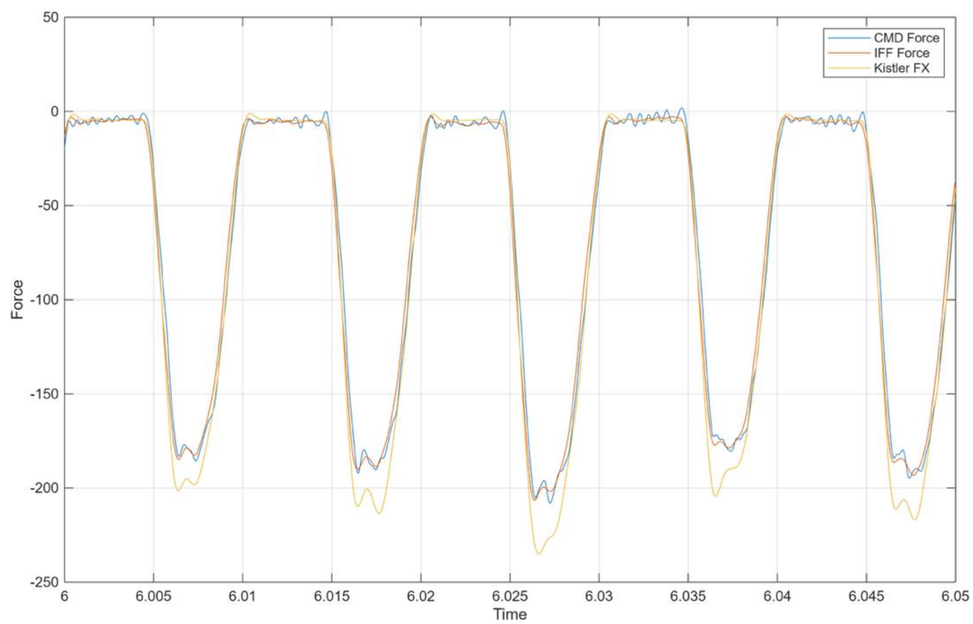

Figure A.27 Ti 6Al-4V x-direction milling force comparison 0.200 mm/tooth (3-flute endmill)

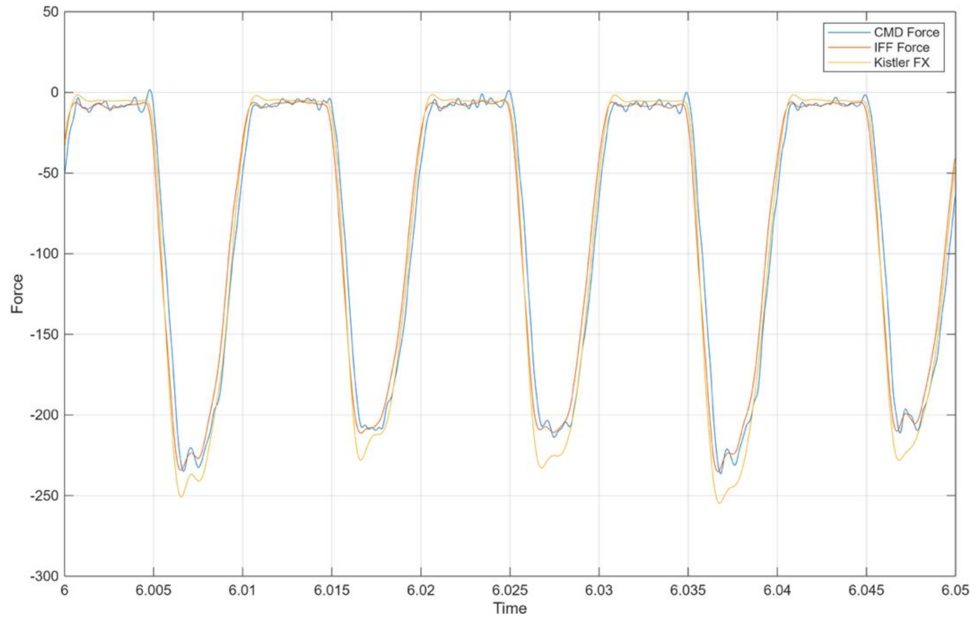

Figure A.28 Ti 6Al-4V x-direction milling force comparison 0.225 mm/tooth (3-flute endmill)

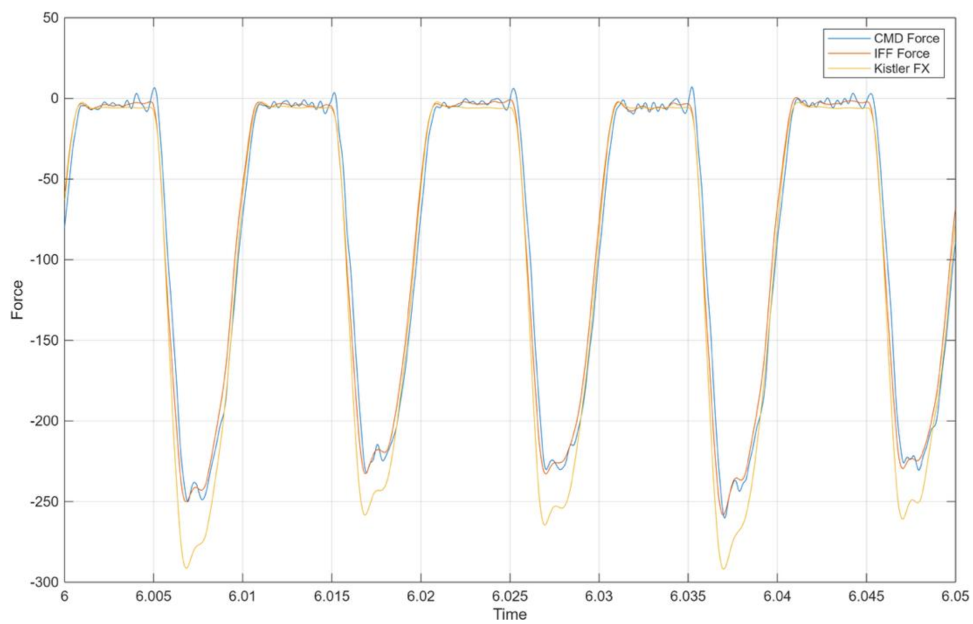

Figure A.29 Ti 6Al-4V x-direction milling force comparison 0.250 mm/tooth (3-flute endmill)

Table A.6 Ti 6Al-4V measurement comparison for three fluted endmill

	FPT	TSA	SD	Kistler	TSA/Kister	TSA/SD
	0.150	156.780	157.110	171.143	92%	100%
	0.175	176.980	183.650	200.090	88%	96%
	0.200	206.570	208.110	234.970	88%	99%
	0.225	235.250	236.450	254.740	92%	99%
Ti 6Al-4V 3 Flute	0.250	258.280	260.250	291.900	88%	99%

Four flute x-direction endmill force comparison

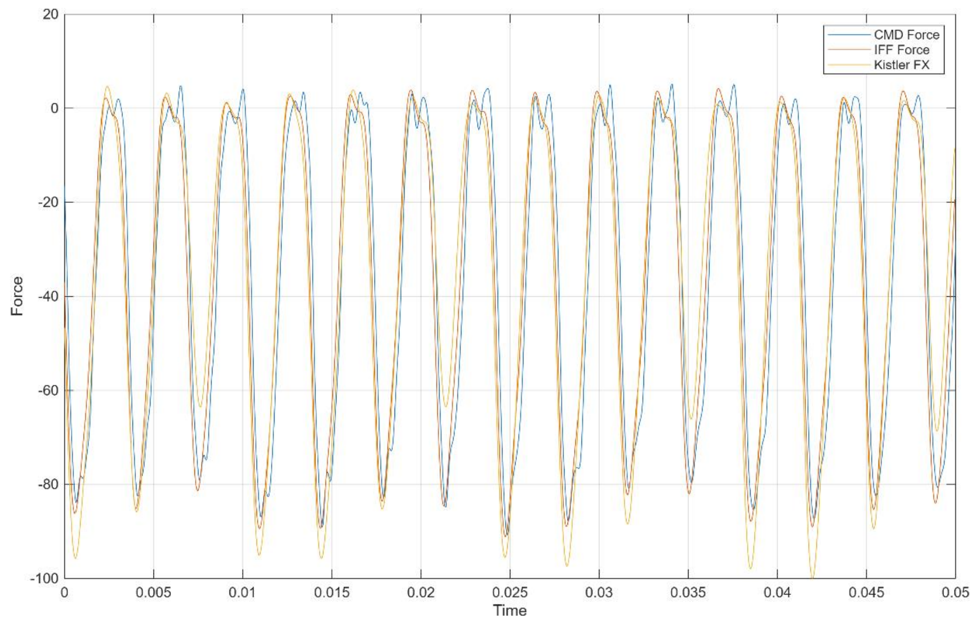

Figure A.30 6061 x-direction milling force comparison 0.150 mm/tooth (4-flute endmill)

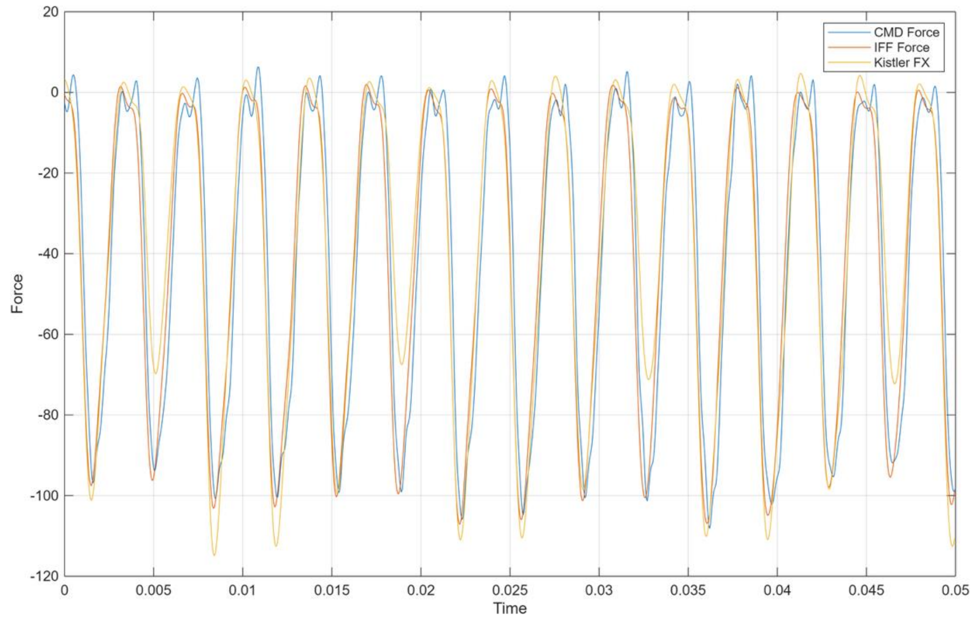

Figure A.31 6061 x-direction milling force comparison 0.175 mm/tooth (4-flute endmill)

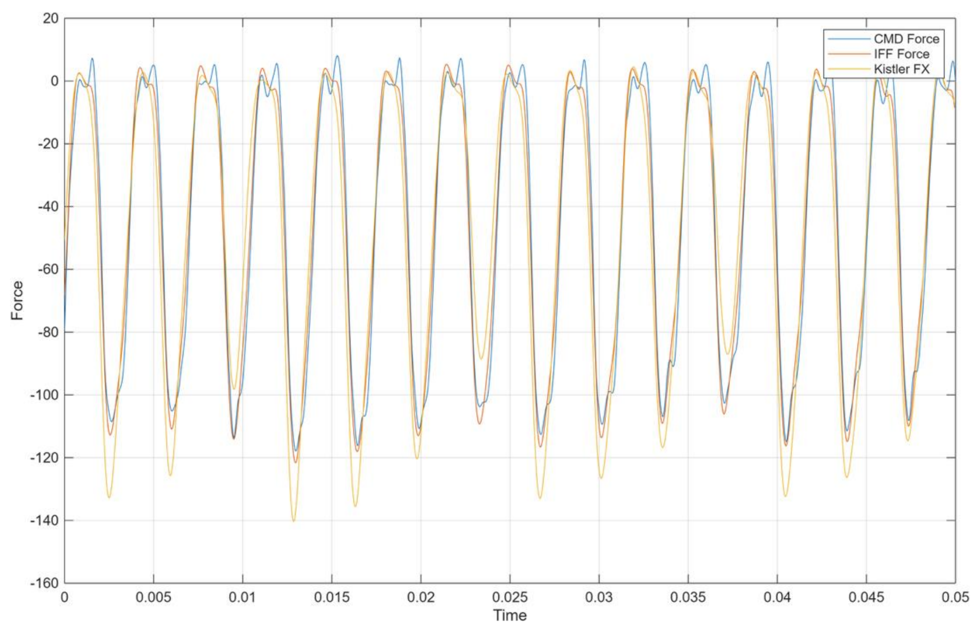

Figure A.32 6061 x-direction milling force comparison 0.200 mm/tooth (4-flute endmill)

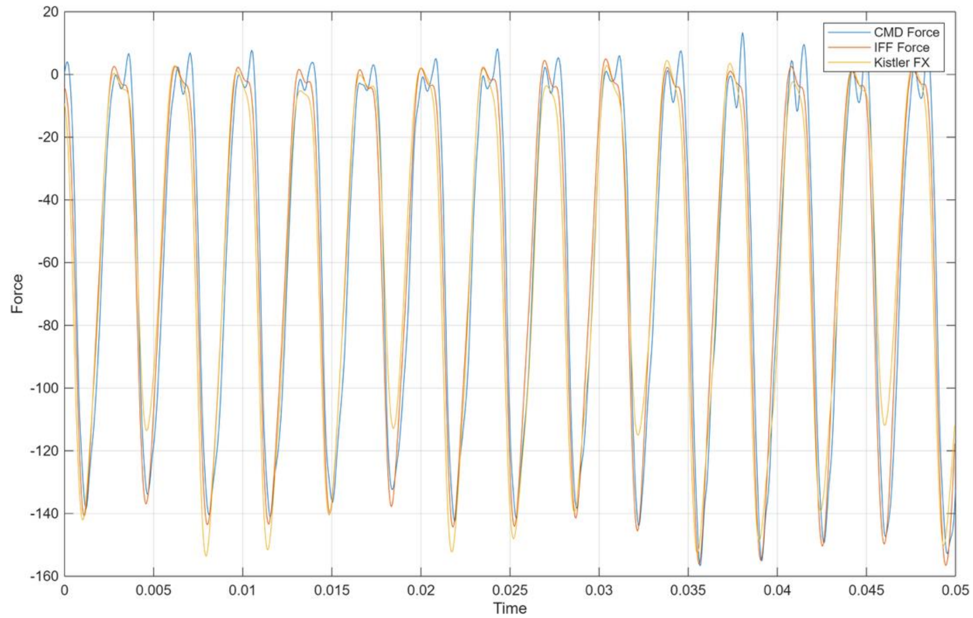

Figure A.33 6061 x-direction milling force comparison 0.225 mm/tooth (4-flute endmill)

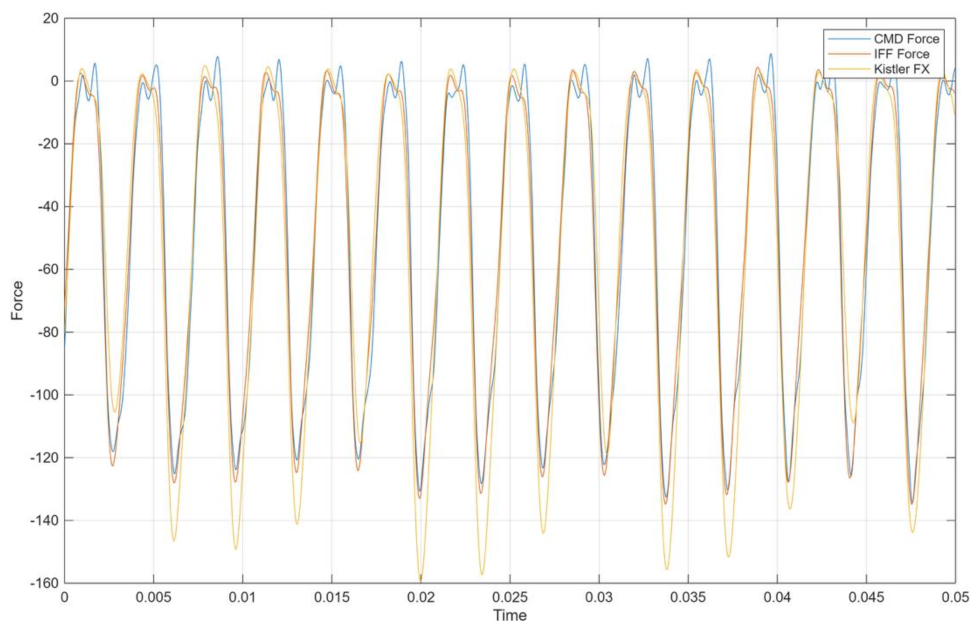

Figure A.34 6061 x-direction milling force comparison 0.250 mm/tooth (4-flute endmill)

Table A.7 6061measurement comparison for four fluted endmill

	FPT	TSA	SD	Kistler	TSA/Kister	TSA/SD
	0.150	87.560	89.640	96.720	91%	98%
	0.175	107.060	107.780	117.460	91%	99%
	0.200	117.360	120.400	135.520	87%	97%
	0.225	132.510	133.230	146.540	90%	99%
6061-T6 4 Flute	0.250	151.400	154.520	166.190	91%	98%

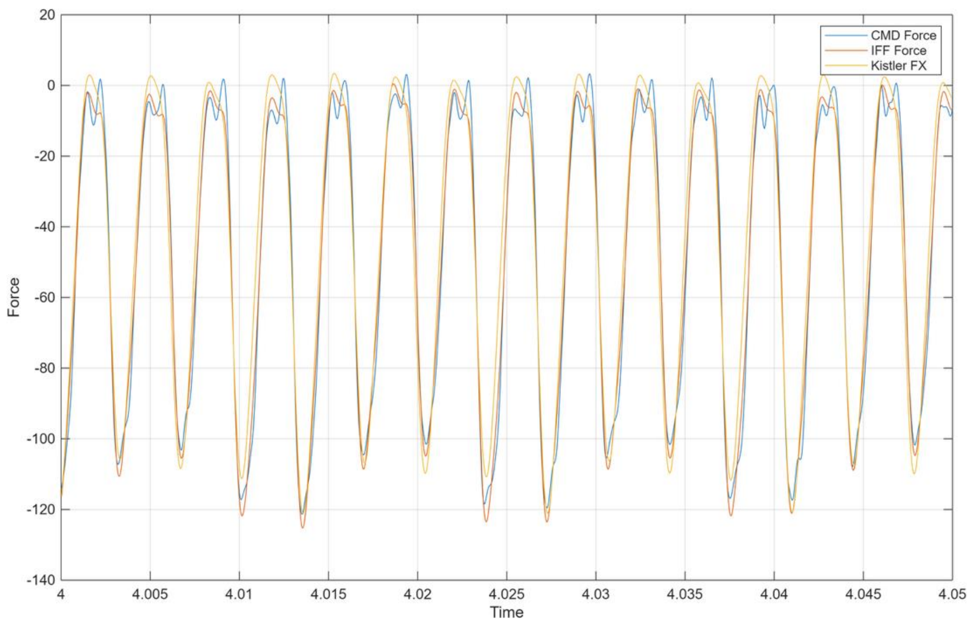

Figure A.35 7075 x-direction milling force comparison 0.150 mm/tooth (4-flute endmill)

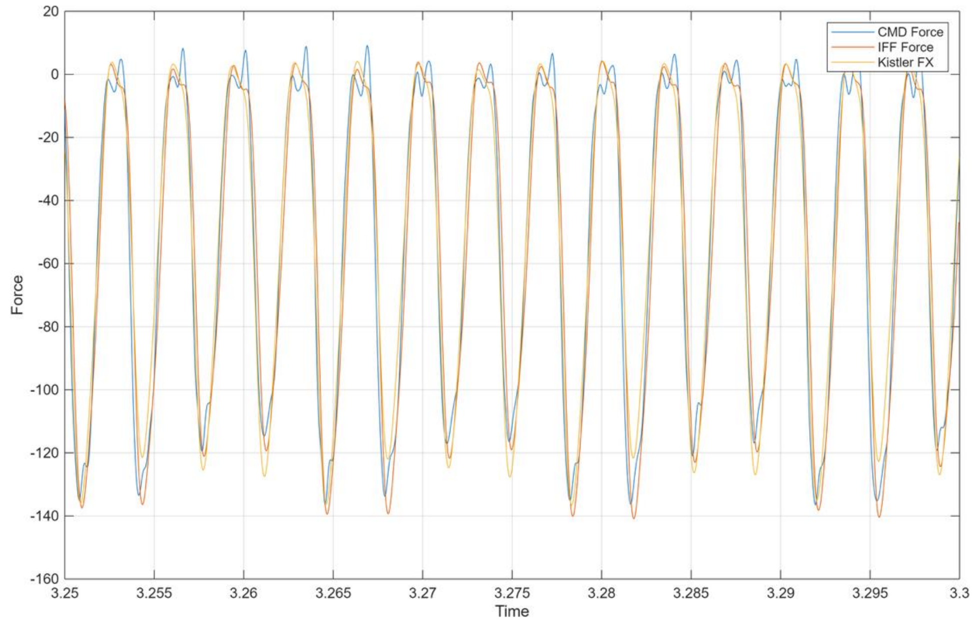

Figure A.36 7075 x-direction milling force comparison 0.175 mm/tooth (4-flute endmill)

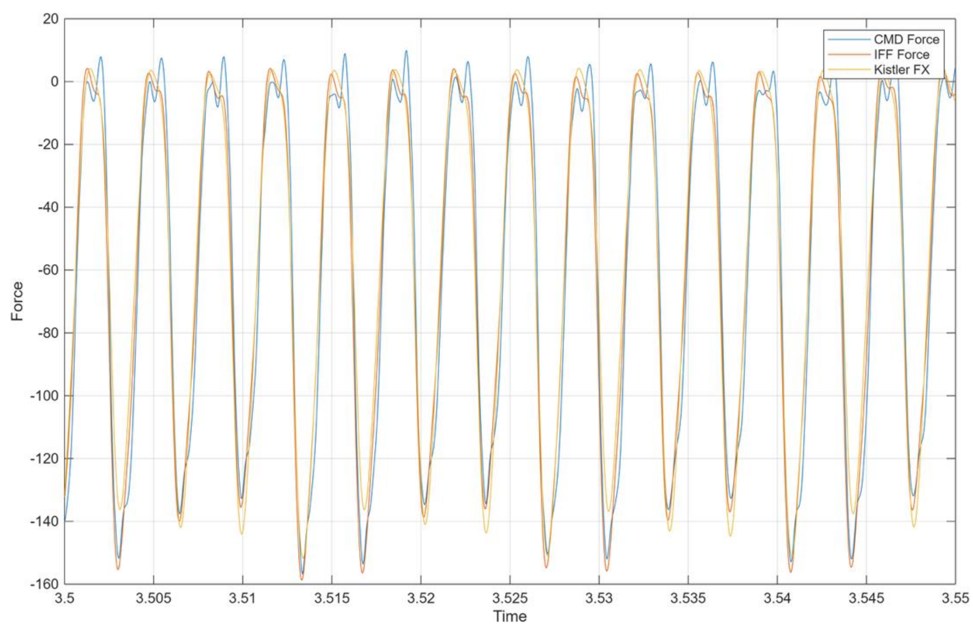

Figure A.37 7075 x-direction milling force comparison 0.200 mm/tooth (4-flute endmill)

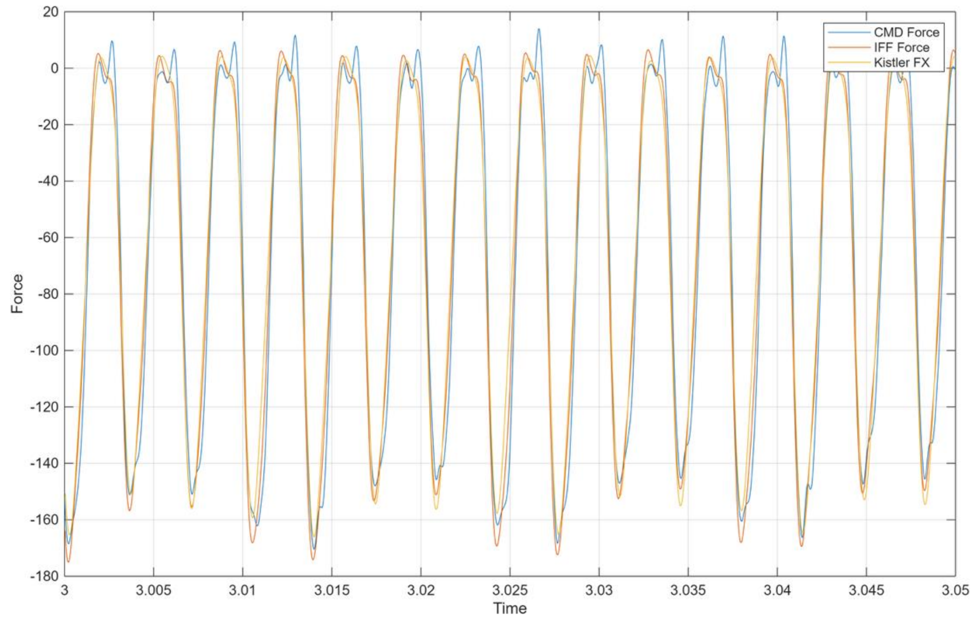

Figure A.38 7075 x-direction milling force comparison 0.225 mm/tooth (4-flute endmill)

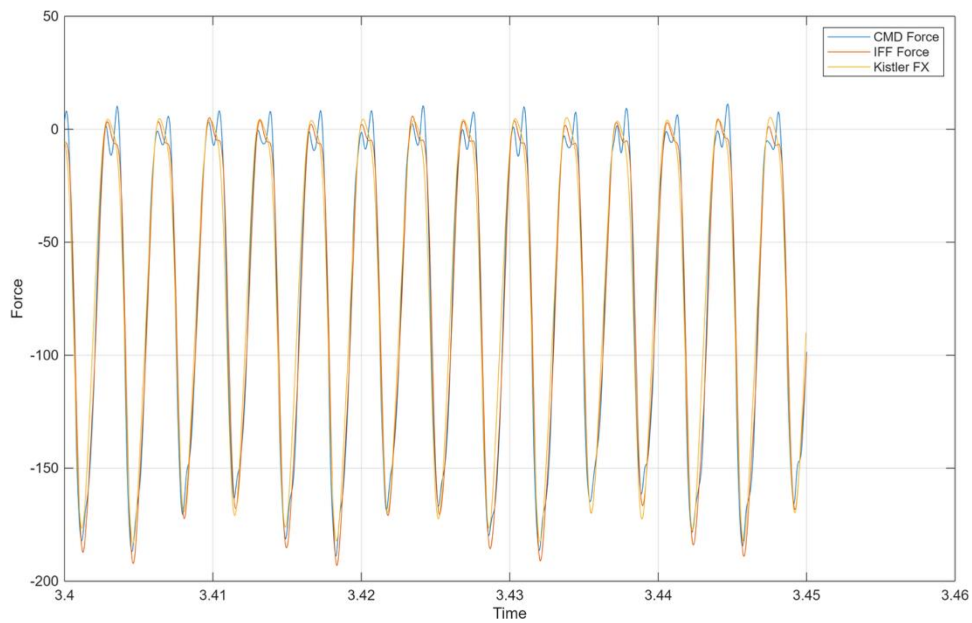

Figure A.39 7075 x-direction milling force comparison 0.250 mm/tooth (4-flute endmill)

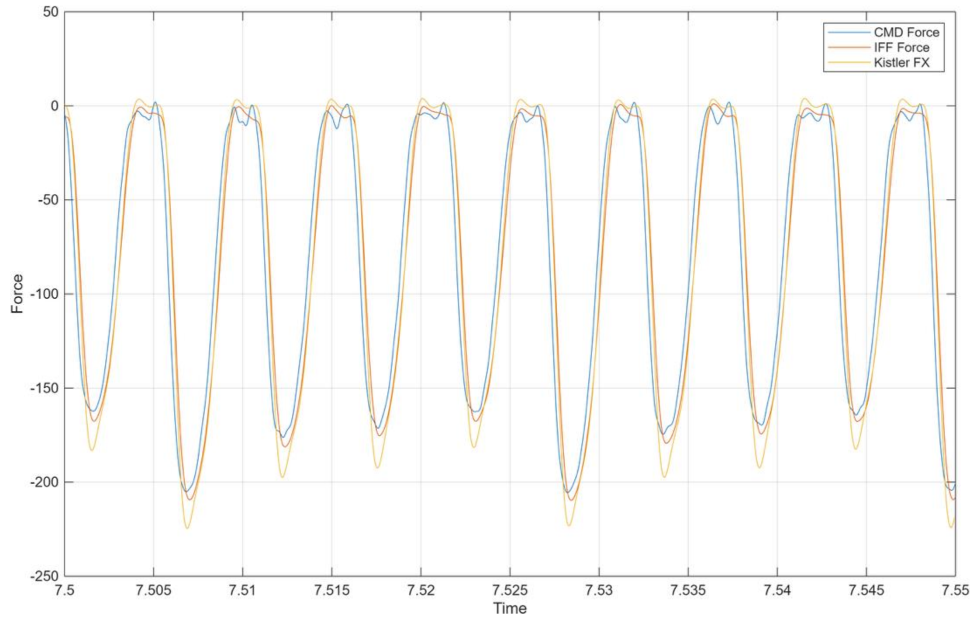

Figure A.40 1018 x-direction milling force comparison 0.150 mm/tooth (4-flute endmill)

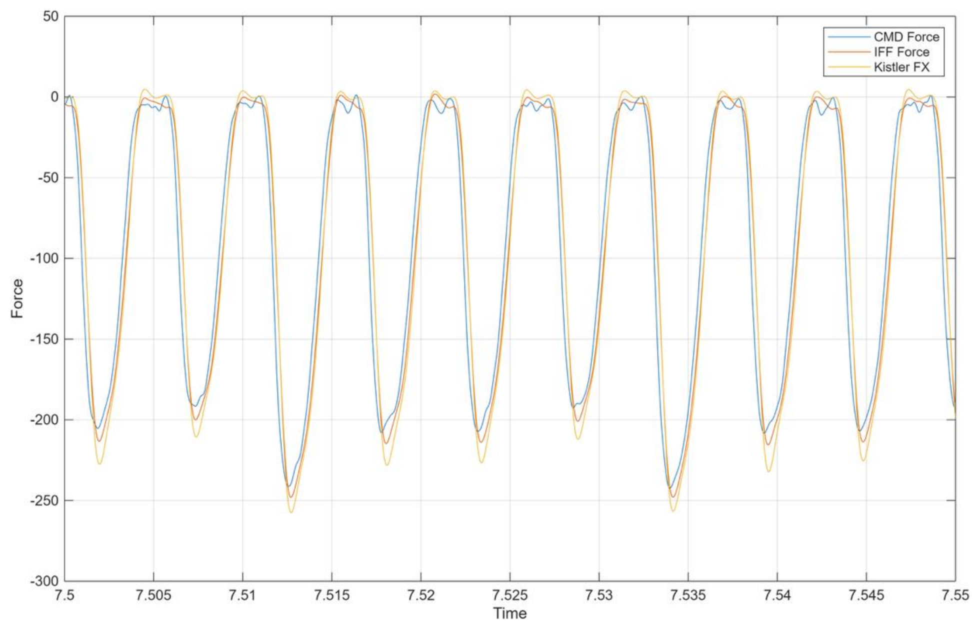

Figure A.41 1018 x-direction milling force comparison 0.175 mm/tooth (4-flute endmill)

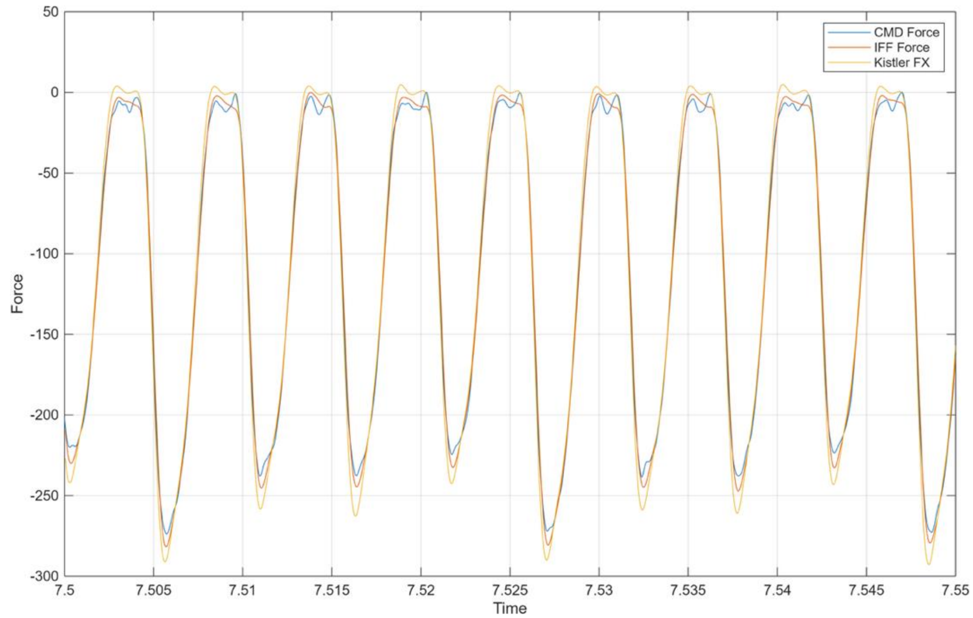

Figure A.42 1018 x-direction milling force comparison 0.200 mm/tooth (4-flute endmill)

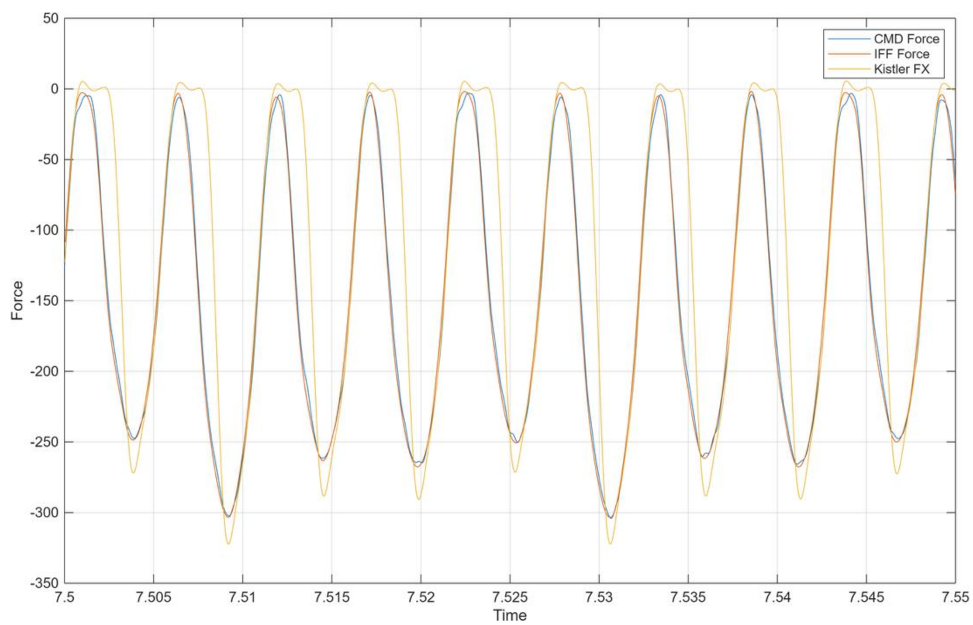

Figure A.43 1018 x-direction milling force comparison 0.225 mm/tooth (4-flute endmill)

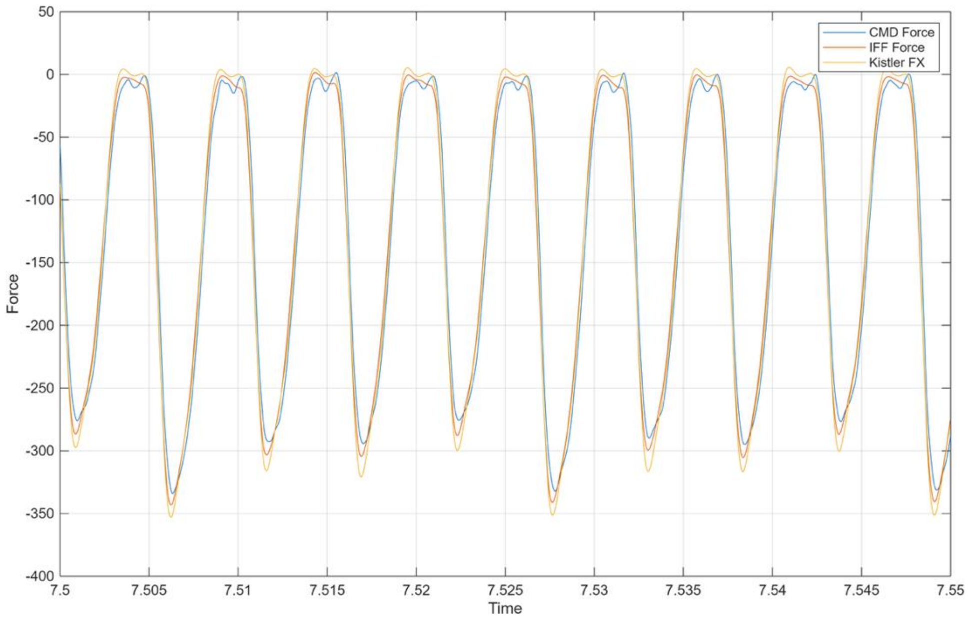

Figure A.44 1018 x-direction milling force comparison 0.250 mm/tooth (4-flute endmill)

Table A.8 1018 measurement comparison for four fluted endmill

	FPT	TSA	SD	Kistler	TSA/Kister	TSA/SD
	0.150	197.540	201.440	207.110	95%	98%
	0.175	231.320	237.150	266.030	87%	98%
	0.200	259.230	266.720	297.560	87%	97%
	0.225	290.110	296.550	333.190	87%	98%
1018 4 Flute	0.250	315.840	324.340	375.410	84%	97%

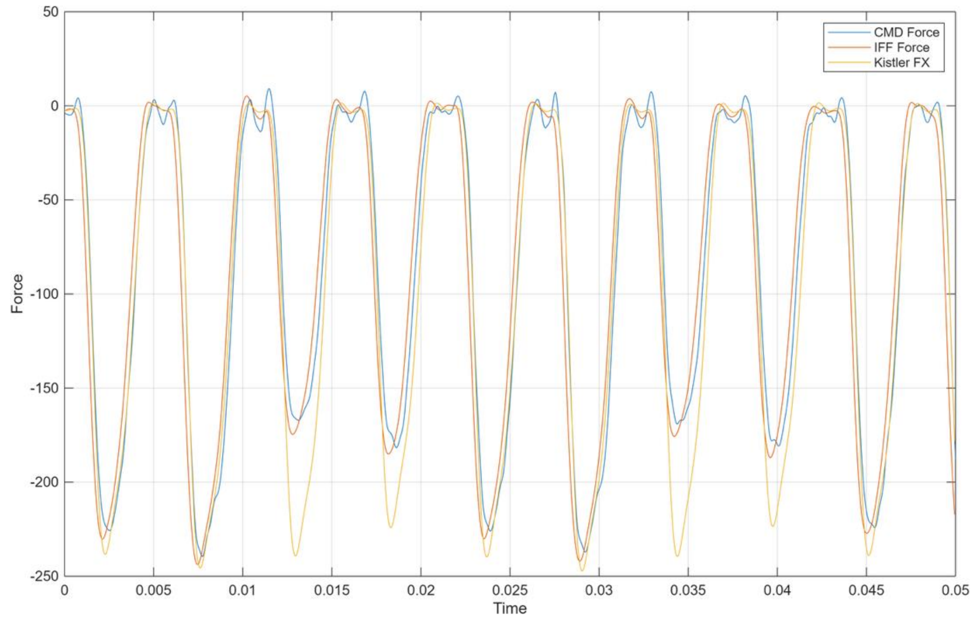

Figure A.45 4140 x-direction milling force comparison 0.150 mm/tooth (4-flute endmill)

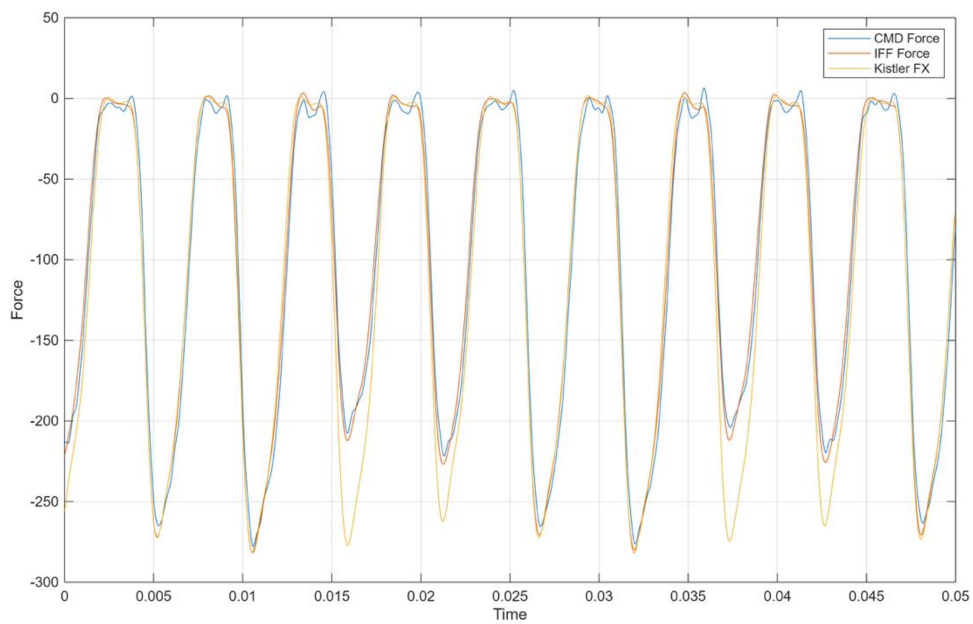

Figure A.46 4140 x-direction milling force comparison 0.175 mm/tooth (4-flute endmill)

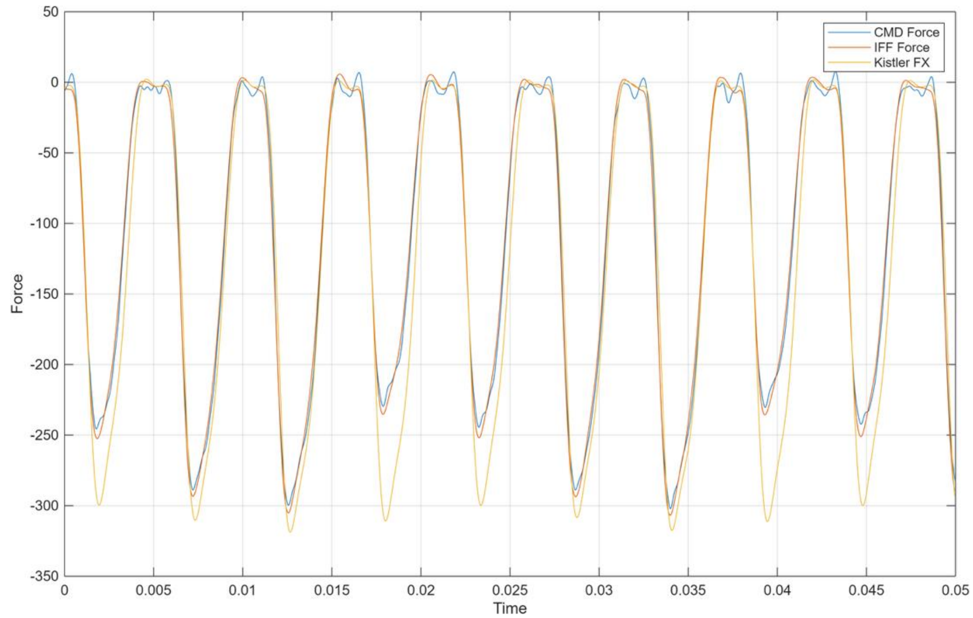

Figure A.47 4140 x-direction milling force comparison 0.200 mm/tooth (4-flute endmill)

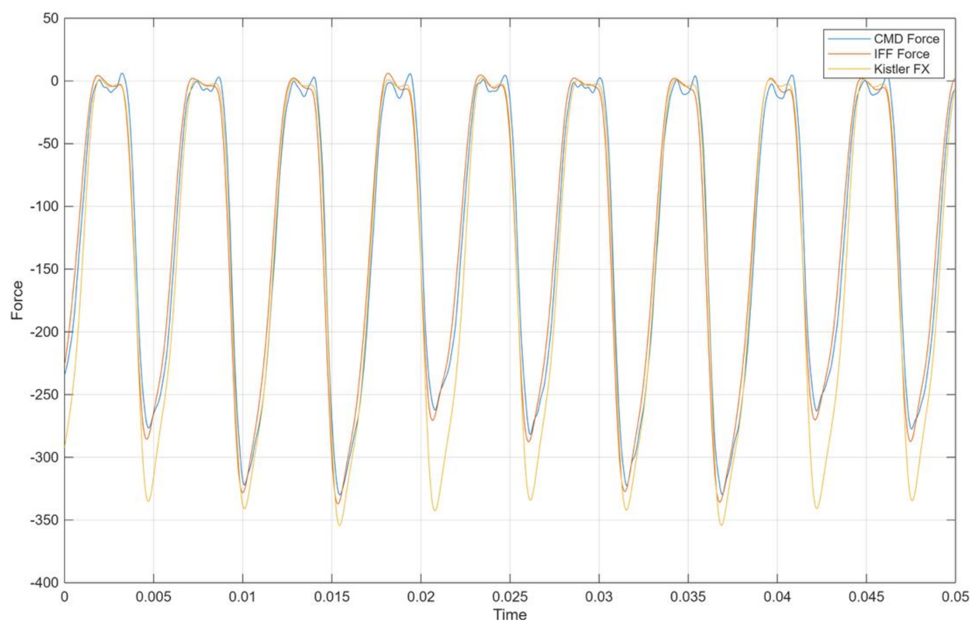

Figure A.48 4140 x-direction milling force comparison 0.225 mm/tooth (4-flute endmill)

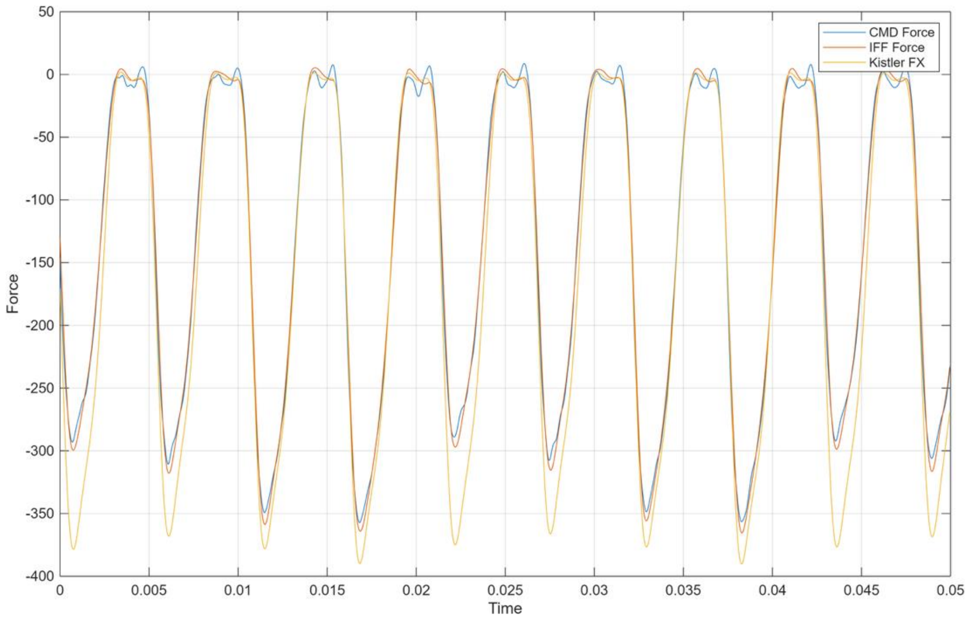

Figure A.49 4140 x-direction milling force comparison 0.250 mm/tooth (4-flute endmill)

Table A.9 4140 measurement comparison for four fluted endmill

	FPT	TSA	SD	Kistler	TSA/Kister	TSA/SD
	0.150	242.630	248.380	246.450	98%	98%
	0.175	276.210	280.820	281.620	98%	98%
	0.200	311.030	315.990	315.840	98%	98%
	0.225	341.490	347.880	351.990	97%	98%
4140 4 Flute	0.250	370.810	380.790	385.310	96%	97%

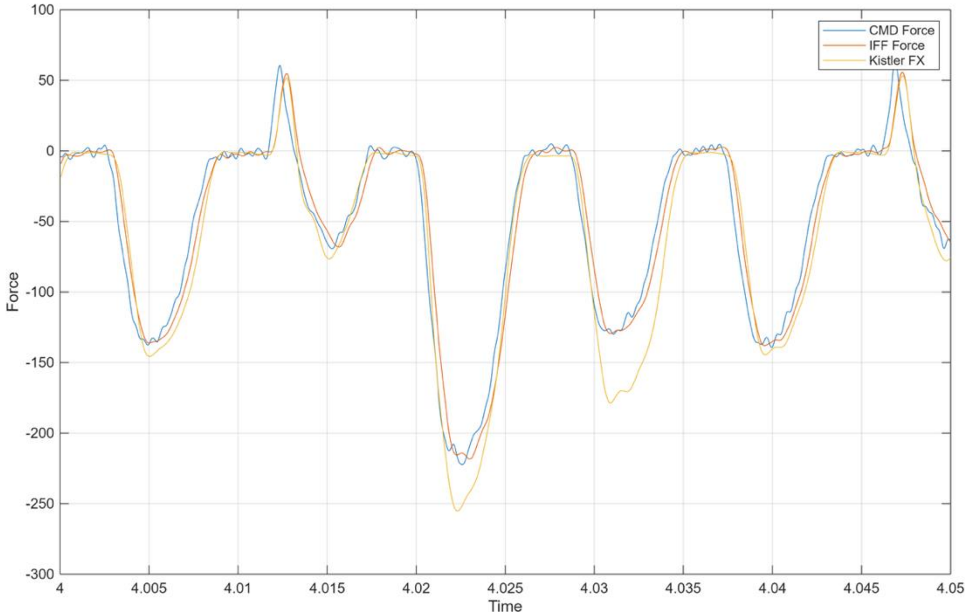

Figure A.50 Ti 6Al-4V x-direction milling force comparison 0.150 mm/tooth (4-flute endmill)

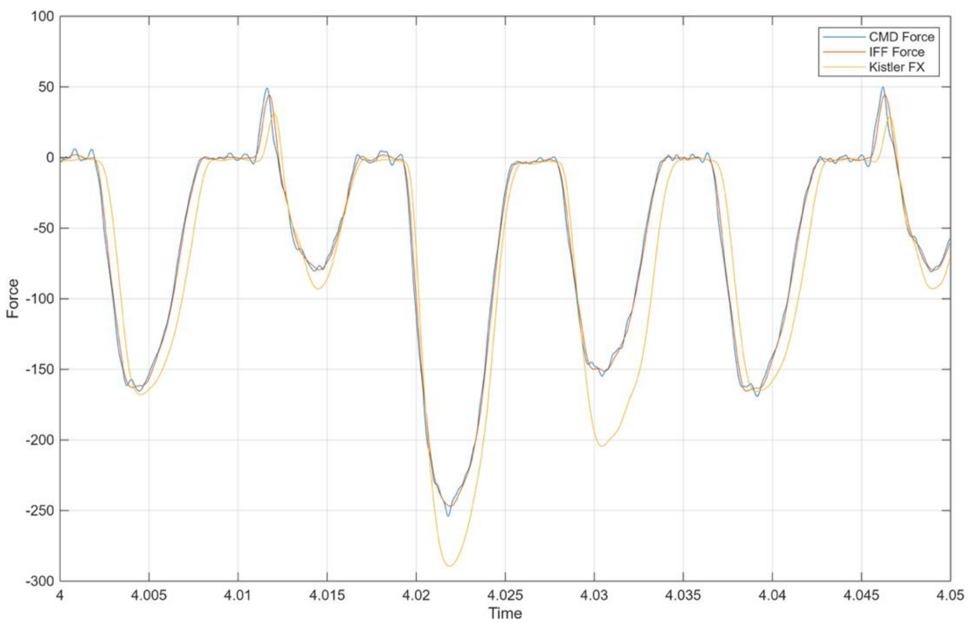

Figure A.51 Ti 6Al-4V x-direction milling force comparison 0.175 mm/tooth (4-flute endmill)

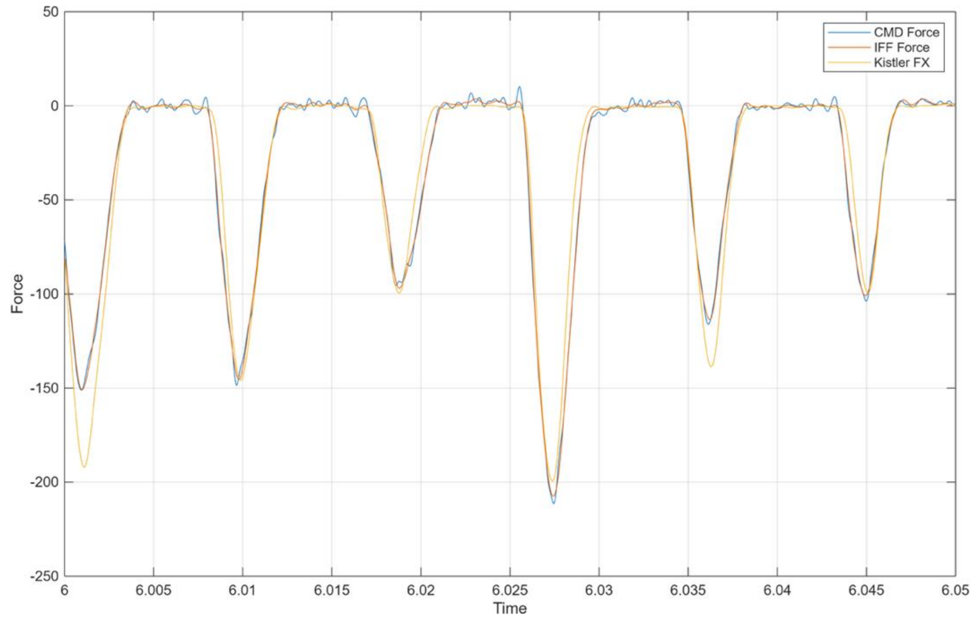

Figure A.52 Ti 6Al-4V x-direction milling force comparison 0.200 mm/tooth (4-flute endmill)

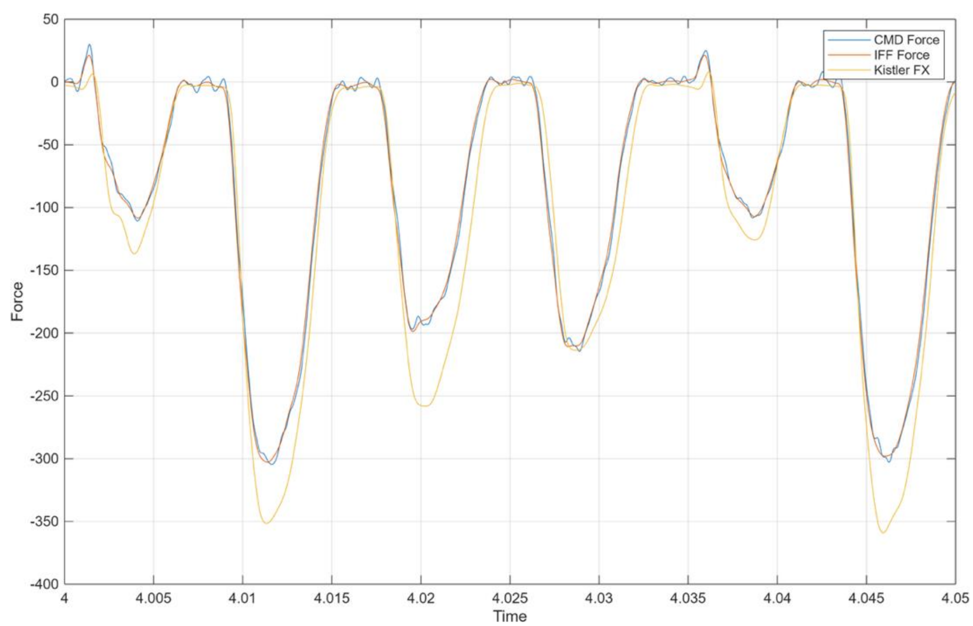

Figure A.53 Ti 6Al-4V x-direction milling force comparison 0.225 mm/tooth (4-flute endmill)

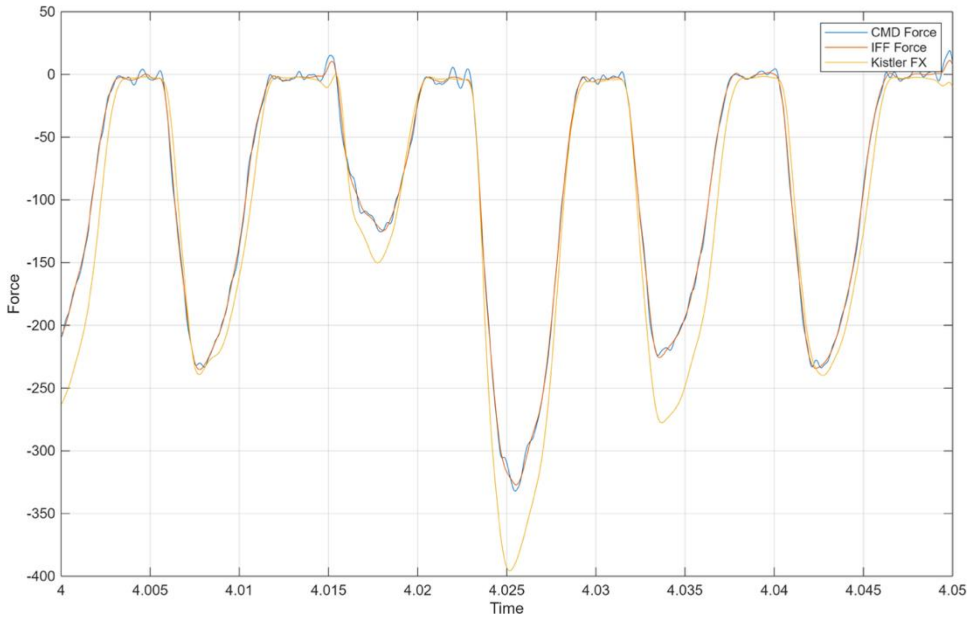

Figure A.54 Ti 6Al-4V x-direction milling force comparison 0.250 mm/tooth (4-flute endmill)

Table A.10 Ti 6Al-4V measurement comparison for four fluted endmill

	FPT	TSA	SD	Kistler	TSA/Kister	TSA/SD
	0.150	222.300	218.370	255.181	87%	102%
	0.175	254.020	246.790	289.370	88%	103%
	0.200	211.420	207.380	199.510	106%	102%
	0.225	304.660	302.750	359.060	85%	101%
Ti 6Al-4V 4 Flute	0.250	332.130	327.090	395.570	84%	102%

VITA

Jose Nazario Moreno was born to Jose Nazario Ruiz and Cecilia Nazario Moreno. Jose grew up in Knoxville, Tennessee and attended Knoxville Catholic High School. Jose received his bachelor's in science in Mechanical Engineering at Case Western Reserve University in January of 2018. After graduation, Jose worked as a manufacturing engineer and continued his education by receiving his master's in science in Mechanical Engineering in August of 2024 and his Pd.D. in Mechanical Engineering in August of 2025 from the University of Tennessee – Knoxville.